

DEVELOPMENT OF VISIBLE-LIGHT-ACTIVE  
PHOTOCATALYST FOR HYDROGEN PRODUCTION AND  
ENVIRONMENTAL APPLICATION

Thesis by

Jina Choi

In Partial Fulfillment of the Requirements

for the Degree of

Doctor of Philosophy

California Institute of Technology

Pasadena, California

2010

(Defended October 13, 2009)

© 2010

Jina Choi

All Rights Reserved

## ACKNOWLEDGEMENTS

Over the last six years of my graduate school time at Caltech, I have learned great things not only about science and academics, but also about the life, the truth, and the faith. It was a quite tough lesson especially in the beginning, but I have to say I have truly enjoyed every moment of learning and I am so grateful to have these kinds of experience in my life. I believe this is possible only because of all the people supporting me in many ways and I would like to acknowledge them.

First of all, I would like to thank my advisor, Prof. Michael Hoffmann, for all the support and guide throughout the years. He gave me many opportunities, which are very important to build up my academic career, and he was always supportive whenever I proposed new research topics or brought some problems of ongoing study or even personal matter. I also thank to the committee members, Prof. Paul Wennberg, Prof. Harry Gray in Chemistry, and Prof. Mark Davis in Chemical Engineering. As the option representative, Prof. Paul Wennberg was always ready to help and cheer me when I went through a hard time in the beginning as the international graduate student. Prof. Harry Gray and Prof. Mark Davis gave me helpful comments for future research. I also thank Prof. Nathan Lewis in Chemistry, who served as a committee chair of my Ph.D. candidacy exam, for his great advice in the middle of graduate research.

Also, I want to thank all my collaborators. Dr. Suyong Ryu and Dr. Bill Balcerski help me when I started my first research works in the lab. and Prof. Hyunwoong Park helps me to figure out a new research topic when he was a postdoc in Hoffman group. Prof. Luciana Silva who was a visiting professor from Brazil showed me her passion for science and soccer when we worked together and also sent me a greeting postcard and

photo-book of her hometown, Salvador, when she went back. Prof. Wonyong Choi and Prof. Kwang-ho Choo gave me helpful comments not only for my research, but also for my future academic career during their sabbatical staying at Caltech. I would like to thank Dr. A. J. Colussi for his insightful comments during every group meeting and Dr. Nathan Dalleska for his great technical support. I also worked with several visiting students and surf students like Sheng Hong Soong and Ning Du. They helped some experiments, and at the same time, gave me a great opportunity to help and teach them as a mentor.

I would like to thank all the former and current members of Hoffmann group for the helps. We had many group meetings, lab cleaning/organization (which is the most difficult job!), and fun group activities together; Dr. Christopher Boxe, Dr. Marcelo Guzman, and Dr. Chad Vercitis welcomed me when I joined Hoffmann group and showed good examples in academic after graduation. Jie Cheng was the one of the longest friend in the lab. and Dr. Shinichi Enami was always a supportive friend. Tammy Campbell and Rifka Kameel were the best officemates and I am so grateful that I could have never-ending girls-only chatting time in the office. Dr. Rich Wildman was a super-nice friend and my savior in the first year. Dr. Megan Ferguson and Dr. Kate Campbell were great woman colleagues when I worked in Prof. Janet Hering group. I also thank all the department/Keck lab. crew, Fran Matzen, Cecilia Gamboa, Linda Scott, Dian Buchness, and Mike Vondrus for their support and kindness.

I want to thank all my friends that I met during my graduate school life for their help and encouragement. Especially, I thank Dong-whan Kim and Jung-sook Kim GSN for their spiritual advice. Through their passion and dedication, I could learn and practice

what the faith is and how I should live my life as Jesus' disciple and as a lifetime Soonjang, which means a true spiritual leader serving others with love.

Finally, I want to give all my thanks to my family. My husband, Wonhee is my biggest supporter, greatest friend, and closest spiritual partner in all ways. I truly believe Wonhee is a man who God sent to me to express His love and show His will in my life. I also thank my beloved parents, sister Jihye and brother Jiwon. With their consistent love, support, and prayers in tears, I could be able to go through all the hardships. My parents-in-law always supported and cheered me so that I could focus on my study.

## ABSTRACT

Semiconductor photocatalysis has been intensively studied in recent decades for a wide variety of application such as hydrogen production from water splitting and water and air treatment. The majority of photocatalysts are, however, wide band-gap semiconductors which are active only under UV irradiation. In order to effectively utilize visible solar radiation, this thesis investigates various types of visible-light active photocatalysts including metal ion-doped  $\text{TiO}_2$ , nanocomposites of potassium niobate ( $\text{KNbO}_3$ ) and CdS with Ni co-catalyst, and a mixed-phase CdS matrix interlinked with elemental Pt deposits.

Thirteen different metal ion-doped  $\text{TiO}_2$  nanoparticles are synthesized. I compare the effects of individual dopants on the resulting physicochemical properties and corresponding photocatalytic activities with respect to the catalysis of several reactions under visible-light irradiation. I found several metal ion-doped  $\text{TiO}_2$  nanoparticles such as Pt, Cr, and V had visible-light photocatalytic activities and the presence of rutile phase in these metal ion-doped  $\text{TiO}_2$  may affect their photoreactivities. In addition, visible-light photocatalytic activities of  $\text{TiO}_2$  are enhanced by co-doping with two metal ions.

Hybrid nanocomposite photocatalysts based on CdS nanoparticles (e.g.,  $\text{Ni}(0)/\text{NiO}/\text{KNbO}_3/\text{CdS}$ , Zeolite/CdS, and nanocomposites of Q-sized cubic phase CdS and bulk-phase hexagonal CdS interlinked with elemental Pt deposits) are also studied. Different types of CdS nanocomposite photocatalysts are synthesized, optimized, and characterized using various analytical techniques. It is shown that these nanocomposites can enhance inherent photocatalytic activity of bulk-phase CdS for hydrogen production via effective

charge separation of photogenerated electrons and holes in CdS under visible-light irradiation.

Additionally, a sub-pilot size hybrid electrochemical system with Bi-doped TiO<sub>2</sub> anodes and SS cathodes for the degradation of organic pollutants and simultaneous hydrogen production has been developed to make the electrochemical system more economically viable. This system degrades a variety of organic pollutants and real wastewater with simultaneous production of hydrogen at the current efficiencies of 50~70%. Furthermore, it is demonstrated that this electrochemical system can be driven by a photovoltaic (PV) cell.

**TABLE OF CONTENTS**

Abstract .....	vi
Table of Contents .....	viii
List of Figures .....	ix
List of Tables .....	xiii
Chapter 1: Introduction and Summary .....	1
Chapter 2: Effects of Single Metal-Ion Doping on the Visible-Light Photo-reactivity of TiO <sub>2</sub> .....	17
Chapter 3: Combinatorial Doping of TiO <sub>2</sub> with Platinum (Pt), Chromium (Cr), Vanadium (V), and Nickel (Ni) to Achieve Enhanced Photocatalytic Activity with Visible Light Irradiation .....	57
Chapter 4: Photocatalytic Production of Hydrogen on Ni/NiO/KNbO <sub>3</sub> /CdS Nanocomposite using Visible Light .....	89
Chapter 5: Photocatalytic Production of H <sub>2</sub> on Nanocomposite Catalysts .....	124
Chapter 6: Photocatalytic Hydrogen Production with Visible Light over Pt-Interlinked Hybrid Composites of Cubic-Phase and Hexagonal-Phase CdS .....	178
Chapter 7: Sub-Pilot-Scale Hybrid Electrochemical System for Water Treatment and Hydrogen Production using a Solar Panel .....	199

## LIST OF FIGURES

FIGURE	PAGE
Figure 1.1: Simplified mechanism of semiconductor photocatalytic process .....	12
Figure 1.2: Visible-light induced photocatalysis with sensitizations .....	13
Figure 2.1: XRD pattern measured for La-TiO <sub>2</sub> , Pt-TiO <sub>2</sub> , and Ru-TiO <sub>2</sub> at various calcination temperatures .....	41
Figure 2.2: The fraction of rutile (%) as a function of doping level of Pt(II) in TiO <sub>2</sub> .....	42
Figure 2.3: The fraction of rutile (%) as a function of valence state of dopant and ionic radius of trivalent ion dopants .....	43
Figure 2.4: BET surface area and the fraction of rutile of Pt-TiO <sub>2</sub> as function of calcination temperature .....	44
Figure 2.5: SEM images of Pt-TiO <sub>2</sub> and Cr-TiO <sub>2</sub> synthesized by sol-gel method .....	45
Figure 2.6: UV-vis diffuse reflectance spectra (DRS) for various M-TiO <sub>2</sub> samples .....	46
Figure 2.7: Visible-light Photocatalytic Activities of Pt-TiO <sub>2</sub> and Cr-TiO <sub>2</sub> : (a) The production of tri-iodide by iodide oxidation and (b) the degradation of phenol .....	47
Figure 2.8: Correlation between photocatalytic activities for MB degradation and fractions of rutile ( $X_R$ ) in Pt-TiO <sub>2</sub> with different doping level .....	48
Figure 2.9: Photocatalytic activities for I <sup>-</sup> oxidation in terms of the amount of I <sub>3</sub> <sup>-</sup> (μM) produced after 6 min at > 400 nm irradiation .....	49
Figure 3.1: XRD pattern measured for M-TiO <sub>2</sub> .....	74
Figure 3.2: UV/vis diffuse reflectance spectra (DRS) for M-TiO <sub>2</sub> samples .....	75
Figure 3.3: XRD pattern measured for Pt-Cr-TiO <sub>2</sub> and Cr-Ni-TiO <sub>2</sub> .....	76
Figure 3.4: SEM images of Pt(IV)-Cr-TiO <sub>2</sub> and 0.3 at.% Pt(II)-Cr-TiO <sub>2</sub> and EDS spectra of Pt(II)-Ni-TiO <sub>2</sub> .....	77

Figure 3.5: UV/vis diffuse reflectance spectra (DRS) for Pt-Cr-TiO <sub>2</sub> .....	78
Figure 3.6: UV/vis diffuse reflectance spectra (DRS) for Pt(II)-V-TiO <sub>2</sub> , Pt(II)-Ni-TiO <sub>2</sub> , Cr-Ni-TiO <sub>2</sub> , and Cr-V-TiO <sub>2</sub> .....	79
Figure 3.7: The comparison of MB degradation rate constant for various single-doped or co-doped TiO <sub>2</sub> samples .....	80
Figure 3.8: The production of tri-iodide by iodide oxidation with selected MM-TiO <sub>2</sub> under visible-light irradiation .....	81
Figure 3.9: The comparison of various single-doped or co-doped TiO <sub>2</sub> samples for iodide oxidation .....	82
Figure 3.10: The degradation of phenol with Pt-Cr-TiO <sub>2</sub> and Cr-V-TiO <sub>2</sub> under visible-light Irradiation .....	83
Figure 4.1: Schematic flow chart outlining the synthetic procedures for Ni/NiO/ KNbO <sub>3</sub> /CdS catalyst preparation .....	108
Figure 4.2: XRD patterns of KNbO <sub>3</sub> synthesized from different conditions .....	109
Figure 4.3: SEM images of KNbO <sub>3</sub> .....	110
Figure 4.4: TEM images of Ni/NiO/KNbO <sub>3</sub> /CdS nanocomposite .....	111
Figure 4.5: UV-vis diffuse reflectance spectra for Ni/NiO/ KNbO <sub>3</sub> /CdS .....	112
Figure 4.6: Effect of CdS loading on KNbO <sub>3</sub> surface on photocatalytic H <sub>2</sub> Production .....	113
Figure 4.7: Photocatalytic H <sub>2</sub> production as a function of oxidation states of Ni deposited on KNbO <sub>3</sub> . .....	114
Figure 4.8: H <sub>2</sub> production with Ni/NiO/KNbO <sub>3</sub> /CdS under natural sunlight irradiation on the rooftop of KECK laboratories at Caltech (August 2006) .....	115
Figure 4.9: Solvent effects on photocatalytic H <sub>2</sub> production .....	116
Figure 4.10: pH-dependent H <sub>2</sub> production .....	117
Figure 5.1: Fluorescence emission spectra of CdS colloids .....	152

Figure 5.2: Fluorescence emission intensity of CdS as a function of ethanol in water .....	153
Figure 5.3: Fluorescence emission spectra of CdS as a function of $[\text{SO}_3^{2-}]$ .....	154
Figure 5.4: Diffuse reflectance and fluorescence emission spectra of CdS embedded in NaY zeolite .....	155
Figure 5.5: $\text{H}_2$ production on nanoparticulate CdS as a function of pH .....	156
Figure 5.6: Plot of the energy gap, $\Delta E$ (eV), as a function of ethanol in water .....	157
Figure 5.7: $\text{H}_2$ production on various CdS, CdS/TiY zeolite, and CdS/NaY zeolite under visible-light irradiation .....	158
Figure 5.8: $\text{H}_2$ production on CdS/NaY zeolite as a function of ionic strength .....	159
Figure 5.9: $\text{H}_2$ production on Ni/NiO/ $\text{KNbO}_3$ /CdS nanocomposites .....	160
Figure 5.10: Comparison of $\text{H}_2$ production on Ni/NiO/ $\text{KNbO}_3$ /CdS under visible-light irradiation with UV light irradiation .....	161
Figure 5.11: $\text{H}_2$ production rates as a function of Ni (wt %) on Ni/NiO/ $\text{KNbO}_3$ /CdS .....	162
Figure 5.12: UV-vis diffuse reflectance spectra for Ni/NiO/ $\text{KNbO}_3$ /CdS .....	163
Figure 5.13: UV-vis spectra for Ni/NiO/ $\text{KNbO}_3$ /CdS as a function of the CdS (wt %) .....	164
Figure 5.14: $\text{H}_2$ production on Ni/NiO/ $\text{KNbO}_3$ /CdS vs. Ni/ $\text{KNbO}_3$ /CdS .....	165
Figure 5.15: $\text{H}_2$ production rates as a function of the electron donor on $\text{KNbO}_3$ /CdS .....	166
Figure 6.1: XRD patterns of the high-temperature, hexagonal phase CdS and cubic crystalline bulk-phase CdS .....	192
Figure 6.2: UV-vis diffuse reflectance spectra for quantum-sized c-CdS, yellow crystalline bulk-phase cubic c-CdS, and orange hexagonal hex-CdS .....	193
Figure 6.3: The structures of CdS .....	194
Figure 6.4: The schemes of synthesized nanocomposites .....	195
Figure 7.1: Schematic diagram of a sub-pilot hybrid electrochemical reactor .....	218

Figure 7.2: $E_{\text{cell}}-I_{\text{cell}}$ plot and the current density ( $J_{\text{cell}}$ ) as a function of the concentration of the electrolyte .....	219
Figure 7.3: Electrochemical degradation of methylene blue and triclosan as a function of applied current density .....	220
Figure 7.4: Electrochemical degradation of methylene blue as a function of different type and concentration of electrolytes .....	221
Figure 7.5: The substrates removal vs. COD removal for MB and phenol .....	222
Figure 7.6: Time profile of current efficiencies (ICE) and average current efficiencies (EOI) for various substrates oxidations .....	223
Figure 7.7: Electrochemical oxidation of industrial wastewater samples .....	224
Figure 7.8: Solar-powered rooftop experiment .....	225

## LIST OF TABLES

TABLE	PAGE
Table 1.1: Band-gap energies for several common semiconductor materials .....	14
Table 2.1: Ionic radii of dopants, rutile content by XRD, surface area, and color of various M-TiO <sub>2</sub> nanoparticles .....	50
Table 2.2: Visible-light photocatalytic activities of various M-TiO <sub>2</sub> samples for MB degradation, iodide oxidation and phenol degradation .....	51
Table 3.1: Characterization of MM-TiO <sub>2</sub> photocatalysts .....	84
Table 3.2: Photocatalytic activities of Pt(II)-Cr-TiO <sub>2</sub> with different doping level for iodide oxidation under visible-light irradiation .....	85
Table 4.1: Photocatalytic activities of potassium niobates nanocomposites for H <sub>2</sub> production from water-isopropanol mixed solution .....	118
Table 5.1: H <sub>2</sub> evolution rates of Q-CdS/KNbO <sub>3</sub> Nanocomposites .....	167
Table 6.1: H <sub>2</sub> production rates over CdS Composites with different sacrificial electron donors: isopropanol vs. sulfide/sulfite/hydroxide .....	196
Table 7.1: The degradation rate constants for anodic substrates oxidation .....	226
Table 7.2: The production rate, cathodic current efficiency (CE), and energy efficiency (EE) for H <sub>2</sub> production .....	227

# **Chapter 1**

## Introduction and Summary

## Photocatalysis

Semiconductor photocatalysis has received much attention during last three decades as a promising solution for both energy generation and environmental problems. Since the discovering of Fujishima and Honda<sup>1</sup> that water can be photo-electrochemically decomposed into hydrogen and oxygen using a semiconductor (TiO<sub>2</sub>) electrode under UV irradiation, extensive works have been carried out to produce hydrogen from water splitting using a variety of semiconductor photocatalysts. In recent years, scientific and engineering interest in heterogeneous photocatalysis has been also focused on environmental applications such as water treatment and air purification. Many review papers on semiconductor photocatalysis can be found in literature.<sup>2-6</sup>

Semiconductor photocatalysis is initiated by electron-hole pairs after bandgap excitation. When a photocatalyst is illuminated by light with energy equal to or greater than band-gap energy, the valence band electrons can be excited to the conduction band, leaving a positive hole in the valence band:



The excited electron-hole pairs can recombine, releasing the input energy as heat, with no chemical effect. However, if the electrons (and holes) migrate to the surface of the semiconductor without recombination, they can participate in various oxidation and reduction reactions with adsorbed species such as water, oxygen, and other organic or inorganic species. These oxidation and reduction reactions are the basic mechanisms of photocatalytic water/air remediation and photocatalytic hydrogen production, respectively. A simplified mechanism for photocatalytic process on a semiconductor is presented in Figure 1.1.

For photocatalytic water/air remediation as an environmental application, valence band (VB) holes are the important elements that induce the oxidative decomposition of environmental pollutants. The positive hole can oxidize pollutants directly, but mostly they react with water (i.e., hydroxide ion,  $\text{OH}^-$ ) to produce the hydroxyl radical ( $\bullet\text{OH}$ ), which is the very powerful oxidant with the oxidation potential of 2.8 V (NHE).  $\bullet\text{OH}$  rapidly attacks pollutants at the surface and in solution as well and can mineralize them into  $\text{CO}_2$ ,  $\text{H}_2\text{O}$ , etc.  $\text{TiO}_2$ , the most popular photocatalyst because of its relatively high activity, chemical stability, availability with low production costs, and non-toxicity has been widely studied and proven to have a potential to completely oxidize a variety of organic compounds, including persistent organic pollutants.

The reducing conduction band (CB) electrons are more important when photocatalytic reaction is applied for hydrogen production from water splitting. In order to initiate hydrogen production, the conduction band level must be more negative than the hydrogen production level:



The redox potential for overall reaction (eq. 1.2) at pH 7 is  $E_{\text{H}} = -1.23$  V (NHE), with the corresponding half-reactions of  $-0.41$  V (eq 1.4) and  $0.82$  V (eq 1.5), which gives a  $\Delta G^\circ = +237$  kJ/mole).<sup>7</sup>

A large number of metal oxides and sulfides have been examined as photocatalysts for hydrogen production and environmental application. The majority of the simple metal

oxide photocatalysts, however, are primarily active under UV irradiation ( $\lambda < 385$  nm or  $E_{\text{bg}} \geq 3.0$  eV), present in only a small portion of solar light (Table 1.1). For example,  $\text{TiO}_2$  has a wide band-gap energy of  $3.0 \sim 3.2$  eV which prevents the utilization of visible-light that accounts for most of solar energy. More recently, significant efforts have also been made to develop new or modified semiconductor photocatalysts that are capable of using visible-light ( $\lambda = 400\text{--}700$  nm) including metal ion doping, nonmetallic element doping, and sensitization with organic dyes or small band-gap semiconductors such as CdS.

Metal ion doping has been primarily studied to enhance the photocatalytic activity under UV irradiation. In recent years, however, extensive research works have focused on visible-light induced photocatalysis by metal ion-doped semiconductor, since some of these have shown the extended absorption spectra into visible-light region. This property has been explained by the excitation of electrons of dopant ion to the conduction band of semiconductor (i.e., a metal to conduction band charge-transfer). Numerous metal ions, including transition metal ions (e.g., vanadium, chromium, iron, nickel, cobalt, ruthenium and platinum) and rare earth metal ions (e.g., lanthanum, cerium, and ytterbium), have been investigated as potential dopants for visible-light induced photocatalysis. However, metal ion dopant can also serve as a recombination center, resulting in decreased photocatalytic activities.

The studies of visible-light active semiconductors doped with nonmetallic elements such as nitrogen (N), sulfur (S), and carbon (C) have been intensively carried out since the study of N-doped  $\text{TiO}_2$  by Asahi and coworkers in 2001.<sup>8</sup> It was originally proposed that N doping of  $\text{TiO}_2$  can shift its photo-response into the visible region by mixing of p

states of nitrogen with 2p states of lattice oxygen and increase photocatalytic activity by narrowing the  $\text{TiO}_2$  band-gap. However, more recent studies have shown both theoretically and experimentally that the nitrogen species result in localized N 2p states above the valence band and the electronic transitions from localized N 2p state to the CB are made in  $\text{TiO}_2$  under visible-light irradiation.<sup>9-11</sup> Unlike metal ion doping, nonmetallic dopants replace lattice oxygen and are less likely form recombination centers.

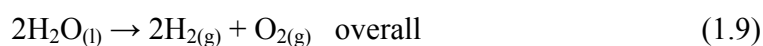
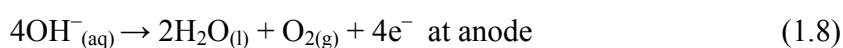
Sensitization methods are widely used to utilize visible-light for energy conversion. In case of sensitization with organic dyes, dye molecule electrons excited by visible light can be injected to the CB of semiconductor to initiate the catalytic reactions as shown in Figure 1.2(a). Similarly, sensitization with a small band-gap semiconductor is made by coupling a large band-gap semiconductor with a small band-gap semiconductor with a more negative conduction level (i.e., hybrid or composite photocatalyst). In composite photocatalyst, the CB electrons photo-generated from a small band-gap semiconductor by the absorption of visible-light can be injected to the CB of a large band gap semiconductor, while the photo-generated holes are trapped in a small band-gap semiconductor. Thus, an effective electron-hole separation can be achieved, as shown in Figure 1.2(b). CdS with band-gap energy of 2.4 eV has been frequently used to form hybrid or composite photocatalysts.

## **Electrolysis**

Water electrolysis is considered the easiest and cleanest method to produce a large quantity of hydrogen without carbon emission when the required electricity is derived from renewable energy resources. Water electrolysis, first demonstrated in 1800 by

Nicholson et al., has grown in a variety of industrial markets in recent years.<sup>12</sup> Two electrolyzer technologies, alkaline and proton exchange membrane (PEM), currently exist at the commercial level with solid oxide electrolysis in the research phase.<sup>13</sup> Nowadays the research has focused on development of a high efficiency electrolyzer. The U.S. Department of Energy (DOE) has established a target energy efficiency of 76% (corresponding to \$2.75/GGE H<sub>2</sub>) for hydrogen generation via electrolysis by 2015 from a current average energy efficiency of 62%.<sup>14</sup> In addition, solar-light-driven water electrolysis integrated with photovoltaic (PV) system has been suggested and widely tested, since the primary disadvantage of water electrolysis is the high electric consumption, especially in large-scale application.

Water electrolysis is defined as splitting of water with an electric current. When a direct current (DC) is passed between two electrodes immersed in water in the presence of electrolyte, water can be decomposed to hydrogen at the negatively biased electrode (cathode) and to oxygen at the positively biased electrode (anode). The voltage applied to the cell must be greater than the free energy of formation of water plus the corresponding activation and Ohmic losses:



In addition, there has been increasing interest in development of electrochemical oxidation technology for environmental application (i.e., water and wastewater treatment) because of its advantages, including versatility, energy efficiency, amenability to

automation, and robustness. This technology has been applied to the electrochemical degradation of various environmental organic contaminants such as dyes, phenols, surfactants, herbicides, and endocrine-disrupting chemicals, and (more recently) for the treatment of domestic wastewater, industrial wastewater and landfill leachate. The electrochemical oxidation of environmental organic contaminants can occur via direct oxidation on the anode surface or indirect oxidation mediated by electro-generated oxidants such as  $\text{OH}\cdot$  radicals, ozone,  $\text{H}_2\text{O}_2$ , and active chlorine species ( $\text{Cl}\cdot$ ,  $\text{Cl}_2\cdot^-$ , and  $\text{OCl}^-$ ) in the presence of chloride ions.

## **Thesis Overview and Summary**

This thesis consists of 7 chapters. Chapter 1 (this chapter) describes the general background of photocatalysis and electrolysis. Chapter 2 through Chapter 6 are research works for the development of visible-light active photocatalysts for environmental application and hydrogen production. Chapter 2 and Chapter 3 examine the metal ion-doped titanium dioxide ( $\text{TiO}_2$ ) photocatalysts for environmental applications, and Chapter 4 through Chapter 6 are studies of hybrid (composite) photocatalysts with cadmium sulfide ( $\text{CdS}$ ) semiconductor for hydrogen production. Finally, Chapter 7 focuses on a hybrid electrochemical system for the production of hydrogen and simultaneous degradation of organic pollutants.

Chapter 2 investigates 13 different metal ion-doped  $\text{TiO}_2$  nanoparticles synthesized by standard sol-gel method and compares the effects of individual dopants on the resulting physicochemical properties (e.g., a crystal structure and UV-vis absorption), and their corresponding photocatalytic activities with respect to the catalysis of several reactions

under visible-light irradiation. Metal ion doping results in changing anatase to rutile phase transformation (A-R phase transformation) temperature and the photophysical response of TiO<sub>2</sub>. However, the results of visible-light induced photocatalysis with metal ion-doped TiO<sub>2</sub> suggest that the presence of the rutile structure in the doped TiO<sub>2</sub> may affect photocatalytic activities of M-TiO<sub>2</sub> whereas their corresponding UV-vis absorption spectra seem to be not directly correlated with the visible-light photocatalytic activities of various metal ion-doped TiO<sub>2</sub> materials. This chapter was accepted at *Journal of Physical Chemistry C* in November 2009.

Chapter 3 examines the efficacy of double-doping with metal ions, including platinum (Pt), chromium (Cr), vanadium (V), and nickel (Ni), which are individually shown visible-light photoreactivity. The two metals co-doped TiO<sub>2</sub> materials are also prepared by standard sol-gel methods with the doping levels of 0.1 to 0.5 atom-%, and the changes of physicochemical properties induced by co-doping of two metal ions are investigated by various techniques such as XRD, BET surface-area measurement, SEM, and UV-Vis diffuse reflectance spectroscopy. Some of the co-doped TiO<sub>2</sub> nanoparticles showed the enhanced visible-light photocatalytic activities, and 0.3 atom-% Pt-Cr-TiO<sub>2</sub> and 0.3 atom-% Cr-V-TiO<sub>2</sub> showed the highest photoreactivity with respect to MB degradation and iodide oxidation, respectively. However, none of the co-doped TiO<sub>2</sub> samples have enhanced photocatalytic activity for phenol degradation when compared to their single-doped TiO<sub>2</sub> counterparts. This chapter is currently in press with the *Journal of Materials Research* for a focus issue (Energy and Environmental Sustainability) that will be published in January 2010.

Chapter 4 explores the Ni/NiO/KNbO<sub>3</sub>/CdS nanocomposite system synthesized by solid-state reactions. Their physicochemical properties and visible-light photocatalytic activity for H<sub>2</sub> production are investigated in the presence of isopropanol as an electron donor. It is shown that the inherent photocatalytic activity of bulk-phase CdS was enhanced by combining Q-sized CdS with KNbO<sub>3</sub> and Ni deposited on KNbO<sub>3</sub>, which is most likely due to effective charge separation of photogenerated electrons and holes in CdS that is achieved by electron injection into the conduction band of KNbO<sub>3</sub>, and the reduced states of niobium (e.g., Nb(IV) and Nb(III)) by mediating effective electron transfer to bound protons. We also observe that efficient attachment of Q-size CdS and the deposition of nickel on the KNbO<sub>3</sub> surface increases H<sub>2</sub> production rates. Other factors that influence H<sub>2</sub> production rate, including the nature of the electron donors and the solution pH are also determined in this chapter. This chapter was published in *Journal of Materials Chemistry* in 2008.

Chapter 5 further investigates CdS combined photocatalyst composite systems such as CdS/zeolite and CdS/potassium niobates (KNbO<sub>3</sub>) in the presence of various electron donors. The relative order of visible-light photocatalytic activity for hydrogen production is determined: Ni(0)/NiO/KNbO<sub>3</sub>/CdS > Ni(0)/KNbO<sub>3</sub>/CdS > KNbO<sub>3</sub>/CdS > CdS/NaY-Zeolite > CdS/TiY-Zeolite > CdS. The photoreactivity order with respect to the array of electron donors is 2-propanol > ethanol > methanol > sulfite > sulfide > H<sub>2</sub>O. The rates of hydrogen production from water and water-alcohol mixtures were correlated with fluorescent emission spectra and fluorescence lifetimes. In addition, the partial reduction of Cd(II) to Cd(0) on the surface of CdS in various composite systems is observed. This project is a collaboration with Dr. Su-Young Ryu and William Balcerski. I synthesized

and optimized the nanocomposites materials. This chapter is published in *Industrial & Engineering Chemistry Research* (Ryu, S.Y.; Choi, J.; Balcerski, W.; Lee, T.K.; Hoffmann, M. R. *Ind. & Eng. Chem. Res.* **2007**, *46*, 7476).

Chaper 6 examines a mixed-phase CdS matrix interlinked with elemental Pt deposits (i.e., c-CdS/Pt/hex-CdS composites) for visible-light induced photocatalytic hydrogen production. The quantum-sized cubic-phase CdS (c-CdS) with average particle diameters of 13 nm and a band-gap energy of 2.6 eV is synthesized and then coupled with hexagonal phase CdS (hex-CdS) in the bulk-phase size domain that has a band-gap energy of 2.4 eV with interlink of Pt metal deposits. Under visible-light irradiation, the resulting hybrid nanocomposites efficiently produce hydrogen in the presence of sodium sulfide and sodium sulfite at pH 14. Hydrogen production rates were very low with the same composite at pH 7 in a water-isopropanol solvent. The relative order of reactivity for the synthesized hybrid catalysts is: c-CdS/Pt/hex-CdS > Pt/c-CdS/hex-CdS > c-CdS/hex-CdS > Pt/hex-CdS > hex-CdS > quantum-sized c-CdS. This project is a collaboration with Dr. Luciana A. Silva and I participated in development of the synthetic method of hybrid materials, characterization, and discussion of results. (Silva, L.A.; Ryu, S.Y.; Choi, J.; Choi, W.; Hoffmann, M. R. *Journal of Physical Chemistry C* **2008**, *112*, 12069)

Finally Chapter 7 focuses on the hybridized electrochemical system for the production of hydrogen and simultaneous degradation of organic pollutants. Electrolytic hydrogen production is less economically viable due to its high electric energy consumption. By hybridizing electrolytic hydrogen production with water treatment, however, the electrochemical system can be more economically viable. Our group previously

introduced a hybridized electrochemical cell composed of a stainless steel cathode and a Bi-doped TiO<sub>2</sub> anode for the oxidation of phenol with simultaneous hydrogen production.<sup>15-17</sup> As a follow-on study, this chapter investigates a sub-pilot size scaled-up hybrid electrochemical system with Bi-doped TiO<sub>2</sub> anodes and SS cathodes for practical applications. This system degrades a variety of common organic pollutants such as methylene blue (MB), rhodamine B (Rh.B), phenol, and triclosan. Industrial wastewater is effectively treated as well. The kinetics of substrates oxidation are investigated as a function of the cell current, substrate concentration, and background electrolyte such as NaCl and Na<sub>2</sub>SO<sub>4</sub>; average current efficiencies were in the range of 4~22 %. The cathodic current efficiency and energy efficiency for simultaneous hydrogen production were determined to be 50~70% and 20~40 %, respectively. A solar-powered electrochemical system driven by a commercial photovoltaic (PV) panel for both wastewater treatment and hydrogen production is successfully demonstrated in this chapter.

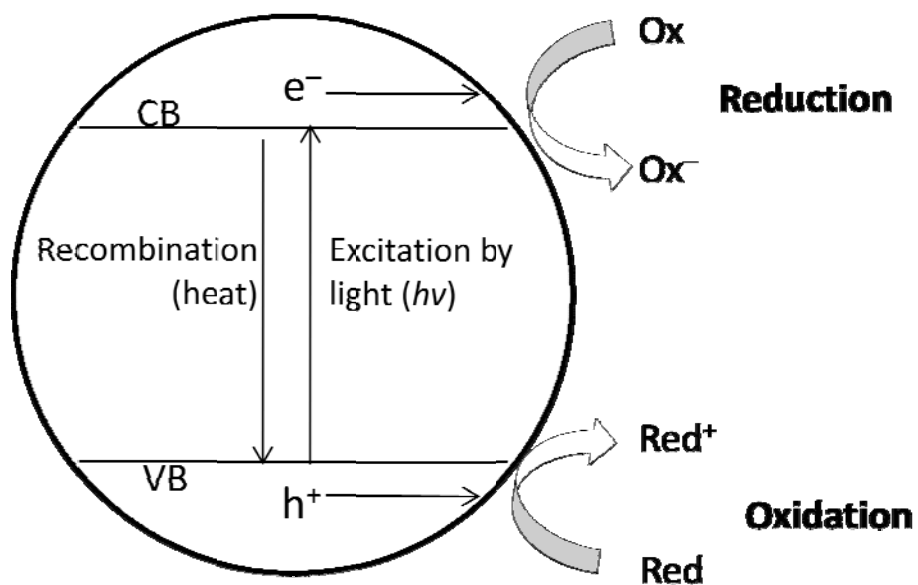


**Figure 1.1.** Simplified mechanism of semiconductor photocatalytic process

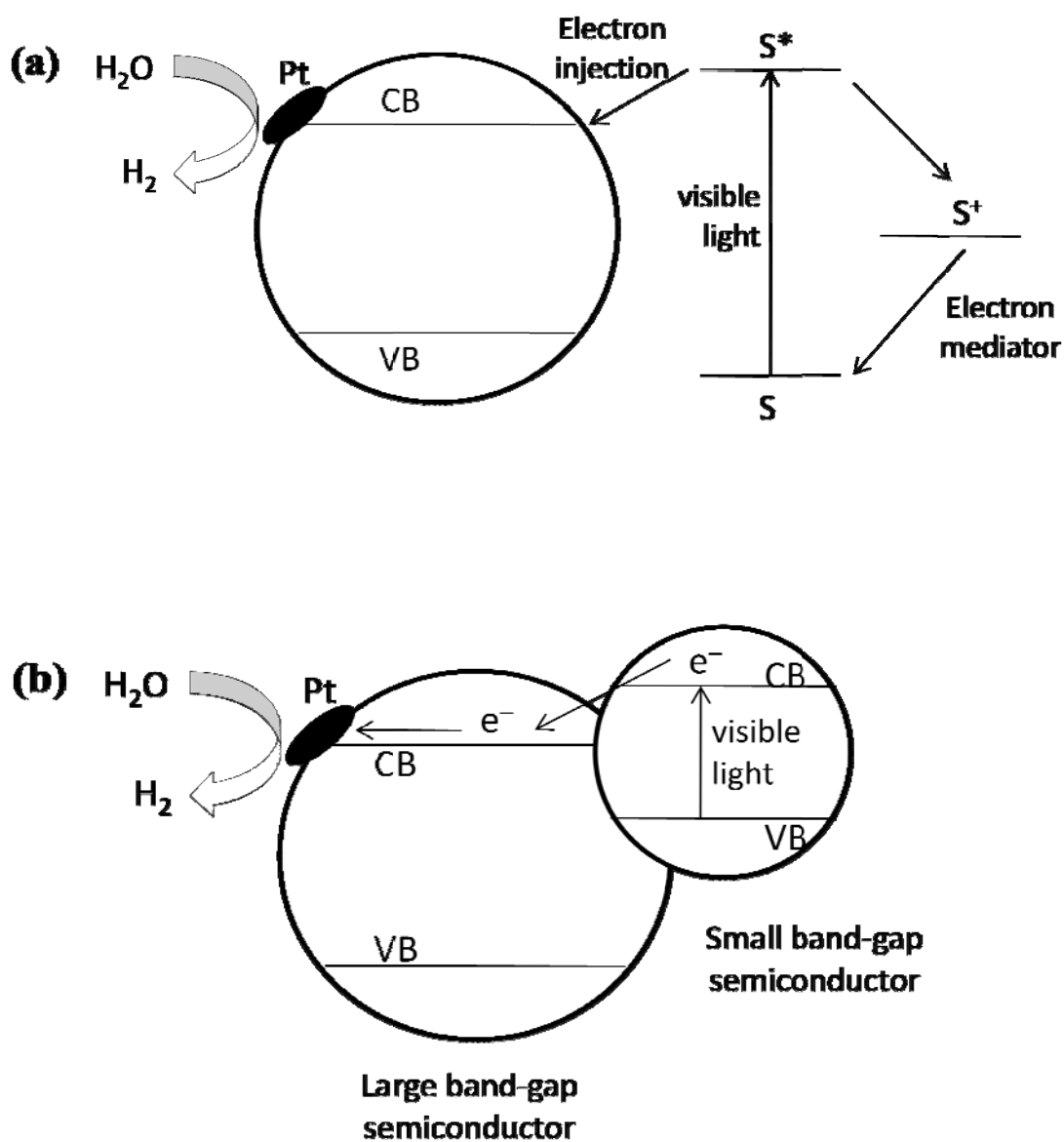


**Figure 1.2.** Schematic diagram of visible-light induced photocatalysis with sensitizations: (a) sensitization with organic dyes and (b) sensitization with small band-gap semiconductor (photocatalyst composites)

**TABLE 1.1.** Band-gap energies for several common semiconductor materials<sup>18,19</sup>

Semiconductor	Band-gap energy (eV)
Diamond	5.4
TiO <sub>2</sub>	3.0~3.2
WO <sub>3</sub>	2.7
ZnO	3.2
SnO <sub>2</sub>	3.5
SrTiO <sub>3</sub>	3.4
Fe <sub>2</sub> O <sub>3</sub>	2.2
CdS	2.4
ZnS	3.7
CdSe	1.7
GaP	2.3
GaAs	1.4
SiC	3.0

## References

- (1) Fujishima, A.; Honda, K. *Nature* **1972**, *238*, 37.
- (2) Hoffmann, M. R.; Martin, S. T.; Choi, W. Y.; Bahnemann, D. W. *Chem. Rev.* **1995**, *95*, 69.
- (3) Linsebigler, A. L.; Lu, G. Q.; Yates, J. T. *Chem. Rev.* **1995**, *95*, 735.
- (4) Mills, A.; LeHunte, S. *J. Photochem. Photobiol. A* **1997**, *108*, 1.
- (5) Zhao, J.; Yang, X. D. *Building and Environment* **2003**, *38*, 645.
- (6) Bahnemann, D. *Sol. Energ.* **2004**, *77*, 445.
- (7) Kudo, A.; Kato, H.; Tsuji, I. *Chem. Lett.* **2004**, *33*, 1534.
- (8) Asahi, R.; Morikawa, T.; Ohwaki, T.; Aoki, K.; Taga, Y. *Science* **2001**, *293*, 269.
- (9) Batzill, M.; Morales, E. H.; Diebold, U. *Phys. Rev. Lett.* **2006**, *96*,
- (10) Livraghi, S.; Paganini, M. C.; Giamello, E.; Selloni, A.; Di Valentin, C.; Pacchioni, G. *J. Am. Chem. Soc.* **2006**, *128*, 15666.
- (11) Di Valentin, C.; Pacchioni, G.; Selloni, A.; Livraghi, S.; Giamello, E. *J. Phys. Chem. B* **2005**, *109*, 11414.
- (12) <http://www.rsc.org/chemistryworld/Issues/2003/August/electrolysis.asp>
- (13) *Solar Hydrogen Generation: Toward a Renewable Energy Future*; Springer: New York, 2008.
- (14) *Solar and Wind Technologies for Hydrogen Production*, (available at [http://www.hydrogen.energy.gov/congress\\_reports.html](http://www.hydrogen.energy.gov/congress_reports.html).)
- (15) Park, H.; Vecitis, C. D.; Choi, W.; Weres, O.; Hoffmann, M. R. *J. Phys. Chem. C* **2008**, *112*, 885.
- (16) Park, H.; Vecitis, C. D.; Hoffmann, M. R. *J. Phys. Chem. A* **2008**, *112*, 7616.
- (17) Park, H.; Vecitis, C. D.; Hoffmann, M. R. *J. Phys. Chem. C* **2009**, *113*, 7935.

- (18) Bhatkhande, D. S.; Sawant, S. B.; Schouten, J. C.; Pangarkar, V. G. *J. Chem. Technol. Biotechnol.* **2004**, *79*, 354.
- (19) Gratzel, M. *Nature* **2001**, *414*, 338.

## Chapter 2

# Effects of Single Metal-Ion Doping on the Visible-Light Photo-reactivity of TiO<sub>2</sub>

The text of this chapter has been accepted for publication in *Journal of Physical Chemistry C*  
Choi, J.; Park, H.; Hoffmann, M.R. November 2009.

## Abstract

Titanium dioxide (M-TiO<sub>2</sub>), which was doped with 13 different metal ions (i.e., silver (Ag<sup>+</sup>), rubidium (Rb<sup>+</sup>), nickel (Ni<sup>2+</sup>), cobalt (Co<sup>2+</sup>), copper (Cu<sup>2+</sup>), vanadium (V<sup>3+</sup>), ruthenium (Ru<sup>3+</sup>), iron (Fe<sup>3+</sup>), osmium (Os<sup>3+</sup>), yttrium (Y<sup>3+</sup>), lanthanum (La<sup>3+</sup>), platinum (Pt<sup>4+</sup>, Pt<sup>2+</sup>), and chromium (Cr<sup>3+</sup>, Cr<sup>6+</sup>)) at doping levels ranging from 0.1 to 1.0 atom-% was synthesized by standard sol-gel methods and characterized by X-ray diffraction (XRD), BET surface area measurement, SEM, and UV-Vis diffuse reflectance spectroscopy (DRS). Doping with Pt(IV), Cr(III), V(III), and Fe(III) resulted in a lower anatase to rutile phase transformation (A-R phase transformation) temperature for the resultant TiO<sub>2</sub> particles, while doping with Ru(III) inhibited the A-R phase transformation. Metal-ion doping also resulted in a red-shift of the photophysical response of TiO<sub>2</sub> that was reflected in an extended absorption in the visible between 400 and 700 nm. In contrast, doping with Ag(I), Rb(I), Y(III), and La(III) did not result in a red-shift of the absorption spectrum of TiO<sub>2</sub>. As confirmed by elemental composition analysis by Energy Dispersive X-ray Spectroscopy (EDS), the latter group of ions was unable to be substituted for Ti(IV) in the crystalline matrix due to their incompatible ionic radii. The photocatalytic activities of doped TiO<sub>2</sub> samples were quantified in terms of the photo-bleaching of methylene blue (MB), the oxidation of iodide (I<sup>-</sup>), and the oxidative degradation of phenol in aqueous solution both under visible-light irradiation ( $\lambda > 400$  nm) and under broader-band UV-vis irradiation ( $\lambda > 320$  nm). Pt- and Cr-doped TiO<sub>2</sub>, which had relatively percentages of high rutile in the particle phase, showed significantly enhanced visible-light photocatalytic activity for all three reaction classes.

## Introduction

Titania ( $\text{TiO}_2$ ) has been extensively studied as a photocatalyst for applications such as water and air remediation because of its relatively high photocatalytic activity, robust chemical stability, relatively low production costs, and non-toxicity. Redox reactions of environmental interests are initiated on the  $\text{TiO}_2$  surface with trapped electron-hole after band-gap excitation. However,  $\text{TiO}_2$  is active only under near-ultraviolet irradiation due to its wide band gap energy of  $3.0 \sim 3.2$  eV. Therefore, significant efforts have been made over the last 20 years to develop modified  $\text{TiO}_2$  particles that are active under visible-light irradiation ( $\lambda > 400$  nm). Various strategies have been pursued including doping with metal ions (e.g., iron,<sup>1-3</sup> nickel,<sup>4,5</sup> vanadium,<sup>6-8</sup> and chromium<sup>9-11</sup>) or nonmetallic element (e.g., nitrogen,<sup>12-14</sup> sulfur,<sup>15,16</sup> and carbon<sup>17,18</sup>).

Metal ion-doped  $\text{TiO}_2$  has been primarily studied to enhance the photocatalytic activity under UV irradiation.<sup>19-23</sup> Choi et al.<sup>19</sup> reported that doping with  $\text{Fe}^{3+}$ ,  $\text{Ru}^{3+}$ ,  $\text{V}^{4+}$ ,  $\text{Mo}^{5+}$ ,  $\text{Os}^{3+}$ ,  $\text{Re}^{5+}$ , and  $\text{Rh}^{3+}$  ions increased photoactivity for the degradation of  $\text{CHCl}_3$  under UV irradiation, whereas doping with  $\text{Co}^{3+}$  and  $\text{Al}^{3+}$  decreased photoactivity. The relative photocatalytic efficiency of a metal-ion dopant depends on whether it serves as a mediator of interfacial charge transfer or as a recombination center. Chen et al.<sup>22</sup> also showed that Fe- or Ni-doped  $\text{TiO}_2$  have higher photoactivities than undoped  $\text{TiO}_2$  under UV irradiation.

Numerous metal ions have been investigated as potential dopants including iron,<sup>1-3</sup> nickel,<sup>4,5</sup> vanadium,<sup>6-8</sup> chromium,<sup>9-11</sup> platinum,<sup>24</sup> ruthenium,<sup>25</sup> and cobalt ions.<sup>26,27</sup> However, there are conflicting results on the effects of doping on the visible-light photoactivity of  $\text{TiO}_2$ . The wide-variability in reported impact on visible light activity

may be due to the specific preparation methods, the actual photolysis and experimental conditions used to quantify activity, and broad array of chemical reactions used to verify photoactivity over a broad range of wavelengths at  $\lambda > 400$  nm. For example, metal ion-doped TiO<sub>2</sub> is prepared in the form of powders<sup>2,25,27</sup> and films<sup>6,7</sup> by different synthetic methods such as sol-gel syntheses,<sup>6,8,11</sup> MOCVD,<sup>1</sup> hydrothermal synthesis,<sup>3</sup> solid-state reactions,<sup>4</sup> and ion implantation.<sup>10,28</sup> Photoactivity in the visible has been quantified using a wide array of substrates including dyes,<sup>1,3,6,8,11</sup> phenolic compounds,<sup>2,24,29</sup> acetaldehyde,<sup>6,27</sup> and nitric oxide.<sup>10,28</sup> Therefore, it is difficult to compare the net effects of metal-ion dopants on the photocatalytic activity of TiO<sub>2</sub>. Several reports<sup>30-32</sup> compare the effects of metal-ion dopants on visible-light photocatalytic activities of TiO<sub>2</sub> using high-throughput (HT) screening techniques. However, the physicochemical properties of various doped TiO<sub>2</sub> samples were not made in such combinatorial approaches.

Herein, we report on the synthesis of sol-gel TiO<sub>2</sub> doped with 13 different metal ions and compare the effects of individual dopants on the resulting physicochemical properties (e.g., a crystal structure and UV-vis absorption) and their corresponding photocatalytic activities with respect to the catalysis of several reactions under visible-light irradiation ( $\lambda > 400$  nm). In this regard, the photocatalytic activities of metal ion-doped TiO<sub>2</sub> are quantified in terms of the photo-bleaching of methylene blue (MB), the oxidation of iodide (I<sup>-</sup>), and the degradation of phenol in aqueous suspensions.

## **Experimental**

### **Chemicals**

The specific reagents used in this study include: titanium tetraisopropoxide (TTIP, Aldrich), absolute ethanol (Mallinckrodt), nitric acid (HNO<sub>3</sub>, Aldrich), methylene blue (MB, J.T. Baker), potassium iodide (KI, EM Science), and phenol (Mallinckrodt). The metal ion salts used in the preparations include: AgNO<sub>3</sub> (Mallinckrodt), Cu(NO<sub>3</sub>)<sub>2</sub>·4H<sub>2</sub>O (Alfar Aesar), Ni(NO<sub>3</sub>)<sub>2</sub>·6H<sub>2</sub>O (Alfar Aesar), Cr(NO<sub>3</sub>)<sub>3</sub>·9H<sub>2</sub>O (Aldrich), CrO<sub>3</sub> (Aldrich), CoCl<sub>2</sub> (Aldrich), VCl<sub>3</sub> (Aldrich), RuCl<sub>3</sub> (Aldrich), FeCl<sub>3</sub>·6H<sub>2</sub>O (Aldrich), YCl<sub>3</sub>·6H<sub>2</sub>O (Aldrich), LaCl<sub>3</sub>·7H<sub>2</sub>O (Aldrich), OsCl<sub>3</sub> (Aldrich), PtCl<sub>4</sub> (Aldrich), Pt(NH<sub>3</sub>)<sub>4</sub>(NO<sub>3</sub>)<sub>2</sub> (Alfar Aesar), RbClO<sub>4</sub> (MP Biomedicals Inc.).

### **Synthesis and Characterization of Catalysts**

TiO<sub>2</sub> nanoparticles were prepared by standard sol-gel methods. TiO<sub>2</sub> sols were prepared by dropwise addition of 5 mL of an ethanolic TTIP solution, which had been dissolved in 50 mL of absolute ethanol, into 50 mL of distilled water adjusted to pH 1.5 with nitric acid under vigorous stirring at room temperature. After continuously stirring for 24 hours, the resulting transparent solution was evaporated using a rotary evaporator at 45 °C and dried in the oven (70 °C) overnight. The obtained powder was calcined at various temperatures from 200 °C to 700 °C (typically at 400 °C) for 1 hour under air. Metal ion-doped TiO<sub>2</sub> samples (M-TiO<sub>2</sub>) were prepared according to the above procedure in the presence of the corresponding metal ion salt precursors to give a doping level from 0.1 to 1.0 atomic-% (at.%). The appropriate amount of metal-ion precursor was added to the distilled water before hydrolysis of TTIP and the remaining procedures were the same as described above. The doped TiO<sub>2</sub> products exhibited a variety of different colors. Doping with Cr<sup>3+</sup>, Cu<sup>2+</sup>, and Ni<sup>2+</sup> produced TiO<sub>2</sub> samples with a green color. Os<sup>3+</sup>, Pt<sup>4+</sup>

and  $\text{Pt}^{2+}$  doping- produced brown products;  $\text{Ru}^{3+}$  doping yielded a dark brown product;  $\text{V}^{3+}$  doping produced an orange product;  $\text{Fe}^{3+}$  doping produced a light orange product; and  $\text{Co}^{2+}$  doping gave a light yellow  $\text{TiO}_2$  product. All the other metal doped samples are white colored.

Crystal structure patterns of the M- $\text{TiO}_2$  powder samples were examined by X-ray diffraction (XRD) using a Philips diffractometer (X'pert Pro) with  $\text{Cu-K}\alpha$  radiation. Brunauer-Emmett-Teller (BET) surface area measurement were carried out by using  $\text{N}_2$  as the adsorptive gas (Micromeritics Gemini), and the morphology and elemental composition analysis were performed by scanning electron microscopy (SEM, LEO 1550VP) equipped with EDS (Energy Dispersive X-ray Spectroscopy). UV-vis diffuse reflectance spectra (DRS) were obtained on a Shimadzu UV-2101PC spectrophotometer.

### **Determination of Photocatalytic Activity**

The photocatalytic activities of the array of synthesized  $\text{TiO}_2$  samples were quantified by measuring the rates of photo-bleaching and degradation of MB, the rates of  $\text{I}^-$  oxidation, and the rates of degradation of phenol. Synthesized  $\text{TiO}_2$  samples were dispersed in distilled water ( $1 \text{ gL}^{-1}$ ). This was followed by the addition of an aliquot of the target substrate stock solution to the catalyst suspension to give a specific substrate concentration (i.e.,  $[\text{MB}]_0 = 10 \text{ }\mu\text{M}$ ,  $[\text{I}^-]_0 = 50 \text{ mM}$ , and  $[\text{PhOH}]_0 = 50 \text{ }\mu\text{M}$ ). The reaction suspensions pH were circum-neutral at  $t=0$ . Before irradiation, the suspension was stirred in the dark for 30 min to obtain a state of sorption equilibrium of the specific substrate on  $\text{TiO}_2$ . A high-pressure Hg(Xe) Arc lamp (500 W) was used as the light source. The incident light beam was passed through an IR water filter and a UV cut-off filter giving  $\lambda$

> 320 nm for UV irradiation or  $\lambda > 400$  nm for visible irradiation before being focused onto a cylindrical Pyrex reactor through a quartz window. The reactor was open to ambient laboratory air during photolysis with a few exceptions. Time-sequenced sample aliquots were collected from the reactor during the time-course of illumination for analysis and filtered through a 0.45  $\mu\text{m}$  PTFE syringe filter to remove  $\text{TiO}_2$  particles. Multiple photolysis experiments were performed under the identical reaction conditions to determine reproducibility.

The rate constants for the observed degradation of MB during photolysis were determined by measuring the absorbance of sample aliquots at 665 nm with a conventional spectrophotometer. In the case of the photocatalytic oxidation of iodide, triiodide ion ( $\text{I}_3^-$ ), which is the principal product of iodide oxidation in the presence of excess iodide ion, was determined spectrophotometrically by measuring its absorbance at 352 nm. The degradation of phenol in aqueous solution was measured using high performance liquid chromatography (HPLC, HP 1100 series with a C18 column).

## **Results and Discussion**

### **X-ray Diffraction Analysis of Metal-Ion-Doped $\text{TiO}_2$ (M- $\text{TiO}_2$ )**

The structure of  $\text{TiO}_2$  samples synthesized by standard sol-gel methods appeared to be amorphous thermal annealing; however, post-synthesis treatment at various temperatures ranging from 200 to 700  $^\circ\text{C}$  resulted in higher degree crystallinity primarily as anatase. The increasing calcination temperatures resulted in an increase in the intensity and sharpness of the anatase peaks. This trend is clearly indicative of an improvement in the degree of crystallinity corresponding to the formation of larger particles with fewer

defects. However, above a given temperature XRD peaks corresponding to the rutile phase appear. No diffraction peaks that could be attributed to doping metals were observed. Thus, the crystal structure of TiO<sub>2</sub> indicates a mixture of anatase and rutile for all the synthesized M-TiO<sub>2</sub> samples. These results suggest that at the doping levels we employed or the subsequent thermal treatment did not induce the formation of discrete impurity phases and that the metal ion appears to have been integrated into the basic structure of TiO<sub>2</sub>. However, it is conceivable that metal impurities, which were formed during synthesis, were nanoscopic or possibly dispersed on the surface. We have assumed that some of the metal ion dopants such as Pt<sup>4+</sup>, Cr<sup>3+</sup>, and V<sup>3+</sup> ions are most likely to be substituted at Ti<sup>4+</sup> sites within TiO<sub>2</sub> because ionic radii of dopants (Pt<sup>4+</sup>: 0.765 Å, Cr<sup>3+</sup>: 0.755 Å, and V<sup>3+</sup>: 0.78 Å) are similar to that of Ti<sup>4+</sup> (0.745 Å), whereas some other metal dopants such as Co<sup>2+</sup>, Cu<sup>2+</sup> and Pt<sup>2+</sup> ions are possibly located in interstitial positions of the lattice rather than directly in Ti<sup>4+</sup> sites because of the relatively large size difference between dopant ions (Co<sup>2+</sup>: 0.89 Å, Cu<sup>2+</sup>: 0.87 Å and Pt<sup>2+</sup>: 0.94 Å) and Ti<sup>4+</sup>. However, Ag<sup>+</sup>, Rb<sup>+</sup>, Y<sup>3+</sup> and La<sup>3+</sup> ions seem to be too large to be incorporated in TiO<sub>2</sub> lattice and thus, they are more likely to be found as dispersed metal oxides within the crystal matrix or they are dispersed on the surface of TiO<sub>2</sub>.

The anatase-to-rutile phase transformation (i.e., the A-R phase transformation) of pure TiO<sub>2</sub> normally occurs between 600 and 700 °C.<sup>33-36</sup> In our case, pure (undoped) TiO<sub>2</sub> samples that were calcined at 400 °C showed only the anatase phase. Calcination at 700 °C produced with a relatively small fraction of the rutile phase. However, it was observed that, in some cases, metal-ion doping altered the temperature of the A-R phase transformation of TiO<sub>2</sub>. In this regard, the XRD patterns of representative M-TiO<sub>2</sub>

samples that were calcined at different temperatures are shown in Figure 2.1. Similar to undoped TiO<sub>2</sub>, La-TiO<sub>2</sub> prepared at 400 °C was entirely in the anatase phase. Anatase remained as the dominant phase until a minor rutile component was observed at 700 °C (Figure 2.1a). However, in the case of Pt-TiO<sub>2</sub>, a rutile peak at  $2\theta = 27.5^\circ$  appeared at 400 °C as shown in Figure 2.1(b). This rutile peak was clearly dominant at 700 °C, while the anatase peak at  $2\theta = 25.7^\circ$  disappeared at 700 °C. In comparison, Ru-TiO<sub>2</sub> was almost exclusively pure anatase phase even at 700 °C in Figure 2.1(c), implying Ru ion inhibited A-R phase transformation of TiO<sub>2</sub>.

In order to compare the effects of metal-ion doping on the A-R phase transformation, the fraction of rutile,  $X_R$ , was calculated from the respective peak intensities using following equation:<sup>37</sup>

$$X_R (\%) = \{1 - (1 + 1.26I_R/I_A)^{-1}\} \times 100 \quad (2.1)$$

where  $I_R$  and  $I_A$  are the X-ray intensities of the rutile (101) and anatase (110) peaks, respectively. These relative rutile fractions are listed in Table 2.1 with ionic radii of the dopants. Pt-TiO<sub>2</sub>, Cr-, V-, Fe-, Y-, and Rb-TiO<sub>2</sub> also exhibited evidence of a rutile phase after calcinations at 400 °C. Their rutile fractions were estimated to be 15 ~ 30 %, whereas the undoped samples and remaining M-TiO<sub>2</sub> samples were in the pure anatase phase. Pt- and Y-TiO<sub>2</sub>, which were calcined at 700 °C, also exhibited high rutile fractions ( $X_R = 100\%$  and 62 %, respectively) when compared to undoped TiO<sub>2</sub> ( $X_R = 15\%$ ). Therefore, we conclude that certain dopants Pt, Cr, V, Fe, Y, and Rb) lowered the A-R phase transformation temperature of TiO<sub>2</sub>. In the specific case of Ru-TiO<sub>2</sub> calcined at 700 °C, the  $X_R$  fraction was estimated to be only 3%, which indicates that Ru increased

the apparent temperature of A-R phase transformation. Similar results have been reported elsewhere.<sup>1,38-42</sup>

However, some previous studies reported controversial results of doping effect on A-R phase transformation. For example, Ruiz et al.<sup>43</sup> reported that Cr-TiO<sub>2</sub> inhibited the A-R phase transformation. However, they observed an additional XRD peaks due to Cr<sub>2</sub>O<sub>3</sub> as well as TiO<sub>2</sub>. The formation of chromium oxide is most likely due to the high doping level of Cr at 5 ~ 10 at.%. In comparison, no Cr-related peaks were observed at our doping level of Cr (0.3 at.%). Therefore, it is likely that an effect of doping on A-R phase transformation temperature depends on the actual doping concentration. Doping at high Cr ion concentrations, which may result in Cr segregated on TiO<sub>2</sub> surface as opposed to direct substitution in Ti<sup>4+</sup> may impact the A-R phase transformation differently. Some studies also showed that doping with Ce, La, or Y ions also inhibits the A-R phase transformation.<sup>34,38,44</sup> The inhibiting phenomena of these dopants has been explained in terms of the formation of Ti-O-Ce (or La, Y) bonds at the interface since they could be located primarily on the surface of TiO<sub>2</sub> because of relatively large differences in the ionic radii resulting in inhibited crystal grain growth.<sup>45,46</sup> A similar inhibition of A-R phase transformation has been pointed out for TiO<sub>2</sub>/SiO<sub>2</sub> mixture as well.<sup>33,36</sup> However, our results indicate that La doping had little impact on the A-R phase transformation, while Y accelerated the transformation. It should be noted that the doping levels of La, Y, and Ce ions in TiO<sub>2</sub> are about 5 ~10 at.% in most studies in contrast to a level of 0.3 at.% in this study. In addition, Ghosh et al.<sup>38</sup> showed that peaks due to Y<sub>2</sub>Ti<sub>2</sub>O<sub>7</sub> or La<sub>4</sub>Ti<sub>9</sub>O<sub>24</sub> were identified in the XRD patterns of Y- or La-doped TiO<sub>2</sub>

samples that showed an inhibiting effect on the A-R phase transformation, whereas no Y or La-derived peaks were observed in our XRD results.

In order to investigate the effect of doping level concentration on the A-R phase transformation, the fractions of rutile ( $X_R$ ) in Pt(II)-TiO<sub>2</sub> with different Pt concentration from 0.1 to 1.0 at.% were determined. As shown in Figure 2.2,  $X_R$  fraction increases to approximately 22 % when Pt is doped in the range of 0.1~0.3 at.% and then decreases at higher doping levels in the range of 0.5~1.0 at.%. These results indicate that doping effect of metal ions on the A-R phase transformation is dependent on not only the intrinsic physicochemical properties of doping metal ion but also the concentrations of the dopants. Shannon et al.<sup>47</sup> also reported that the total impurity content can affect the transformation through the structure stuffing effect and large quantities of impurities may raise the transformation temperatures.

There are only a few concepts or rules to clarify the effects of impurities doped into TiO<sub>2</sub> on the A-R phase transformation. The primary factor that has been invoked in order to explain the doping effect on A-R phase transformation is the creation of oxygen vacancies since the A-R phase transformation involves a contraction or shrinking of the oxygen structure.<sup>47</sup> It is also believed that impurities can affect the rate of the transformation by modifying the defect structures of TiO<sub>2</sub>. Based on this concept, Shannon et al.<sup>47</sup> suggested that processes that increase oxygen vacancies such as the addition of ions of valence less than four and of small ionic radius which can enter the structure via direct substitution, accelerate the A-R phase transformation (and *vice versa*). They also hypothesized that an increase of oxygen vacancy concentration reduces the strain energy that must be overcome before the rearrangement of Ti-O octahedral occurs.

In addition, Mackenzie et al.<sup>48</sup> proposed a rank-ordered list of dopants in terms of their effectiveness in accelerating the A-R phase transformation and concluded that monovalent ions are more effective than divalent or trivalent ions since more oxygen vacancies would be created in the doping of monovalent ions compared to divalent or trivalent ions.

According to our results, however, there is no such a correlation observed between valence state of dopant and the fraction of rutile phase of M-TiO<sub>2</sub>. For example, the fractions of the rutile phase of Pt(IV)-TiO<sub>2</sub> and Cr(III)-TiO<sub>2</sub> are compared to Pt(II)-TiO<sub>2</sub> and Cr(VI)-TiO<sub>2</sub> in Table 2.1. The doping with Pt(IV) ion also accelerated the A-R phase transformation with the fraction of rutile from 0 % to 26 % and it was similar to rutile fraction of Pt(II)-TiO<sub>2</sub> sample (22 %). With respect to Cr doping, both Cr(VI) and Cr(III) accelerated the A-R phase transformation as well. In addition, the data as shown in Figure 2.3 demonstrates that there are no obvious correlations between  $X_R$  in various M-TiO<sub>2</sub> samples as a function of valence state or ionic radius of each metal dopant. Figure 2.3(a) also shows that the doping with monovalent ions was not more effective for A-R phase transformation than divalent or trivalent ions and the fraction of rutile was varied even with the same valence state of dopant ions. Figure 2.3(b) also shows the  $X_R$  fraction of the various trivalent ion-doped TiO<sub>2</sub> samples as a function of their ionic radii. It is clear that there is no correlation observed. Therefore, the valence state or ionic radius of dopant metal ion is not a good predictor of the effectiveness of specific dopants on the A-R phase transformation even if oxygen vacancies, which might be induced by metal-ion doping, affect the A-R phase transformation of M-TiO<sub>2</sub> samples.

### BET Surface Areas and SEM Characterization

BET surface areas (Table 2.1) were determined using nitrogen adsorption and desorption isotherms. The BET surface area of the unadulterated sol-gel synthesized  $\text{TiO}_2$ , which was calcined at  $400\text{ }^\circ\text{C}$ , was determined to be  $104\text{ m}^2\text{ g}^{-1}$ . In comparison, the surface area of the commercial product, Degussa P25  $\text{TiO}_2$ , is listed at  $50\text{ m}^2\text{ g}^{-1}$  and confirmed by our measurements. The BET surface areas of M- $\text{TiO}_2$  samples were found to be slightly larger than the undoped  $\text{TiO}_2$  ( $110\sim 130\text{ m}^2\text{ g}^{-1}$  for M- $\text{TiO}_2$  samples). Figure 2.4 shows the change of BET surface areas and rutile fractions of 0.3 at.% Pt(II)- $\text{TiO}_2$  as a function of calcination temperature. The BET surface area of Pt(II)- $\text{TiO}_2$  is  $\sim 150\text{ m}^2\text{ g}^{-1}$  without heat treatment and at  $200\text{ }^\circ\text{C}$  calcination. Calcination at  $400\text{ }^\circ\text{C}$  decreases the observed surface area as the rutile phase appears. At  $700\text{ }^\circ\text{C}$ , where Pt- $\text{TiO}_2$  is found in the pure rutile phase, the surface area was decreased to  $57\text{ m}^2\text{ g}^{-1}$ .

The SEM images of Pt- $\text{TiO}_2$  and Cr- $\text{TiO}_2$  particles, which are shown in Figure 2.5, show that the particles are highly aggregated and surfaces are clearly rough. In addition, the characteristic particle sizes become larger at higher calcination temperatures with a corresponding decrease in surface area. Images of other M- $\text{TiO}_2$  samples (which are not shown here) were similar to Pt- $\text{TiO}_2$  (or Cr- $\text{TiO}_2$ ).

The elemental composition of the various M- $\text{TiO}_2$  samples was estimated by EDS. The EDS spectra of most of M- $\text{TiO}_2$  samples including  $\text{TiO}_2$  doped with  $\text{Pt}^{2+}$  and  $\text{Ni}^{2+}$  ions (relatively larger ionic radii of metal dopants) showed no apparent signals directly related to metal dopants. These results indicate that these metal ions are well incorporated into  $\text{TiO}_2$  lattice (possibly interstitials of  $\text{TiO}_2$  in the case of Pt- $\text{TiO}_2$  or Ni- $\text{TiO}_2$ ) and not located on or near the surface of the particles. On the other hand, the EDS

spectra of the larger ionic radii dopants (M-TiO<sub>2</sub>) such as Ag-TiO<sub>2</sub> and Rb-TiO<sub>2</sub> showed the signals of the metal ions, which indicates that these metal-ion dopants (i.e., Ag, Rb, Y, and La) were located near surface region, not incorporated into TiO<sub>2</sub> lattice because of their much larger ionic radii than Ti<sup>4+</sup>.

### UV-vis Diffuse Reflectance Spectra

The UV-vis diffuse reflectance spectra of the array of metal ion-doped TiO<sub>2</sub> samples are shown in Figure 2.6. The sol-gel synthesized, undoped TiO<sub>2</sub> (TiO<sub>2</sub>-SG) and Degussa P25 TiO<sub>2</sub> are characterized by sharp absorption edges at about 400 nm ( $E_{bg} \sim 3.1$  eV). However, most of M-TiO<sub>2</sub> samples show extended absorption spectra into visible region in the range of 400 ~ 700 nm. Figure 2.6(a) shows TiO<sub>2</sub> samples doped with Fe, Cu, and Ni ions exhibited relatively small absorption only between 400 and 550 nm, while Co-, Os-, V-, Ru-, or Cr-doped TiO<sub>2</sub> samples showed substantial and broader absorption shoulders up to 700 nm (Figure 2.6b). Figure 2.6(c) illustrates the difference between the absorption spectra of Pt(IV)-TiO<sub>2</sub> and Pt(II)-TiO<sub>2</sub>. Pt(II)-TiO<sub>2</sub> shows a much broader absorption over most of the visible region similar to V-TiO<sub>2</sub> (Figure 2.6(b)). However, Pt(IV)-TiO<sub>2</sub> has a smaller absorption peak between 400 and 550 nm.

The extended absorption of the M-TiO<sub>2</sub> samples into the visible region has been explained in terms of the excitation of electrons of dopant ion to TiO<sub>2</sub> conduction band (i.e., a metal to conduction band charge-transfer). For example, the enhanced absorption observed for the M-TiO<sub>2</sub> samples doped with Fe, Cr, V, Co, Ni, and Cu in visible region can be considered to involve excitation of 3d electrons of dopant ion to TiO<sub>2</sub> conduction band according to their respective energy levels.<sup>2,3,6,7,49-51</sup> However, the absorption

spectra of modified TiO<sub>2</sub> in visible region may originate from defects associated with oxygen vacancies that give rise to colored centers.<sup>52,53</sup> Kuznetsov and Serpone pointed out the similarities of the spectra in the range of 400~600 nm shown among different types of visible-light-active TiO<sub>2</sub> samples and these similarities were found even in reduced TiO<sub>2</sub> samples.<sup>52,54,55</sup> They also observed that the absorption spectra were given by the sum of overlapping absorption bands with maxima at 2.81 eV and 2.55 eV, which correlate with oxygen vacancies.<sup>52,53</sup> In fact, the metal-ion dopants used in this study have different valence states than Ti<sup>4+</sup> and, as a consequence, may induce the generation of oxygen vacancies during synthesis. In addition, similarities of the absorption spectra in the range of 400~600 nm that Kuznetsov et al. observed were also found among several M-TiO<sub>2</sub> samples in this study, even though the absorption intensities were different. Therefore, the generation of new energy levels due to the injection of impurities within the bandgap coupled with the generation of oxygen vacancies by metal-ion doping may contribute to the observed visible-light absorption of the M-TiO<sub>2</sub> samples. Consistent with this hypothesis, we find that there are no visible-light extended absorption spectra for M-TiO<sub>2</sub> with Ag-, Rb-, Y-, and La-TiO<sub>2</sub>. As discussed above, the ionic radii of these dopants are too large to substitute with Ti<sup>4+</sup> in the lattice of TiO<sub>2</sub> and are considered to be dispersed on the surface of TiO<sub>2</sub> particles. This interpretation is consistent with the results of the EDS analysis.

### **Visible-light Photocatalytic Activities of M-TiO<sub>2</sub>**

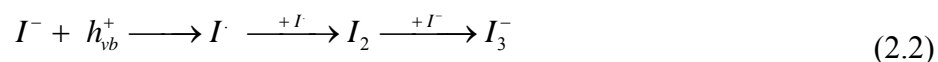
The photo-bleaching and degradation of MB under visible light irradiation follows apparent first-order kinetics. The observed reaction rate constants ( $k_{MB}$ ) with the various

M-TiO<sub>2</sub>, which are prepared at doping level of 0.3 at.% and calcined at 400 °C under both UV and visible-light irradiation, are listed in Table 2.2. Under visible-light irradiation at  $\lambda > 400$  nm,  $k_{\text{MB}}$  for direct photolysis without TiO<sub>2</sub> particles is estimated 0.003 min<sup>-1</sup>. The observed rate constant was increased slightly to 0.005 min<sup>-1</sup> in the presence of undoped TiO<sub>2</sub>. This activity may be due to additional light absorption above 400 nm of TiO<sub>2</sub> particles or enhanced direct electron injection from adsorbed MB to the conduction band of TiO<sub>2</sub>. However, Pt-, Cr-, V-, Ni-, and Rb-TiO<sub>2</sub> showed significantly enhanced photocatalytic activities under the visible-light irradiation by an order of magnitude ( $k_{\text{MB}} > 0.01$  min<sup>-1</sup>). Among all tested M-TiO<sub>2</sub> samples, Pt-TiO<sub>2</sub> (both Pt(II)-TiO<sub>2</sub> and Pt(IV)-TiO<sub>2</sub>) showed the best visible-light photo-activity for MB degradation. Most of other M-TiO<sub>2</sub> samples (i.e., Fe-, Co-, Cu-, Os-, Ag-, and Y-TiO<sub>2</sub>) showed slightly increased  $k_{\text{MB}}$ , while Ru- and La-TiO<sub>2</sub> had negligible effect when compared to undoped TiO<sub>2</sub>. None of the M-TiO<sub>2</sub> samples had lower photocatalytic activities when compared to the undoped SG-TiO<sub>2</sub>. Under UV irradiation ( $> 320$  nm), Pt-TiO<sub>2</sub> and Rb-TiO<sub>2</sub> had significantly enhanced photocatalytic activities for MB degradation as well. However, Cr- and V-TiO<sub>2</sub>, which had comparable  $k_{\text{MB}}$  values to Pt-TiO<sub>2</sub> under visible-light irradiation, had slightly enhanced photocatalytic activities under UV irradiation.

In some case, the rates of degradation of MB were increased even with several M-TiO<sub>2</sub> samples that did not show extended visible-light absorption. For example, Rb-TiO<sub>2</sub>, which has same absorption spectrum as undoped TiO<sub>2</sub>, gave a higher  $k_{\text{MB}}$  value than undoped TiO<sub>2</sub> under visible-light irradiation. In a similar fashion, Ag- and Y-TiO<sub>2</sub> also showed slightly enhanced visible-light photocatalytic activities. Therefore, the enhanced photocatalytic activities of Rb-, Ag-, and Y-TiO<sub>2</sub> for MB degradation were not attributed

to efficient utilization of visible-light with M-TiO<sub>2</sub>. It might be due to other effects of dopants located on the surface of TiO<sub>2</sub> such as enhanced transfer of charge carriers generated by visible-light absorbed MB molecules. Therefore, it suggests that MB seems to be inappropriate as model compounds to evaluate photocatalytic activities of new visible-light photocatalysts (i.e., modified TiO<sub>2</sub>), and visible-light photocatalytic activity should be evaluated by various reactions. Yan et al.<sup>56</sup> also reported that the photo-action spectrum for photocatalytic degradation of MB under visible-light irradiation is similar to the photoabsorption spectrum of the dye, which supports their suggestion that the MB molecules directly absorb photons, and thus the photoexcited electrons may be injected into the underlying M-TiO<sub>2</sub>. However, some studies only showed extended absorption of modified photocatalysts into visible range and enhanced degradation rates of dyes as compared to unmodified ones and then concluded that their modified photocatalysts have intrinsic visible-light photoactivities.<sup>3,8,15,16,57,58</sup>

Iodide is oxidized readily by valence-band holes or surface-bound hydroxyl radical in aqueous solution to form tri-iodide (I<sub>3</sub><sup>-</sup>) according to the reaction sequence:



The production of I<sub>3</sub><sup>-</sup> ions from I<sup>-</sup> oxidation during photolysis in the presence of Pt-TiO<sub>2</sub> and Cr-TiO<sub>2</sub> is shown in Figure 2.7(a). No I<sub>3</sub><sup>-</sup> was produced in the absence of TiO<sub>2</sub> particles at λ > 400 nm and undoped TiO<sub>2</sub> showed little photocatalytic activity with respect to the net photo-oxidation of I<sup>-</sup> to I<sub>3</sub><sup>-</sup>. In contrast, Cr-TiO<sub>2</sub> and Pt(IV)-TiO<sub>2</sub> had significantly enhanced photocatalytic activities with respect to iodide oxidation. Unlike undoped TiO<sub>2</sub>, the production of I<sub>3</sub><sup>-</sup> with Cr-TiO<sub>2</sub> or Pt(IV)-TiO<sub>2</sub> occurred in a relatively fast at initial period of irradiation followed by an approach to a steady-state that may be

due to the reduction of  $I_3^-$  to  $I^-$  by conduction band electrons (i.e., the rate of the back electron transfer reaction increases as the concentration of  $I_3^-$  ions increases and thus a steady-state is achieved).

The comparative photocatalytic activities of the all M-TiO<sub>2</sub> samples ranked in terms of the total amount of  $I_3^-$  produced during 15 min of irradiation are given in Table 2.2. Cr-TiO<sub>2</sub> and Pt(IV)-TiO<sub>2</sub> have substantially enhanced visible-light photocatalytic activity for  $I^-$  oxidation, while Pt(II)-, V-, and Ni-TiO<sub>2</sub> are slightly enhanced. In contrast, the other M-TiO<sub>2</sub> products had negligible activity during the 15 min reaction time. Unlike the degradation reaction of MB, Ag-, Rb-, Y-, and La-TiO<sub>2</sub> exhibited no enhanced effects on visible-light activities with respect to  $I^-$  oxidation.

The oxidation of iodide in suspensions of Pt-, Cr-, V-, and Ni-TiO<sub>2</sub>, which showed enhanced visible-light photocatalytic activities, were also investigated under UV irradiation at  $\lambda > 320$  nm. In the case of UV light illumination, Pt-TiO<sub>2</sub> had a higher photoactivity than undoped TiO<sub>2</sub>. However, the other M-TiO<sub>2</sub> materials showed almost same photocatalytic activities as undoped TiO<sub>2</sub>. Pt(II)-TiO<sub>2</sub> had comparable photocatalytic activities to Pt(IV)-TiO<sub>2</sub> under UV irradiation, whereas it had lower photoactivity than Pt(IV)-TiO<sub>2</sub> under visible-light irradiation.

The photocatalytic degradation of phenol vs. time in suspensions of Pt-TiO<sub>2</sub> and Cr-TiO<sub>2</sub> under visible-light irradiation is shown in Figure 2.7(b). Pt(IV)-TiO<sub>2</sub> was also the most effective photocatalyst for phenol degradation. Pt(II)-TiO<sub>2</sub> and Cr-TiO<sub>2</sub> also showed significantly enhanced visible-light photocatalytic activity, while V-TiO<sub>2</sub> had a moderately enhanced photoactivity. The results in terms of phenol degradation were similar to those observed for  $I^-$  oxidation. However, the other M-TiO<sub>2</sub> materials did not

show any improvement in photocatalytic activities for phenol degradation under visible-light irradiation as shown in Table 2.2.

From our kinetics observations, we can conclude that the visible-light photocatalytic activities of various M-TiO<sub>2</sub> materials are not directly correlated with their corresponding UV-vis absorption spectra of M-TiO<sub>2</sub>. For example, Ru- and Os-TiO<sub>2</sub> did not have significant visible-light photocatalytic activities, even though they had extended absorption bands above 420 nm. V-TiO<sub>2</sub>, which has larger visible absorption than Cr- and Pt-TiO<sub>2</sub>, was found to be less active under visible light illumination. The efficient absorption of visible-light does not appear to be a decisive factor that determines the visible-light photocatalytic activity of M-TiO<sub>2</sub>, although visible-light absorption is clearly necessary to initiate photo-reactions. Moreover, visible-light photocatalytic activity of M-TiO<sub>2</sub> material also appears to be substrate-dependent. For MB degradation, most of M-TiO<sub>2</sub> samples were found to have enhanced photocatalytic activities, although Pt-, Cr-, V-, Ni-, and Rb-TiO<sub>2</sub> were clearly the most efficient. The photo-oxidation rate of I<sup>-</sup> under visible-light irradiation was increased with Pt-, Cr-, V-, Ni-, and Fe-TiO<sub>2</sub> samples. However, only Pt-TiO<sub>2</sub> and Cr-TiO<sub>2</sub> showed significantly enhanced activities for the degradation of phenol. Therefore, it seems to be difficult to correlate visible-light photocatalytic activities with certain obvious physicochemical properties such as color, surface area, and absorption of M-TiO<sub>2</sub> materials as a function of the variation in M. However, it is interesting to note that visible-light photocatalytic activity of M-TiO<sub>2</sub> materials was influenced by the fraction of rutile in M-TiO<sub>2</sub>. Pt-TiO<sub>2</sub> and Cr-TiO<sub>2</sub>, which showed the most enhanced visible-light photocatalytic activities for all tested reactions, have higher fractions of rutile in TiO<sub>2</sub> as shown in Table 2.1. On the other hand, Ru-TiO<sub>2</sub>

and Os-TiO<sub>2</sub>, having pure anatase structure, did not show significantly enhanced visible-light photocatalytic activities for all reactions, although they exhibited relatively large absorption in visible region of the spectrum. In cases of Rb-TiO<sub>2</sub> and Y-TiO<sub>2</sub>, even though they had relatively high rutile contents, no enhancement in visible-light photoactivity was observed, since they had no measurable absorption in the visible region.

In order to investigate the effect of the fraction of rutile on visible-light photocatalytic activity, the photo-bleaching and degradation rate constants of MB,  $k_{MB}$ , under visible-light irradiation were measured as a function of the fractional content of rutile,  $X_R$ , in Pt(II)-TiO<sub>2</sub> calcined at 400 °C with different doping levels. As shown in Figure 2.8,  $k_{MB}$  is increased with an increasing fractional content of rutile in Pt-TiO<sub>2</sub>. This result suggests clearly that the fractional content of rutile in TiO<sub>2</sub> plays an important role in photocatalytic activity in our experiments.

TiO<sub>2</sub> particles in rutile phase are generally considered to be much less photochemically active than their anatase phase counterparts.<sup>59-61</sup> However, there are a number of specific chemical reactions for which higher photoactivity has been reported with rutile as the photocatalyst.<sup>62,63</sup> For example, Kim et al.<sup>63</sup> reported the Ni-TiO<sub>2</sub> in the rutile phase had a much higher photocatalytic activity than the anatase form of Ni-TiO<sub>2</sub> for the decomposition of 4-chlorophenol under both UV and visible light irradiation, whereas they found the anatase phase of undoped TiO<sub>2</sub> have higher photocatalytic activity than undoped rutile. Furthermore, Torimoto and Ohtani<sup>59</sup> established that the photoactive crystalline phase of anatase/rutile mixed TiO<sub>2</sub> powder is dependent even on the kind of photocatalytic reaction. They observed that the photoreactivities of TiO<sub>2</sub> in

anatase/rutile mixed phase for H<sub>2</sub> production were between pure anatase and pure rutile and shifted toward that of pure rutile with increase of rutile fraction; whereas the photoreactivities of mixed TiO<sub>2</sub> for Ag deposition and acetic acid decomposition were similar to that of pure rutile and pure anatase phases, respectively, and not dependent on the rutile fraction. In addition, it has been reported that TiO<sub>2</sub> in anatase/rutile mixed phases have higher activity than the pure anatase phase alone under UV irradiation.<sup>60,64,65</sup> Another example from our study shows that the visible-light photocatalytic activity of Pt(II)-TiO<sub>2</sub> with respect to I<sup>-</sup> oxidation is strongly influenced by the calcination temperature. The photocatalytic activity of Pt-TiO<sub>2</sub> gave a maximum at 400 °C where a mixed rutile/anatase structure of Pt-TiO<sub>2</sub> predominates. The pure anatase end member of Pt-TiO<sub>2</sub> at 200 °C and pure rutile end member of Pt-TiO<sub>2</sub> at 700 °C clearly were less photoactive than mixed-phase structural form of Pt-TiO<sub>2</sub> at 400 °C.

Higher photocatalytic activities of Pt-TiO<sub>2</sub> or Cr-TiO<sub>2</sub> having a significant fraction of the rutile phase due to calcinations at 400 °C may be due to a larger number of oxygen vacancies<sup>66-68</sup> For example, Li et al.<sup>68</sup> proposed that the formation of sub-energy defect level in Ce-TiO<sub>2</sub> may be one of the critical reasons to reduce the recombination of electron-hole pairs and to enhance photocatalytic activity. Ihara et al. also reported that the oxygen deficient TiO<sub>2</sub> induced by RF H<sub>2</sub> plasma treatment (without doping) absorbed visible light and showed visible light photocatalytic activity.<sup>69,70</sup> In a similar fashion, the formation of oxygen vacancies in Pt-TiO<sub>2</sub> or Cr-TiO<sub>2</sub>, which results in a lowering of the temperature of the A-R phase transformation leading to a rutile structure at 400 °C, appears to lead to an enhancement of the photocatalytic activities of M-TiO<sub>2</sub> under visible-light irradiation.

Our group previously investigated metal-ion doping on photocatalytic activities of TiO<sub>2</sub> under UV light irradiation in terms of the transient charge-carrier recombination dynamics.<sup>19,42,71,72</sup> Choi et al.<sup>19</sup> used laser flash photolysis measurements to show that the lifetimes of the blue electron in the Fe-, V-, Mo-, and Ru-doped TiO<sub>2</sub> were increased to ~50 ms, whereas undoped Q-sized TiO<sub>2</sub> had a shorter lifetime of < 200 μs. Hoffmann and co-workers found a good correlation between experimental quantum yields for oxidation or reduction and the measured absorption signals of the charge carriers that survived from recombination over nano- to microsecond time domain (i.e., an increase in concentration of the long-lived charge carriers is expected to result in higher photoreactivity). In addition, Martin et al.<sup>42,71,72</sup> used time-resolved microwave conductivity (TRMC) measurements of various TiO<sub>2</sub> samples including V-TiO<sub>2</sub> and Fe-TiO<sub>2</sub>. The charge-carrier recombination lifetime and the interfacial electron-transfer rate constants were estimated from the decays of TRMC signals and also found to correlate well with measured quantum efficiencies. Furthermore, in the case of V-doped TiO<sub>2</sub>, the vanadium doping was shown to influence photoreactivity varied in samples prepared at different sintering temperatures.<sup>42</sup> For examples, V(IV) is found to reduce the photoreactivity of TiO<sub>2</sub> by promoting charge-carrier recombination via electron trapping at  $>VO_2^+$  present in V-TiO<sub>2</sub> (25 °C) or via hole trapping at V(IV) impurities in surficial V<sub>2</sub>O<sub>5</sub> islands on V-TiO<sub>2</sub> (200 or 400 °C); whereas in case of V-TiO<sub>2</sub> prepared at 600 or 800 °C, substitutional V(IV) in the lattice of TiO<sub>2</sub> appears to act as a charge-carrier recombination center that resulted in reduced photoreactivity. The above observations emphasize that metal-ion dopants influence the photoreactivity of TiO<sub>2</sub> by altering the charge-carrier recombination and interfacial charge-transfer rate constants. In

conclusion, we believe that these effects are also important for the M-TiO<sub>2</sub> materials prepared as part of this study as well.

## Conclusions

In conclusion, we have synthesized an array of metal-doped titanium dioxide materials, M-TiO<sub>2</sub>, in order to evaluate their visible-light photocatalytic activities. Pt-, Cr-, V-, Fe-, Rb-, Y-TiO<sub>2</sub> lowered the temperature of the anatase-to-rutile phase transformation whereas Ru-TiO<sub>2</sub> increased the temperature of A-R phase transformation. The fraction of rutile in M-TiO<sub>2</sub> is observed to be dependent on the doping level. However, there appears to be no correlation between the effectiveness of an individual dopant on the A-R phase transformation and its valence state or ionic radius, as previously suggested.<sup>47,48</sup> The majority of M-TiO<sub>2</sub> materials prepared herein gave absorption spectra that were extended into visible beyond 400 nm. Ag-, Rb-, Y-, and La-TiO<sub>2</sub> did not change the original absorption spectrum of pristine SG-TiO<sub>2</sub>. As verified by EDS analysis, the latter group of ions were most likely not incorporated into the lattice of TiO<sub>2</sub> and most likely concentrated in near surface region because of their relatively large ionic radii. The photocatalytic activities of M-TiO<sub>2</sub> were evaluated for MB degradation, I<sup>-</sup> oxidation, and phenol degradation under visible-light irradiation at  $\lambda > 400$  nm. Pt-TiO<sub>2</sub> and Cr-TiO<sub>2</sub>, which were prepared at a 0.3 at% doping level and annealed at 400 °C, had a relatively high fraction of rutile and showed significantly enhanced photocatalytic activity compared to SG-TiO<sub>2</sub> for all test reactions under visible-light irradiation. These results indicate that the presence of the rutile structure in the doped TiO<sub>2</sub> may affect photocatalytic activities of M-TiO<sub>2</sub>. Pt-TiO<sub>2</sub> substantially improved the observed

photocatalytic activity under UV irradiation at  $\lambda > 320$  nm as well. On the other hand, V-, Rb-, Ni-, and Fe-TiO<sub>2</sub> showed visible-light photocatalytic activities only for one or two of the three test reactions.

## **Acknowledgements**

We gratefully acknowledge the generous support for this research that has been provided by the Northrop-Grumman Corporation. In particular, we would like to give special credit to Dr. Ronald Pirich for his enthusiastic encouragement and intellectual support for our joint projects over the years.

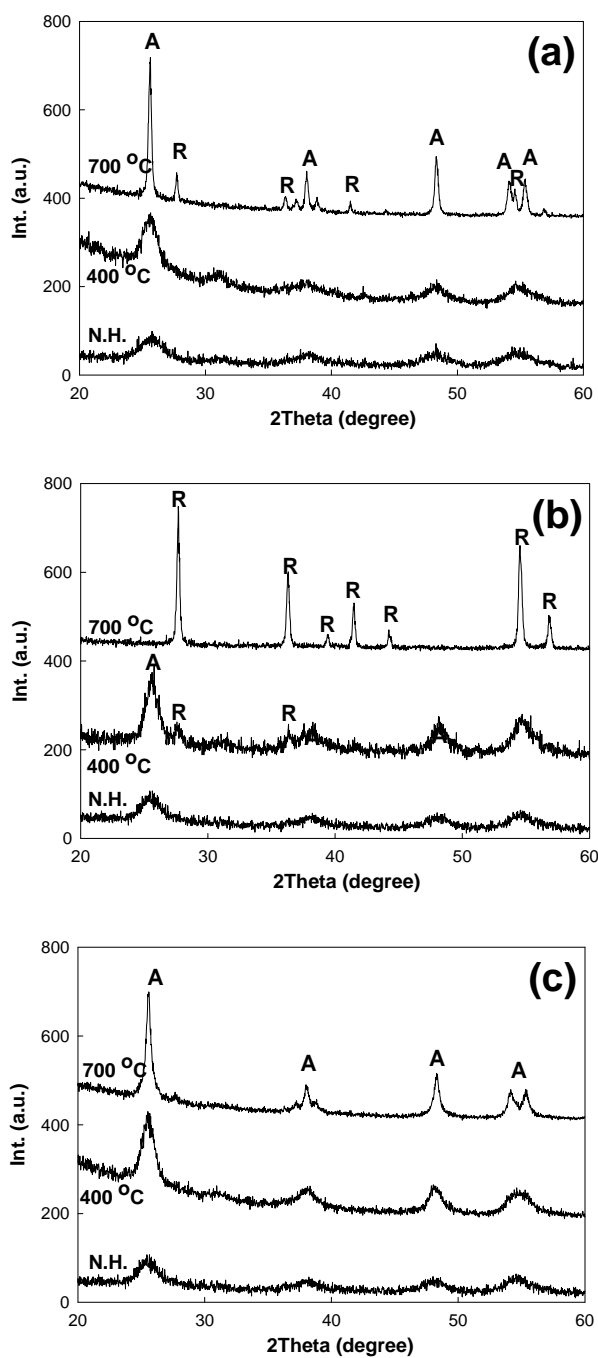


**Figure 2.1.** X-ray diffraction pattern measured for (a) 0.3 at.% La-TiO<sub>2</sub>, (b) 0.3 at.% Pt-TiO<sub>2</sub>, (c) 0.3 at.% Ru-TiO<sub>2</sub> with various calcination temperatures (at 700 °C, 400 °C, and no heat treatment)

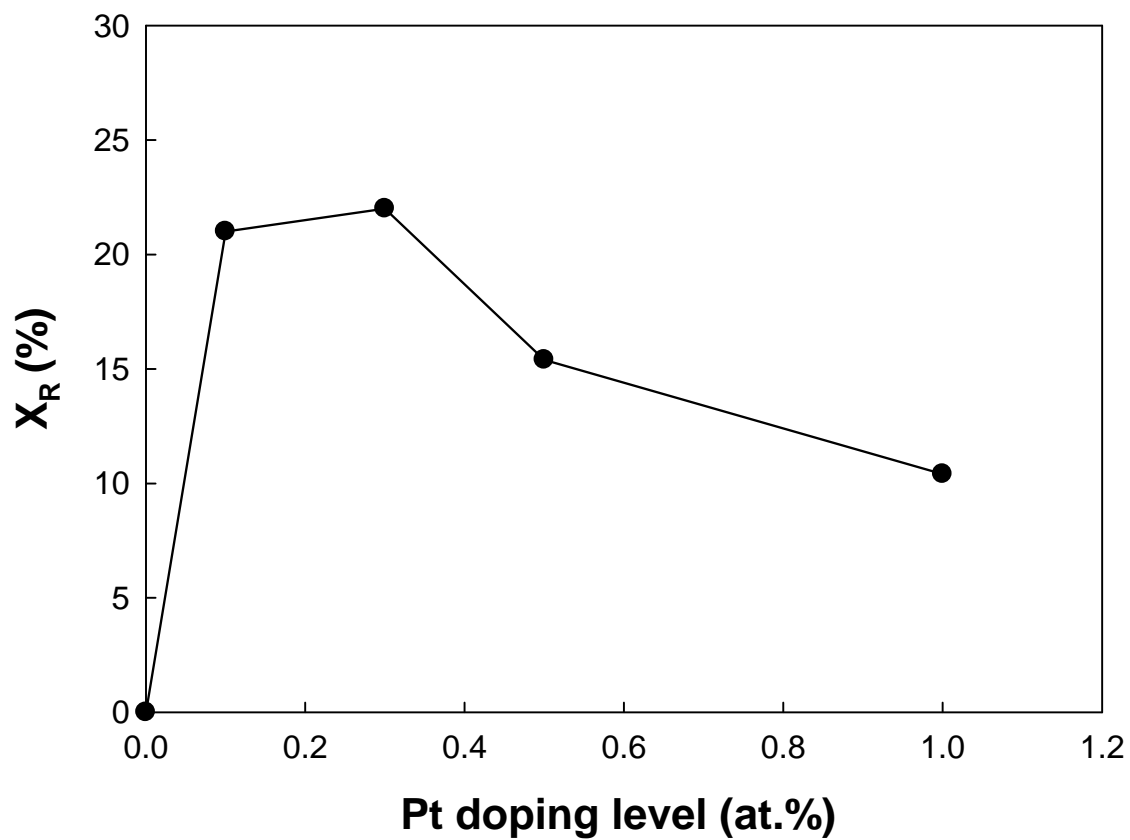


**Figure 2.2.** The fraction of rutile (%) as a function of doping level of Pt(II) in  $\text{TiO}_2$  (at.%). Samples have been prepared by sol-gel method and calcined at 400 °C for 1 hour.

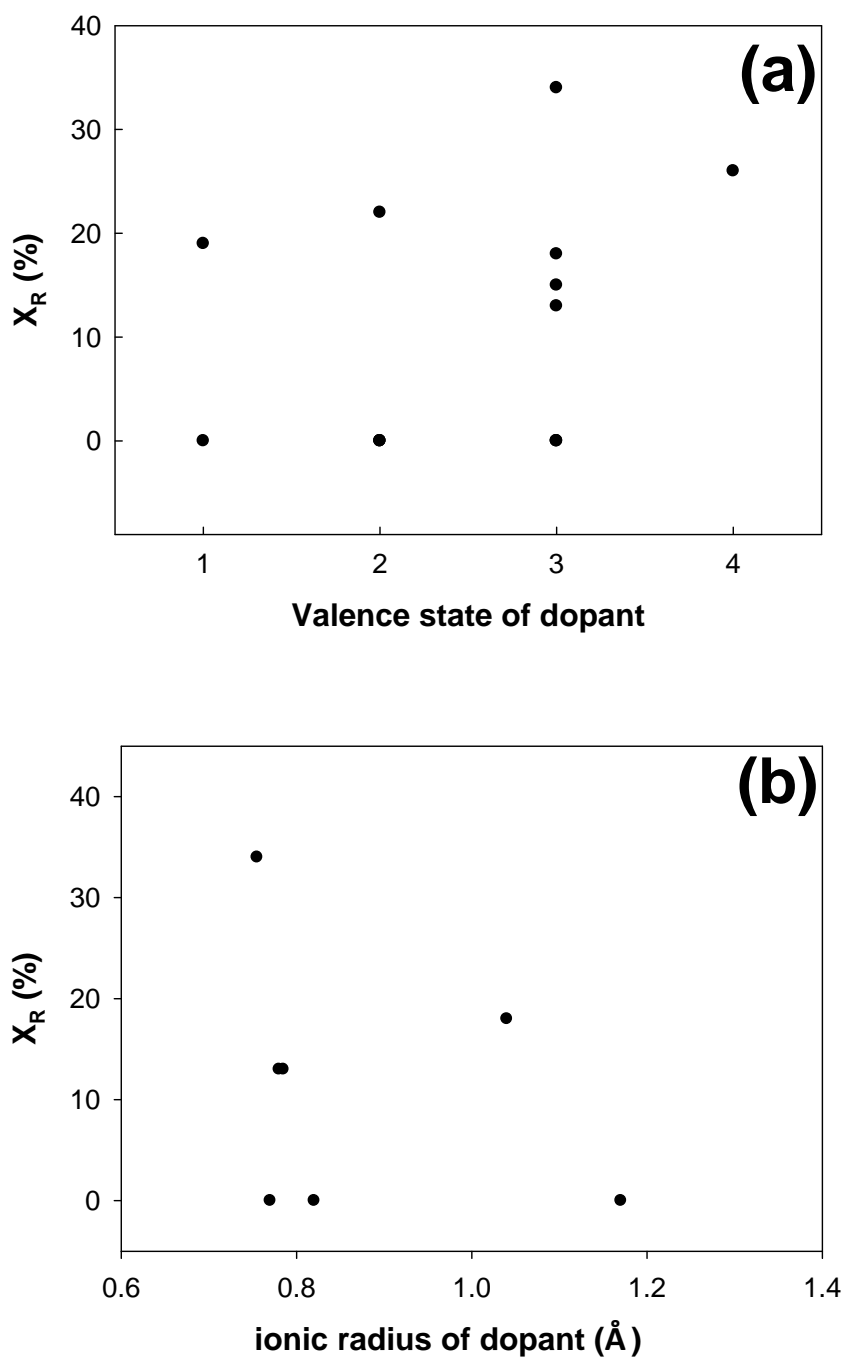


**Figure 2.3.** The fraction of rutile phase (%) in M-TiO<sub>2</sub> as a function of (a) valence state of dopant and (b) ionic radius of trivalent ion dopants

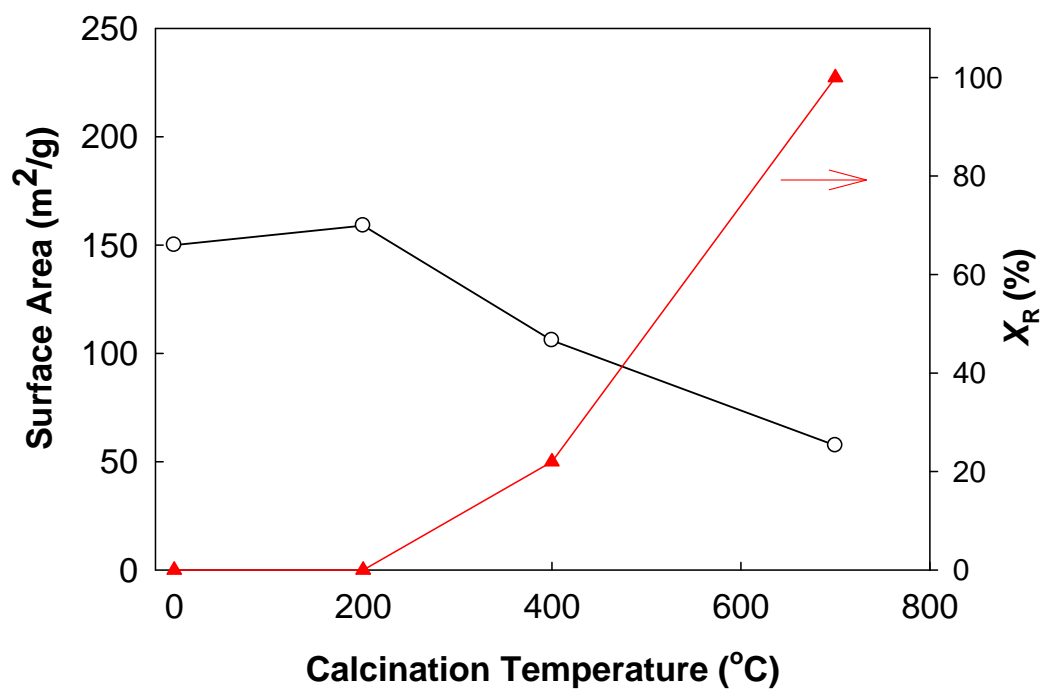


**Figure 2.4.** BET surface area and the fraction of rutile ( $X_R$ ) of 0.3 at.% Pt-TiO<sub>2</sub> as function of calcination temperature.

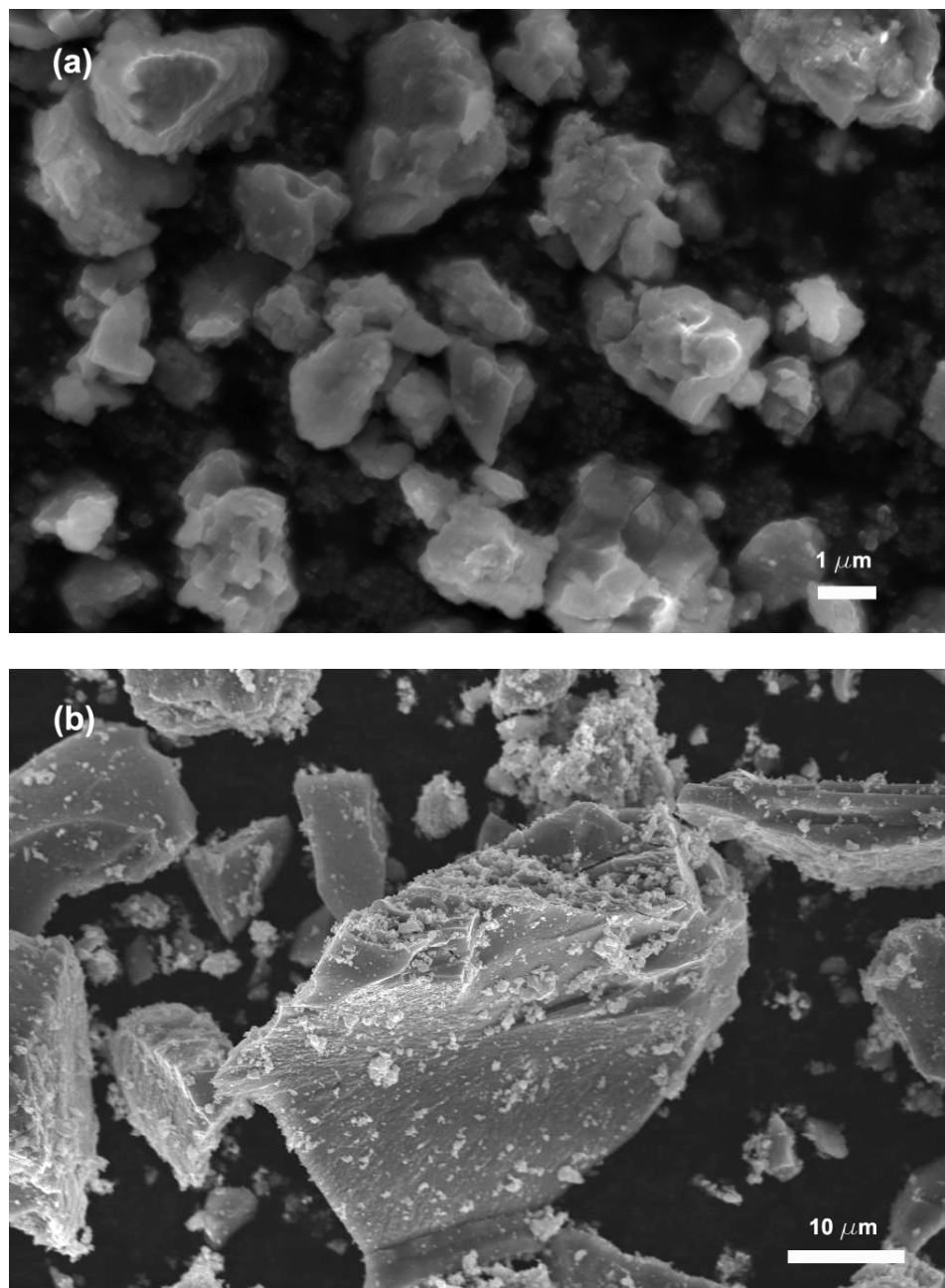


**Figure 2.5.** SEM images of (a) 0.3 at.% Pt-TiO<sub>2</sub> and (b) 0.3 at.% Cr-TiO<sub>2</sub> synthesized by sol-gel method with 400 °C calcination.

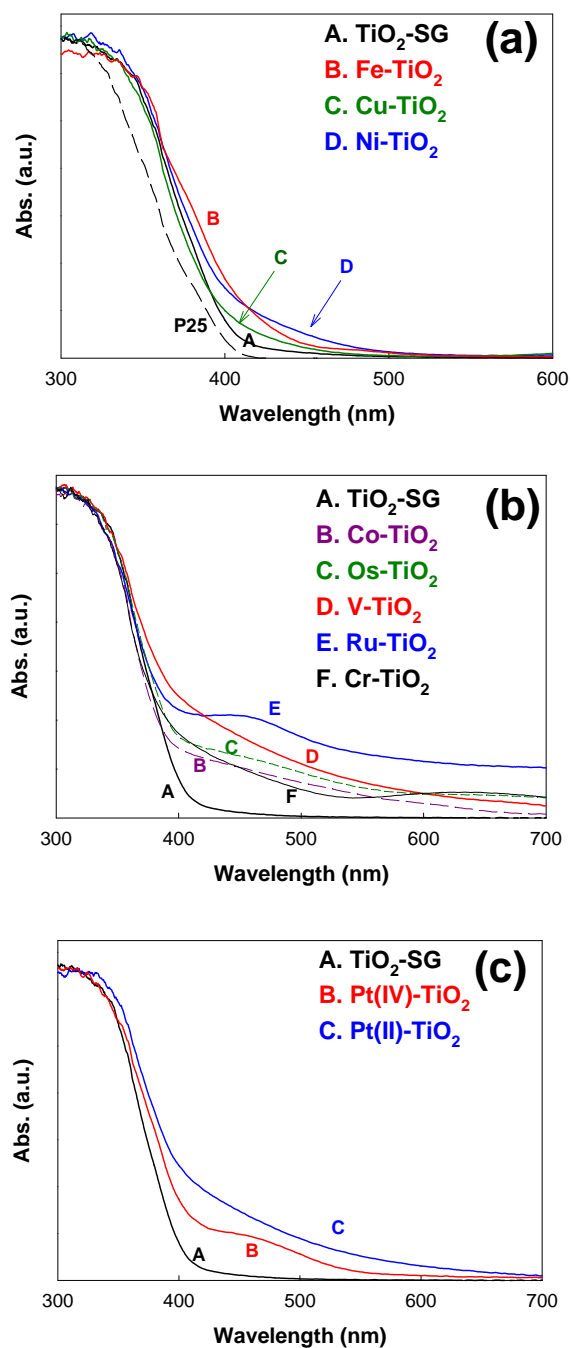


**Figure 2.6.** UV-vis diffuse reflectance spectra (DRS) for various M-TiO<sub>2</sub> samples (0.3 at.% doping). Absorption spectra for Ag-, Rb-, Y-, and La- TiO<sub>2</sub> samples, which are not shown here, are identical with that of undoped TiO<sub>2</sub>.

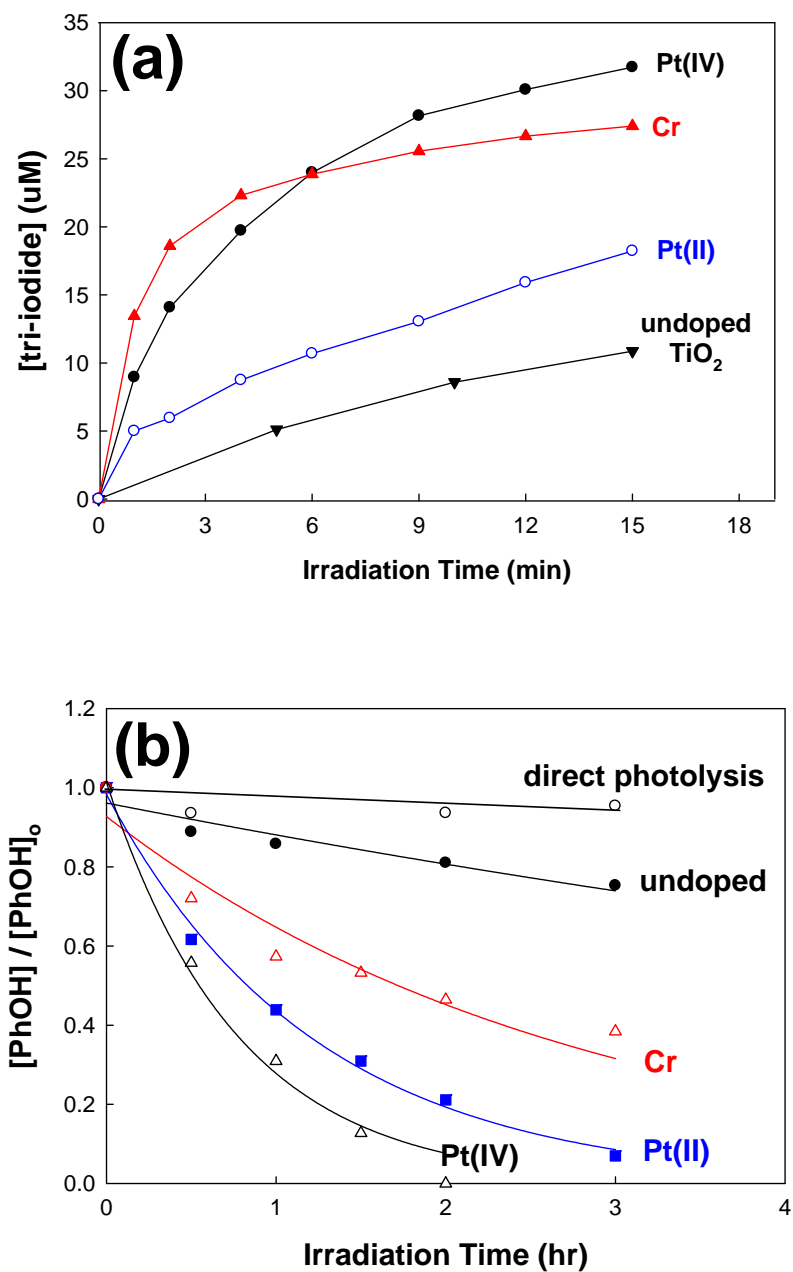


**Figure 2.7.** Visible-light photocatalytic activities of 0.3 at.% Pt-TiO<sub>2</sub> and 0.3 at.% Cr-TiO<sub>2</sub>: (a) The production of tri-iodide by iodide oxidation with  $[I^-]_0 = 50$  mM, (b) the degradation of phenol with  $[\text{phenol}]_0 = 50$   $\mu\text{M}$ . (total volume = 30 mL, 1 g/L suspension, 500 W,  $\lambda > 400$  nm)

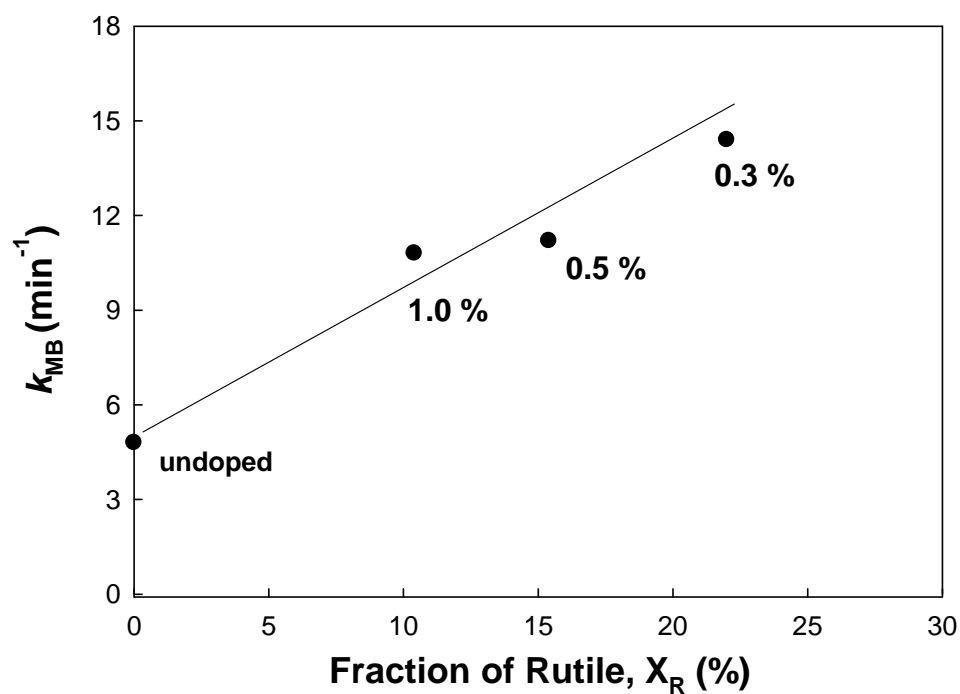


**Figure 2.8.** Correlation between photocatalytic activities for MB degradation (the degradation rate constant,  $k_{MB}$ ) at  $> 400$  nm irradiation and the fractions of rutile ( $X_R$ ) in Pt-TiO<sub>2</sub> prepared at 400 °C with different doping level

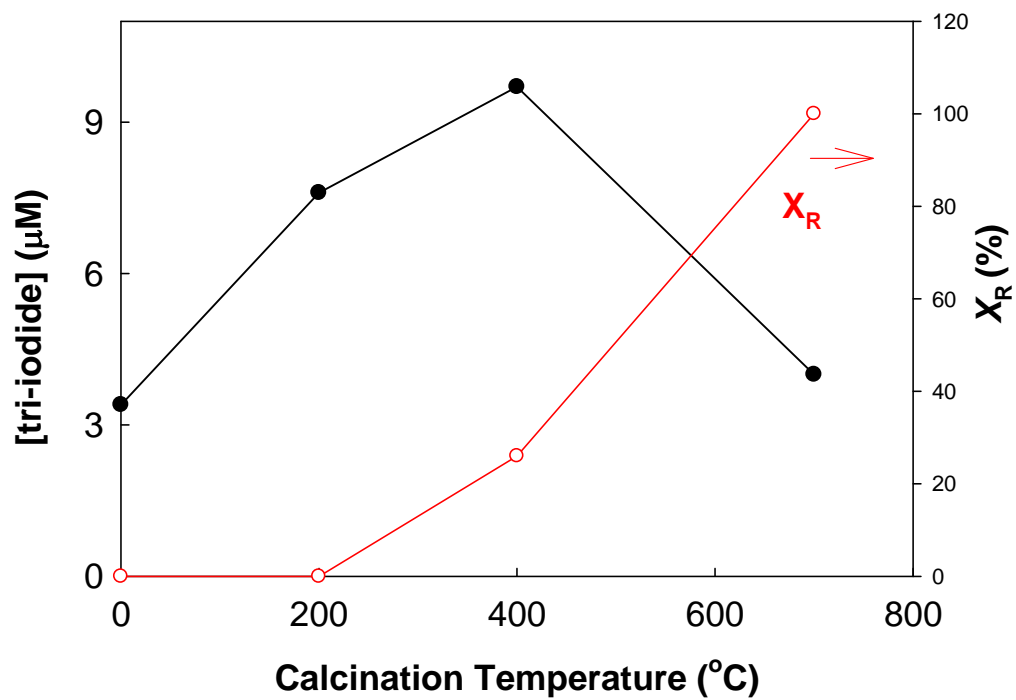


**Figure 2.9.** Photocatalytic activities for  $I^-$  oxidation in terms of the amount of  $I_3^-$  ( $\mu\text{M}$ ) produced after 6 min at  $> 400$  nm irradiation and the fractions of rutile ( $X_R$ ) of 0.3 at.% Pt-TiO<sub>2</sub> as function of calcination temperature

**TABLE 2.1:** Ionic radii of dopants, rutile content by XRD, surface area, and color of various metal ion-doped TiO<sub>2</sub> nanoparticles (at 0.3 at.% doping)

Dopant	Ion size <sup>a</sup> (Å)	Rutile (%)	Surface Area (m <sup>2</sup> g <sup>-1</sup> )	Color <sup>e</sup>
<b>@ 400 °C calcination</b>				
Undoped TiO <sub>2</sub>	0.745	0	104	White
Pt (II)	0.940	22	111	Light brown
Pt (IV)	0.765	26	106	Light brown
Cr (III)	0.755	34	115	Green
Cr (VI)	0.580	29	125	Green
V (III)	0.780	13	132	Orange
Ru (III)	0.820	0	112	Dark brown
Ni (II)	0.830	0	112	Green
Fe (III)	0.785 <sup>b</sup>	13	113	Light orange
Co (II)	0.885 <sup>b</sup>	0	102	Light yellow
Cu (II)	0.870	0	110	Light green
Os (III)	0.770 <sup>c</sup>	0	117	Light brown
Ag (I)	1.290	0	117	White
Rb (I)	1.660	19	108	White
Y (III)	1.040	18	121	White
La (III)	1.170	0	132	White
<b>@ 700 °C calcination</b>				
Undoped TiO <sub>2</sub>		15		
Pt (II)		100		
Y (III)		62		
La (III)		18		
Ru (III)		3		

<sup>a</sup> from literature: Shannon, R. D. *Acta Crystallographica Section A* **1976**, 32, 751.

<sup>b</sup> values for high spin in literature (a)

<sup>c</sup> value for Os (IV), no available value for Os (III) in literature (a)

<sup>d</sup> from literature: Ryu, J. *Environ. Sci. Technol.* **2008**, 42, 294.

<sup>e</sup> with samples before heat treatment

**TABLE 2.2:** Visible-light photocatalytic activities of various M-TiO<sub>2</sub> samples for the degradation of methylene blue (MB), the oxidation of iodide (I<sup>-</sup>), and the degradation of phenol (PhOH)

<b>Dopant</b>	<b><math>k_{\text{MB}}</math> (min<sup>-1</sup>)</b>		<b>[I<sub>3</sub><sup>-</sup>]<sub>prod.15min</sub> (μM)</b>		<b><math>k_{\text{PhOH}}</math> (hr<sup>-1</sup>)</b>
	<b>Vis</b>	<b>UV</b>	<b>Vis</b>	<b>UV</b>	<b>Vis</b>
<i>Direct Photolysis</i>	0.003	0.011	0	0	0
Undoped TiO <sub>2</sub>	0.005	0.014	10	24	0.09
Pt (II)	0.014	0.053	19	40	0.80
Pt (IV)	0.013	0.057	32	42	1.29
Cr (III)	0.013	0.016	27	25	0.36
V (III)	0.012	0.015	16	21	0.13
Ni (II)	0.011	0.010	15	27	0.09
Ru (III)	0.005	0.007	8		0.07
Fe (III)	0.007	0.015	12		0.10
Cu (II)	0.009	0.016	8		0.08
Co (II)	0.009	0.015	12		0.11
Os (III)	0.009	0.013	12		0.09
Ag (I)	0.008	0.016	12		0.07
Rb (I)	0.011	0.033	12		0.07
Y (III)	0.007	0.018	9		0.08
La (III)	0.005	0.016	10		0.10

## References

- (1) Zhang, X. W.; Lei, L. C. *Mater. Lett.* **2008**, *62*, 895.
- (2) Nahar, S.; Hasegawa, K.; Kagaya, S. *Chemosphere* **2006**, *65*, 1976.
- (3) Zhu, J. F.; Chen, F.; Zhang, J. L.; Chen, H. J.; Anpo, M. *J. Photochem. Photobiol. A-Chem.* **2006**, *180*, 196.
- (4) Niishiro, R.; Kato, H.; Kudo, A. *Phys. Chem. Chem. Phys.* **2005**, *7*, 2241.
- (5) Kim, D. H.; Lee, K. S.; Kim, Y. S.; Chung, Y. C.; Kim, S. J. *J. Am. Ceram. Soc.* **2006**, *89*, 515.
- (6) Iketani, K.; Sun, R. D.; Toki, M.; Hirota, K.; Yamaguchi, O. *Mater. Sci. Eng., B* **2004**, *108*, 187.
- (7) Klosek, S.; Raftery, D. *J. Phys. Chem. B* **2001**, *105*, 2815.
- (8) Wu, J. C. S.; Chen, C. H. *J. Photochem. Photobiol., A* **2004**, *163*, 509.
- (9) Borgarello, E.; Kiwi, J.; Gratzel, M.; Pelizzetti, E.; Visca, M. *J. Am. Chem. Soc.* **1982**, *104*, 2996.
- (10) Anpo, M.; Ichihashi, Y.; Takeuchi, M.; Yamashita, H. *Sci. Technol. Catal.* **1999**, *121*, 305.
- (11) Pan, C. C.; Wu, J. C. S. *Mater. Chem. Phys.* **2006**, *100*, 102.
- (12) Asahi, R.; Morikawa, T.; Ohwaki, T.; Aoki, K.; Taga, Y. *Science* **2001**, *293*, 269.
- (13) Gole, J. L.; Stout, J. D.; Burda, C.; Lou, Y. B.; Chen, X. B. *J. Phys. Chem. B* **2004**, *108*, 1230.
- (14) Mrowetz, M.; Balcerski, W.; Colussi, A. J.; Hoffman, M. R. *J. Phys. Chem. B* **2004**, *108*, 17269.
- (15) Umebayashi, T.; Yamaki, T.; Tanaka, S.; Asai, K. *Chem. Lett.* **2003**, *32*, 330.
- (16) Wang, Y.; Meng, Y. L.; Ding, H. M.; Shan, Y. K.; Zhao, X.; Tang, X. Z. *J. Phys.*

*Chem. C* **2008**, *112*, 6620.

(17) Yang, X.; Cao, C.; Hohn, K.; Erickson, L.; Maghirang, R.; Hamal, D.; Klabunde, K. *J. Catal.* **2007**, *252*, 296.

(18) Tachikawa, T.; Tojo, S.; Kawai, K.; Endo, M.; Fujitsuka, M.; Ohno, T.; Nishijima, K.; Miyamoto, Z.; Majima, T. *J. Phys. Chem. B* **2004**, *108*, 19299.

(19) Choi, W. Y.; Termin, A.; Hoffmann, M. R. *J. Phys. Chem.* **1994**, *98*, 13669.

(20) Karakitsou, K. E.; Verykios, X. E. *J. Phys. Chem.* **1993**, *97*, 1184.

(21) Soria, J.; Conesa, J. C.; Augugliaro, V.; Palmisano, L.; Schiavello, M.; Sclafani, A. *J. Phys. Chem.* **1991**, *95*, 274.

(22) Chen, J. H.; Yao, M. S.; Wang, X. L. *J. Nano. Res.* **2008**, *10*, 163.

(23) Di Paola, A.; Garcia-Lopez, E.; Ikeda, S.; Marci, G.; Ohtani, B.; Palmisano, L. *Catal. Today* **2002**, *75*, 87.

(24) Kim, S.; Hwang, S. J.; Choi, W. Y. *J. Phys. Chem. B* **2005**, *109*, 24260.

(25) Ohno, T.; Tanigawa, F.; Fujihara, K.; Izumi, S.; Matsumura, M. *J. Photochem. Photobiol. A-Chem.* **1999**, *127*, 107.

(26) Amadelli, R.; Samiolo, L.; Maldotti, A.; Molinari, A.; Valigi, M.; Gazzoli, D. *Int. J. Photoenergy* **2008**,

(27) Iwasaki, M.; Hara, M.; Kawada, H.; Tada, H.; Ito, S. *J. Colloid Interface Sci.* **2000**, *224*, 202.

(28) Anpo, M. *Pure Appl. Chem.* **2000**, *72*, 1787.

(29) Amadelli, R.; Samiolo, L.; Maldotti, A.; Molinari, A.; Valigi, M.; Gazzoli, D. *Int. J. Photoenergy* **2008**, *9*.

(30) Lettmann, C.; Hinrichs, H.; Maier, W. F. *Angew. Chem., Int. Ed.* **2001**, *40*, 3160.

- (31) Woodhouse, M.; Parkinson, B. A. *Chem. Soc. Rev.* **2009**, *38*, 197.
- (32) Sohn, J. M.; Oh, K. S.; Woo, S. I. *Korean J. Chem. Eng.* **2004**, *21*, 123.
- (33) Ding, Z.; Lu, G. Q.; Greenfield, P. F. *J. Phys. Chem. B* **2000**, *104*, 4815.
- (34) Jing, L. Q.; Sun, X. J.; Xin, B. F.; Wang, B. Q.; Cai, W. M.; Fu, H. G. *J. Solid State Chem.* **2004**, *177*, 3375.
- (35) Pillai, S. C.; Periyat, P.; George, R.; McCormack, D. E.; Seery, M. K.; Hayden, H.; Colreavy, J.; Corr, D.; Hinder, S. J. *J. Phys. Chem. C* **2007**, *111*, 1605.
- (36) Anderson, C.; Bard, A. J. *J. Phys. Chem. B* **1997**, *101*, 2611.
- (37) Spurr, R. A.; Myers, H. *Anal. Chem.* **1957**, *29*, 760.
- (38) Ghosh, S. K.; Vasudevan, A. K.; Rao, P. P.; Warriar, K. G. K. *Br. Ceram. Trans.* **2001**, *100*, 151.
- (39) Borkar, S. A.; Dharwadkar, S. R. *J. Therm. Anal. Calorim.* **2004**, *78*, 761.
- (40) Matteucci, F.; Cruciani, G.; Dondi, M.; Raimondo, M. *Ceram. Int.* **2006**, *32*, 385.
- (41) Iida, Y.; Ozaki, S. *J. Am. Ceram. Soc.* **1961**, *44*, 120.
- (42) Martin, S. T.; Morrison, C. L.; Hoffmann, M. R. *J. Phys. Chem.* **1994**, *98*, 13695.
- (43) Ruiz, A. M.; Sakai, G.; Cornet, A.; Shimanoe, K.; Morante, J. R.; Yamazoe, N. *Sensors and Actuators B-Chemical* **2003**, *93*, 509.
- (44) Sibin, C. P.; Kumar, S. R.; Mukundan, P.; Warriar, K. G. K. *Chem. Mater.* **2002**, *14*, 2876.
- (45) Ruiz, A. M.; Cornet, A.; Morante, J. R. *Sens. Actuators, B* **2004**, *100*, 256.
- (46) Ogata, S.; Iyetomi, H.; Tsuruta, K.; Shimojo, F.; Nakano, A.; Kalia, R. K.; Vashishta, P. *J. Appl. Phys.* **2000**, *88*, 6011.
- (47) Shannon, R. D.; Pask, J. A. *J. Am. Ceram. Soc.* **1965**, *48*, 391.

- (48) Mackenzie, K. J. D. *Trans. J. British Ceram. Soc.* **1975**, *74*, 29.
- (49) Umebayashi, T.; Yamaki, T.; Itoh, H.; Asai, K. *J. Phys. Chem. Solids* **2002**, *63*, 1909.
- (50) Zhao, Z. Y.; Liu, Q. J.; Zhang, J.; Zhu, Z. Q. *Acta Physica Sinica* **2007**, *56*, 6592.
- (51) Kudo, A.; Niishiro, R.; Iwase, A.; Kato, H. *Chem. Phys.* **2007**, *339*, 104.
- (52) Kuznetsov, V. N.; Serpone, N. *J. Phys. Chem. B* **2006**, *110*, 25203.
- (53) Serpone, N. *J. Phys. Chem. B* **2006**, *110*, 24287.
- (54) Lisachenko, A. A.; Kuznetsov, V. N.; Zakharov, M. N.; Mikhailov, R. V. *Kinet. Catal.* **2004**, *45*, 189.
- (55) Kuznetsov, V. N.; Krutitskaya, T. K. *Kinet. Catal.* **1996**, *37*, 446.
- (56) Yan, X. L.; Ohno, T.; Nishijima, K.; Abe, R.; Ohtani, B. *Chem. Phys. Lett.* **2006**, *429*, 606.
- (57) Ohno, T.; Tsubota, T.; Nishijima, K.; Miyamoto, Z. *Chem. Lett.* **2004**, *33*, 750.
- (58) Bettinelli, M.; Dallacasa, V.; Falcomer, D.; Fornasiero, P.; Gombac, V.; Montini, T.; Romano, L.; Speghini, A. *J. Hazard. Mater.* **2007**, *146*, 529.
- (59) Torimoto, T.; Nakamura, N.; Ikeda, S.; Ohtani, B. *Phys. Chem. Chem. Phys.* **2002**, *4*, 5910.
- (60) Zhang, Q. H.; Gao, L.; Guo, J. K. *Appl. Catal., B* **2000**, *26*, 207.
- (61) Lucarelli, L.; Nadtochenko, V.; Kiwi, J. *Langmuir* **2000**, *16*, 1102.
- (62) Addamo, M.; Bellardita, M.; Di Paola, A.; Palmisano, L. *Chem. Commun.* **2006**, 4943.
- (63) Kim, D. H.; Choi, D. K.; Kim, S. J.; Lee, K. S. *Catal. Commun.* **2008**, *9*, 654.
- (64) Bakardjieva, S.; Subrt, J.; Stengl, V.; Dianez, M. J.; Sayagues, M. J. *Appl. Catal.,*

*B* **2005**, 58, 193.

(65) Jung, K. Y.; Park, S. B. *J. Photochem. Photobiol. A-Chem.* **1999**, 127, 117.

(66) Yang, J.; Bai, H. Z.; Jiang, Q.; Lian, H. S. *Thin Solid Films* **2008**, 516, 1736.

(67) Kim, H. Y.; Lee, H. M.; Pala, R. G. S.; Shapovalov, V.; Metiu, H. *J. Phys. Chem. C* **2008**, 112, 12398.

(68) Li, F. B.; Li, X. Z.; Hou, M. F.; Cheah, K. W.; Choy, W. C. H. *Appl. Catal., A* **2005**, 285, 181.

(69) Ihara, T.; Miyoshi, M.; Ando, M.; Sugihara, S.; Iriyama, Y. *J. Mater. Sci.* **2001**, 36, 4201.

(70) Ihara, T.; Miyoshi, M.; Iriyama, Y.; Matsumoto, O.; Sugihara, S. *Appl. Catal., B* **2003**, 42, 403.

(71) Martin, S. T.; Herrmann, H.; Choi, W. Y.; Hoffmann, M. R. *Journal of the Chemical Society-Faraday Transactions* **1994**, 90, 3315.

(72) Martin, S. T.; Herrmann, H.; Hoffmann, M. R. *Journal of the Chemical Society-Faraday Transactions* **1994**, 90, 3323.

## Chapter 3

# Combinatorial Doping of TiO<sub>2</sub> with Platinum (Pt), Chromium (Cr), Vanadium (V), and Nickel (Ni) to Achieve Enhanced Photocatalytic Activity with Visible Light Irradiation

The text of this chapter has been accepted for publication in *Journal of Materials Research* Choi, J.; Park, H.; Hoffmann, M.R. July 2009.

## Abstract

Titanium dioxide (TiO<sub>2</sub>) was doped with the combination of several metal ions including platinum (Pt), chromium (Cr), vanadium (V), and nickel (Ni). The doped TiO<sub>2</sub> materials were synthesized by standard sol-gel methods with the doping levels of 0.1 to 0.5 atom-%. The resulting materials were characterized by the X-ray diffraction (XRD), BET surface-area measurement, Scanning Electron Microscopy (SEM), and UV-Vis diffuse reflectance spectroscopy (DRS). The visible-light photocatalytic activity of the co-doped samples was quantified by measuring the rate of the oxidation of iodide, the rate of degradation of methylene blue (MB), and the rate of oxidation of phenol in aqueous solutions at  $\lambda > 400$  nm. 0.3 atom-% Pt-Cr-TiO<sub>2</sub> and 0.3 atom-% Cr-V-TiO<sub>2</sub> showed the highest visible-light photocatalytic activity with respect to MB degradation and iodide oxidation, respectively. However, none of the co-doped TiO<sub>2</sub> samples were found to have enhanced photocatalytic activity for phenol degradation when compared to their single-doped TiO<sub>2</sub> counterparts.

## Introduction

Titania ( $\text{TiO}_2$ ) is the most widely used photocatalyst for the purification of water, air, and other environmental application because of its high photocatalytic activity, excellent chemical stability, relatively low price, and its lack of any known toxicity. Redox reactions of environmental interest are initiated on the  $\text{TiO}_2$  surface with trapped electrons and holes after band-gap excitation. However, because of its wide band gap energy of  $\sim 3.2$  eV,  $\text{TiO}_2$  is active only in the ultraviolet portion of the solar spectrum. As a consequence, significant efforts have been made to develop modified forms of  $\text{TiO}_2$  that are active under visible-light ( $\lambda > 400$  nm) irradiation. Several different strategies have been employed to extend photoactivity into the visible region. They include (i) doping with anions (e.g., nitrogen,<sup>1-3</sup> sulfur,<sup>4</sup> iodine,<sup>5-7</sup> and fluorine<sup>8</sup>), (ii) doping with metal ions,<sup>9-18</sup> and (iii) functionalizing  $\text{TiO}_2$  with photo-sensitizers that absorb visible-light.<sup>19,20</sup>

The most actively pursued strategy has been to increase the photoactive wavelength range and to enhance the photocatalytic activity under UV irradiation by metal ion-doping of  $\text{TiO}_2$ .<sup>21-23</sup> Numerous metal ions have been investigated as potential dopants while several metal ions such as iron,<sup>9-11</sup> vanadium,<sup>12-14</sup> chromium,<sup>15,16</sup> nickel,<sup>17</sup> and platinum<sup>18</sup> have been reported to show visible-light photocatalytic activity.

In addition, efforts have been made to improve the visible-light photocatalytic activity of  $\text{TiO}_2$  by co-doping with two metal ions.<sup>24-28</sup> Ahmad et al. reported that Sc and Nb co-doped  $\text{TiO}_2$  nanoparticles are relatively more photoactive for 2-chlorophenol degradation under visible-light than the particles doped with Sc or Nb alone.<sup>25</sup> Kato and Kudo showed that  $\text{TiO}_2$  co-doped with  $\text{Sb}^{5+}$  and  $\text{Cr}^{3+}$  ions showed higher activity than  $\text{TiO}_2$  doped only with  $\text{Cr}^{3+}$  ions alone for  $\text{O}_2$  evolution because of the charge compensation achieved with

Sb<sup>5+</sup> doping.<sup>26</sup> Furthermore, TiO<sub>2</sub> co-doped with Ni<sup>2+</sup> and Ta<sup>5+</sup> (or Ni<sup>2+</sup> and Nb<sup>5+</sup>) and TiO<sub>2</sub> co-doped with Rh<sup>3+</sup> and Sb<sup>5+</sup> were also shown to improve photocatalytic activity for O<sub>2</sub> evolution under visible-light irradiation.<sup>27,28</sup> However, there have been relatively few studies reported for double metal ion co-doping of TiO<sub>2</sub>, while TiO<sub>2</sub> co-doped with two nonmetallic elements (e.g., N and F co-doping,<sup>29,30</sup> N and S co-doping<sup>31,32</sup>) or with metal ions and nonmetallic elements<sup>33-39</sup> (e.g., Cr and N co-doping<sup>35</sup> Pt and N co-doping,<sup>36</sup> V and N co-doping,<sup>37</sup> and Bi and S co-doping<sup>38</sup>) have been widely investigated.

In order to examine the efficacy of double-doping with metal ions, we have prepared co-doped TiO<sub>2</sub> with Pt<sup>4+</sup> (or Pt<sup>2+</sup>), Cr<sup>3+</sup>, V<sup>3+</sup>, and Ni<sup>2+</sup> ions and characterized their physicochemical properties and photocatalytic activities for the bleaching and degradation of methylene blue (MB), the oxidation of iodide to tri-iodide, and the oxidative degradation of phenol in aqueous solution under visible-light irradiation ( $\lambda > 400$  nm).

## Experimental

### Sample Preparation

TiO<sub>2</sub> nanoparticles were prepared by standard sol-gel methods. 5.0 mL of titanium tetraisopropoxide (TTIP, Aldrich) was dissolved in 50 mL of absolute ethanol (Mallinckrodt) and then added dropwise to 50 mL of distilled water adjusted to pH 1.5 with nitric acid under vigorous stirring at room temperature. After 24 hours, the resulting transparent colloidal suspensions were evaporated using a rotary evaporator at 45 °C and dried in the oven (70 °C) overnight. The resulting powders were calcined at 400 °C for 1 hour under air. Single or double-doped TiO<sub>2</sub> samples (M-TiO<sub>2</sub> or MM-TiO<sub>2</sub>) were

prepared by adding one or two metal precursors to the distilled water prior to the hydrolysis of TTIP to give a doping level from 0.1 to 0.5 atomic % (at.%). Platinum ( $\text{Pt}^{4+}$  and  $\text{Pt}^{2+}$ ), chromium ( $\text{Cr}^{3+}$ ), vanadium ( $\text{V}^{3+}$ ), and nickel ( $\text{Ni}^{2+}$ ) were selected as metal-ion dopants in this study.  $\text{PtCl}_4$  (Aldrich),  $\text{Pt}(\text{NH}_3)_4(\text{NO}_3)_2$  (Alfar Aesar),  $\text{Cr}(\text{NO}_3)_3 \cdot 9\text{H}_2\text{O}$  (Aldrich),  $\text{VCl}_3$  (Aldrich), and  $\text{Ni}(\text{NO}_3)_2 \cdot 6\text{H}_2\text{O}$  (Alfar Aesar) were used as precursor reagents. Six different  $\text{TiO}_2$  samples were synthesized and co-doped with (i)  $\text{Pt}^{4+}$  and  $\text{Cr}^{3+}$  ions ( $\text{Pt}(\text{IV})\text{-Cr-TiO}_2$ ), (ii)  $\text{Pt}^{2+}$  and  $\text{Cr}^{3+}$  ions ( $\text{Pt}(\text{II})\text{-Cr-TiO}_2$ ), (iii)  $\text{Cr}^{3+}$  and  $\text{V}^{3+}$  ions ( $\text{Cr-V-TiO}_2$ ), (iv)  $\text{Pt}^{2+}$  and  $\text{V}^{3+}$  ions ( $\text{Pt}(\text{II})\text{-V-TiO}_2$ ), (v)  $\text{Pt}^{2+}$  and  $\text{Ni}^{2+}$  ions ( $\text{Pt}(\text{II})\text{-Ni-TiO}_2$ ), and (vi)  $\text{Cr}^{3+}$  and  $\text{Ni}^{2+}$  ions ( $\text{Cr-Ni-TiO}_2$ ). In addition, a control sample without doping was prepared along with singly-doped  $\text{TiO}_2$  (i.e.,  $\text{Pt}(\text{IV})\text{-TiO}_2$ ,  $\text{Pt}(\text{II})\text{-TiO}_2$ ,  $\text{Cr-TiO}_2$ ,  $\text{V-TiO}_2$ , and  $\text{Ni-TiO}_2$ ) for comparison with co-doped  $\text{TiO}_2$ .

### Characterization

We used X-ray diffraction (XRD) to examine the crystal structures of synthesized  $\text{TiO}_2$  particles by using a Philips diffractometer (X'pert Pro) with  $\text{Cu-K}\alpha$  radiation. Brunauer-Emmett-Teller (BET) surface area measurement was carried out by using  $\text{N}_2$  as the adsorptive gas (Micromeritics Gemini series). Scanning electron microscopic images (SEM, LEO 1550VP model) were taken to investigate the morphology of  $\text{TiO}_2$  particles and analysis of elemental composition was also performed with EDS (Energy Dispersive X-ray Spectroscopy). Diffuse reflectance UV-Vis absorption spectra (DRS) of powder samples were obtained using UV-Vis spectrometer (Shimadzu UV-2101PC) equipped with a diffuse reflectance accessory.

## Photocatalytic Activity Measurements

Photocatalytic activities of the synthesized TiO<sub>2</sub> samples were quantified with respect to rates of photo-bleaching and degradation of Methylene Blue (MB), the rates of oxidation of iodide (I<sup>-</sup>), and the rates of oxidative degradation of phenol (PhOH). The individual photocatalyst powders were dispersed in distilled water to give a mass concentration of 1 g L<sup>-1</sup>. An aliquot of the target substrate stock solution was then added to the catalyst suspension to give the specific substrate concentration (e.g., [MB]<sub>0</sub> = 10 μM, [I<sup>-</sup>]<sub>0</sub> = 50 mM, and [PhOH]<sub>0</sub> = 50 μM). The reaction suspension pH was circum-neutral. Before irradiation, the suspension was stirred in the dark for 30 min to obtain a state of sorption equilibrium of the specific substrate on TiO<sub>2</sub>.

A high-pressure Hg(Xe) Arc lamp (500 W) was used as the light source. The light beam emitted from the arc lamp was passed through an IR water filter and a UV cut-off filter ( $\lambda > 400$  nm) before being focused onto a cylindrical Pyrex reactor through a quartz window. The reactor was open to ambient air during most experiments. Time-sequenced sample aliquots were collected from the reactor during the illumination for analysis and filtered through a 0.45 μm PTFE syringe filter to remove the TiO<sub>2</sub> particles. Multiple photolysis (and photocatalysis) experiments were performed under identical reaction conditions to determine reproducibility.

The degradation rates and rate constants for MB loss during photocatalysis were determined by measuring the absorbance of MB at 665 nm with a spectrophotometer (Shimadzu UV-2101PC). For the photocatalytic oxidation of I<sup>-</sup>, tri-iodide (I<sub>3</sub><sup>-</sup>), which is the principal product of I<sup>-</sup> oxidation in the presence of excess iodide ion, was spectrophotometrically determined by measuring the absorbance at 352 nm. The

degradation of phenol in aqueous solution was measured using high performance liquid chromatography (HPLC, HP 1100 series with C18 column).

## Results and Discussion

### Characterization of Single Metal Doped TiO<sub>2</sub> (M-TiO<sub>2</sub>)

Singly-doped TiO<sub>2</sub> (M-TiO<sub>2</sub>) samples were prepared by sol-gel synthesis where M = Pt<sup>4+</sup>, Cr<sup>3+</sup>, V<sup>3+</sup>, and Ni<sup>2+</sup>. In order to compare the effect of oxidation state of Pt dopant, TiO<sub>2</sub> doped with Pt<sup>2+</sup> ions was also prepared. Figure 3.1 shows the XRD patterns of the singly-doped M-TiO<sub>2</sub> samples at the doping level of 0.3 at.%. The XRD patterns were consistent with the standard crystal structure of TiO<sub>2</sub> (i.e., a mixture of anatase and rutile phases) with no diffraction peaks associated with any of doped metals elements in the M-TiO<sub>2</sub> samples. This indicates that the doping process did not induce the formation of separate impurity phases and that the specific dopant could be considered to be fully incorporated into TiO<sub>2</sub> lattice. Pt<sup>4+</sup>, Cr<sup>3+</sup>, and V<sup>3+</sup> ions may be substituted into Ti site of TiO<sub>2</sub> because the ionic radii of dopants (Pt<sup>4+</sup>: 0.765 Å, Cr<sup>3+</sup>: 0.755 Å, and V<sup>3+</sup>: 0.78 Å)<sup>40</sup> are similar to that of Ti<sup>4+</sup> (0.745 Å).<sup>40</sup> However, Ni<sup>2+</sup> and Pt<sup>2+</sup> ions are possibly located in the interstitial position of the lattice rather than Ti site because of relatively large size difference between dopant ions (Ni<sup>2+</sup>: 0.83 Å and Pt<sup>2+</sup>: 0.94 Å)<sup>40</sup> and Ti<sup>4+</sup> ions. Undoped TiO<sub>2</sub> samples prepared by sol-gel synthesis and calcined at 400 °C (TiO<sub>2</sub>-SG) showed only the pure anatase phase. However, the rutile phase was apparent in some M-TiO<sub>2</sub> samples prepared and treated at the same temperature. This result suggests that metal-ion doping lowered relative temperature of the anatase-to-rutile phase transformation (A-R phase transformation). 0.3 at.% Cr-TiO<sub>2</sub> and 0.3 at.% Pt-TiO<sub>2</sub> (both Pt(IV)-TiO<sub>2</sub> and

Pt(II)-TiO<sub>2</sub>) exhibited a characteristic rutile peak whereas 0.3 at.% V-TiO<sub>2</sub> appeared to have a smaller fraction of the rutile phase. 0.3 at.% Ni-TiO<sub>2</sub>, by contrast, showed pure anatase phase, as in the case of undoped TiO<sub>2</sub>. Therefore, we conclude that doping TiO<sub>2</sub> with Cr, Pt, and V ions modifies the temperature dependence of the A-R phase transformation.

Figure 3.2 shows the UV/vis diffuse-reflectance spectra for the various M-TiO<sub>2</sub> samples. Undoped TiO<sub>2</sub> exhibited a sharp absorption edge at about 400 nm ( $E_{bg} \sim 3.1$  eV). However, the M-TiO<sub>2</sub> samples showed absorption spectra extended into the visible region over the range of 400 ~ 700 nm. Thus, visible-light activation and photocatalytic activity could be expected from these M-TiO<sub>2</sub> samples. As shown in Figure 3.2a, 0.3 at.% Ni-TiO<sub>2</sub> gave a relatively small absorption between 400 and 500 nm while 0.3 at.% V-TiO<sub>2</sub> exhibited a more substantial and broader absorption shoulder up to 700 nm. 0.3 at.% Cr-TiO<sub>2</sub> also showed extended absorption spectra over the 400~500 nm range with an additional absorption peak near 650 nm; this may be due to the d-d transitions of Cr<sup>3+</sup> ions.<sup>26,41</sup> Figure 3.2b shows the difference between the absorption spectra of 0.3 at.% Pt(IV)-TiO<sub>2</sub> and 0.3 at.% Pt(II)-TiO<sub>2</sub>. Pt(II)-TiO<sub>2</sub> gave a broad absorption over most of the visible region similar to 0.3 at.% V-TiO<sub>2</sub>. In contrast, 0.3 at.% Pt(IV)-TiO<sub>2</sub> gave a smaller absorption peak between 400 and 550 nm; this indicates that the origins of the absorption spectra were different in the two different Pt-TiO<sub>2</sub> samples. The extended absorption of the M-TiO<sub>2</sub> into the visible region has been explained in terms of the excitation of electrons of dopant ion to TiO<sub>2</sub> conduction band (i.e., a metal to conduction band charge-transfer) according to their respective energy levels.<sup>12,13,42,43</sup> However, recent proposals suggest that the absorption spectra of modified TiO<sub>2</sub> in the visible region

most likely originate from defects associated with oxygen vacancies that give rise to colored centers.<sup>44,45</sup> Kuznetsov and Serpone pointed out the similarities of the spectra in the range of 400~600 nm shown among different types of visible-light-active TiO<sub>2</sub> samples.<sup>44</sup> It was also reported that similar absorption spectra in the visible region was found in reduced TiO<sub>2</sub> samples with observed absorption spectra being the sum of overlapping absorption bands with the maxima at 2.81 eV and 2.55 eV, which correlate with oxygen vacancies.<sup>46,47</sup> The metal-ion dopants used in this study have different valence states than Ti<sup>4+</sup>, and as a consequence, may induce the generation of oxygen vacancies during synthesis. In addition, some of the M-TiO<sub>2</sub> samples (e.g., Ni-TiO<sub>2</sub>, V-TiO<sub>2</sub>, Pt(II)-TiO<sub>2</sub>) exhibited similar absorption in the range of 400~600 nm, even though the absorption intensities were different. Therefore, both the generation of new energy levels due to the injection of impurities within the bandgap energies range and the generation of oxygen vacancies by metal doping may contribute to the observed visible light absorption of M-TiO<sub>2</sub> samples.

### **Characterization of metal co-doped TiO<sub>2</sub> (MM-TiO<sub>2</sub>)**

The properties of 0.3 at.% MM-TiO<sub>2</sub> samples are summarized in Table 3.1. The doubly-doped MM-TiO<sub>2</sub> samples exhibited a variety of colors; TiO<sub>2</sub> samples doped with Cr or Ni are green; Pt doped samples are brown; and V doped samples are orange. The BET surface area of the sol-gel synthesized, undoped TiO<sub>2</sub>, which was calcined at 400 °C, was determined to be 104 cm<sup>2</sup>/g, whereas surface area of Degussa P25 TiO<sub>2</sub> was measured at 50 cm<sup>2</sup>/g, indicating that the TiO<sub>2</sub> particles synthesized by sol-gel methods have substantially higher surfaces areas and adsorption capacities per unit weight than

Degussa P25. The surface areas of 0.3 at.% M-TiO<sub>2</sub> samples were found to be slightly larger than the undoped TiO<sub>2</sub> (106 ~ 132 cm<sup>2</sup>/g). However, there were no significant increases in the surface areas of doubly-doped samples (~110 cm<sup>2</sup>/g).

XRD patterns of 0.3 at.% Pt(IV)- 0.3 at.% Cr-TiO<sub>2</sub> and 0.3 at.% Cr-0.3 at.% Ni-TiO<sub>2</sub> are shown in Figure 3.3 with XRD patterns of each singly-doped TiO<sub>2</sub>. Crystal structures of all MM-TiO<sub>2</sub> samples are also listed in Table 3.1 along with the BET surface areas. Figure 3.3a shows that a rutile phase of Cr or Pt singly-doped TiO<sub>2</sub> was well maintained in doubly-doped Pt(IV)-Cr-TiO<sub>2</sub> samples. In Figure 3.3b, however, 0.3 at.% Cr-0.3 at.% Ni-TiO<sub>2</sub> sample appeared to lack evidence for a rutile phase that was clearly shown in singly-doped 0.3 at.% Cr-TiO<sub>2</sub>. Similarly, 0.3 at.% Pt(II)- 0.3 at.% Ni-TiO<sub>2</sub> appeared to be a pure anatase phase material in spite of 0.3 at.% Pt(II) doping. Therefore, we suggest that co-doping with Ni ions may inhibit the A-R phase transformation in Cr-TiO<sub>2</sub> or Pt-TiO<sub>2</sub>.

For comparison, the fraction of rutile,  $X_R$ , was calculated from the respective peak intensities using the following equation:<sup>48</sup>

$$X_R (\%) = \{1 - (1 + 1.26I_R/I_A)^{-1}\} \times 100 \quad (3.1)$$

where  $I_R$  and  $I_A$  are the X-ray intensities of the rutile (101) and anatase (110) peaks, respectively. These relative rutile fractions are listed in Table 3.1. These results show that the fraction of rutile ( $X_R$ ) in MM-TiO<sub>2</sub> was not higher than that for each of M-TiO<sub>2</sub> samples. For example,  $X_R$  of 0.3 at.% Pt(IV)-Cr-TiO<sub>2</sub> was estimated to be 32% while  $X_R$  of 0.3 at.% Pt(IV)-TiO<sub>2</sub> and 0.3 at.% Cr-TiO<sub>2</sub> were estimated as 26% and 34%, respectively. Furthermore, 0.3 at.% Pt(II)- 0.3 at.% V-TiO<sub>2</sub> and 0.3 at.% Cr-0.3 at.% V-

TiO<sub>2</sub> had similar or lesser X<sub>R</sub> values than those of 0.3 at.% Pt(II)-TiO<sub>2</sub>, 0.3 at.% V-TiO<sub>2</sub>, or 0.3 at.% Cr-TiO<sub>2</sub>.

Figure 3.4 shows SEM images of 0.3 at.% Pt-0.3 at.% Cr-TiO<sub>2</sub>. In Figure 3.4a, 0.3 at.% Pt(IV)- 0.3 at.% Cr-TiO<sub>2</sub> particles were aggregated together and showed rough morphologies. 0.3 at.% Pt(II)- 0.3 at.% Cr-TiO<sub>2</sub> (Figure 3.4b) and other MM-TiO<sub>2</sub> (images were not shown here) also showed SEM images similar to 0.3 at.% Pt(IV)- 0.3 at.% Cr-TiO<sub>2</sub>. Niishiro et al. reported that doping with Sb<sup>3+</sup> ions in TiO<sub>2</sub> suppressed sintering due to the difference in size between Sb<sup>3+</sup> (0.90 Å) and Ti<sup>4+</sup>, which resulted in the formation of finer and smoother crystalline particles.<sup>28</sup> However, in our case, the doping of 0.3 at.% Pt<sup>2+</sup> (0.94 Å) did not significantly change either the size of particle or their morphologies (Figure 3.4b). This may be due to relatively low doping level (0.3 % vs. 0.5~2 %) and a lower calcination temperature (400 °C vs. 1150 °C). In addition, the EDS spectrum of 0.3 at.% Pt(II)- 0.3 at.% Ni-TiO<sub>2</sub> (Figure 3.4c) shows that no apparent signals for Pt and Ni; only those of Ti and O were observed. This indicates that metal ions with larger ionic radii than Ti<sup>4+</sup> such as Pt<sup>2+</sup> or Ni<sup>2+</sup> ions are well incorporated into the TiO<sub>2</sub> lattice and not located in the surface region; these results are consistent with XRD results.

There were no significant differences between 0.3 at.% Pt(IV)- 0.3 at.% Cr-TiO<sub>2</sub> and 0.3 at.% Pt(II)- 0.3 at.% Cr-TiO<sub>2</sub> in terms of the XRD pattern, BET surface areas, morphology, or element analysis as determined by EDS. However, UV/vis DRS results clearly show the difference between two samples, as shown in Figure 3.5. 0.3 at.% Pt(IV)- 0.3 at.% Cr-TiO<sub>2</sub> shows an enhanced absorption compared to 0.3 at.% Pt-TiO<sub>2</sub> or 0.3 at.% Cr-TiO<sub>2</sub>. The spectral response of 0.3 at.% Pt(IV)- 0.3 at.% Cr-TiO<sub>2</sub> appears to

be an additional spectrum of the singly-doped 0.3 at.% Pt-TiO<sub>2</sub> combined with that of 0.3 at.% Cr-TiO<sub>2</sub> (Figure 3.5a). On the other hand, the absorption of 0.3 at.% Pt(II)- 0.3 at.% Cr-TiO<sub>2</sub> was almost identical to 0.3 at.% Cr-TiO<sub>2</sub> (Figure 3.5b). Therefore, we could expect that absorption of visible light is more efficient in the 0.3 at.% Pt(IV)- 0.3 at.% Cr-TiO<sub>2</sub> samples than the singly-doped 0.3 at.% Pt(IV)-TiO<sub>2</sub> samples.

Figure 3.6 shows UV/vis DRS results for other doubly-doped MM-TiO<sub>2</sub> materials. The absorption spectra of the 0.3 at.% Pt(II)- 0.3 at.% V-TiO<sub>2</sub> sample (Figure 3.6a) and the 0.3 at.% Pt(II)- 0.3 at.% Ni-TiO<sub>2</sub> sample (Figure 3.6b) were the same as those of the 0.3 at.% singly-doped V-TiO<sub>2</sub> and Ni-TiO<sub>2</sub> samples, respectively. In all the cases of Pt(II)-M-TiO<sub>2</sub>, the Pt(II) did not attribute to the absorption spectra of the co-doped TiO<sub>2</sub>. In contrast, Pt(IV) was the only effective co-dopant for enhanced visible-light absorption in the Cr-M-TiO<sub>2</sub> samples. For example, 0.3 at.% Cr-0.3 at.% Ni-TiO<sub>2</sub> (Figure 3.6c) and 0.3 at.% Cr-0.3 at.% V-TiO<sub>2</sub> (Figure 3.6d) did not show enhanced absorption compared to the sum of singly-doped TiO<sub>2</sub>, while 0.3 at.% Cr-0.3 at.% Pt(IV)-TiO<sub>2</sub> has a significantly enhanced absorption in the visible region (Figure 3.5a).

### **Visible-light Photocatalytic Activity**

Figure 3.7 shows visible-light photocatalytic activities of various M-TiO<sub>2</sub> and MM-TiO<sub>2</sub> preparations for the degradation of methylene blue (MB) in aqueous solution. The degradation and bleaching reaction followed apparent first-order kinetics. Under visible-light irradiation at  $\lambda > 400$  nm, direct photolysis of MB was observed in the absence of TiO<sub>2</sub> particles since MB molecules can absorb visible-light and become photolyzed without the photocatalyst. The measured first-order rate constant,  $k_{\text{MB}}$ , was increased

slightly in the presence of undoped TiO<sub>2</sub>. This increase may be due to additional light absorption above 400 nm by the TiO<sub>2</sub> particles or by an enhanced electron transfer from MB to the conduction band of TiO<sub>2</sub>. All the singly-doped M-TiO<sub>2</sub> preparations showed visible-light photocatalytic activities for MB degradation while the 0.3 at.% Pt(II)-TiO<sub>2</sub> samples gave the highest values for  $k_{\text{MB}}$ . Among doubly-doped MM-TiO<sub>2</sub> samples, only 0.3 at.% Pt-0.3 at.% Cr-TiO<sub>2</sub> (both Pt(IV) and Pt(II)) and Pt(II)-Ni-TiO<sub>2</sub> showed higher  $k_{\text{MB}}$  values than those measured for the singly-doped TiO<sub>2</sub> samples. Therefore, co-doping with Pt appears to be effective for enhancing the visible-light degradation of MB degradation. On the other hand, the doubly-doped Pt-V-TiO<sub>2</sub> samples had lower photocatalytic activity, which may be due to the effect of V doping.

0.3 at.% Pt(IV)- 0.3 at.% Cr-TiO<sub>2</sub>, which has enhanced visible-light absorption (Figure 3.5a), proved to be less photo-active than 0.3 at.% Pt(II)- 0.3 at.% Cr-TiO<sub>2</sub>. On the other hand, 0.3 at.% Cr-0.3 at.% V-TiO<sub>2</sub> and 0.3 at.% Pt(II)- 0.3 at.% V-TiO<sub>2</sub> had significantly decreased  $k_{\text{MB}}$  values compared to their singly-doped TiO<sub>2</sub> counterparts. In comparison to the 0.3 at.% Cr-0.3 at.% Ni-TiO<sub>2</sub> and 0.3 at.% Pt(II)- 0.3 at.% Ni-TiO<sub>2</sub> samples, V co-doping of Cr-TiO<sub>2</sub> and Pt-TiO<sub>2</sub> showed a net negative effect on photocatalytic activity. However, these samples still showed better photocatalytic activity than undoped TiO<sub>2</sub>.

The photocatalytic oxidation of iodide ions (I<sup>-</sup>) can also be used to compare the visible-light photocatalytic activities of various MM-TiO<sub>2</sub> preparations. Iodide in aqueous solution is readily oxidized to tri-iodide (I<sub>3</sub><sup>-</sup>) according to the following reaction:

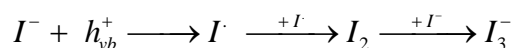


Figure 3.8 shows the production of  $I_3^-$  ions from  $I^-$  oxidation under visible-light irradiation in the presence of doubly-doped MM-TiO<sub>2</sub> materials. As a control measurement, no  $I_3^-$  was produced in the absence of TiO<sub>2</sub> particles at  $\lambda > 400$  nm. Undoped TiO<sub>2</sub>, 0.3 at.% V-TiO<sub>2</sub>, and 0.3 at.% Pt(II)-TiO<sub>2</sub> showed little photo-catalytic activity with respect to the net photooxidation of  $I^-$  to  $I_3^-$ . However, 0.3 at.% V-0.3 at.% Cr-TiO<sub>2</sub> and 0.3 at.% Pt(II)- 0.3 at.% Cr-TiO<sub>2</sub> had higher photoactivities. Therefore, Cr is clearly an effective co-dopant with respect to  $I^-$  photo-oxidation in the visible.  $I_3^-$  production is very fast during the initial phases of the reaction, but it slows noticeably as irradiation continues. This is due to the back photo-reaction of  $I_3^-$  with conduction band electrons to reform  $I^-$  ions. The back reaction effectively competes with the forward reaction of iodide with valence-band holes or surface hydroxyl radicals as the concentration of  $I_3^-$  increases with time.

In Figure 3.9, the photo-catalytic activities of the singly-doped M-TiO<sub>2</sub> samples and the doubly-doped MM-TiO<sub>2</sub> samples are compared in terms of total amount of  $I_3^-$  ions produced during 15 min of irradiation. Similar to MB degradation, all the M-TiO<sub>2</sub> samples improved the  $I^-$  oxidation rates; 0.3 at.% Pt(IV)-TiO<sub>2</sub> and 0.3 at.% Cr-TiO<sub>2</sub> showed the highest activity. However, 0.3 at.% Pt(II)-TiO<sub>2</sub>, 0.3 at.% V-TiO<sub>2</sub>, and 0.3 at.% Ni-TiO<sub>2</sub>, which had comparable activities to 0.3 at.% Pt(IV)-TiO<sub>2</sub> or 0.3 at.% Cr-TiO<sub>2</sub> in terms of MB degradation, showed only slightly enhanced  $I^-$  oxidation rates. Most of MM-TiO<sub>2</sub> samples also showed some enhanced photocatalytic activity. 0.3 at.% Pt(II)-0.3 at.% V-TiO<sub>2</sub> had the least visible-light activity among the doubly-doped MM-TiO<sub>2</sub> samples.

The doping level of each dopant in Pt(II)-Cr-TiO<sub>2</sub> was also optimized. Table 3.2 shows photocatalytic activities of Pt(II)-Cr-TiO<sub>2</sub> with different concentration of Pt and Cr over the range of 0.1~0.5 atom-%. The optimal concentration for increased photocatalytic activity was found to be 0.3 at.% Pt(II) and 0.3 at.% Cr, respectively. It was also observed that photocatalytic activity with respect to I<sup>-</sup> oxidation strongly depended on Cr concentration.

The photocatalytic degradation of phenol under visible-light irradiation is shown in Figure 3.10. Phenol was degraded effectively with Pt-TiO<sub>2</sub> (both Pt(IV)-TiO<sub>2</sub> and Pt(II)-TiO<sub>2</sub>) and totally degraded within 2 hr with 0.3 at.% Pt(IV)-TiO<sub>2</sub>. However, 0.3 at.% Pt-0.3 at.% Cr-TiO<sub>2</sub> did not exhibit any enhancement in the photo-degradation of phenol (Figure 3.10a). Phenol degradation with 0.3 at.% Pt(IV)-TiO<sub>2</sub> was slightly decreased by Cr co-doping. Moreover, the resultant photocatalytic activity of 0.3 at.% Pt(II)-0.3 at.% Cr-TiO<sub>2</sub> proved to be much less than 0.3 at.% Pt(II)-TiO<sub>2</sub>. Similarly, there was no advantage shown by the doubly-doped Cr-V-TiO<sub>2</sub> samples (Figure 3.10b). The other doubly-doped MM-TiO<sub>2</sub> samples, which are not shown here, also had negative co-doping effects with respect to phenol degradation. These results clearly indicate that the co-doping effects on TiO<sub>2</sub> photo-catalytic activity are substrate-dependent. Several doubly-doped MM-TiO<sub>2</sub> samples showed enhanced photocatalytic activities for MB degradation or I<sup>-</sup> oxidation. For example, 0.3 at.% Pt(II)-0.3 at.% Cr-TiO<sub>2</sub> and 0.3 at.% Cr-0.3 at.% V-TiO<sub>2</sub> showed the highest visible-light photocatalytic activities for MB degradation and I<sup>-</sup> oxidation, respectively. However, there was no apparent enhancement observed for doubly-doped TiO<sub>2</sub> materials for phenol photo-degradation.

It is worth mentioning that photocatalytic activities of MM-TiO<sub>2</sub> were observed substrate-dependent and were not correlated with any physicochemical property of MM-TiO<sub>2</sub>. Neither absorption spectra in the visible region nor the crystal structures (anatase and rutile) of MM-TiO<sub>2</sub> appeared to play an important role in the visible-light induced photocatalytic reactions. For example, Pt(IV)-Cr-TiO<sub>2</sub>, which was expected more efficient absorption of visible-light than Pt(II)-Cr-TiO<sub>2</sub>, showed less photocatalytic activities than Pt(II)-Cr-TiO<sub>2</sub> for both MB degradation and I<sup>-</sup> oxidation. However, Pt(IV)-Cr-TiO<sub>2</sub> showed higher photocatalytic activity than Pt(II)-Cr-TiO<sub>2</sub> for phenol degradation. In addition, Pt(II)-V-TiO<sub>2</sub> that has larger visible-light absorption than Pt(II)-Ni-TiO<sub>2</sub> were less photo-active for MB degradation and I<sup>-</sup> oxidation, as well. Similarly, structure (i.e., the fraction of rutile) in MM-TiO<sub>2</sub> did not affect to visible-light photocatalytic activities of MM-TiO<sub>2</sub>. Pt(IV)-Cr-TiO<sub>2</sub> with a high relative rutile content and Pt(II)-Ni-TiO<sub>2</sub> with no rutile at all showed comparable photocatalytic activities for MB degradation. For I<sup>-</sup> oxidation, Pt(II)-Ni-TiO<sub>2</sub> and Cr-Ni-TiO<sub>2</sub> also showed comparable photocatalytic activities to Pt(II)-Cr-TiO<sub>2</sub>.

## Conclusions

Two metal ions co-doped TiO<sub>2</sub> was prepared by adding Pt (Pt<sup>4+</sup> and Pt<sup>2+</sup>), Cr<sup>3+</sup>, V<sup>3+</sup>, and Ni<sup>2+</sup> ions during sol-gel synthesis. The metal-ion dopants used in this study were effectively incorporated into TiO<sub>2</sub> lattice either in Ti(IV) sites or in interstitial sites. Single and double-ion doping changed some of the physicochemical properties such as the reactive surface area and photophysical response of pristine TiO<sub>2</sub>. 0.3 at.% Pt-0.3 at.% Cr-TiO<sub>2</sub> (both Pt<sup>4+</sup> and Pt<sup>2+</sup>), 0.3 at.% Cr-0.3 at.% V-TiO<sub>2</sub>, and 0.3 at.% Pt-0.3 at.%

V-TiO<sub>2</sub> samples lowered A-R phase transformation temperature, since the individual dopant used for co-doping also had enhancing effect on A-R phase transformation. However, 0.3 at.% Pt-0.3 at.% Ni-TiO<sub>2</sub> and 0.3 at.% Cr-0.3 at.% Ni-TiO<sub>2</sub> remained strictly in the anatase phase due to Ni co-doping although doping with Pt and Cr alone accelerated A-R phase transformation. All co-doped TiO<sub>2</sub> materials gave extended UV-vis absorption between 400 and 700 nm, but only 0.3 at.% Pt(IV)- 0.3 at.% Cr-TiO<sub>2</sub> enhanced visible-light absorption compared to singly-doped TiO<sub>2</sub>. Visible-light photocatalytic activities were evaluated for the degradation of MB, phenol and the oxidation of I<sup>-</sup> in aqueous solution. The photocatalytic activities of co-doped TiO<sub>2</sub> strongly depended on the nature of the electron-donating substrate and were not correlated with any physicochemical property of the co-doped TiO<sub>2</sub>. Pt-Cr-TiO<sub>2</sub> and Pt-Ni-TiO<sub>2</sub> enhanced the rate of MB degradation while Pt-Cr-TiO<sub>2</sub>, Cr-V-TiO<sub>2</sub>, Pt-Ni-TiO<sub>2</sub>, and Cr-Ni-TiO<sub>2</sub> showed enhanced activity for I<sup>-</sup> oxidation. However, none of the co-doped samples showed enhanced photocatalytic activity for phenol degradation compared to their singly-doped TiO<sub>2</sub> counterparts. All co-doped TiO<sub>2</sub> samples exhibited some enhancement in photo-catalytic activity for all three reactions compared to undoped nano-particulate TiO<sub>2</sub>.

## **Acknowledgement**

We are grateful to the Hydrogen Energy Research & Development Center and 21<sup>st</sup> Century Frontier Research and Development Program of the Ministry of Science and Technology of Korea for research support.

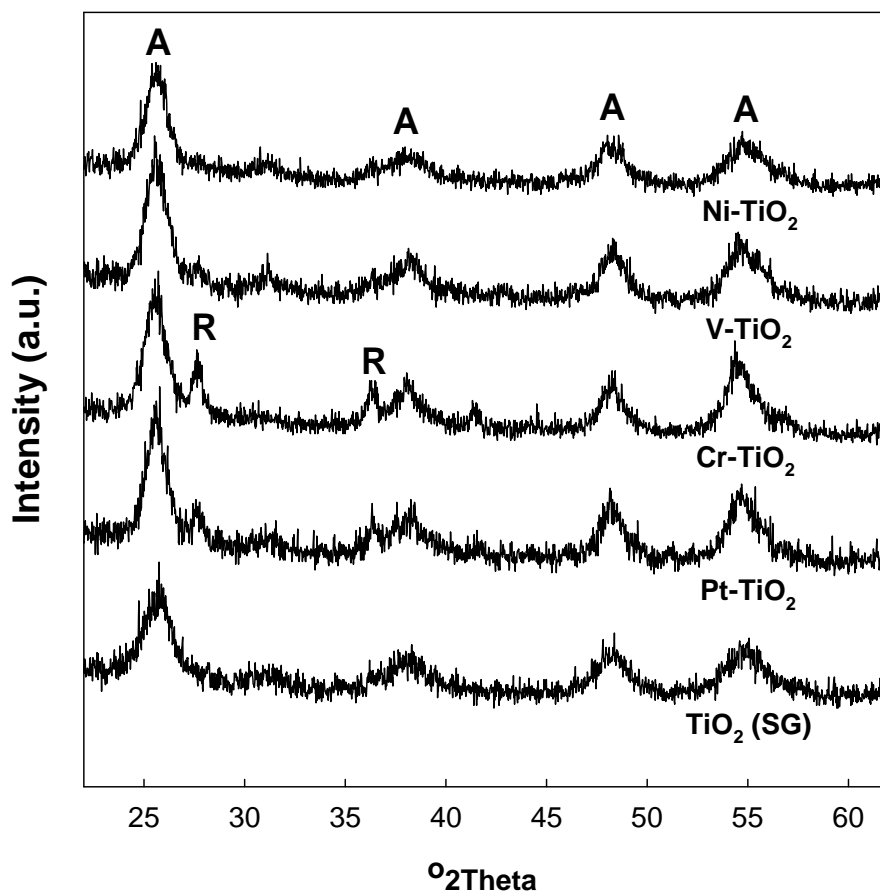


**Figure 3.1.** X-ray diffraction (XRD) pattern measured for 0.3 at.% M-TiO<sub>2</sub> prepared at 400 °C. (A: anatase phase, R: rutile phase)

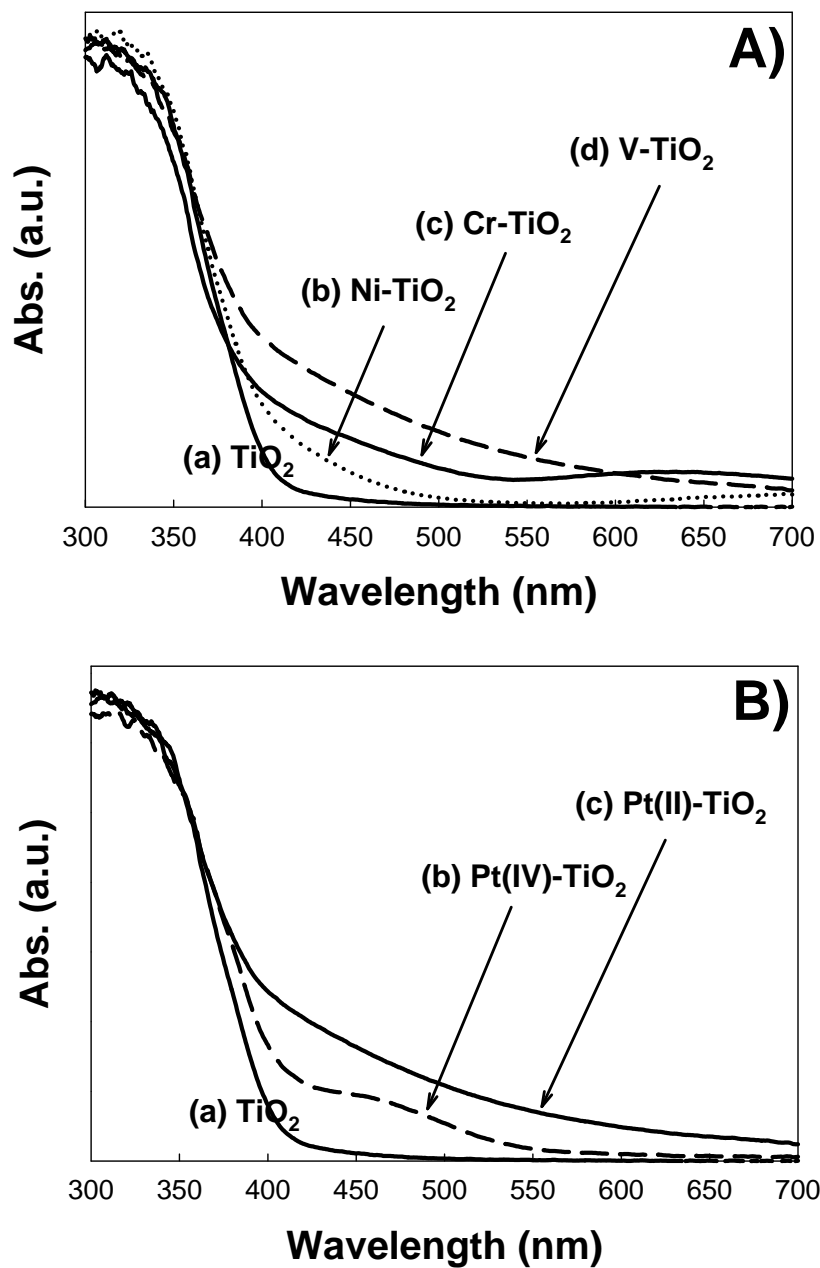


**Figure 3.2.** UV/vis diffuse reflectance spectra (DRS) for 0.3 at.% M-TiO<sub>2</sub> samples: A) undoped TiO<sub>2</sub>, Cr-TiO<sub>2</sub>, Ni-TiO<sub>2</sub>, and V-TiO<sub>2</sub>. B) Pt(IV)-TiO<sub>2</sub> and Pt(II)-TiO<sub>2</sub>

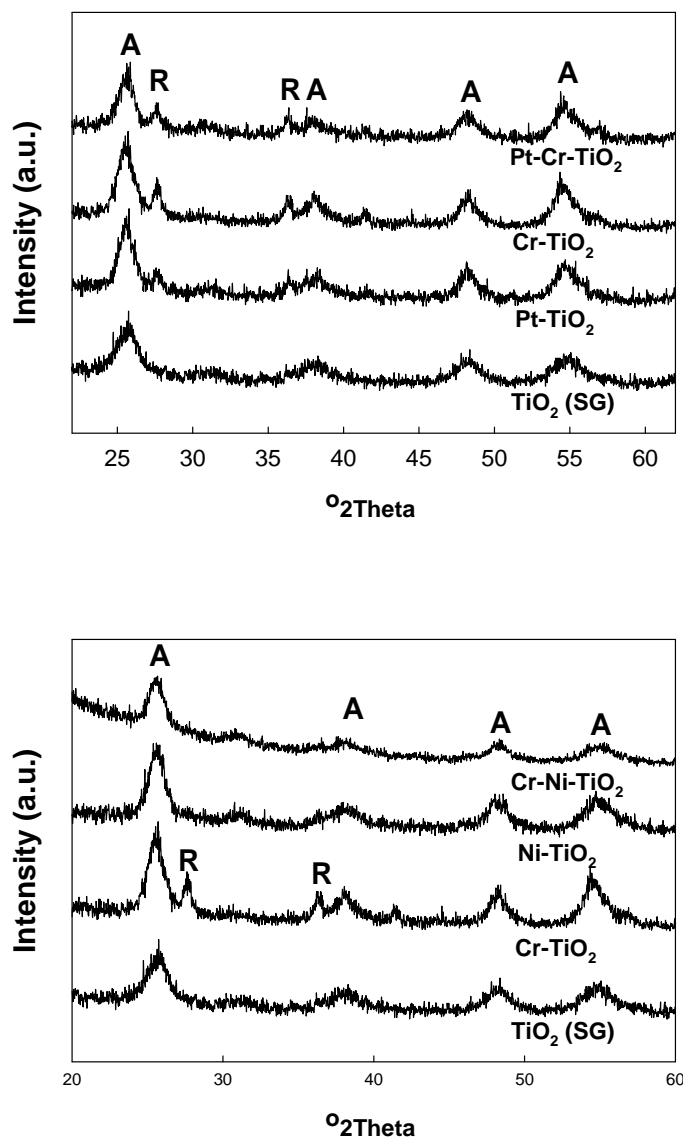


**Figure 3.3.** X-ray diffraction (XRD) pattern measured for 0.3 at.% Pt-Cr-TiO<sub>2</sub> and Cr-Ni-TiO<sub>2</sub>. (A: anatase phase, R: rutile phase)

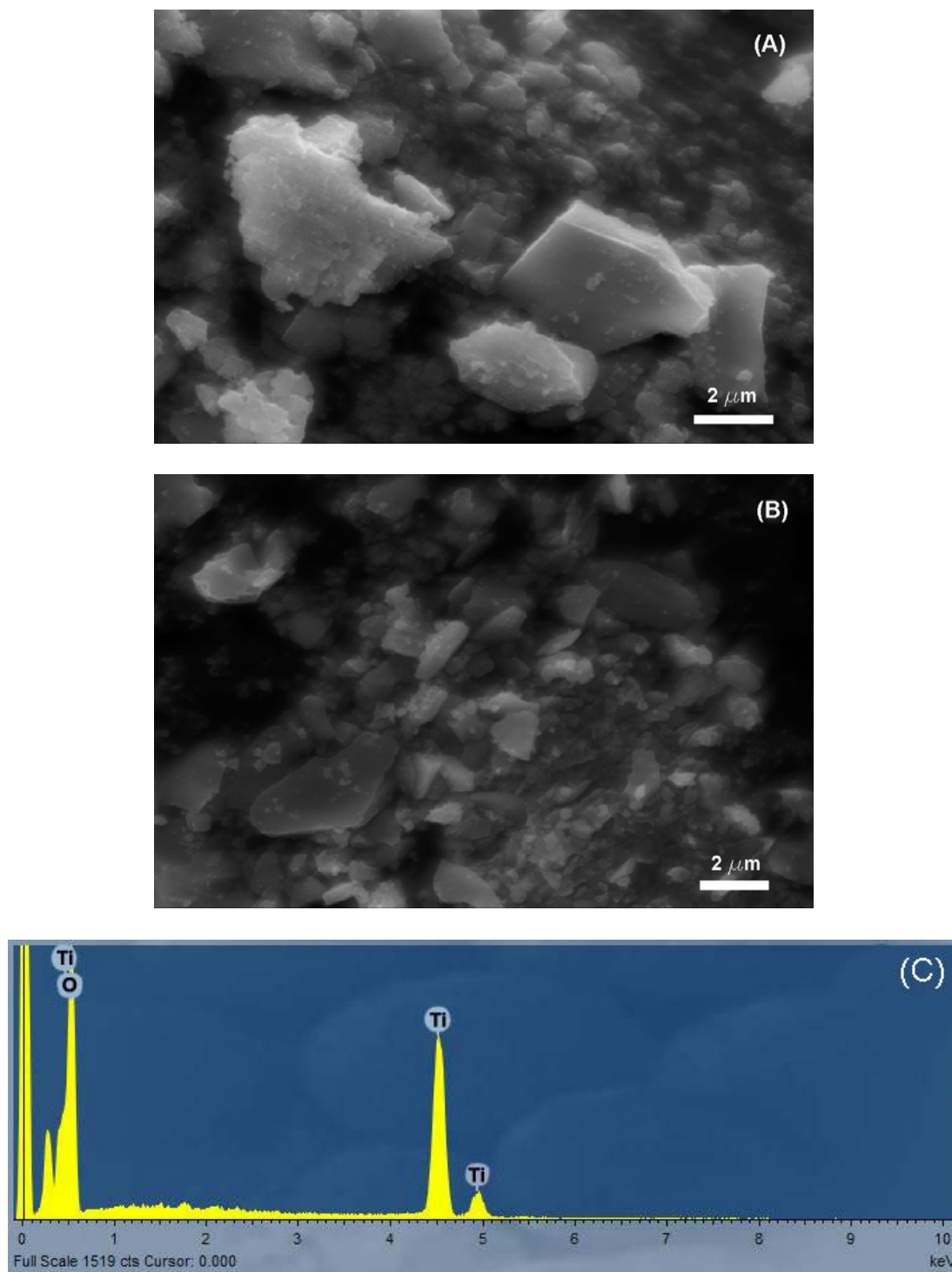


**Figure 3.4.** SEM images of (a) 0.3 at.% Pt(IV)-Cr-TiO<sub>2</sub>, (b) 0.3 at.% Pt(II)-Cr-TiO<sub>2</sub> and EDS spectra of Pt(II)-Ni-TiO<sub>2</sub> (c) that clearly shows dopants signals (i.e., Pt and Ni) other than Ti and O signals were not observed.

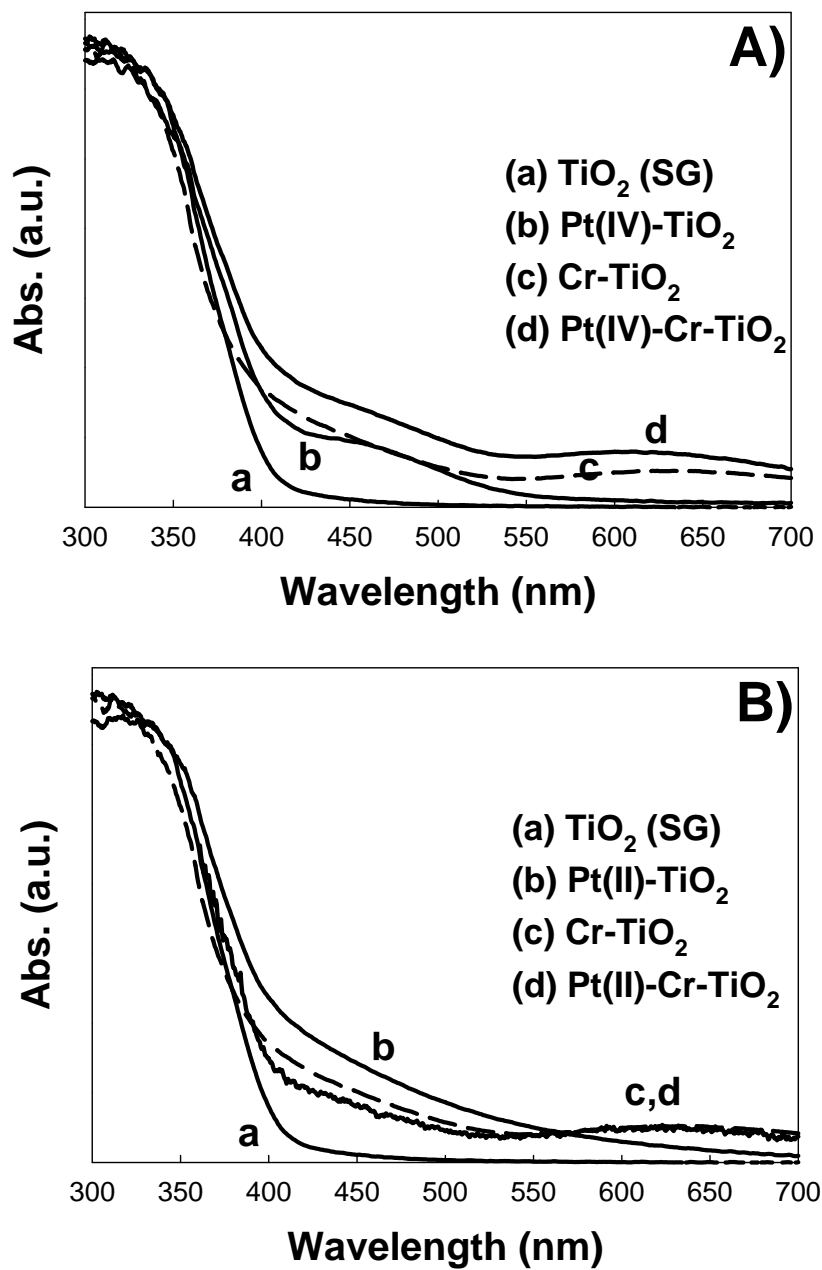


**Figure 3.5.** UV/vis diffuse reflectance spectra (DRS) for 0.3 at.% Pt-Cr-TiO<sub>2</sub>: A) Pt(IV)-Cr-TiO<sub>2</sub>, B) Pt(II)-Cr-TiO<sub>2</sub> samples

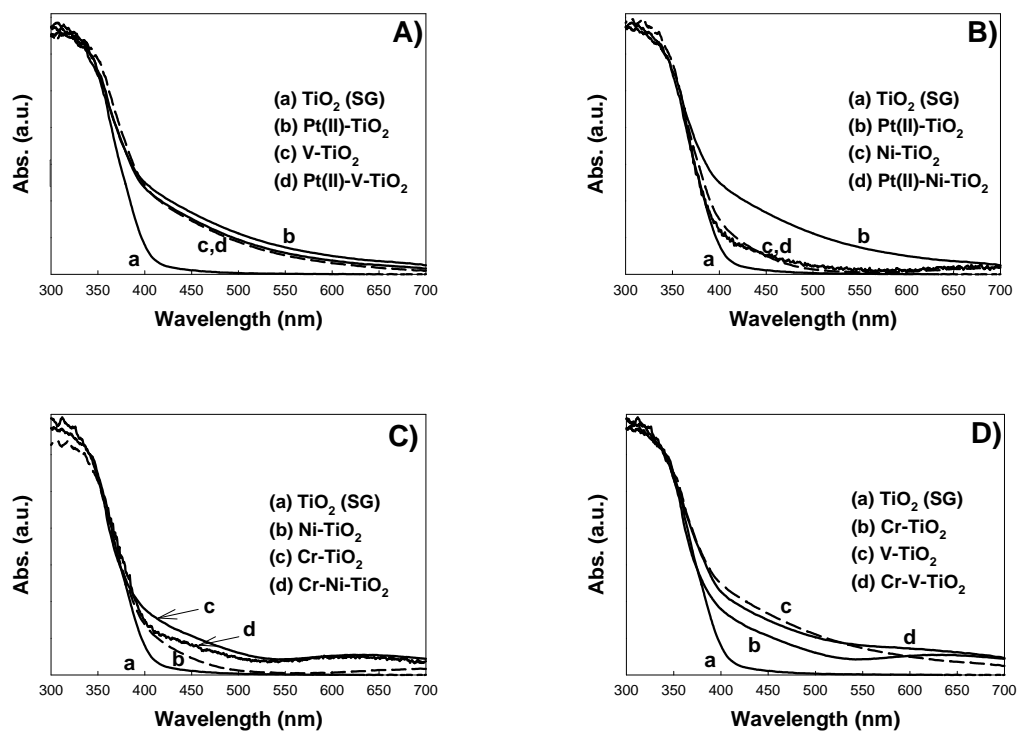


**Figure 3.6.** UV/vis diffuse reflectance spectra (DRS) for A) 0.3 at.% Pt(II)-V-TiO<sub>2</sub>, B) 0.3 at.% Pt(II)-Ni-TiO<sub>2</sub>, C) 0.3 at.% Cr-Ni-TiO<sub>2</sub>, D) 0.3 at.% Cr-V-TiO<sub>2</sub>

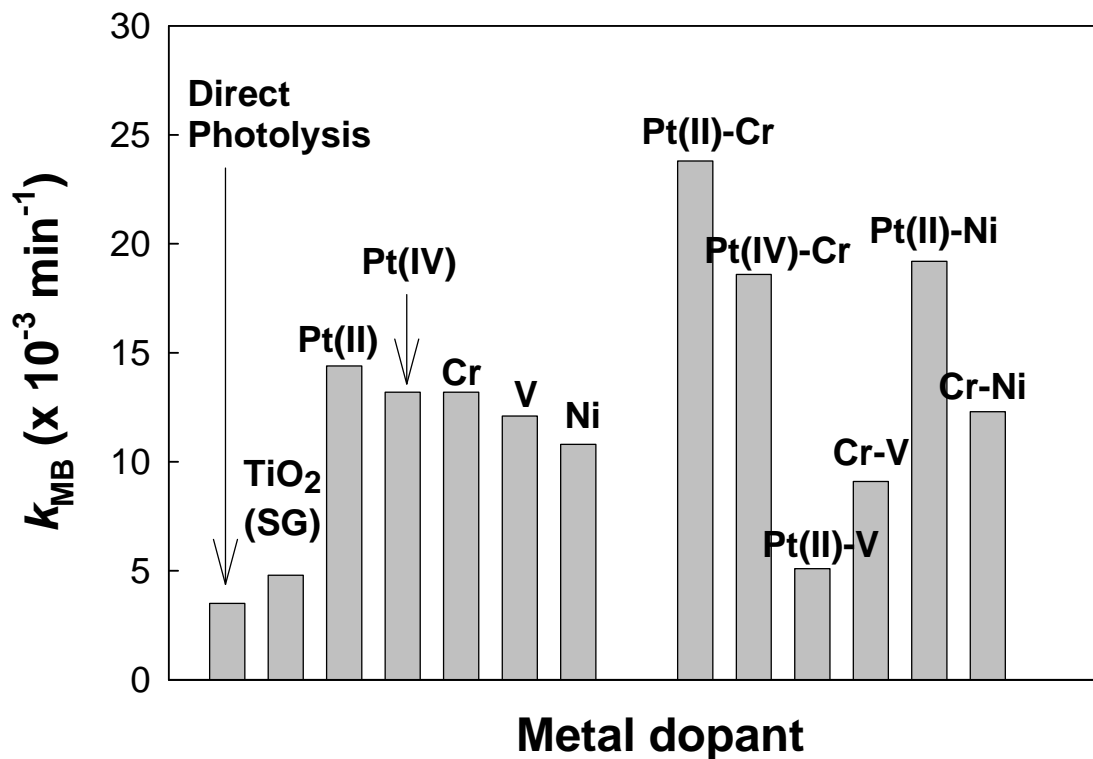


**Figure 3.7.** The comparison of degradation rate constant ( $k_{MB}$ ) of MB for various single-doped or co-doped TiO<sub>2</sub> samples (0.3 at.% doping)

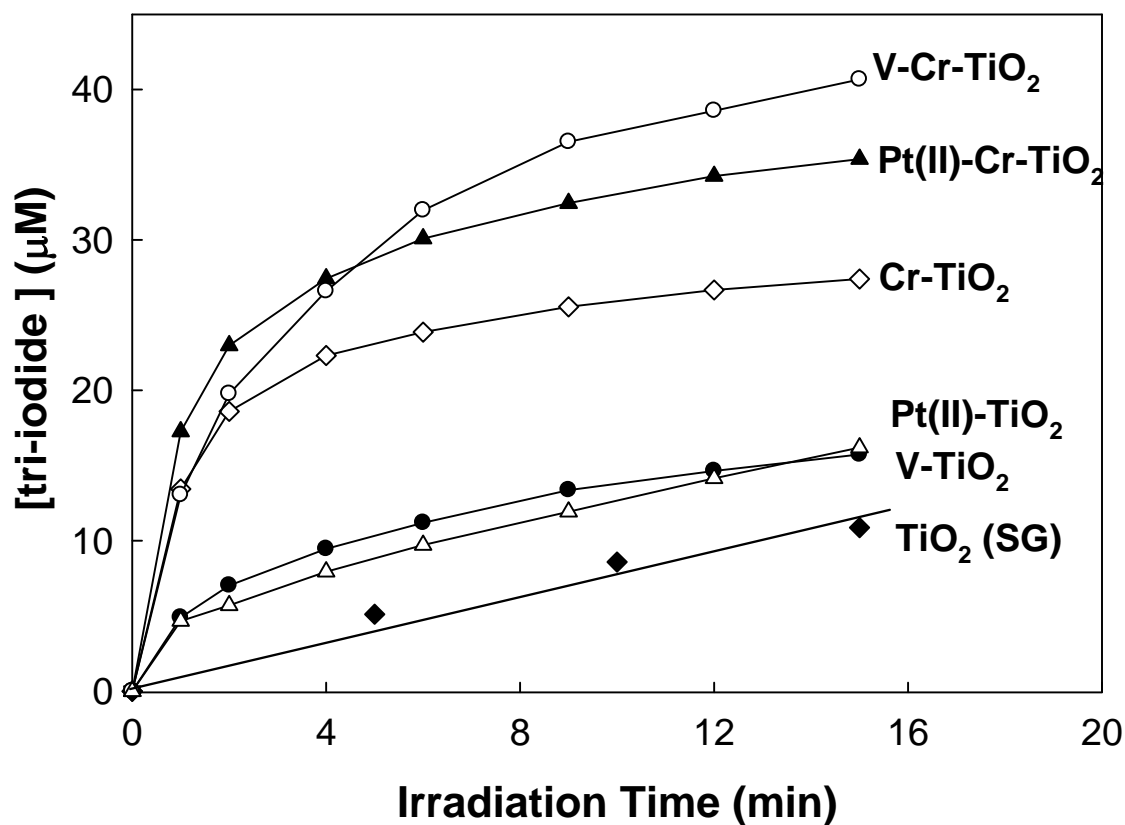


**Figure 3.8.** The production of tri-iodide by iodide oxidation ( $[\text{I}^-]_0 = 50 \text{ mM}$ , total volume = 30 mL) with selected MM-TiO<sub>2</sub> (0.3 at.% doping level, 1 g/L) under visible-light irradiation (500 W, > 400 nm)

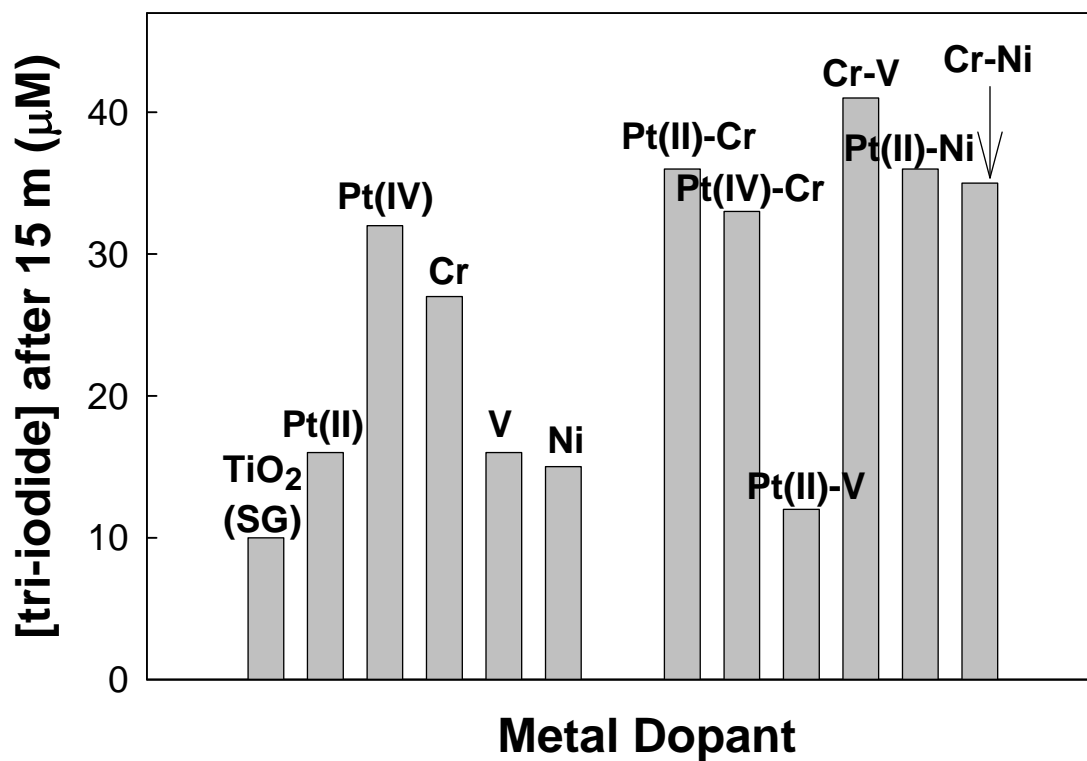


**Figure 3.9.** The comparison of various single-doped or co-doped TiO<sub>2</sub> samples (0.3 at.% doping) for I<sup>-</sup> oxidation

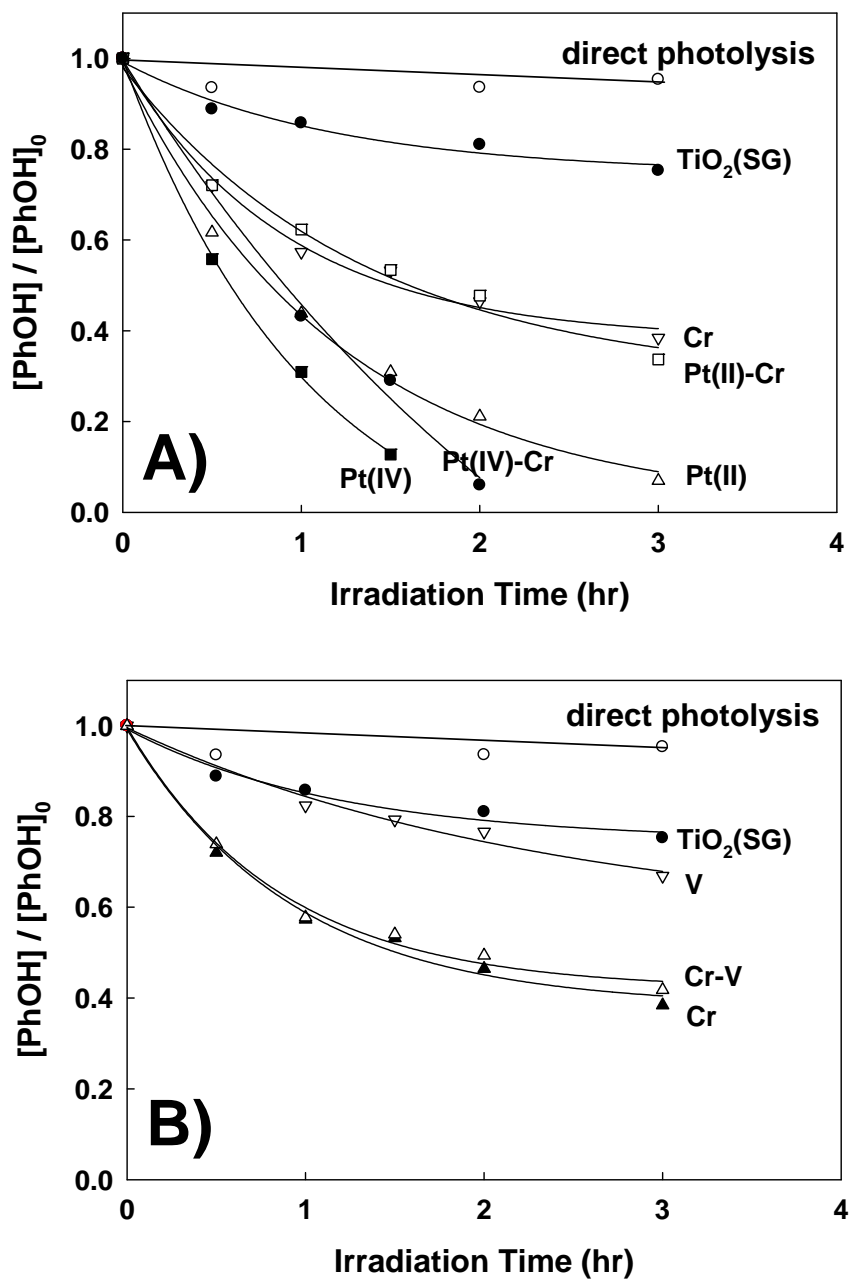


**Figure 3.10.** The degradation of phenol ( $[\text{phenol}]_0 = 50 \mu\text{M}$ , 1 g/L of 0.3 at.% single-doped or co-doped-TiO<sub>2</sub>, > 400 nm): A) Pt-Cr-TiO<sub>2</sub>, (B) Cr-V-TiO<sub>2</sub>

**TABLE 3.1.** Characterization of MM-TiO<sub>2</sub> photocatalysts at 0.3 at.% doping level

Sample	Color	Surface Area (m <sup>2</sup> g <sup>-1</sup> )	Crystal structure (X <sub>R</sub> %)
TiO <sub>2</sub> (SG)	White	104	Anatase (0)
Pt(II)-TiO <sub>2</sub>	Light brown	111	Anatase/Rutile (22)
Pt(IV)-TiO <sub>2</sub>	Light brown	106	Anatase/Rutile (26)
Cr-TiO <sub>2</sub>	Green	115	Anatase/Rutile (34)
V-TiO <sub>2</sub>	Orange	132	Anatase/Rutile (13)
Ni-TiO <sub>2</sub>	Green	112	Anatase (0)
Pt(II)-Cr-TiO <sub>2</sub>	Dark green	112	Anatase/Rutile (30)
Pt(IV)-Cr-TiO <sub>2</sub>	Dark green	108	Anatase/Rutile (32)
Cr-V-TiO <sub>2</sub>	Brown	115	Anatase/Rutile (28)
Pt(II)-V-TiO <sub>2</sub>	Brown	118	Anatase/Rutile (24)
Pt(II)-Ni-TiO <sub>2</sub>	Light green	110	Anatase (0)
Cr-Ni-TiO <sub>2</sub>	Green	115	Anatase (0)

**TABLE 3.2.** Photocatalytic activities of Pt(II)-Cr-TiO<sub>2</sub> with different doping level for I<sup>-</sup> oxidation under visible-light irradiation (> 400 nm)

Sample	[I <sub>3</sub> <sup>-</sup> ] <sub>prod.</sub> (μM) after 15 min
0.3 % Pt(II) with	
0 % Cr	16
0.1 % Cr	19
0.2 % Cr	21
0.3 % Cr	36
0.5 % Cr	32
0.3 % Cr with	
0 % Pt	29
0.1 % Pt	31
0.2 % Pt	28
0.3 % Pt	36
0.5 % Pt	32

## References

- (1) Asahi, R.; Morikawa, T.; Ohwaki, T.; Aoki, K.; Taga, Y. *Science* **2001**, *293*, 269.
- (2) Mrowetz, M.; Balcerski, W.; Colussi, A. J.; Hoffman, M. R. *J. Phys. Chem. B* **2004**, *108*, 17269.
- (3) Sauthier, G.; Gyorgy, E.; Figueras, A. *J. Mater. Res.* **2008**, *23*, 2340.
- (4) Umabayashi, T.; Yamaki, T.; Tanaka, S.; Asai, K. *Chem. Lett.* **2003**, *32*, 330.
- (5) Su, W. Y.; Zhang, Y. F.; Li, Z. H.; Wu, L.; Wang, X. X.; Li, J. Q.; Fu, X. Z. *Langmuir* **2008**, *24*, 3422.
- (6) Liu, G.; Chen, Z. G.; Dong, C. L.; Zhao, Y. N.; Li, F.; Lu, G. Q.; Cheng, H. M. *J. Phys. Chem. B* **2006**, *110*, 20823.
- (7) Hong, X. T.; Wang, Z. P.; Cai, W. M.; Lu, F.; Zhang, J.; Yang, Y. Z.; Ma, N.; Liu, Y. J. *Chem. Mater.* **2005**, *17*, 1548.
- (8) Zhou, J. K.; Lv, L.; Yu, J. Q.; Li, H. L.; Guo, P. Z.; Sun, H.; Zhao, X. S. *J. Phys. Chem. C* **2008**, *112*, 5316.
- (9) Zhang, X. W.; Lei, L. C. *Mater. Lett.* **2008**, *62*, 895.
- (10) Zhang, X. W.; Zhou, M. H.; Lei, L. C. *Catal. Commun.* **2006**, *7*, 427.
- (11) Teoh, W. Y.; Amal, R.; Madler, L.; Pratsinis, S. E. *Catal. Today* **2007**, *120*, 203.
- (12) Iketani, K.; Sun, R. D.; Toki, M.; Hirota, K.; Yamaguchi, O. *Mater. Sci. Eng., B* **2004**, *108*, 187.
- (13) Klosek, S.; Raftery, D. *J. Phys. Chem. B* **2001**, *105*, 2815.
- (14) Wu, J. C. S.; Chen, C. H. *J. Photochem. Photobiol., A* **2004**, *163*, 509.
- (15) Borgarello, E.; Kiwi, J.; Gratzel, M.; Pelizzetti, E.; Visca, M. *J. Am. Chem. Soc.* **1982**, *104*, 2996.

- (16) Anpo, M.; Ichihashi, Y.; Takeuchi, M.; Yamashita, H. *Sci. Technol. Catal.* **1999**, *121*, 305.
- (17) Kim, D. H.; Lee, K. S.; Kim, Y. S.; Chung, Y. C.; Kim, S. J. *J. Am. Ceram. Soc.* **2006**, *89*, 515.
- (18) Kim, S.; Hwang, S. J.; Choi, W. Y. *J. Phys. Chem. B* **2005**, *109*, 24260.
- (19) Park, H.; Choi, W.; Hoffmann, M. R. *J. Mater. Chem.* **2008**, *18*, 2379.
- (20) Bae, E.; Choi, W. *Environ. Sci. Technol* **2003**, *37*, 147.
- (21) Choi, W. Y.; Termin, A.; Hoffmann, M. R. *J. Phys. Chem.* **1994**, *98*, 13669.
- (22) Chen, J. H.; Yao, M. S.; Wang, X. L. *J. Nano. Res.* **2008**, *10*, 163.
- (23) Di Paola, A.; Garcia-Lopez, E.; Ikeda, S.; Marci, G.; Ohtani, B.; Palmisano, L. *Catal. Today* **2002**, *75*, 87.
- (24) Srinivasan, S. S.; Wade, J.; Stefanakos, E. K.; Goswami, Y. *J. Alloys Compd.* **2006**, *424*, 322.
- (25) Ahmad, A.; Shah, J. A.; Buzby, S.; Shah, S. I. *Eur. J. Inorg. Chem.* **2008**, 948.
- (26) Kato, H.; Kudo, A. *J. Phys. Chem. B* **2002**, *106*, 5029.
- (27) Niishiro, R.; Kato, H.; Kudo, A. *Phys. Chem. Chem. Phys.* **2005**, *7*, 2241.
- (28) Niishiro, R.; Konta, R.; Kato, H.; Chun, W. J.; Asakura, K.; Kudo, A. *J. Phys. Chem. C* **2007**, *111*, 17420.
- (29) Huang, D. E.; Liao, S. J.; Quan, S. Q.; Liu, L.; He, Z. J.; Wan, J. B.; Zhou, W. B. *J. Mater. Res.* **2007**, *22*, 2389.
- (30) Li, D.; Haneda, H.; Hishita, S.; Ohashi, N. *Chem. Mater.* **2005**, *17*, 2588.
- (31) Yu, J. G.; Zhou, M. H.; Cheng, B.; Zhao, X. J. *J. Mol. Cat. A: Chem.* **2006**, *246*, 176.

- (32) Liu, H. Y.; Gao, L. *J. Am. Ceram. Soc.* **2004**, *87*, 1582.
- (33) Sakatani, Y.; Ando, H.; Okusako, K.; Koike, H.; Nunoshige, J.; Takata, T.; Kondo, J. N.; Hara, M.; Domen, K. *J. Mater. Res.* **2004**, *19*, 2100.
- (34) Sakatani, Y.; Nunoshige, J.; Ando, H.; Okusako, K.; Koike, H.; Takata, T.; Kondo, J. N.; Hara, M.; Domen, K. *Chem. Lett.* **2003**, *32*, 1156.
- (35) Pan, C. C.; Wu, J. C. S. *Mater. Chem. Phys.* **2006**, *100*, 102.
- (36) Kim, S.; Lee, S.-K. *J. Photochem. Photobiol. A-Chem.* **2009**, *203*, 145.
- (37) Zhao, Z. Y.; Liu, Q. J. *Catal. Lett.* **2008**, *124*, 111.
- (38) Wang, Y.; Meng, Y. L.; Ding, H. M.; Shan, Y. K.; Zhao, X.; Tang, X. Z. *J. Phys. Chem. C* **2008**, *112*, 6620.
- (39) He, Z. Q.; Xu, X.; Song, S.; Xie, L.; Tu, J. J.; Chen, J. M.; Yan, B. *J. Phys. Chem. C* **2008**, *112*, 16431.
- (40) Shannon, R. D. *Acta Crystallogr., Sec. A* **1976**, *32*, 751.
- (41) Serpone, N.; Lawless, D.; Disdier, J.; Herrmann, J. M. *Langmuir* **1994**, *10*, 643.
- (42) Umebayashi, T.; Yamaki, T.; Itoh, H.; Asai, K. *J. Phys. Chem. Solids* **2002**, *63*, 1909.
- (43) Kudo, A.; Niishiro, R.; Iwase, A.; Kato, H. *Chem. Phys.* **2007**, *339*, 104.
- (44) Kuznetsov, V. N.; Serpone, N. *J. Phys. Chem. B* **2006**, *110*, 25203.
- (45) Serpone, N. *J. Phys. Chem. B* **2006**, *110*, 24287.
- (46) Lisachenko, A. A.; Kuznetsov, V. N.; Zakharov, M. N.; Mikhailov, R. V. *Kinet. Catal.* **2004**, *45*, 189.
- (47) Kuznetsov, V. N.; Krutitskaya, T. K. *Kinet. Catal.* **1996**, *37*, 446.
- (48) Spurr, R. A.; Myers, H. *Anal. Chem.* **1957**, *29*, 760.

## Chapter 4

# Photocatalytic Production of Hydrogen on Ni/NiO/ $\text{KNbO}_3$ /CdS Nanocomposites using Visible Light

Sections reprinted with permission from Choi, J.; Ryu, S.Y.; Balcerski, W.; Lee, T.K.; Hoffmann, M. R. *Journal of Materials Chemistry* **2008**, *18*, 2371.  
© 2008 The Royal Society of Chemistry

## Abstract

The photocatalytic production of H<sub>2</sub> from water splitting was demonstrated on Ni/NiO/KNbO<sub>3</sub>/CdS nanocomposites using visible light irradiation at wavelengths > 400 nm in presence of isopropanol. The inherent photocatalytic activity of bulk-phase CdS was enhanced by combining Q-sized CdS with KNbO<sub>3</sub> and Ni deposited on KNbO<sub>3</sub>. Enhanced activity is most likely due to effective charge separation of photogenerated electrons and holes in CdS that is achieved by electron injection into the conduction band of KNbO<sub>3</sub> and the reduced states of niobium (e.g., Nb(IV) and Nb(III)) are shown to contribute to enhanced reactivity in the KNbO<sub>3</sub> composites by mediating effective electron transfer to bound protons. We also observed that the efficient attachment of Q-size CdS and the deposition of nickel on the KNbO<sub>3</sub> surface increases H<sub>2</sub> production rates. Other factors that influence the rate of H<sub>2</sub> production including the nature of the electron donors and the solution pH were also determined. The Ni/NiO/KNbO<sub>3</sub>/CdS nanocomposite system appears to be a promising candidate for possible practical applications including the production of H<sub>2</sub> under visible light.

## Introduction

Hydrogen ( $H_2$ ) production from water splitting using semiconductor photocatalysts has attracted considerable interest since the pioneering work of Fujishima and Honda,<sup>1</sup> who discovered that water can be photo-electrochemically decomposed into hydrogen and oxygen using a semiconductor ( $TiO_2$ ) electrode under UV irradiation. A large number of metal oxides and sulfides (e.g.  $TiO_2$ ,<sup>1-3</sup>  $WO_3$ ,<sup>4-6</sup>  $SrTiO_3$ ,<sup>7,8</sup>  $ZnO$ ,<sup>9-11</sup>  $CdS$ ,<sup>12-17</sup>  $ZnS$ ,<sup>13,16,18,19</sup> niobates,<sup>20-24</sup> and tantalates<sup>25-28</sup>) have been examined as photocatalysts for hydrogen production from splitting water. However, the majority of the simple and mixed-metal oxides photocatalysts are primarily active for  $H_2$  production under UV irradiation ( $\lambda < 385$  nm or  $E_{bg} \geq 3.0$  eV) present in only a small portion of solar light. More recently, there is a focused effort on the development of photocatalysts that are capable of using visible light ( $\lambda = 400-700$  nm) for the photocatalytic production of  $H_2$  including transition metal doping (e.g., platinum,<sup>29</sup> chromium,<sup>30</sup> and vanadium<sup>31</sup>) and nonmetallic element doping (e.g., nitrogen,<sup>32-35</sup> sulfur,<sup>36,37</sup> and carbon<sup>35,38</sup>).

$CdS$ , n-type semiconductor with  $E_g = 2.4$  eV, has been shown to have photocatalytic activity for  $H_2$  production under visible light irradiation, although, sacrificial electron donors such as  $C_2H_5OH$ ,<sup>39</sup>  $HS^-$ ,<sup>40,41</sup> or  $SO_3^{2-19}$  are used to obtain measurable rates of  $H_2$  production and to avoid the photocorrosion of  $CdS$  in the presence of  $O_2$ . On the other hand, the electronic levels and photoactivity of  $CdS$  can be tuned by changing or controlling particle size without changing the chemical composition. For example in the case of nanoparticulate  $ZnO$ , Hoffmann and co-workers<sup>9,42</sup> reported a tenfold increase in photoefficiency for the photocatalytic production of hydrogen peroxide with a decrease in particle size from 40 to 23 nm. In another example, Hoffman et al.<sup>43</sup> found an increase

in quantum efficiency for photo-polymerization of methylmethacrylate with a corresponding decrease in particle size using Q-size CdS.

In order to enhance the photocatalytic activity of CdS, efforts have been made to combine CdS with other semiconductors having different band energies (e.g., TiO<sub>2</sub>,<sup>44-47</sup> ZnS,<sup>13,48,49</sup> K<sub>4</sub>Nb<sub>6</sub>O<sub>17</sub>,<sup>50</sup> or K<sub>2</sub>Ti<sub>4</sub>O<sub>9</sub><sup>51,52</sup>) since the coupling of two semiconductor particles with different energy levels is useful to achieve effective charge separation. For example in a colloidal TiO<sub>2</sub>/CdS composite system, the electrons photogenerated from CdS band gap excitation can be transferred to the conduction band (CB) of TiO<sub>2</sub> particles, while the holes remain in the CdS particle. It is also observed that this charge separation in a colloidal composite system can accelerate the degradation of azo-dye<sup>44</sup> and increase H<sub>2</sub> production in aqueous H<sub>2</sub>S solution.<sup>46</sup>

In this study, we synthesized nanocomposites of potassium niobate (KNbO<sub>3</sub>) and CdS by solid-state reactions and investigated their properties and photoactivity for H<sub>2</sub> production under visible light irradiation ( $\lambda > 400$  nm) in presence of isopropanol as an electron donor. KNbO<sub>3</sub> is used in optical waveguides, in nonlinear optical devices (e.g., frequency doubling and wavelength mixing), in piezoelectric devices (e.g., tunable frequency ultrasound transducers), in holographic image storage, and as a wide-band gap photocatalyst ( $\Delta E_g = 3.4$  eV) because of its unusual chemical and physical properties. KNbO<sub>3</sub>/CdS nanocomposites are characterized by XRD, SEM, TEM, UV-vis reflectance spectra and show better visible-light photoactivity for H<sub>2</sub> production than other composites (e.g., TiO<sub>2</sub> or K<sub>4</sub>Nb<sub>6</sub>O<sub>17</sub>). Moreover, the efficiency of H<sub>2</sub> production is significantly enhanced by loading Ni on KNbO<sub>3</sub>.

## Experimental

### Sample Preparation

Stoichiometric KNbO<sub>3</sub> was synthesized from Nb<sub>2</sub>O<sub>5</sub> (Aldrich) and K<sub>2</sub>CO<sub>3</sub> (Aldrich) in a standard solid-state reaction. K<sub>2</sub>CO<sub>3</sub> and Nb<sub>2</sub>O<sub>5</sub> were mixed together in a mortar at 1:1 mole ratio and the powdered mixture was pressed into a pellet at 27.6 Mpa and then heated at 650~925 °C for 10 hours with a heating and cooling temperature ramp of ±200 °C/h. With slight variations of the K:Nb mole ratio of 1:1.1 and a heating temperature at 1025 °C, a mixture of KNbO<sub>3</sub> and K<sub>4</sub>Nb<sub>6</sub>O<sub>17</sub> was obtained. Synthesis of K<sub>4</sub>Nb<sub>6</sub>O<sub>17</sub> was carried out for comparison using K<sub>2</sub>CO<sub>3</sub> and Nb<sub>2</sub>O<sub>5</sub> in the K:Nb mole ratio of 1:1.5 and calcination at 1150 °C for 10 hours. The crystal structures were confirmed by X-ray diffraction (XRD) at room temperature.

KNbO<sub>3</sub>/CdS composite samples were prepared by stirring KNbO<sub>3</sub> powders in a 20 mL of ethanol of 2 x 10<sup>-2</sup> M Cd(CH<sub>3</sub>COO)<sub>2</sub>·2H<sub>2</sub>O for 1 day, followed by sulfurization with a 20 mL of ethanol of 2 x 10<sup>-2</sup> M Na<sub>2</sub>S for 1 day. Composite samples were collected by filtration, which was followed by washing and subsequent drying.

Elemental nickel (Ni) and NiO (0.1~3.6 wt %) was loaded on the surface of KNbO<sub>3</sub> by a method that Domen and coworkers<sup>23,53,54</sup> reported. KNbO<sub>3</sub> samples were suspended in a Ni(NO<sub>3</sub>)<sub>2</sub> aqueous solution for 1 day, followed by it being filtered, washed, and dried. The solid was reduced in H<sub>2</sub> atmosphere at 500 °C for 2 h, and subsequently oxidized in an O<sub>2</sub> atmosphere at 200 °C for 1 h. In the case of elemental Ni-loaded KNbO<sub>3</sub> samples (Ni/KNbO<sub>3</sub>), the O<sub>2</sub> oxidation step was eliminated. The NiO-loaded KNbO<sub>3</sub> samples (NiO/KNbO<sub>3</sub>) were obtained by complete O<sub>2</sub> oxidation at 500 °C for 1 h. A schematic flow chart is shown in Figure 4.1.

## Characterization

The crystal structures of synthesized  $\text{KNbO}_3$  samples were confirmed by a powder X-ray diffraction (XRD) using a Phillips diffractometer (X'pert Pro) with  $\text{Cu-K}\alpha$  radiation. Diffuse reflectance spectra were obtained with UV-vis spectrometer (Shimadzu UV-2101PC) and were converted from reflection to absorption spectra by the Kubelka-Munk method. Brunauer-Emmett-Teller (BET) surface area analyses were also performed to compare the surface areas of  $\text{KNbO}_3$  samples that were prepared under different conditions. Microstructures and composition were also analyzed with a LEO 1550VP Field Emission Scanning Electron Microscope (SEM) and Philips EM201 Transmission Electron Microscope (TEM). Inductivity Coupled Plasma-Mass Spectrometry (HP 4500 ICP-MS) was used to determine the amounts of  $\text{Ni}^{2+}$  and  $\text{Cd}^{2+}$  adsorbed on the surface of  $\text{KNbO}_3$ . Pottassium ions released from  $\text{KNbO}_3$  during ion-exchange with  $\text{Ni}^{2+}$  were determined by Dionex DX-500 Ion Chromatography system. X-ray Photoelectron Spectroscopy (XPS) was used to observe the changes in the oxidation state of Nb species and Ni species adsorbed on the surface of  $\text{KNbO}_3$  with Al  $\text{K-}\alpha$  radiation.

## Photocatalytic Reaction

Photocatalytic reactions for hydrogen production were carried out in an air-tight reactor vessel under visible light irradiation ( $\lambda > 400$  nm). Catalyst samples (0.2 g) were suspended in 50 mL of a water/isopropanol mixture (30 v/v %) in a Pyrex glass reactor. Samples were purged with Ar or  $\text{N}_2$  gas for 30 min before reaction in order to eliminate dissolved  $\text{O}_2$ . A high-pressure 500 W Hg-Xe arc lamp in combination with a 400 nm cut-off filter was used as the primary light source. The intensity of incident

light was determined by ferrioxalate actinometry to obtain quantum yields for H<sub>2</sub> production. The amount of H<sub>2</sub> evolved during photolysis was analyzed by GC/TCD (HP 5890, N<sub>2</sub> carrier) with a molecular sieve column (30 m × 0.32 mm × 12.00 μm).

## Results and Discussion

### Ni/NiO/KNbO<sub>3</sub>/CdS Nanocomposite Characterization

Figure 4.2 shows XRD patterns of synthesized KNbO<sub>3</sub> under different calcination temperatures and mole ratios. XRD pattern for KNbO<sub>3</sub> calcined at 925°C with 1:1 mole ratio of K:Nb (Figure 4.2(a)) shows exactly same 2θ peaks that correspond to standard KNbO<sub>3</sub>. Samples calcined over the range of temperature from 650 to 925°C also show the same peak patterns. However, a sample produced at 1025 °C with 1:1.1 mole ratio of K:Nb (Figure 4.2(b)) has an extra 2θ peaks that are attributed to potassium hexaniobate (K<sub>4</sub>Nb<sub>6</sub>O<sub>17</sub>). K<sub>4</sub>Nb<sub>6</sub>O<sub>17</sub> has a perovskite structure similar to KNbO<sub>3</sub>, but it consists of a layered structure composed of two different types of niobate sheets. The material structures are also confirmed by SEM images. A layered structure is only observed for the sample calcined at 1025°C by SEM as shown in Figure 4.3. The diffraction peaks of KNbO<sub>3</sub> samples are more intense and sharper, with an increase in calcination temperature. The broadening of XRD peaks at low calcination temperatures may be due to smaller crystallite size. The particle sizes of KNbO<sub>3</sub> at different calcination temperatures can be estimated with the Scherrer equation; the estimated particle sizes were 28, 32, and 39 nm for KNbO<sub>3</sub> samples prepared at 650 °C, 775 °C and 925 °C, respectively. BET surface areas were also measured at 4.35, 3.08, and 2.14 m<sup>2</sup>g<sup>-1</sup> for 650 °C, 775 °C, and 925 °C samples, respectively, and it is apparent that the

specific surface area decreases with an increase in calcination temperature. Furthermore, there appears to be no observable structural difference between  $\text{KNbO}_3$  samples before and after Ni deposition or with the addition of nanoparticulate CdS. Figure 4.4 is the TEM picture of nanocomposite sample of Ni/NiO/ $\text{KNbO}_3$ /CdS which shows that Ni or CdS nanoparticles were loaded on the surface of  $\text{KNbO}_3$ .

Figure 4.5 shows the light absorption properties of nanocomposite samples. The  $\text{KNbO}_3$ /CdS nanocomposite absorbs visible light at  $\lambda > 400$  nm. This is primarily due to the band gap excitation of Q-size CdS, since  $\text{KNbO}_3$  does not absorb visible light. The respective band gaps are estimated to be 3.4 eV and 2.6 eV for  $\text{KNbO}_3$  and Q-CdS, from the plots of Kubelka-Munk functions vs. photon energy. It should be noted that absorption edge of Q-size CdS synthesized for CdS/ $\text{KNbO}_3$  nanocomposite is blue-shifted from absorption edge of bulk CdS particles.<sup>43</sup>

The synthesized  $\text{KNbO}_3$  samples were suspended in an aqueous  $\text{Ni}(\text{NO}_3)_2$  solution for 1 day to load  $\text{Ni}^{2+}$  as a co-catalyst. ICP-MS and IC results show that most of  $\text{Ni}^{2+}$  ions are adsorbed on the surface of  $\text{KNbO}_3$  particles and some of them are ion-exchanged with  $\text{K}^+$  ions located in  $\text{KNbO}_3$  framework. However, in synthesis of CdS nanoparticle on  $\text{KNbO}_3$  surface, only 20~30% of  $\text{Cd}^{2+}$  ions are adsorbed on the surface and ion exchange with  $\text{K}^+$  are not observed. Then  $\text{Ni}^{2+}$ -adsorbed (or ion-exchanged)  $\text{KNbO}_3$  samples were treated under proper conditions, i.e.,  $\text{H}_2$  reduction at 500 °C followed by  $\text{O}_2$  oxidation at 200 °C. After thermal reduction by  $\text{H}_2$ , the doped samples turned gray from the initial white undoped  $\text{KNbO}_3$ . However, oxidation at 500 °C converts elemental nickel to NiO with a corresponding change in color from gray to light yellow. XPS analysis of the various samples was used to identify the oxidation states of Ni in each sample.

## Photocatalytic H<sub>2</sub> production

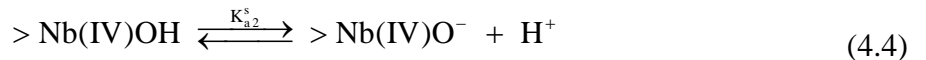
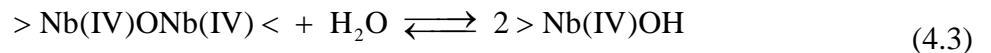
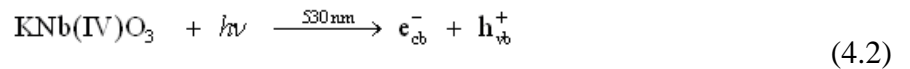
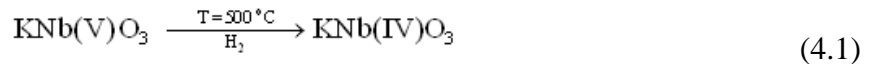
The measured H<sub>2</sub> production rates in illuminated aqueous isopropanol solutions under visible light with CdS, KNbO<sub>3</sub>, Ni/NiO/KNbO<sub>3</sub>, and Ni/NiO/KNbO<sub>3</sub>/CdS composites are compiled in Table 4.1. The naked KNbO<sub>3</sub>, nickel-doped KNbO<sub>3</sub>, and Ni/NiO/KNbO<sub>3</sub> samples showed no activity for H<sub>2</sub> production under the visible light since its band gap energy (3.4 eV) was larger than the excitation energies ( $\lambda > 400$  nm). Simple Q-CdS nanoparticle suspensions produce H<sub>2</sub>, but at very low rates. However, H<sub>2</sub> production rates increase significantly in the KNbO<sub>3</sub>/CdS nanocomposites. This may be due to effective charge separation of electrons and holes in illuminated CdS, with electron injection into the conduction band of KNbO<sub>3</sub> possible in the KNbO<sub>3</sub>/CdS nanocomposites. H<sub>2</sub> production with TiO<sub>2</sub> (Degussa P-25)/CdS nanocomposites was also performed for comparison. TiO<sub>2</sub>/CdS had lower H<sub>2</sub> production activity than KNbO<sub>3</sub>/CdS. H<sub>2</sub> production rates for the KNbO<sub>3</sub>/CdS nanocomposites were enhanced significantly in the presence of the deposited Ni/NiO co-catalysts. Ni most likely serves to collect conduction band electrons. However, a significant enhancement of H<sub>2</sub> production rate was not observed in Pt deposited KNbO<sub>3</sub> samples (Pt/KNbO<sub>3</sub>/CdS) as compared to Ni/KNbO<sub>3</sub>/CdS nanocomposites. We also synthesized potassium hexaniobate (K<sub>4</sub>Nb<sub>6</sub>O<sub>17</sub>) for comparison because K<sub>4</sub>Nb<sub>6</sub>O<sub>17</sub> is known as a good photocatalyst for H<sub>2</sub> production under UV light irradiation.<sup>20,22,23</sup> However, the result shows that KNbO<sub>3</sub>/CdS nanocomposite produces more H<sub>2</sub> than K<sub>4</sub>Nb<sub>6</sub>O<sub>17</sub>/CdS under visible light irradiation.

The enhanced reactivity of the KNbO<sub>3</sub> nanocomposites may be due to involvement of the reduced states of niobium and/or oxygen vacancies that allow for the photoexcitation

of mobile electrons with visible light. For example, Ewart et al.<sup>55</sup> reported that mobile electrons are generated in electrochemically reduced and Fe-doped KNbO<sub>3</sub> upon excitation at 532 nm. The electrons photoexcited at 532 nm had lifetimes of 4 ns and electron mobilities of 0.5 cm<sup>2</sup> V<sup>-1</sup> s<sup>-1</sup>. They concluded that the photoexcited electrons are trapped within 4 ns (i.e., loss of detectable mobility), however, the trapped-state electrons are thermally activated on a millisecond timeframe and eventually recombine with the internal donor states. Kesselman et al.<sup>56</sup> observed a similar reduction in Nb<sub>2</sub>O<sub>5</sub>/TiO<sub>2</sub> composites that were reduced over hydrogen at high temperatures. Reduction of Nb<sub>2</sub>O<sub>5</sub> is known to form a variety of phases such as Nb<sub>12</sub>O<sub>29</sub>, Nb<sub>22</sub>O<sub>54</sub>, Nb<sub>25</sub>O<sub>62</sub>, and Nb<sub>47</sub>O<sub>116</sub> that involve partial oxygen loss coupled with the formation of Nb(IV). Therefore, the longer lifetimes ( $\tau_{tr} > \text{ms}$ ) of the trapped electrons may contribute to the higher reduction rates for bound protons or hydroxides. Similar mixed valence state phase should coexist within the framework of reduced KNbO<sub>3</sub> and contribute to the photo-excitation of electrons and to the overall photoactivity with visible light. The Ni/NiO/KNbO<sub>3</sub> samples were thermally treated at 500 °C under H<sub>2</sub> atmosphere to reduce Ni<sup>2+</sup> to elemental nickel. This treatment step may lead to creation of oxygen vacancies or formation of the reduced states (e.g., Nb(IV) and Nb(III) states) of niobium. The thermal treatment of pure, white KNbO<sub>3</sub> at 500 °C under H<sub>2</sub> produced a light gray product that is consistent with Nb(V) reduction. We performed XPS analysis to compare the oxidation states of Nb between KNbO<sub>3</sub> samples before and after H<sub>2</sub> reduction, however, the reduced states were not readily observed. However, it was measured that reduced states of Nb are formed during the photolytic reaction. Another relevant feature of the metal niobates (e.g., LiNbO<sub>3</sub><sup>57</sup> and KNbO<sub>3</sub><sup>58</sup>), which is critical for

electro-optic and photorefractive applications, is the activation of surface protons (i.e., protons bound in hydroxyl ions,  $^-\text{OH}$ ). The hydroxyl bound protons have activation energies in the range of 1 eV for mobility in  $\text{KNbO}_3$  crystals.

In light of the above photophysical properties related to surface hydroxyl groups, an alternative pathway may involve excitation of reduced  $\text{KNbO}_3$  with visible light followed by conduction band reduction of surface bound protons on  $\text{KNbO}_3$ . The pH of zero point of charge,  $\text{pH}_{\text{zpc}}$ , of  $\text{KNbO}_3$  was measured  $\sim \text{pH } 3.2$ , thus  $\text{KNbO}_3$  surface may be dominated by  $>\text{NbOH}$  and  $>\text{NbO}^-$  under our optimal experimental conditions ( $\sim \text{pH } 8$ ). Given this situation, we can write the following set of reactions that may result in  $\text{H}_2$  production on  $\text{KNbO}_3$  surface sites or  $\text{Ni/NiO/KNbO}_3$  composite sites:



In addition, we compared three different procedures for attachment of CdS particles on the  $\text{KNbO}_3$  surface as shown in Figure 4.6. To form  $\text{KNbO}_3/\text{CdS}$  nanocomposites, we first added  $\text{Cd}^{2+}$  ions in  $\text{KNbO}_3$  suspension, and then we added sulfide ( $\text{HS}^-/\text{S}^{2-}$ ) ions after stirring for 1 day (Figure 4.6(a)). ICP-MS results show that only 20~30 % of the Cd in CdS particles are directly synthesized on the  $\text{KNbO}_3$  surface and the remainder of

the CdS particles are suspended freely in the solution. One sample was prepared by mechanical mixing of CdS and KNbO<sub>3</sub> by addition of KNbO<sub>3</sub> after Q-CdS synthesis in ethanol (Figure 4.6(b)) and another sample has only CdS adsorbed on the KNbO<sub>3</sub> surface by removing free Cd<sup>2+</sup> ions in suspension before adding S<sup>2-</sup> ions (Figure 4.6(c)). The CdS surface adsorption sample (Figure 4.6(c)) shows reasonable photoactivity even though the amounts of CdS are quite small (20~30 %) compared to samples having CdS synthesized both on KNbO<sub>3</sub> surface and in solution (Figure 4.6(a)). As a consequence, we conclude that direct CdS contact with the KNbO<sub>3</sub> surface plays an important role for effective charge separation with increased H<sub>2</sub> production rates, although externally mixed sample (Figure 4.6(b)) also has measurable H<sub>2</sub> production rates. From these results, we can infer that Q-CdS particles are attached to the surface of KNbO<sub>3</sub> under our experimental conditions (~ pH 8) even though CdS was synthesized initially in solution phase.

The KNbO<sub>3</sub> surface is negatively charged under the pH conditions of our experiments since the p*H*<sub>zpc</sub> of KNbO<sub>3</sub> is measured ~ pH 3.2. The actual determination of p*H*<sub>zpc</sub> of the nanoparticulate CdS colloids is more difficult. Park and Huang<sup>59</sup> reported a p*H*<sub>zpc</sub> = 7.5 for colloidal CdS based on electrophoretic mobility measurements and acid-base titrations. At an ionic strength of  $\mu = 0.05$  M, they determined that p*K*<sub>a1</sub><sup>s</sup> = 6.1 and p*K*<sub>a2</sub><sup>s</sup> = 9.0 for [Cd<sup>2+</sup>] = 2.5  $\mu$ M and  $\sigma_0 = 20$  mC cm<sup>-2</sup>. Liu and Huang<sup>60</sup> subsequently reported a p*H*<sub>zpc</sub> for cubic CdS of 7.0 and p*H*<sub>zpc</sub> = 7.5 for hexagonal CdS. In contrast, other researchers<sup>61-63</sup> have reported substantially lower values for the p*H*<sub>zpc</sub> for CdS in aqueous suspensions. Under experimental conditions that were quite different from those employed by Park and Huang,<sup>59</sup> Nicolau et al.<sup>63</sup> determined a p*H*<sub>zpc</sub> = 1.8 for 0.01

M  $\text{Na}_2\text{SO}_4$  and  $\text{KCl}$  as background electrolytes based on electrophoretic mobility measurements. Guindo et al.<sup>62</sup> found even lower values of  $\text{pH}_{\text{zpc}}$  between 1 and 1.5 for spherical  $\text{CdS}$  particles differently prepared. However, they pointed out that the IEP (isoelectric point) was sensitive to the specific surface characteristics of  $\text{CdS}$  that depends on the degree of oxidation or aging as noted by the shift in IEP to higher values for samples that were synthesized over longer periods of time. According to our observations, it may be true that  $\text{pH}_{\text{zpc}}$  of  $\text{CdS}$  is relatively high value under our experimental conditions, so that  $\text{CdS}$  colloid in solution are positively-charged and then electrostatically attracted to the negatively charged  $\text{KNbO}_3$  particles under our experimental pH condition.

The rates of  $\text{H}_2$  production on the four-component composite,  $\text{Ni/NiO/KNbO}_3/\text{CdS}$  are compared to the three-component composite containing only  $\text{Ni}$  or  $\text{NiO}$ . The data presented in Figure 4.7 shows that elemental  $\text{Ni}$  on  $\text{KNbO}_3$  is a more active species than  $\text{NiO}$  on  $\text{KNbO}_3$  to improve  $\text{H}_2$  production, although its external surface is partially oxidized to  $\text{NiO}$ . However, the  $\text{H}_2$  production rates are not greatly enhanced in the three-component composite containing only  $\text{NiO}$ . This tendency is consistent with previous results obtained for  $\text{Ni/NiO}$  loaded onto  $\text{SrTiO}_3$  as reported by Domen et al.<sup>53</sup> They reported that  $\text{Ni/NiO/SrTiO}_3$  produced substantially more  $\text{H}_2$  from aqueous methanol than the simpler  $\text{NiO/SrTiO}_3$  system under UV irradiation. They concluded that the presence of  $\text{Ni}$  metal in contact with the  $\text{SrTiO}_3$  surface plays an important role in the  $\text{H}_2$  production activity. Domen et al.<sup>64</sup> also found small amounts of  $\text{H}_2$  evolved under the band gap irradiation of  $\text{Ni/SrTiO}_3$ . They attributed their low activity to loss of  $\text{Ni}$  by release of  $\text{Ni}^{2+}$  due to oxidation of  $\text{Ni}$  metal by direct hole transfer from  $\text{SrTiO}_3$

during band gap irradiation. In contrast, our results show that the three-component Ni/KNbO<sub>3</sub>/CdS composite can produce a comparable amount of H<sub>2</sub> compared to the four-component Ni/NiO/KNbO<sub>3</sub>/CdS composite. In both the 3- and 4-component catalyst, the primary absorption occurs at  $\lambda > 400$  nm (compared to SrTiO<sub>3</sub> with  $\lambda < 400$  nm) with CdS as a chromophore. Thus, elemental nickel deposited on KNbO<sub>3</sub> is unlikely to be directly oxidized by holes in our composite material.

As shown in Table 4.1, the highest H<sub>2</sub> production rates were obtained with a Ni-deposition level of 0.1 wt. % as (Ni<sub>T</sub> = Ni + NiO), and above this level, enhancement due to nickel deposition was marginal. However, we observed the enhanced H<sub>2</sub> production with higher wt% of Ni deposition on KNbO<sub>3</sub> samples prepared at low calcination temperatures. The increase of photoactivities with 0.5 ~ 1.0 wt. % Ni-loaded on KNbO<sub>3</sub> prepared at low calcination temperatures may be only due to a simple increase in the total reactive surface area. It is noted that KNbO<sub>3</sub> sample mixed with K<sub>4</sub>Nb<sub>6</sub>O<sub>17</sub> structure which was calcined at 1025°C produces comparable amounts of H<sub>2</sub> to KNbO<sub>3</sub> samples calcined at 925°C.

We observed fairly dramatic color changes taking place during irradiation of the Q-size CdS and the CdS nanocomposite materials. In all cases, the catalysts suspensions are yellow before illumination because of CdS chromophore. However, after exposure to a focused beam of light at  $\lambda > 400$  nm, the color changes very quickly to a silver gray. As the color changes from yellow to gray, H<sub>2</sub> production is observed as a steady stream of gas bubbles rising up in the photolysis cell. The observed color change may be due to the rapid photoreduction of Cd(II) to Cd(I) and then to Cd(0) on the surface of CdS in the absence of oxygen. There is also some probability that S(-II) in the CdS matrix is

also oxidized partially by trapped valence band holes to form S(0) and eventually polysulfide ion ( $S_2^{2-}$ ). Upon exposure to oxygen, the yellow color is regenerated over several hours with the return of yellow CdS on the nanocomposite structures.

Apparent quantum yields,  $\phi$ , for  $H_2$  production, were determined as follows:

$$\phi = \frac{\frac{dm_{H_2}}{dt}}{I_{abs}^o} \times 2 \quad (4.7)$$

where  $dm_{H_2}/dt$  is an initial production rate of  $H_2$  ( $mol\ s^{-1}$ ) and  $I_{abs}^o$  is photon absorption rate in units of Einstein  $s^{-1}$  ( $mol(e^-)\ s^{-1}$ ). We also considered the fact that two electrons are consumed to produce one hydrogen molecule from two protons for quantum yield calculation. The photon flux through the cell was  $2.3 \times 10^{17}$  photons  $s^{-1}$ , as determined by ferrioxalate actinometry with an apparent quantum yield for  $H_2$  production of 4.4 % for  $\lambda > 400$  nm. It should be noted that the amount of light scattered from nanocomposites suspension was not considered here and therefore actual quantum yield may be higher.

### **Photocatalytic $H_2$ Production Under Natural Sunlight**

Substantial amounts of hydrogen gas are also produced readily using natural sunlight as the irradiation source. For example, the 4-composite was exposed to solar light between 11:30 am and 3:30 pm on the roof of W. M. Keck Laboratories at Caltech on August 13, 2006. Experimental procedures were identical to those employed in the controlled laboratory experiments except for the use of different types of pyrex reactors. As shown in Figure 4.8,  $H_2$  is readily produced from aqueous isopropanol solutions under natural sunlight; however, the amount of  $H_2$  produced is actually larger than that

produced over the same period of time under UV light irradiation in the laboratory. This simple demonstration illustrates the potential of practical application of Ni/NiO/KNbO<sub>3</sub>/CdS nanocomposite for H<sub>2</sub> production with sunlight.

### **Influence of Solvent Composition on Photocatalytic H<sub>2</sub> Production**

The relative effects of a variation of solvent/water mixtures on H<sub>2</sub> production for KNbO<sub>3</sub>/CdS at  $\lambda > 400$  nm are illustrated as shown in Figure 4.9. 30 v/v% of isopropanol (IPA), ethanol (EtOH), and methanol (MeOH) solution were used in the photoreaction. The order of photoreactivity is IPA > EtOH > MeOH, which is in inverse order of their dielectric constants (i.e.,  $\epsilon_{\text{IPA}} = 19 < \epsilon_{\text{EtOH}} = 24.3 < \epsilon_{\text{MeOH}} = 33$ ).

Alcohols function primarily as hole traps that prevent rapid electron-hole recombination. The presence of an electron donor other than water is crucial for photocatalytic H<sub>2</sub> production, since little H<sub>2</sub> is produced without added electron donors even under UV light irradiation. However, the interaction of the various electron donors with the charged CdS surface will also depend on their chemical and physical properties. Alcohols have substantially lower dielectric constants than H<sub>2</sub>O ( $\epsilon = 80.4$ ). As a consequence, we predict that the relative thickness of the electrical double layer (EDL) should decrease when alcohols are added. The EDL thickness should decrease in the order of dielectric constants, as given by the Debye equation:

$$\kappa \equiv \left( \frac{2 F^2 \mu}{\epsilon \epsilon_0 R T} \right)^{0.5} \quad (4.8)$$

where  $\epsilon$  is the dielectric constant of the solvent or mixed solvent system,  $\epsilon_0$  is the permittivity of free space ( $8.854 \times 10^{-12} \text{ C}^2 \text{ J}^{-1} \text{ m}^{-1}$ ),  $\mu$  is the ionic strength of the

background electrolyte ( $\text{mol m}^{-3}$ ),  $R$  is the gas constant ( $8.314 \text{ J mol}^{-1} \text{ K}^{-1}$ ),  $T$  is temperature in units of  $\text{K}$ , and  $F$  is the Faraday constant ( $96485 \text{ C mol}^{-1}$ ). Electrical double layer compression will enhance the physicochemical interaction of the electron donors with the charged CdS surface. Thus, a more efficient hole trapping by the electron donors should increase  $\text{H}_2$  production rates.

We note that  $\text{SO}_3^{2-}$  and  $\text{S}^{2-}$  are also frequently used as sacrificial donors to prevent the photocorrosion of metal sulfide semiconductors;<sup>19,46,47,65</sup> however, the  $\text{H}_2$  production rate of  $\text{KNbO}_3/\text{CdS}$  nanocomposites with the addition of  $0.01 \text{ M SO}_3^{2-}$  and  $0.1 \text{ M S}^{2-}$  was very low relative to adding alcohols as electron donors.

### **Influence of pH on Photocatalytic $\text{H}_2$ Production**

Without the addition of acid or base, the pH of the  $\text{KNbO}_3/\text{CdS}$  suspensions in  $\text{ROH}/\text{H}_2\text{O}$  is between pH 8 and 9. The pH-dependent production of  $\text{H}_2$  from aqueous isopropanol solution under visible light is shown in Figure 4.10. The highest production rates of  $\text{H}_2$  were obtained in the circumneutral pH region, while the rates of  $\text{H}_2$  production decreased at higher and lower pH.

The relative attachment of Q-CdS on the  $\text{KNbO}_3$  particles should be influenced by the  $\text{KNbO}_3$  and CdS surface charges. Since the  $\text{pH}_{\text{zpc}}$  value of  $\text{KNbO}_3$  was determined to be 3.2, the  $\text{KNbO}_3$  surface is negatively charged at both neutral and alkaline pH (i.e.,  $\text{pH} > \text{pH}_{\text{zpc}}$ ) and is positively charged at very acidic pH (i.e.  $\text{pH} < \text{pH}_{\text{zpc}}$ ). In case of Q-CdS,  $\text{pH}_{\text{zpc}}$  value varies from pH 1 to 7, according to the structure and surface characteristics of CdS, and the types and concentrations of background electrolytes. However, we assume that the  $\text{pH}_{\text{zpc}}$  of CdS is more likely to be high under our conditions to possibly account

for the rapid attachment of CdS colloids to the larger KNbO<sub>3</sub> particles (Figure 4.6(c)). Therefore, at circumneutral pH, positively charged CdS can be adsorbed onto the negatively charged KNbO<sub>3</sub> surface. At low pH, the surface charges of CdS and KNbO<sub>3</sub> would be positive, and at high pH, both particles are negatively charged so that effective contact and charge transfer from CdS to KNbO<sub>3</sub> is less likely to occur at extreme pH. Furthermore, proton ion-exchange also occurs for KNbO<sub>3</sub> samples under acidic conditions. K<sup>+</sup> ions in the framework of KNbO<sub>3</sub> may be ion-exchanged with H<sup>+</sup> ions, and a proton-exchanged form, K<sub>1-x</sub>H<sub>x</sub>NbO<sub>3</sub>, may have different structure and physicochemical properties from the original KNbO<sub>3</sub> materials. We prepared K<sub>1-x</sub>H<sub>x</sub>NbO<sub>3</sub> samples by stirring in 0.5 N H<sub>2</sub>SO<sub>4</sub> solutions for several days followed by washing, filtration, and drying, and tested photoactivity of K<sub>1-x</sub>H<sub>x</sub>NbO<sub>3</sub>/CdS nanocomposites for H<sub>2</sub> production. In circumneutral pH region, K<sub>1-x</sub>H<sub>x</sub>NbO<sub>3</sub>/CdS nanocomposites show extremely low H<sub>2</sub> production rates (~ 2.8 μmol h<sup>-1</sup>g<sup>-1</sup>). Therefore, we conclude that proton-exchanged KNbO<sub>3</sub> can be formed in low pH and it may cause low photoactivity of KNbO<sub>3</sub> for H<sub>2</sub> production in acidic pH.

## Conclusions

Efficient H<sub>2</sub> production was obtained with Ni/NiO/KNbO<sub>3</sub>/CdS composites with visible light irradiation ( $\lambda > 400$  nm). H<sub>2</sub> production rates were higher than TiO<sub>2</sub>/CdS or K<sub>4</sub>Nb<sub>6</sub>O<sub>17</sub>/CdS composites. Partially reduced states of niobium (e.g., Nb(IV) and Nb(III)), which are generated during Ni formation under H<sub>2</sub> and by photoreduction, may contribute to the enhanced reactivity of the KNbO<sub>3</sub> composites. Aliphatic alcohols (methanol, ethanol, isopropanol, etc.) serve as alternative electron donors and modified

the near surface environment via electrical double layer compression. The solution pH also influences the rate of photocatalytic H<sub>2</sub> production, with the highest H<sub>2</sub> production rates obtained at circumneutral pH. In addition, the 4-component nanocomposite (Ni/NiO/KNbO<sub>3</sub>/CdS) produces H<sub>2</sub> rapidly under natural sunlight. Our findings suggest that use of solar energy for photocatalytic water splitting with this developed photocatalyst system may give a promising source for hydrogen fuel.

### **Acknowledgement**

We are grateful to the Hydrogen Energy Research & Development Center and 21<sup>st</sup> Century Frontier Research and Development Program of the Ministry of Science and Technology of Korea for research support.

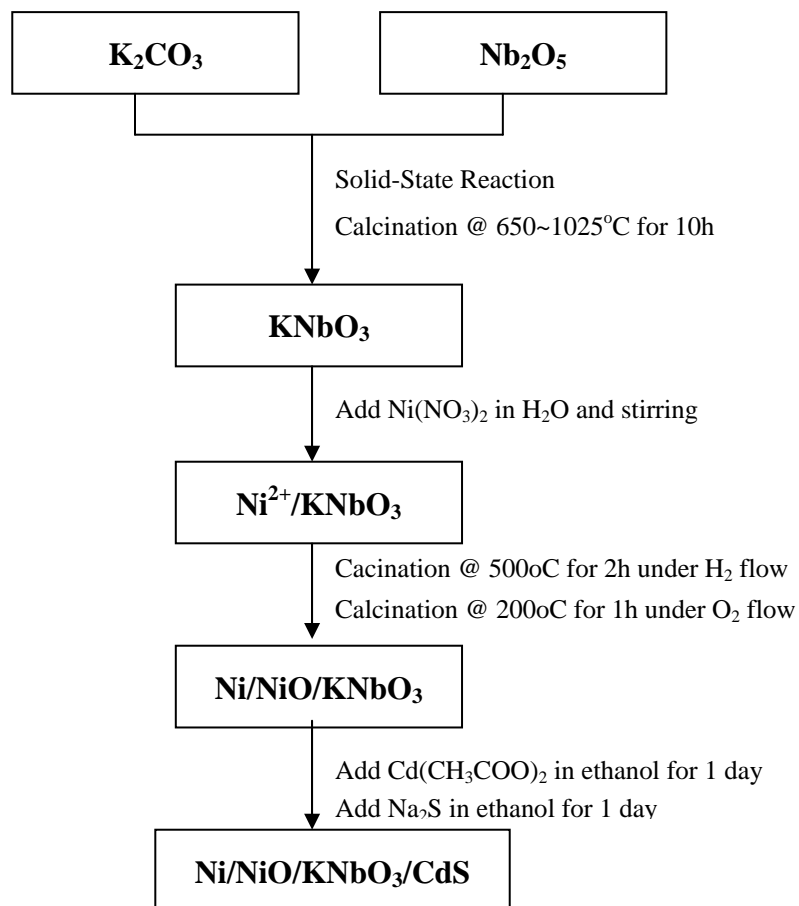


**Figure 4.1.** Schematic flow chart outlining the synthetic procedures for the composite Ni/NiO/  $\text{KNbO}_3/\text{CdS}$  catalyst preparation

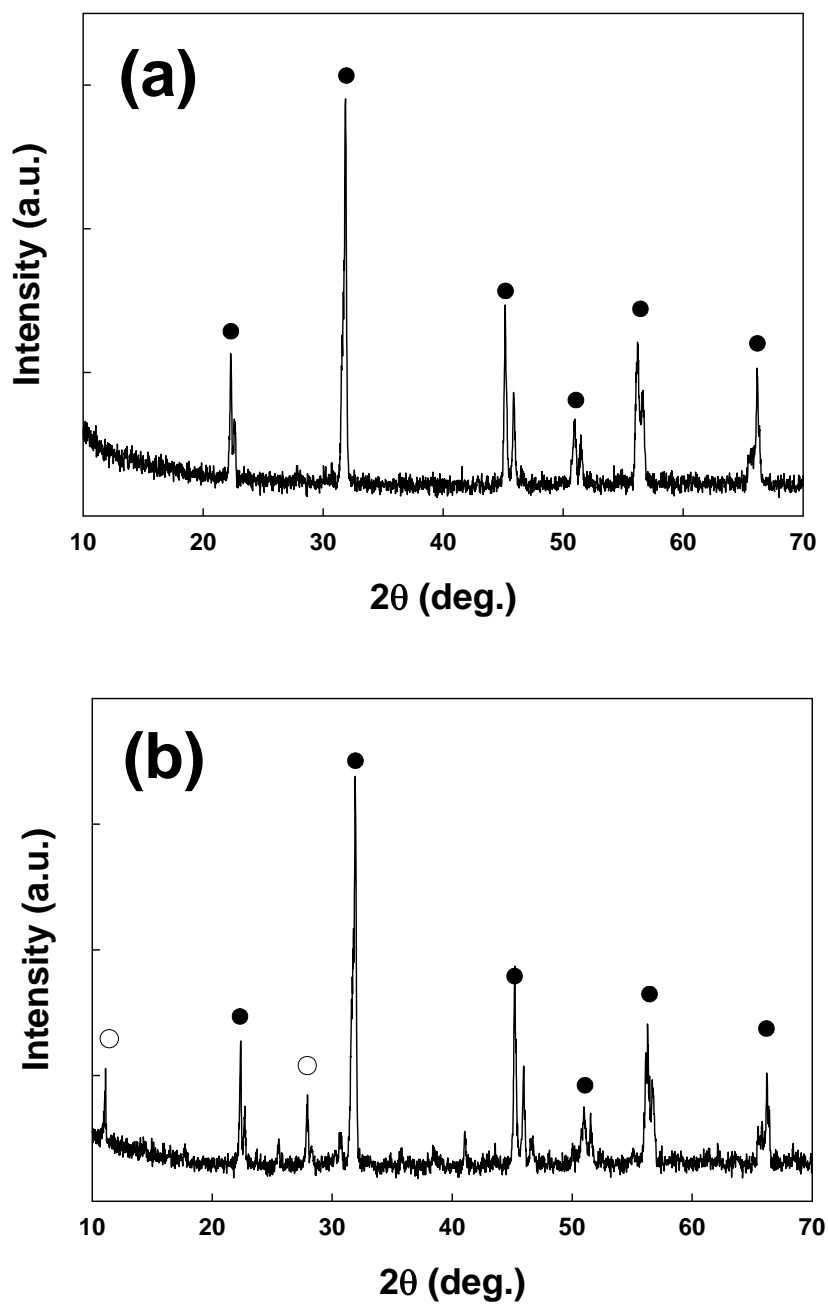


**Figure 4.2.** X-ray diffraction pattern for (a)  $\text{KNbO}_3$  powder sample synthesized from 1:1 mole ratio of  $\text{Nb}_2\text{O}_5$  and  $\text{K}_2\text{CO}_3$  at  $925^\circ\text{C}$  and (b)  $\text{KNbO}_3$  powder sample synthesized from 1:1.1 mole ratio of  $\text{Nb}_2\text{O}_5$  and  $\text{K}_2\text{CO}_3$  at  $1025^\circ\text{C}$ . ( $\bullet$ )  $\text{KNbO}_3$ , ( $\circ$ )  $\text{K}_4\text{Nb}_6\text{O}_{17}$

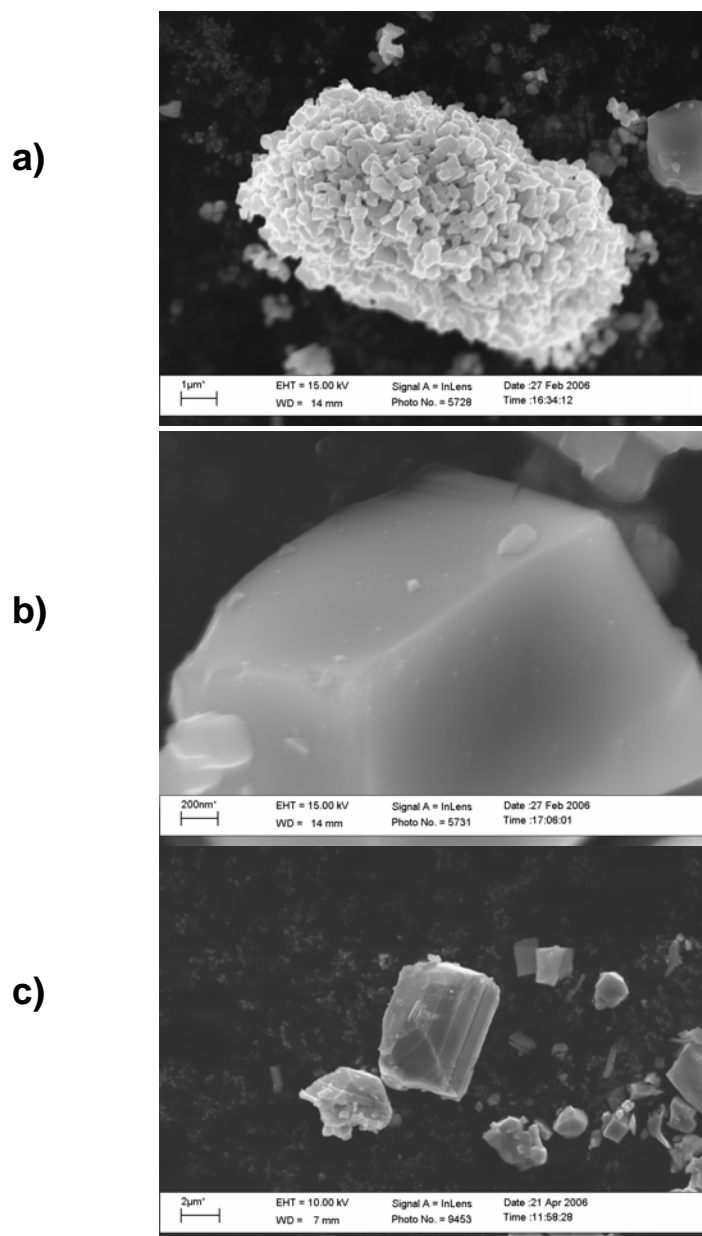


**Figure 4.3.** SEM images of (a), (b)  $\text{KNbO}_3$  synthesized at  $925^\circ\text{C}$  (K:Nb=1:1) and (c)  $\text{KNbO}_3$  synthesized at  $1025^\circ\text{C}$  (K:Nb = 1:1.1)

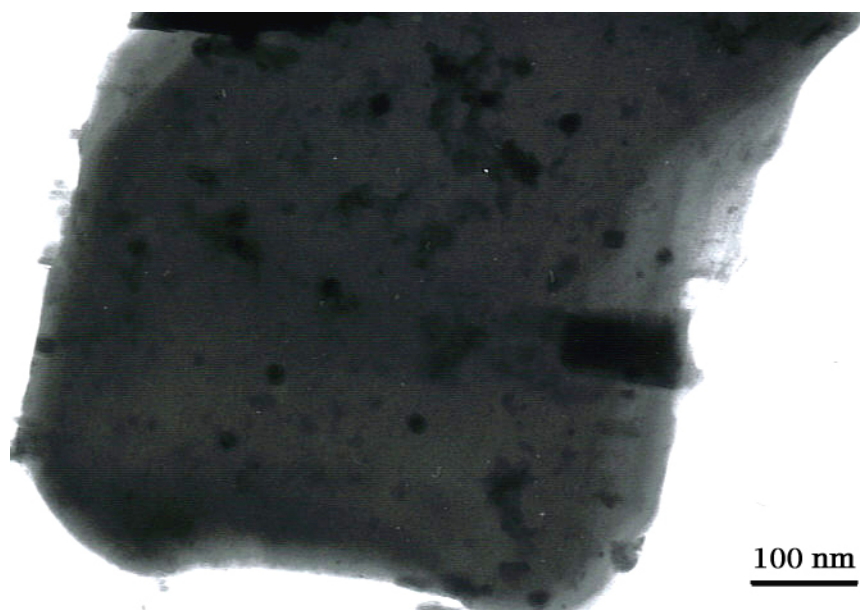


**Figure 4.4.** TEM images of Ni/NiO/KNbO<sub>3</sub>/CdS nanocomposite

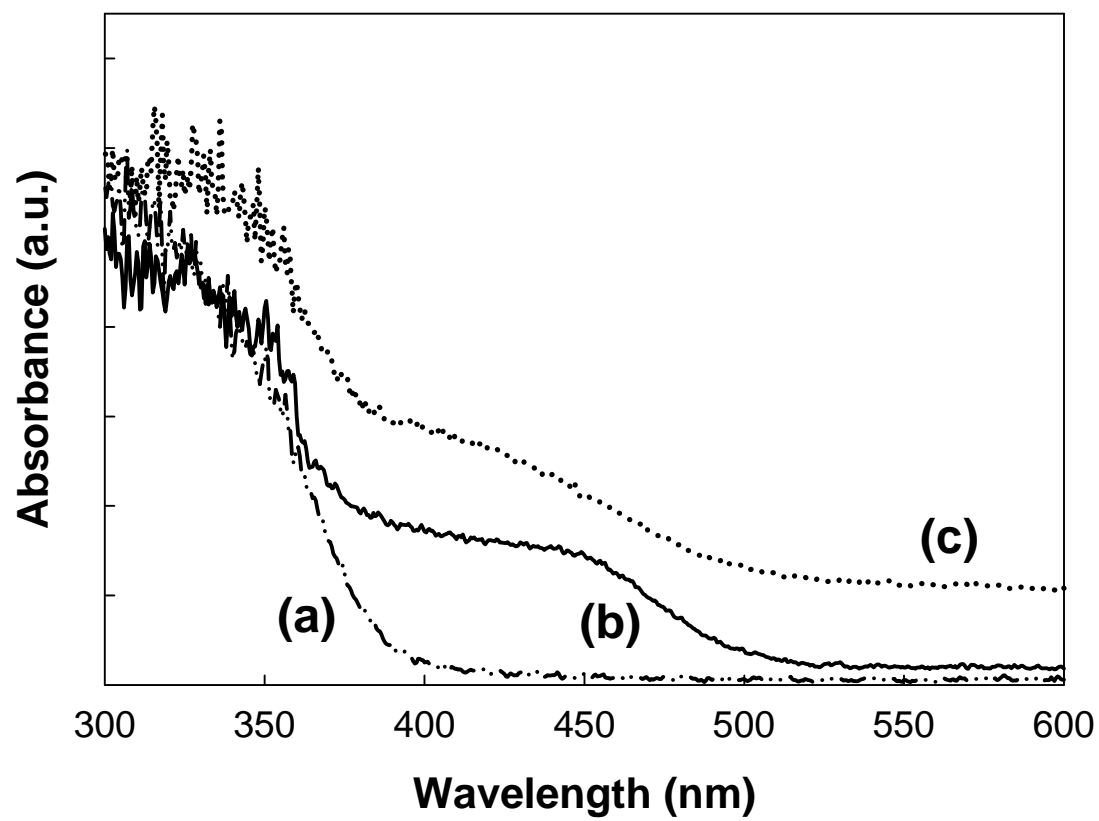


**Figure 4.5.** UV-vis diffuse reflectance spectra for (a)  $\text{KNbO}_3$ , (b)  $\text{KNbO}_3/\text{CdS}$ , (c)  $\text{Ni/NiO}/\text{KNbO}_3/\text{CdS}$

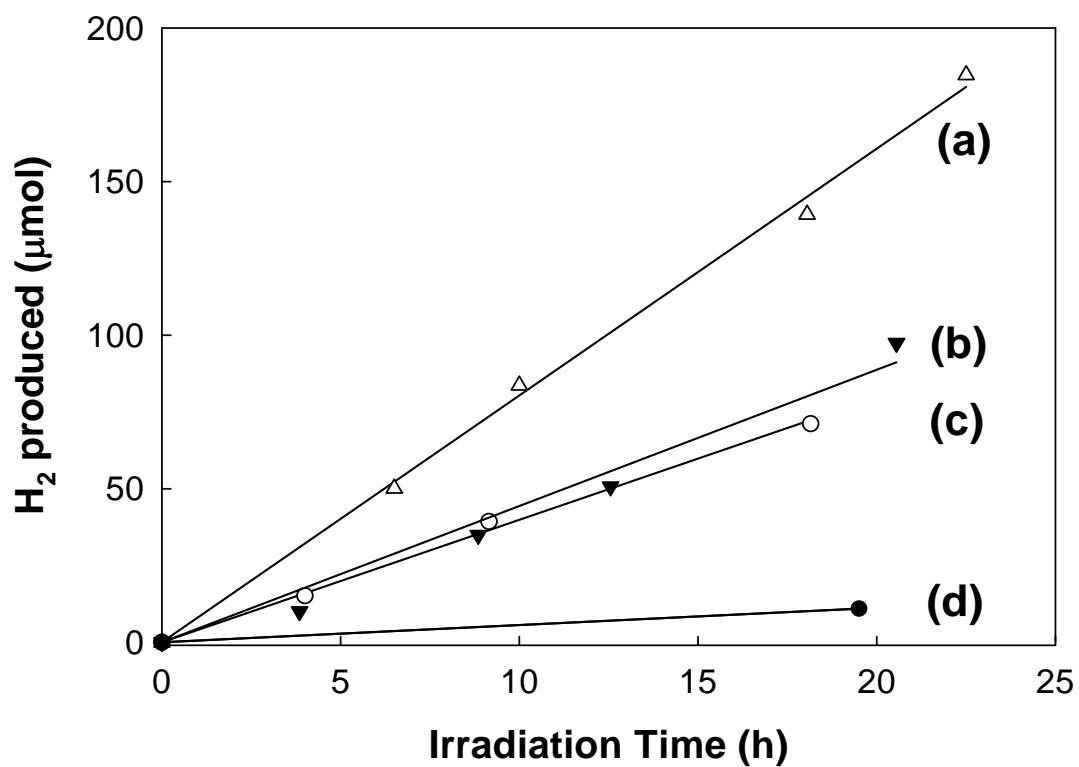


**Figure 4.6.** Effect of CdS loading on KNbO<sub>3</sub> surface on photocatalytic activities for H<sub>2</sub> production: (a) CdS synthesized both on KNbO<sub>3</sub> surface and in solution, (b) CdS synthesized by external mixing with KNbO<sub>3</sub>, (c) CdS adsorbed on KNbO<sub>3</sub>, (d) Q-size CdS only

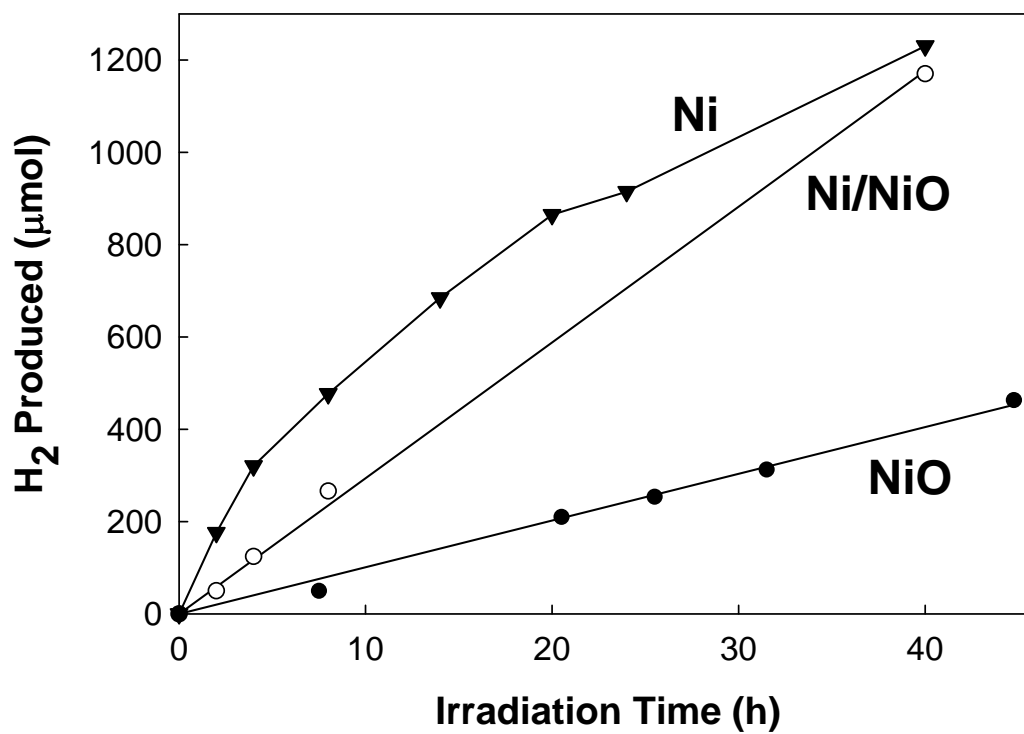


**Figure 4.7.** Effect of oxidation states of Ni deposited  $\text{KNbO}_3$  (0.1 wt % loading as  $\text{Ni}_T$ ) on photocatalytic  $\text{H}_2$  production from water-isopropanol mixed solution

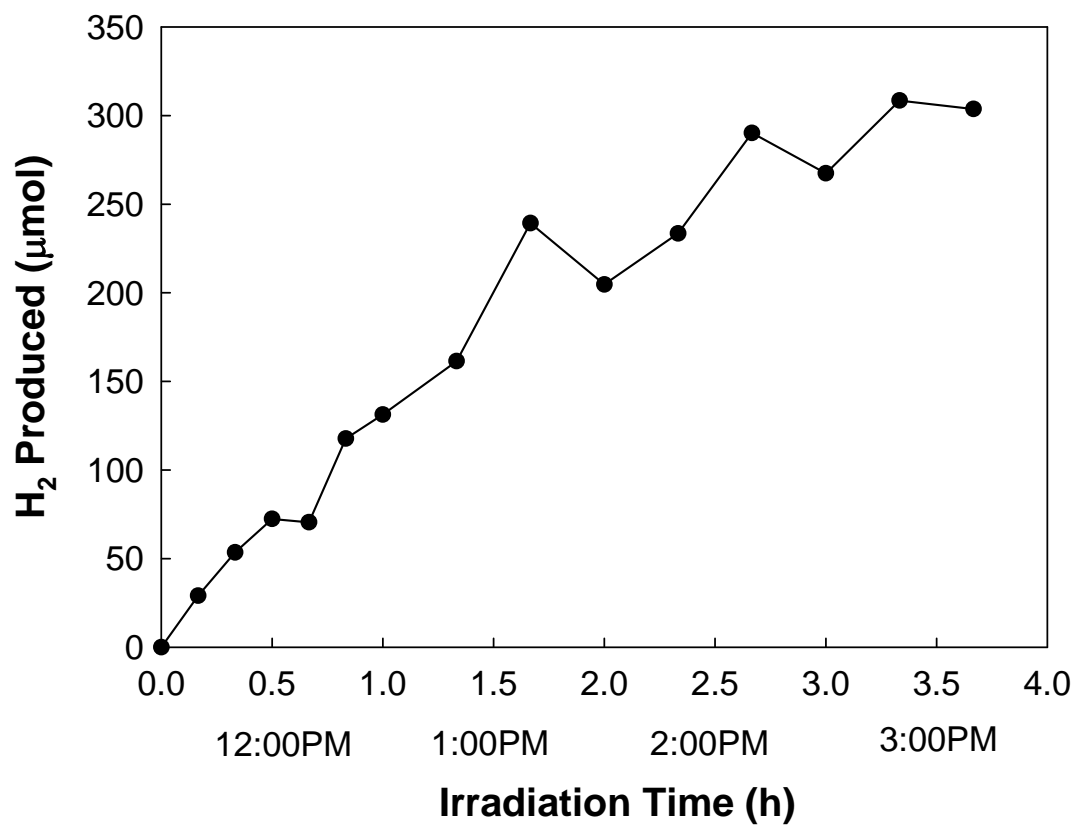


**Figure 4.8.** H<sub>2</sub> production rate from water-isopropanol mixed solution with Ni/NiO/KNbO<sub>3</sub>/CdS under natural sunlight (August 13, 2006; Pasadena, California).\

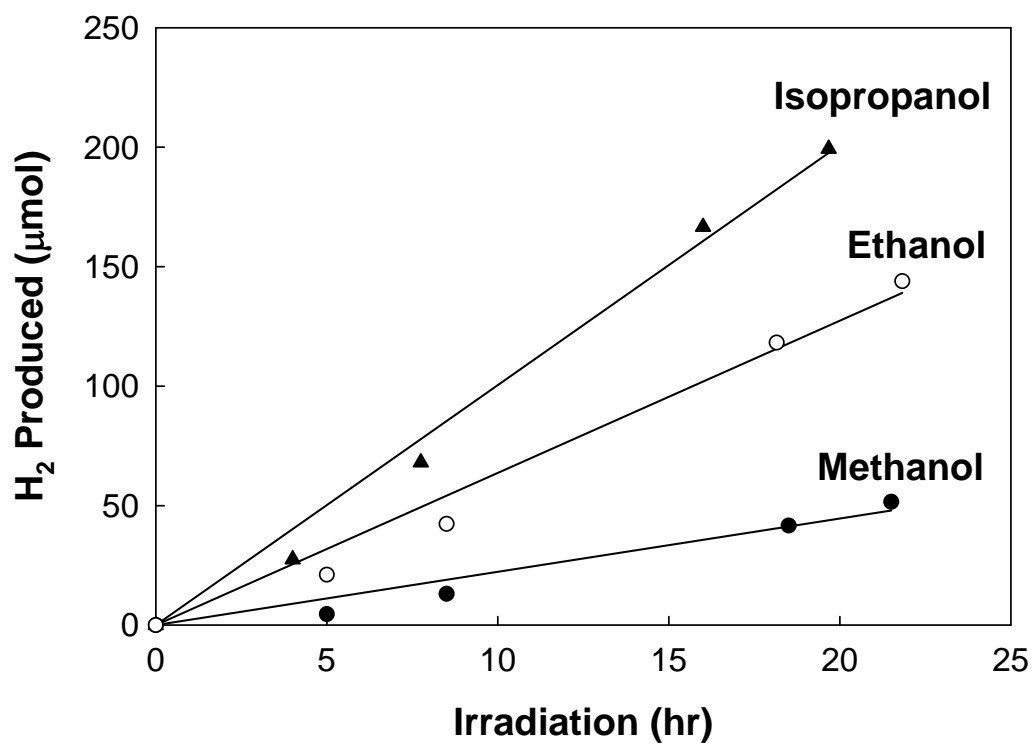


**Figure 4.9.** Solvent effects on photocatalytic H<sub>2</sub> production with Ni/NiO/KNbO<sub>3</sub>/CdS under the visible light ( $\lambda > 400\text{nm}$ )

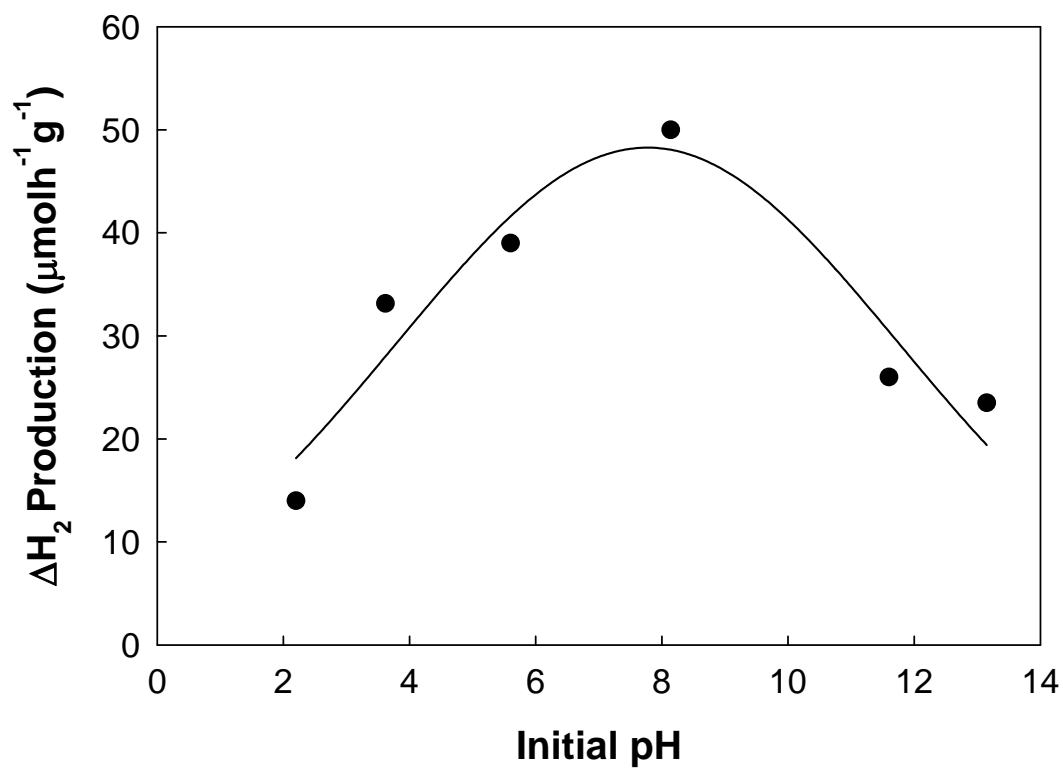


**Figure 4.10.** pH-dependent H<sub>2</sub> production from water-isopropanol mixed solution. pH was adjusted with 0.1~1 M NaOH and HCl.

**TABLE 4.1.** Photocatalytic activities of potassium niobates nanocomposites for H<sub>2</sub> production from water-isopropanol mixed solution

Sample	weight % of Ni <sub>T</sub>	Calcination Temp. (°C)	H <sub>2</sub> Production <sup>a</sup> (μmolh <sup>-1</sup> g <sup>-1</sup> )
KNbO <sub>3</sub>	0	925	0
Ni/NiO/KNbO <sub>3</sub>	0.1	925	0
CdS	0	-	3
TiO <sub>2</sub> /CdS	0	-	12
Ni/NiO/K <sub>4</sub> Nb <sub>6</sub> O <sub>17</sub> /CdS	0.1	1150	37
Ni/NiO/KNbO <sub>3</sub> /CdS	0	925	50
	0.1	925	150
	0.3	925	125
	0.5	925	75
	1.0	925	80
	3.6	925	65
	0.5	650	110
	0.5	775	80
	1.0	650	120
	1.0	775	80

<sup>a</sup> Catalyst, 0.2 g; volume, 50 ml; light source, Hg-Xe lamp (500W) with λ > 400nm, 30 v/v% isopropanol

## References

- (1) Fujishim.A; Honda, K. *Nature* **1972**, 238, 37.
- (2) Karakitsou, K. E.; Verykios, X. E. *J. Catal.* **1992**, 134, 629.
- (3) Sakata, T.; Kawai, T. *Chem. Phys. Lett.* **1981**, 80, 341.
- (4) Abe, R.; Takata, T.; Sugihara, H.; Domen, K. *Chem. Commun.* **2005**, 3829.
- (5) Gondal, M. A.; Hameed, A.; Yamani, Z. H. *Energy Sources* **2005**, 27, 1151.
- (6) Hwang, D. W.; Kim, J.; Park, T. J.; Lee, J. S. *Catal. Lett.* **2002**, 80, 53.
- (7) Domen, K.; Naito, S.; Onishi, T.; Tamaru, K. *Chem. Phys. Lett.* **1982**, 92, 433.
- (8) Zou, J. J.; Liu, C. J. *Acta Physico-Chimica Sinica* **2006**, 22, 926.
- (9) Hoffman, A. J.; Yee, H.; Mills, G.; Hoffmann, M. R. *J. Phys. Chem.* **1992**, 96, 5540.
- (10) Maeda, K.; Takata, T.; Hara, M.; Saito, N.; Inoue, Y.; Kobayashi, H.; Domen, K. *J. Am. Chem. Soc.* **2005**, 127, 8286.
- (11) Steinfeld, A. *Int. J. Hydrogen Energy* **2002**, 27, 611.
- (12) Ashokkumar, M. *Int. J. Hydrogen Energy* **1998**, 23, 427.
- (13) De, G. C.; Roy, A. M.; Bhattacharya, S. S. *Int. J. Hydrogen Energy* **1996**, 21, 19.
- (14) Furlong, D. N.; Grieser, F.; Hayes, D.; Hayes, R.; Sasse, W.; Wells, D. *J. Phys. Chem.* **1986**, 90, 2388.
- (15) Guan, G. Q.; Kida, T.; Kusakabe, K.; Kimura, K.; Fang, X. M.; Ma, T. L.; Abe, E.; Yoshida, A. *Chem. Phys. Lett.* **2004**, 385, 319.
- (16) Kakuta, N.; Park, K. H.; Finlayson, M. F.; Ueno, A.; Bard, A. J.; Campion, A.; Fox, M. A.; Webber, S. E.; White, J. M. *J. Phys. Chem.* **1985**, 89, 732.

- (17) Muradov, N. Z.; Rustamov, M. I.; Guseinova, A. D.; Bazhutin, Y. V. *React. Kinet. Catal. Lett.* **1987**, *33*, 279.
- (18) Kobayashi, J.; Kitaguchi, K.; Tanaka, H.; Tsuiki, H.; Ueno, A. *J. Chem. Soc., Faraday Trans. I* **1987**, *83*, 1395.
- (19) Koca, A.; Sahin, M. *Int. J. Hydrogen Energy* **2002**, *27*, 363.
- (20) Domen, K.; Kudo, A.; Shibata, M.; Tanaka, A.; Maruya, K.; Onishi, T. *J. Chem. Soc., Chem. Commun.* **1986**, 1706.
- (21) Furube, A.; Shiozawa, T.; Ishikawa, A.; Wada, A.; Domen, K.; Hirose, C. *J. Phys. Chem. B* **2002**, *106*, 3065.
- (22) Ikeda, S.; Tanaka, A.; Shinohara, K.; Hara, M.; Kondo, J. N.; Maruya, K. I.; Domen, K. *Microporous Mater.* **1997**, *9*, 253.
- (23) Sayama, K.; Tanaka, A.; Domen, K.; Maruya, K.; Onishi, T. *Catal. Lett.* **1990**, *4*, 217.
- (24) Sayama, K.; Tanaka, A.; Domen, K.; Maruya, K.; Onishi, T. *J. Phys. Chem.* **1991**, *95*, 1345.
- (25) Ikeda, S.; Fubuki, M.; Takahara, Y. K.; Matsumura, M. *Appl. Catal., A* **2006**, *300*, 186.
- (26) Kato, H.; Kudo, A. *J. Phys. Chem. B* **2001**, *105*, 4285.
- (27) Machida, M.; Mitsuyama, T.; Ikeue, K.; Matsushima, S.; Arai, M. *J. Phys. Chem. B* **2005**, *109*, 7801.
- (28) Machida, M.; Yabunaka, J.; Kijima, T. *Chem. Mater.* **2000**, *12*, 812.
- (29) Kim, S.; Hwang, S. J.; Choi, W. Y. *J. Phys. Chem. B* **2005**, *109*, 24260.
- (30) Wang, D. F.; Ye, J. H.; Kako, T.; Kimura, T. *J. Phys. Chem. B* **2006**, *110*, 15824.

- (31) Gu, D. E.; Yang, B. C.; Hu, Y. D. *Catal. Lett.* **2007**, *118*, 254.
- (32) Gole, J. L.; Stout, J. D.; Burda, C.; Lou, Y. B.; Chen, X. B. *J. Phys. Chem. B* **2004**, *108*, 1230.
- (33) Kisch, H.; Sakthivel, S.; Janczarek, M.; Mitoraj, D. *J. Phys. Chem. C* **2007**, *111*, 11445.
- (34) Reyes-Gil, K. R.; Reyes-Garcia, E. A.; Raftery, D. *J. Phys. Chem. C* **2007**, *111*, 14579.
- (35) Yin, S.; Komatsu, M.; Zhang, Q. W.; Saito, F.; Sato, T. *J. Mater. Sci.* **2007**, *42*, 2399.
- (36) Murakami, Y.; Kasahara, B.; Nosaka, Y. *Chem. Lett.* **2007**, *36*, 330.
- (37) Yu, J. C.; Ho, W. K.; Yu, J. G.; Yip, H.; Wong, P. K.; Zhao, J. C. *Environ. Sci. Technol.* **2005**, *39*, 1175.
- (38) Liu, H.; Imanishi, A.; Nakato, Y. *J. Phys. Chem. C* **2007**, *111*, 8603.
- (39) Zhang, W. U.; Zhong, Y.; Fan, J.; Sun, S. Q.; Tang, N.; Tan, M. Y.; Wu, L. M. *Sci. China Ser. B* **2003**, *46*, 196.
- (40) Linkous, C. A.; Muradov, N. Z.; Ramser, S. N. *Int. J. Hydrogen Energy* **1995**, *20*, 701.
- (41) Roy, A. M.; De, G. C. *J. Photochem. Photobiol., A* **2003**, *157*, 87.
- (42) Bahnemann, D. W.; Kormann, C.; Hoffmann, M. R. *J. Phys. Chem.* **1987**, *91*, 3789.
- (43) Hoffman, A. J.; Mills, G.; Yee, H.; Hoffmann, M. R. *J. Phys. Chem.* **1992**, *96*, 5546.

- (44) Bessekhoud, Y.; Chaoui, N.; Trzpit, M.; Ghazzal, N.; Robert, D.; Weber, J. V. *J. Photochem. Photobiol., A* **2006**, *183*, 218.
- (45) Chen, F.; Zhu, Y. P.; Ma, H. L.; Bo, Z. L.; Zhang, J. L. *Acta Physico-Chimica Sinica* **2004**, *20*, 1292.
- (46) Jang, J. S.; Li, W.; Oh, S. H.; Lee, J. S. *Chem. Phys. Lett.* **2006**, *425*, 278.
- (47) Tambwekar, S. V.; Venugopal, D.; Subrahmanyam, M. *Int. J. Hydrogen Energy* **1999**, *24*, 957.
- (48) Innocenti, M.; Cattarin, S.; Loglio, F.; Cecconi, T.; Seravalli, G.; Foresti, M. L. *Electrochim. Acta* **2004**, *49*, 1327.
- (49) Ueno, A.; Kakuta, N.; Park, K. H.; Finlayson, M. F.; Bard, A. J.; Campion, A.; Fox, M. A.; Webber, S. E.; White, J. M. *J. Phys. Chem.* **1985**, *89*, 3828.
- (50) Yoshimura, J.; Tanaka, A.; Kondo, J. N.; Domen, K. *Bull. Chem. Soc. Jpn.* **1995**, *68*, 2439.
- (51) Shangguan, W. F.; Yoshida, A. *Sol. Energy Mater. Sol. Cells* **2001**, *69*, 189.
- (52) Shangguan, W. F.; Yoshida, A. *J. Phys. Chem. B* **2002**, *106*, 12227.
- (53) Domen, K.; Kudo, A.; Onishi, T.; Kosugi, N.; Kuroda, H. *J. Phys. Chem.* **1986**, *90*, 292.
- (54) Kudo, A.; Tanaka, A.; Domen, K.; Maruya, K.; Aika, K.; Onishi, T. *J. Catal.* **1988**, *111*, 67.
- (55) Ewart, M.; Biaggio, I.; Zgonik, M.; Gunter, P. *Phys. Rev. B* **1994**, *49*, 5263.
- (56) Kesselman, J. M.; Weres, O.; Lewis, N. S.; Hoffmann, M. R. *J. Phys. Chem. B* **1997**, *101*, 2637.
- (57) Yariv, A.; Orlov, S. S.; Rakuljic, G. A. *J. Opt. Soc. Am., B* **1996**, *13*, 2513.

- (58) Montemezzani, G.; Gunter, P. *J. Opt. Soc. Am., B* **1990**, 7, 2323.
- (59) Park, S. W.; Huang, C. P. *J. Colloid Interface Sci.* **1987**, 117, 431.
- (60) Liu, J. C.; Huang, C. P. *Langmuir* **1992**, 8, 1851.
- (61) Duran, J. D. G.; Guindo, M. C.; Delgado, A. V.; GonzalezCaballero, F. *J. Colloid Interface Sci.* **1997**, 193, 223.
- (62) Guindo, M. C.; Zurita, L.; Duran, J. D. G.; Delgado, A. V. *Mater. Chem. Phys.* **1996**, 44, 51.
- (63) Nicolau, Y. F.; Menard, J. C. *J. Colloid Interface Sci.* **1992**, 148, 551.
- (64) Domen, K.; Kondo, J. N.; Hara, M.; Takata, T. *Bull. Chem. Soc. Jpn.* **2000**, 73, 1307.
- (65) Uchihara, T.; Matsumura, M.; Tsubomura, H. *J. Phys. Chem.* **1989**, 93, 3207.

## Chapter 5

# Photocatalytic Production of H<sub>2</sub> on Nanocomposite Catalysts

Sections reprinted with permission from Ryu, S.Y.; Choi, J.; Balcerski, W.; Lee, T.K.; Hoffmann, M. R. *Industrial & Engineering Chemistry Research* **2007**, *46*, 7476.  
© 2007 American Chemical Society

## Abstract

The photocatalytic production of H<sub>2</sub> in water with visible light using nanocomposite catalysts, which include Q-sized CdS, CdS nanoparticles embedded in zeolite cavities (CdS/Zeolite), and CdS quantum dots (Q-CdS) deposited on KNbO<sub>3</sub> (CdS/KNbO<sub>3</sub> & Ni/NiO/KNbO<sub>3</sub>/CdS), are investigated. The rate of H<sub>2</sub> production in alcohol/water mixtures and other electron donors at  $\lambda \geq 400$  nm is the highest with the hybrid catalyst, Ni/NiO/KNbO<sub>3</sub>/CdS with a measured quantum yield,  $\phi$ , of 8.8%. The relative order of reactivity as a function of catalyst is Ni(0)/NiO/KNbO<sub>3</sub>/CdS > Ni(0)/KNbO<sub>3</sub>/CdS > KNbO<sub>3</sub>/CdS > Ni/KNbO<sub>3</sub> > CdS/NaY-Zeolite > TiY-Zeolite > CdS, while the reactivity order with respect to the array of electron donors is 2-propanol > ethanol > methanol > sulfite > sulfide > H<sub>2</sub>O. In addition, the rates of H<sub>2</sub> production from water and water-alcohol mixtures are correlated with fluorescent emission spectra and fluorescence lifetimes. Irradiation of Ni/NiO/KNbO<sub>3</sub>/CdS proceeds via the partial reduction of Cd(II) to Cd(0) on surface of CdS. The coupling of Ni(0)/NiO and Cd(0) on the surface of KNbO<sub>3</sub> appears to some of chemical principles a Ni/Cd battery at high overvoltages. Evidence for the formation of nickel hydride as an important intermediate has been obtained.

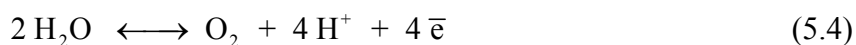
## Introduction

The production of hydrogen from the splitting of water via photocatalysis has been achieved with a variety metal oxide semiconductors such as  $\text{TiO}_2$ <sup>1-3</sup>,  $\text{SrTiO}_3$ <sup>4</sup>,  $\text{BaTi}_4\text{O}_9$ <sup>5</sup>,  $\text{RbPb}_2\text{Nb}_3\text{O}_{10}$ <sup>6</sup>, and  $\text{Na}_2\text{Ti}_6\text{O}_{13}$ <sup>7</sup>. However, the majority of the simple and mixed-metal oxides photocatalysts are primarily active for  $\text{H}_2$  production under UV irradiation ( $\lambda < 385 \text{ nm}$  or  $E_{\text{bg}} \geq 3.0 \text{ eV}$ ). More recently, there has been a focused effort on the development of photocatalysts that are capable of using visible light ( $\lambda = 400\text{--}700 \text{ nm}$ ) for the photocatalytic production of  $\text{H}_2$ .

Hydrogen production from water using semiconductor photocatalysts<sup>8-11</sup> has attracted considerable interest since the pioneering work of Fujishima and Honda<sup>12</sup>, who discovered that water can be photo-electrochemically decomposed into hydrogen and oxygen using a semiconductor ( $\text{TiO}_2$ ) electrode under UV irradiation. Since 1972, a large number of metal oxides and sulfides ( $\text{TiO}_2$ ,  $\text{CdS}$ ,  $\text{ZnO}$ ,  $\text{ZrO}_2$ , titanates, niobates, and tantalates) have been reported to have photocatalytic activity for splitting water<sup>13</sup>.

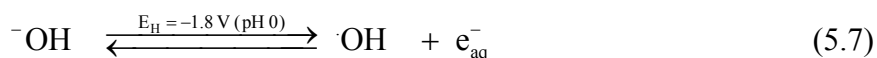
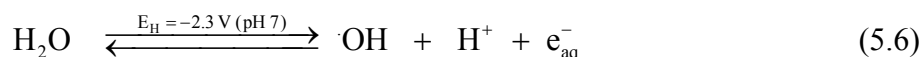
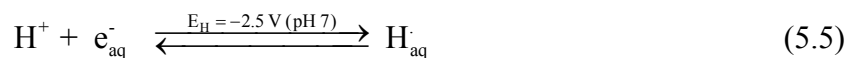


The overall multi-electron redox potentials for the multi-electron reactions at pH 7 suggest that  $\text{H}_2$  production with the input of UV-visible light energy is feasible.



The redox potential for reaction 5.1 at pH 7 is  $E_{\text{H}} = -1.23 \text{ V}$  (NHE) with the corresponding half-reactions of  $-0.41 \text{ V}$  (eq. 5.3) and  $0.82 \text{ V}$  (eq. 5.4), which gives a  $\Delta G^\circ = +237 \text{ kJ/mole}$ <sup>13</sup>. However, with the input of light at wavelengths  $\leq 1000 \text{ nm}$  (i.e.,  $1.23$

eV  $\approx$  1000 nm), the overall energy requirement for the photosynthetic splitting of water can be met with solar radiation in principle. On the other hand, the rate of reaction in the normal Marcus regime should depend on the overall driving force (i.e., lower wavelength irradiation is preferable kinetically) and the thermodynamics of the initial or sequential one-electron transfer processes at the semiconductor surfaces. Moreover, the one-electron transfers<sup>14</sup> (eqs. 5.5–5.7) are much less favorable thermodynamically than the overall two-electron transfer reactions as shown below:



CdS, an n-type semiconductor with  $E_{\text{g}} = 2.4$  eV, has been shown to have photocatalytic activity for  $\text{H}_2$  production under visible light irradiation<sup>15-18</sup>, although, sacrificial electron donors<sup>19</sup> such as  $\text{C}_2\text{H}_5\text{OH}$ <sup>20</sup>,  $\text{HS}^-$ <sup>18,21,22</sup> or  $\text{SO}_3^{2-}$ <sup>16</sup> are used to obtain measurable rates of  $\text{H}_2$  production and to avoid the photocorrosion of CdS in the presence of  $\text{O}_2$ .

In order to enhance the photocatalytic activity of CdS, efforts have been made to combine CdS with other semiconductors having different band energies (e.g.,  $\text{TiO}_2/\text{CdS}$ <sup>23</sup>,  $\text{ZnO}/\text{CdS}$ ,  $\text{ZnS}/\text{CdS}$ <sup>24,25</sup>,  $\text{K}_4\text{Nb}_6\text{O}_{17}/\text{CdS}$ <sup>26</sup>, or  $\text{K}_2\text{Ti}_4\text{O}_9/\text{CdS}$  composites<sup>27,28</sup>). An alternative approach to enhance the photoactivity of CdS is to couple CdS with mesoporous or macroreticular materials to form hybrid or composite photocatalysts<sup>29-46</sup>. In these cases, the photogenerated electrons in CdS are able to move freely into an attached semiconductor or a framework of porous molecules, while the photo-generated

holes are trapped in CdS. Charge separation reduces the frequency of charge recombination, and thus improves the net photocatalytic activity of CdS.

The electronic levels of nanoparticulate or Q-CdS can be tuned by changing or controlling particle size without changing the chemical composition. For example in the case of nanoparticulate ZnO, Hoffmann and co-workers<sup>47,48</sup> reported a tenfold increase in photoefficiency for the photocatalytic production of hydrogen peroxide with a decrease in particle size from 40 to 23 nm. In another example, Hoffman et al.<sup>49,50</sup> found an increase in quantum efficiency for photo-polymerization of methylmethacrylate with a corresponding decrease in particle size using Q-CdS.

In this paper, we report on the synthesis of and optimization of hybrid CdS/Zeolite and CdS/KNbO<sub>3</sub> nanocomposite catalysts that are effective for H<sub>2</sub> production in aqueous suspension.

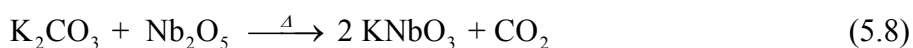
## Experimental

Nanoparticulate CdS was synthesized according to the methods described previously by Hoffmann and co-workers<sup>49</sup> while CdS/Zeolite nanocomposites were synthesized starting with commercially available NaY-Zeolite (Si/Al=6) (Strem Chemicals, Inc.). Nanoparticulate CdS was prepared within the pore structure of NaY-Zeolite by first exchanging Na<sup>+</sup> with Cd<sup>2+</sup>, followed by *in situ* reaction with HS<sup>-</sup> which was formed by the dissolution Na<sub>2</sub>S<sup>51</sup> crystals in 95% ethanol in a Vacuum Atmospheres<sup>®</sup> glove box. In this procedure, 1.0 g of NaY zeolite was mixed into 20 ml of 0.01 M solution of cadmium acetate in ethanol. Na<sup>+</sup> was exchanged with Cd<sup>2+</sup> for 24 hr at 25°C with continuous mixing. After ion exchange was complete, 20 mL of a sodium sulfide solution (0.01 M)

was added drop wise to the CdY-Zeolite suspension resulting in the formation of CdS on the internal and external surfaces of the zeolite matrix. The nanocomposite material was filtered and washed with ethanol for multiple cycles.

TiY zeolite was obtained by mixing an aqueous solution of ammonium titanyl oxalate<sup>52,53</sup> with HY-Zeolite. In a preliminary step, HY-Zeolite was obtained by ion exchange of the NaY-Zeolite with a 0.1 M NH<sub>4</sub>Cl. After rinsing with H<sub>2</sub>O, HY-Zeolite was calcined at 500 °C for 15 h, with an initial temperature ramp of 200°C/hour. Sample cooling was performed at same decreasing rate. The mole fraction of Ti(IV) incorporated into the HY-Zeolite was determined by analytical difference before and after treatment ( $\Delta n_{\text{Ti}} = (n_{\text{Ti}}^{\text{o}} - n_{\text{Ti}}^{\text{f}})$ ). Ti(IV)-Zeolite was repeatedly washed with water to remove any residual species adsorbed on exposed surfaces and then dried in an oven. After an initial low-temperature drying phase, the sample was calcined at 450 to 500 °C for 8 hours. The preparative procedure for CdS/TiY-Zeolite was analogous to that for CdS/NaY-Zeolite (*vide supra*).

Stoichiometric (KNbO<sub>3</sub>)<sup>54</sup> and non-stoichiometric potassium niobate (KNb<sub>1.5</sub>O<sub>4.25</sub>)<sup>55</sup> were prepared via high temperature solid-state reactions between K<sub>2</sub>CO<sub>3</sub> and Nb<sub>2</sub>O<sub>5</sub> as functions of calcination temperature and mole ratio of Nb<sub>2</sub>O<sub>3</sub> to K<sub>2</sub>CO<sub>5</sub>.



Powdered K<sub>2</sub>CO<sub>3</sub> and Nb<sub>2</sub>O<sub>5</sub> were mixed together with constant grinding in a mortar at a mole ratio of 1.0 to 1 of Nb<sub>2</sub>O<sub>5</sub>:K<sub>2</sub>CO<sub>3</sub>. After thorough mixing and grinding to reduce particle size, the powdered mixture was pressed into a pellet at 27.6 Mpa and then heated at 925 °C for 10 hr with a heating and cooling temperature ramp of ±200 °C. The X-ray diffraction pattern confirmed KNbO<sub>3</sub>. With slight variations of the Nb<sub>2</sub>O<sub>5</sub> to

$\text{K}_2\text{CO}_3$  mole ratio and the actual temperature of solid state synthesis,  $\text{K}_4\text{Nb}_6\text{O}_{17}$  ( $T \sim 1125$  °C) or a mixture of  $\text{KNbO}_3$  and  $\text{K}_4\text{Nb}_6\text{O}_{17}$  ( $T \sim 1125$  °C) are obtained. Elemental nickel and NiO coated  $\text{KNbO}_3$  powders were obtained by first treating the pure  $\text{KNbO}_3$  sample with  $\text{Ni}(\text{NO}_3)_2$  in a water suspensions for 1 day, filtered, washed and dried.. After ion-exchange with  $\text{Ni}^{2+}$  the Ni(II)/ $\text{KNbO}_3$  sample was reduced in a  $\text{H}_2$  atmosphere at 500 °C for 2 hr. This was followed by partial oxidation in an  $\text{O}_2$  atmosphere at 200 °C for 1 hr to form NiO on the surface of  $\text{KNbO}_3$ . Following the latter procedure, CdS nanoparticles were deposited by mixing the Ni/NiO/ $\text{KNbO}_3$  powder with a cadmium acetate solution in ethanol for 1 day and then mixing in  $\text{Na}_2\text{S}$  and allowing the formation of CdS for 7 days before filtration, washing and subsequent drying X-ray diffraction patterns for  $\text{KNbO}_3$  and its nanocomposites gave  $2\theta$  peaks that correspond to peaks reported for pure  $\text{KNbO}_3$ .

Diffuse reflectance and absorption spectra were recorded by using a Shimadzu UV-2101PC with an integrating sphere attachment (Shimadzu ISR-260). Steady-state fluorescence spectra were collected on a Hitachi F-2500 fluorometer with samples excited at 400 nm.

Photoluminescence lifetimes in solution were measured with a streak camera (Hamamatsu, Streak Scope C4334) after excitation with the second-harmonic (430 nm) of an amplified femtosecond mode-locked Ti:Sapphire laser. The sample solution was put into a quartz cell (1 cm  $\times$  1 cm), and the fluorescence emission was focused into the streak camera through a cutoff filter ( $< 530$  nm) at a 90° angle with respect to the excitation beam.

DRIFT spectra were acquired using a Bio-Rad FTS-45 FTIR spectrometer with a liquid  $\text{N}_2$ -cooled MCT detector at 4  $\text{cm}^{-1}$  resolution using a Spectra-Tech Collector

diffuse-reflectance accessory. Solid samples were held in the diffuse reflectance accessory in the sample cup of a Spectra-Tech high temperature environmental chamber (HTEC). The sample could be resistively heated to 1000 K ( $\pm 1$  K) and the chamber evacuated to 1  $\mu$ Torr. Gases and vapors can be introduced through a separate port via a manifold.

Photolysis experiments were performed by using the collimated output of a high-pressure 500 W Hg-Xe arc lamp as a light source in combination with 400 nm cut-off filter. The incident light flux per unit area,  $I_0$ , was measured with a potassium ferrioxalate actinometer as  $4.65 \times 10^{15}$  photons  $\text{cm}^{-2} \text{s}^{-1}$ . All samples were purged with Ar gas for 30 min before photolysis in order to eliminate  $\text{O}_2$ . The amount of  $\text{H}_2$  evolved during photolysis was analyzed using gas chromatography (HP G1800A) with TCD. Nitrogen was used as the carrier gas and the separations were achieved with a molecular sieve column (30 m  $\times$  0.32 mm  $\times$  12.00  $\mu\text{m}$ ). Calibration curves were linear over a broad range of  $\text{H}_2$  concentrations in He.

## Results

Nanoparticulate CdS colloids were synthesized in four different solvents by rapidly mixing of  $\text{Na}_2\text{S}$  solutions into cadmium acetate solutions<sup>49,56-59</sup> under anoxic conditions. This resulted in an immediate precipitation of small crystallites. In mixed solvent system, where the pH of the colloidal suspension of CdS was close to 8, the colloidal CdS suspension were stabilized by the net negative charges on particle surfaces (i.e.,  $\text{pH}_{\text{solv}} > \text{pH}_{\text{zpc}} = 2.0$ )<sup>60-63</sup>. The mean particle diameter of the CdS colloids synthesized in ethanol was 4 nm as determined by TEM while the relative size of the CdS particles in

suspension was estimated from the band-gap energies obtained from the UV-vis absorption spectra of the transparent colloidal suspensions. The equilibrium particle size in the CdS solvent suspensions was dependent on the viscosity of solvent and on the temperature of synthesis as reported previously by Hoffman et al.<sup>64</sup>

Cadmium sulfide was synthesized within the pore spaces of the aluminosilicate zeolites (Si:Al = 6:1, NaY zeolite)<sup>65-72</sup> by the direct reaction of sorbed Cd<sup>2+</sup> with the aqueous Na<sub>2</sub>S. The zeolite support, which serves as a mesoporous host material, is used to control CdS particle size and stability. The size of CdS colloids are constrained, in part, by the cavity size of the particular zeolite support. In addition, the zeolite framework should inhibit Ostwald ripening (i.e., continued particle growth).

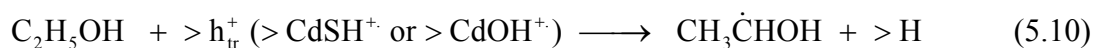
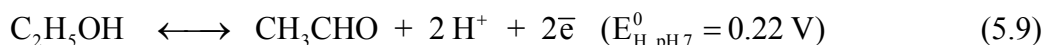
However, formation of CdS clusters or particles may not occur exclusively within the cavities or pores of the zeolite. A fraction of the formed CdS may have precipitated on the external surfaces of NaY-Zeolite, although, the XRD patterns of NaY-Zeolite with embedded CdS were consistent with that of NaY zeolite alone without discernable 2 $\theta$  peaks for CdS. This result indicates that the inherent framework structure of NaY-Zeolite was maintained after ion-exchange, and that CdS was synthesized preferentially within the NaY-Zeolite cavities.

The UV-vis absorption spectra of CdS colloids, which were measured at room temperature, had spectral features that were consistent with our previous results.<sup>64</sup> The corresponding the fluorescence spectra ( $\lambda_{\text{ex}} = 380$  nm) of the CdS colloids in H<sub>2</sub>O and ethanol are shown in Figure 5.1. The emission bands for CdS in ethanol were observed at  $\lambda_{\text{em}} = 554$ , whereas a much weaker emission band was observed at  $\lambda_{\text{em}} = 633$  nm for colloidal, Q-sized CdS suspended in H<sub>2</sub>O. The fluorescence spectra were characterized

by large red-shifted emissions, indicating radiative relaxations from surface trapping states<sup>73</sup>. The relative differences in the photoluminescence response can be attributed to interactions between the surface of CdS and the solvent.

In the case of ethanol, the emission intensity increases (Figure 5.2) with a corresponding blue shift in wavelength as the  $V_{\text{EtOH}}/V_{\text{H}_2\text{O}}$  ratio increases. The responses as a function of the mole fraction of ethanol,  $\chi_{\text{EtOH}}$ , suggest a relatively strong interaction of ethanol at the charged surface of CdS.

Ethanol can act as a potential electron donor to the valence band hole,  $h_{\text{vb}}^+$ , or a trapped hole,  $h_{\text{tr}}^+$ ,



Furthermore, ethanol can modulate the thickness of the electrical double layer surrounding charged CdS in water. The surface interaction of ethanol with CdS is clearly demonstrated by the increase in the fluorescence intensity with a corresponding increase in the mole fraction of ethanol,  $\chi_{\text{EtOH}}$  (*vide supra*). When sulfite ( $\text{HSO}_3^-$  and  $\text{SO}_3^{2-}$ ) is substituted for ethanol as an electron donor, similar increases in fluorescence intensity coupled with shifts in  $\lambda_{\text{em}}$  from 633 nm to 645 nm are observed (Figure 5.3).

The fluorescence emission intensities can be correlated with the fluorescence lifetimes, which, in turn, depend on the dielectric constant of the solvent<sup>74</sup>. In the case of Q-CdS, the fluorescence lifetime was determined to be 2.5 ns in neat ethanol, 0.5 ns in ethanol-water ( $V_{\text{EtOH}}/V_{\text{H}_2\text{O}} = 1:1$ ), and to 20 ps in pure water.

The diffuse reflectance and emission spectra of CdS embedded in NaY-Zeolite

showed distinctly different behavior than those observed for the Q-CdS in EtOH (Figure 5.4). The absorption band edged of CdS/NaY-Zeolite at 524 nm is red-shifted, whereas the emission band at  $\lambda_{em} = 526$  nm is blue-shifted relative to the transparent Q-CdS colloids in EtOH. The shift in the diffuse reflectance spectrum should depend on the size and structure of the embedded colloids or clusters within NaY-Zeolite cavity. Red-shift is most likely due to the formation of CdS clusters in the restricted space of the zeolite cavities ( $d \sim 1.3$  nm) as opposed to the formation of crystalline cubic or hexagonal CdS (e.g., Hawleyite or Greenockite, *vide supra*)<sup>70-72,75,76</sup>. As a consequence, the cavity-bound CdS clusters have very small Stokes shifts<sup>77-81</sup>,  $\Delta\lambda$  (i.e.,  $\lambda_{ex} - \lambda_{em}$ ).

The rates of H<sub>2</sub> evolution were determined from apparent zero-order [H<sub>2</sub>] versus time profiles under an argon atmosphere to minimize oxidative photocorrosion<sup>46,82,83</sup> and subsequent dissolution<sup>84-88</sup>. Typical profiles [H<sub>2</sub>] vs. time plots (Figure 5.5) for photolysis of transparent Q-sized CdS colloids indicates a strong inverse pH dependence<sup>89</sup>. Furthermore, the rate of H<sub>2</sub> production is dependent on the ethanol-to-water volume ratio as shown in Figure 5.6. The rate,  $d[H_2]/dt$ , appears to be the highest in the  $V_{EtOH}/V_{H_2O}$  range of 1:3 (EtOH:H<sub>2</sub>O). However, the photoluminescence suggests that  $d[H_2]/dt$  should increase as  $V_{EtOH}/V_{H_2O}$  increases. In contrast, the H<sub>2</sub> production rate is marginal at pH 8 in the absence of an alternative electron donor, while at the other end of the  $V_{EtOH}/V_{H_2O}$  spectrum (i.e., pure EtOH with a trace of H<sub>2</sub>O = 0.001 M) the linear H<sub>2</sub> production rate was approximately 1/3 of the maximum  $d[H_2]/dt$ .

The rates of H<sub>2</sub> production for the CdS-Zeolite nanocomposites, CdS/NaY-Zeolite and CdS/TiY-Zeolite, at a  $V_{EtOH}/V_{H_2O}$  of 1: 3, are compared to those obtained with Q-CdS

alone in Figures 5.7 and 5.8. The impact of increasing ionic strength on the rate of H<sub>2</sub> production is illustrated in Figure 5.8. The corresponding rates of H<sub>2</sub> production with the KNbO<sub>3</sub> composites are shown in Figures 5.9 and 5.10.

Apparent quantum yields,  $\phi$ , for H<sub>2</sub> production, were determined as follows:

$$\phi = \frac{\frac{dm_{H_2}}{dt}}{I_{abs}^o} \quad (5.11)$$

where  $dm_{H_2}/dt$  is an initial production rate of H<sub>2</sub> (mol s<sup>-1</sup>) and  $I_{abs}^o$  photon absorption rate of Q-size CdS colloids in units of Einstein s<sup>-1</sup> (mol(e<sup>-</sup>) s<sup>-1</sup>). The light absorbed directly by the transparent Q-CdS, ( $I_{abs}^{CdS} = I_o((I_o - I_t)/I_o)A$ ), was determined from the measured incident photon flux,  $I_o$ , in units of photons cm<sup>-2</sup> s<sup>-1</sup>, the exposed reactor cross section,  $A = 74.9$  cm<sup>2</sup>, the fraction of incident light absorbed by CdS where  $I_t$  is the transmitted photon flux, and  $I_o = 4.65 \times 10^{15}$  photons/cm<sup>2</sup> s<sup>-1</sup> as determined by ferrioxalate actinometry<sup>90</sup>.

The specific light absorption rate determined for the transparent Q-CdS colloids is more precise than that obtained for the CdS-Zeolite and KNbO<sub>3</sub>/CdS composites due to differences in light scattering related to their larger particle sizes. In the case of the Q-CdS colloids,  $I_{abs}^{CdS}$  is determined by taking the difference of the light fluxes measurements determined at front and back of the photoreactor cell with ferrioxalate actinometer<sup>91</sup>. Scattered light from the photoreactor is negligible for Q-CdS nanoparticulate suspensions which were transparent (i.e., average particle diameter  $\ll \lambda_{hv}$ ). For the CdS colloids, the fraction of absorbed light,  $(1 - I_t/I_o)$ , was measured as 42.3 ( $\pm$  2.1)% for a CdS concentration of  $2.0 \times 10^{-5}$  M. From the combined measurements of the H<sub>2</sub> mass

production rate in moles per second and the specific light absorption rate, the quantum yield for the CdS colloids was measured as  $\phi = 0.12\%$ .

Using a similar procedure, the quantum yields for CdS-Zeolite and CdS/ $\text{KNbO}_3$  composites were determined as described above, except that the amount of light scattered from nanocomposites zeolite suspension was factored into account by the methods of Cornu et al.<sup>92,93</sup>. In this approach, the absorbed light flux is given by

$$I_{\text{abs}} = [I_0 - (I_B + I_s)] \quad (5.12)$$

where  $I_B$  is light flux measured behind the photoreactor (e.g., ferrioxalate actinometry), and  $I_s$  denotes the total scattered light including back-scattered, side-scattered, and forward-scattered light. For the nanocomposites suspensions,  $I_a$  was measured as  $1.90 \times 10^{15}$  photons  $\text{cm}^{-2} \text{s}^{-1}$ , and the corresponding quantum yields for the CdS/ $\text{NaY-Zeolite}$  and  $\text{Ni/NiO/KNbO}_3/\text{CdS}$  composite of determined to be 0.5 % and 8.8%, respectively, for visible light irradiation ( $\lambda \geq 400$  nm).

In Figure 5.10, we compare irradiations of  $\text{Ni/NiO/KNbO}_3/\text{CdS}$  suspensions at  $\lambda \geq 300$  nm and  $\lambda \geq 400$  nm to the Ni-free  $\text{KNbO}_3/\text{CdS}$  composite. These results show that  $\text{KNbO}_3/\text{CdS}$  was active in the UV range, while the 4-way composite,  $\text{Ni/NiO/KNbO}_3/\text{CdS}$  at 0.1 wt% Ni was active in both the UV and visible portions of the spectrum. The highest  $\text{H}_2$  production rates were obtained with a Ni-deposition level of 0.1 wt% as ( $\text{Ni}_T = \text{Ni}^0 + \text{NiO}$ ) shown in Figure 5.11. The corresponding shifts in the absorption spectra for  $\text{KNbO}_3$  and its composites are shown in Figures 5.12 and 5.13 as functions of the weight percent loadings of Ni and CdS, respectively.

The rate of  $\text{H}_2$  production on the four-component composite,  $\text{Ni(0)/NiO/KNbO}_3/\text{CdS}$ , is compared to the three-component composite containing only elemental nickel,

Ni(0)KNbO<sub>3</sub>/CdS, in Figure 5.14. The Ni(0)/NiO/KNbO<sub>3</sub>/CdS composite production is linear over many hours while the Ni(0)KNbO<sub>3</sub>/CdS composite shows non-linear behavior over the same timeframe. The relative effects of the isopropanol (IPA), ethanol (EtOH), and methanol (MeOH) on H<sub>2</sub> production for KNbO<sub>3</sub>/CdS at  $\lambda > 400$  nm are shown in Figure 5.15. In this case, the order of reactivity is IPA > EtOH > MeOH, which is in inverse order of their dielectric constants (i.e.,  $\epsilon_{\text{IPA}} = 19 < 24.3 < 33 = \epsilon_{\text{MeOH}}$ ). The relative hydrogen production rates are summarized in Table 5.1.

It should be noted that dramatic color changes take place during photolysis of the Q-CdS and the CdS nanocomposite materials. In all cases, the suspensions are yellow before illumination (note: the NaY-Zeolite and KNbO<sub>3</sub> powders are white before deposition of CdS). However, very quickly after exposure to a focused beam of light at  $\lambda \geq 400$  nm, the color changes very quickly to a silver gray. As the color changes from yellow to gray, H<sub>2</sub> production is observed as a steady stream of gas bubbles rising up in the photolysis cell. After the light is removed and the gas-tight reactor is opened to air, the solid samples slowly revert to a yellow color after approximately two hours exposure to oxygen.

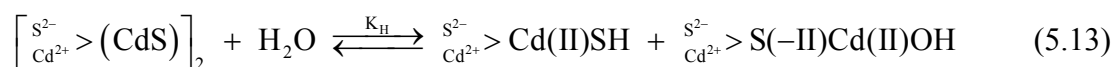
## Discussion

The experimental results for CdS and the CdS composite systems clearly show that the nature of the electron donor plays an important role in determining the photophysical and photochemical properties. The fluorescent emission intensities as shown in Figures 5.1-5.3 are clearly enhanced in the presence of the electron donors, C<sub>2</sub>H<sub>5</sub>OH and HSO<sub>3</sub><sup>-</sup>/SO<sub>3</sub><sup>2-</sup>.

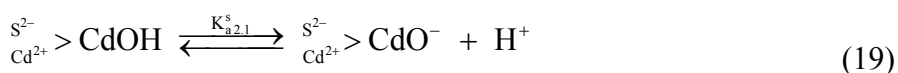
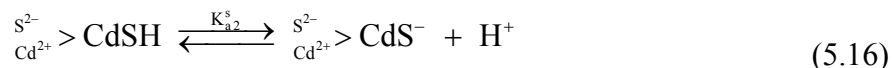
The emissive state appears to lie in a shallow trapping state, which is energetically located between conduction band (CB) and valence band (VB) edges. During the fluorescence excitation, the photogenerated electron, which has been promoted to the excited state (CB), undergoes a very fast non-radiative relaxation to the emissive state (i.e., a shallow trapping state), following a radiative relaxation back to the VB (emission). Ethanol and sulfite which have been added as VB electron donors interact strongly at the CdS surface and provide electron density to surface trapped holes. This has the effect of retarding electron-hole recombination, increasing the fluorescence lifetime, and increasing the measured fluorescence intensity.

In an early study with nano-particulate ZnO, we<sup>47</sup> observed an increase in the steady-state fluorescence intensity with a corresponding increase in electron acceptor concentration (i.e., a strong increase in emission intensity with a increase in the oxygen partial pressure) or donor, depending on the nature of the surface interaction and the ability of the acceptor or donor function as a surface-bound electron- or hole-trap. We also noted that the fluorescence quenching of various cations or anions depended strongly on the surface charge characteristics of the ZnO colloids as a function of pH. Similar effects can be invoked in the case of quantum-sized CdS.

The net surface charge on the CdS colloids arises due to chemical interactions<sup>60,62,63,94</sup> at the interface, which are initiated by the hydrolysis of the near surface layer of CdS to form surface functionalities that are dominated by cadmium mercapto group, >CdSH, and cadmium hydroxyl, >CdOH functionalities as follows:



The variable surface charges arise from protonation and deprotonation of surface sulfhydryl and hydroxyl groups as depicted in eqs. 5.14 to 5.19.



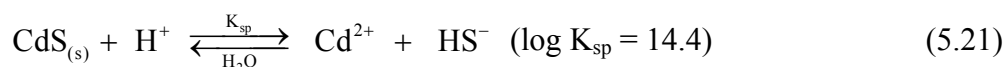
The surface chemistry of hydrated CdS is complicated further by adsorption of chemical species present in the background electrolyte,  $\text{Cd}^{2+}$  and  $\text{HS}^-$ . For example,  $\text{HS}^-$  is often used as a sacrificial electron donor<sup>33</sup> for the photocatalytic production of  $\text{H}_2$  and  $\text{Cd}^{2+}$  has been added in excess<sup>95</sup> in attempts to enhance the photochemical reactivity of CdS. As mentioned above, Henglein<sup>59</sup> has noted that the photophysical properties of CdS colloids are strongly influence by excess hydroxide ion.

In the simplest case, at low ionic strength in the absence of added cations or anions, the isoelectric point or ‘point of zero charge’ is described as follows in terms of the concentrations of the relevant surface species as a function of pH:

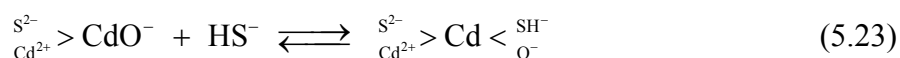
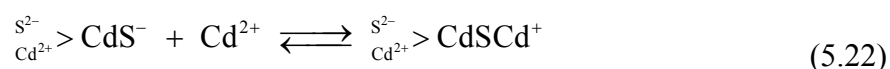
$$\left[ \text{S}_{\text{Cd}^{2+}}^{2-} > \text{CdSH}_2^+ \right] + \left[ \text{S}_{\text{Cd}^{2+}}^{2-} > \text{CdOH}_2^+ \right] = \left[ \text{S}_{\text{Cd}^{2+}}^{2-} > \text{CdS}^- \right] + \left[ \text{S}_{\text{Cd}^{2+}}^{2-} > \text{CdO}^- \right] \quad (5.20)$$

Park and Huang<sup>94</sup> have argued that, in addition to the surface functional groups defined by the equilibria of eqs. 13-19, that the sites depicted by  $\left[ \text{S}_{\text{Cd}^{2+}}^{2-} > \text{CdS}^- \right]$  and

$\left[ \frac{S^{2-}}{Cd^{2+}} > CdO^{-} \right]$  will be involved in surface complexation or chemisorption reactions with other potential determining species in solution, such as  $Cd^{2+}$  and  $HS^{-}$ , when those species are in excess beyond the background concentrations arising from the equilibrium dissolution of  $CdS$ <sup>96</sup>:



Additional surface reactions, which will influence the overall charge on the  $CdS$ , include:



In addition to the equilibrium dissolution of  $CdS$ , we must also consider dissociation of the diprotic  $H_2S$  in terms of the following acid equilibria<sup>97-103</sup>:



where  $pK_{a1} = 7.0$  and  $pK_{a2} = 17.4$ .

For a fixed concentration of  $[Cd^{2+}]$  at  $pH < pK_{a1}$ , the surface charge on  $CdS$  is a function of the solution  $pH$  as follows<sup>104</sup>:

$$\sigma_0 \Big|_{[Cd^{2+}] = \text{const}} = \frac{\partial \sigma_0}{\partial pH} \Big|_{pH \neq pH_{zpc}} (pH - pH_{zpc}) \quad (5.26)$$

Park and Huang<sup>104</sup> determined a  $pH$  of zero point of charge,  $pH_{zpc}$ , of 7.5 using electrophoretic mobility measurements and acid-base titrations. At an ionic strength of  $\mu = 0.05$  M, they determined  $pK_{a1}^s = 6.1$  and  $pK_{a2}^s = 9.0$  for  $[Cd^{2+}] = 2.5$   $\mu$ M and  $\sigma_0 = 20$   $mC$   $cm^{-2}$ .

In contrast, other researchers<sup>60,62,63</sup> have reported substantially lower values for the  $\text{pH}_{\text{zpc}}$  for CdS in aqueous suspensions. Under experimental conditions that were quite different from those employed by Park and Huang<sup>104</sup>, Nicolau et al.<sup>63</sup> determined a  $\text{pH}_{\text{zpc}} = 1.8$  for 0.01 M  $\text{Na}_2\text{SO}_4$  and KCl as background electrolytes based on electrophoretic mobility measurements, although in the presence of added  $\text{CdCl}_2$  found additional isoelectric points at  $\text{pH} = 8.8, 7.8, \text{ and } 7.1$ , respectively, as the  $\text{Cd}^{2+}$  was increased from  $10^{-4}$  to  $10^{-3}$  to  $10^{-2}$  M. Parks<sup>105</sup> reported a  $\text{pH}_{\text{zpc}} = 10.4$  for CdO (i.e.,  $> \text{CdOH}_2^+$ ,  $> \text{CdOH}$ ,  $> \text{CdO}^-$ ) which would correspond to the surface equilibria of eqs. 17-19. In a follow-up study, Liu and Huang<sup>62</sup> reported a  $\text{pH}_{\text{zpc}}$  for cubic CdS (Hawleyite) of 7.0, which can be compared to their reported value for hexagonal CdS (Greenockite) of 7.5.

Guindo et al.<sup>61</sup> found even lower values of  $\text{pH}_{\text{zpc}}$  between 1 and 1.5 for spherical CdS particles prepared by the method of Matijevic and Wilhemy<sup>106</sup>. However, they pointed out that the IEP (isoelectric point) was sensitive to the specific surface characteristics of CdS that depend on the degree of oxidation or aging as noted by the shift in IEP to higher values for samples that were synthesized over longer periods of time.

The interaction of the various electron donors with the charged CdS surface will also depend on their chemical and physical properties. For example, we can compare water and ethanol as electron donors. Clearly, water undergoes surface dynamic surface exchange and hydrolysis reactions at the surface. On the other hand, ethanol has a substantially lower dielectric constant ( $\epsilon = 24.3$ ) than  $\text{H}_2\text{O}$  ( $\epsilon = 80.4$ ). As a consequence, we predict that the relative thickness of the electrical double layer should decrease over the mole fraction range of  $\chi_{\text{EtOH}}$  from 0 to 1. The thickness of the electrical double layer

around the CdS particles, which under the conditions of our experiments is negatively charged, can be determined as follows<sup>107</sup>:

$$\kappa \equiv \left( \frac{2 F^2 \mu}{\epsilon \epsilon_0 R T} \right)^{0.5} \quad (5.27)$$

where  $\epsilon$  is the dielectric constant of the solvent or mixed solvent system,  $\epsilon_0$  is the permittivity of free space ( $8.854 \times 10^{-12} \text{ C}^2 \text{ J}^{-1} \text{ m}^{-1}$ ),  $\mu$  is the ionic strength of the background electrolyte ( $\text{mol m}^{-3}$ ),  $R$  is the gas constant ( $8.314 \text{ J mol}^{-1} \text{ K}^{-1}$ ),  $T$  is temperature in units of K, and  $F$  is the Faraday constant ( $96485 \text{ C mol}^{-1}$ ). With  $\epsilon = 78.5$  ( $X_{\text{EtOH}} = 0$ ) and  $\epsilon = 24.3$  ( $X_{\text{EtOH}} = 1$ ), the thickness of the electrical double layer for an ionic strength of  $1.0 \text{ mol m}^{-3}$  at  $T = 298 \text{ K}$  gives  $\kappa_{\text{H}_2\text{O}}^{-1} = 9.6 \text{ nm}$  and  $\kappa_{\text{EtOH}}^{-1} = 5.4 \text{ nm}$ , respectively. Double layer compression in the presence of an increasing mole fraction of ethanol will impact the fluorescence response by enhancing the physicochemical interaction of ethanol with the charged CdS surface and thus increasing the fluorescence intensity. In addition, the surface-bound or near surface ethanol serves as a more effective hole trap. Therefore, the apparent exponential increase in fluorescence intensity is due to a more efficient hole trapping by ethanol, which is enhanced because of the compression of the electrical double layer at the same ionic strength (i.e., the effective concentration of ethanol at the surface is increased).

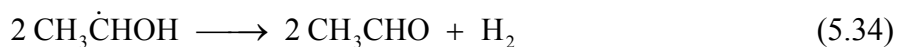
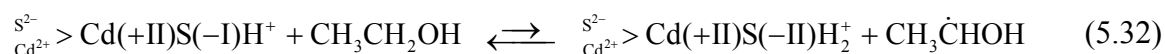
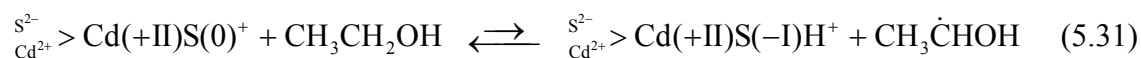
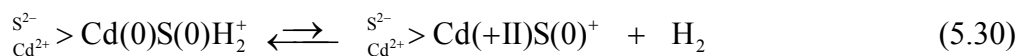
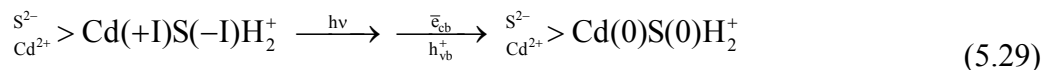
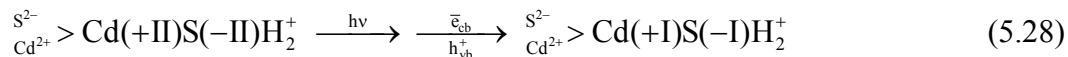
The dramatic color change from yellow to gray during photolysis and  $\text{H}_2$  generation suggests that the traditional mechanistic view of proton reduction or hydrogen generation in the presence of alternative electron donors should be revised. The observed color change is due to the rapid photoreduction of Cd(II) to Cd(I) and then to Cd(0) on the surface of CdS in the absence of oxygen. There is also some probability that S(-II) in the

CdS matrix is also oxidized partially by trapped valence band holes to form S(0) and eventually polysulfide ion ( $S_2^{2-}$ ). Upon exposure to oxygen, the yellow color is regenerated over several hours with the return of yellow CdS on the nanocomposite structures.

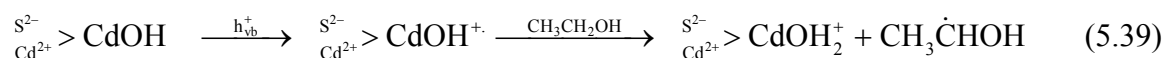
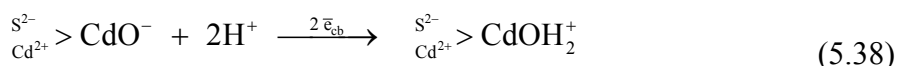
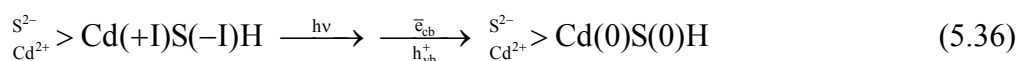
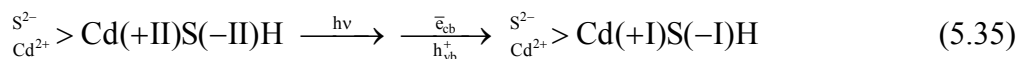
The photoreduction of metal sulfides upon exposure to UV or visible radiation is well documented<sup>108-120</sup>. For example, Stroyuk et al.<sup>121</sup> reported that added  $Cd^{2+}$  adsorbed on the surface of CdS was reduced to Cd(0) upon illumination with visible light, while Job and Ernschwiler<sup>122</sup> noted that ZnS was photoreduced to Zn(0) while S(-II) was oxidized to elemental sulfur, S(0). They<sup>122</sup> also noted that  $H_2$  was liberated via the reaction  $Zn(0) + 2 H^+ \rightarrow H_2 + Zn^{2+}$ . In addition, enhanced photochemical activities have been reported after photoreduction of metal sulfides<sup>110,111,123</sup>.

Gutierrez and Henglein<sup>124</sup> reported that highly reactive elemental Cd deposits were formed during the illumination of colloidal CdS is illuminated in the presence of  $SO_3^{2-}$  or  $S_2O_4^{2-}$ . They reported quantum yields for the formation of Cd(0) of  $\phi = 0.005$  in the absence of excess  $Cd^{2+}$  and  $\phi = 0.053$ . They also noted that  $H_2$  was produced after the formation of Cd(0) on the CdS surface. They argued that hydrogen formation was dependent on a large overpotential for the reduction of water by excess electrons in CdS and the catalytic action of a surface Cd(0) layer. Gutierrez and Henglein<sup>124</sup> also reported that Cd(0) was formed with at close to 100% efficiency when colloidal CdS was irradiated with  $\gamma$ -rays in the presence of organic electron donors.

In our experiments and those of Gutierrez and Henglein<sup>124</sup>,  $H_2$  production is preceded by the initial photoreduction of CdS. A probable set of surface chemical reactions that include photoreduction are as follows:



Similar photoreactions can occur at neutral  $>\text{CdSH}$  and  $>\text{CdOH}$  sites and protonated surface sites involving  $>\text{CdSH}_2^+$  and  $>\text{CdOH}_2^+$ .

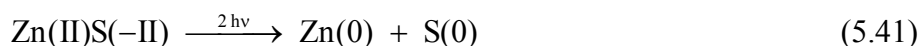


The increase in  $\text{H}_2$  production with an increase in pH suggests that the  $>\text{CdOH}$  surface site may play an important role in the initial steps of proton reduction (a proton bound to  $\text{O}^{2-}$ ) on the surface of CdS.

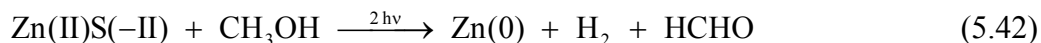


Shiragami et al.<sup>125</sup> reported that CdS suspensions photolyzed in the presence of CH<sub>3</sub>OH turn brown due to the internal reduction of lattice Cd(+II) to Cd(0). In addition, they estimated the amount of Cd(0) produced using the method of Gutierrez and Henglein<sup>124</sup>. They also reported 1) that the brown colored colloidal suspension gave an absorption spectrum that was red-shifted ( $\lambda_{\text{abs}} > 600$  nm), and 2) that the yellow color was restored upon the reintroduction of oxygen into the system as we observed in our experiments.

Reber and Meier<sup>126</sup> reported that ZnS is photoreduced to form metallic zinc clusters on the surface of ZnS as follows:



When methanol was used as an electron donor the following dehydrogenation was observed<sup>126</sup>:



They concluded that the high observed photoreactivity for H<sub>2</sub> production ( $\phi_{\text{H}_2} = 0.9$  at  $\lambda_{\text{max}} = 313$  for  $E_g = 3.66$  eV) was due primarily to the formation of elemental zinc clusters on the surface, and that the Zn(0) clusters served as electron transfer catalysts.

In a later study, Ohtani and co-workers<sup>127</sup> examined the photolysis of an of 2,6-diaminopimelic acid in an anoxic suspension of heat-treated, bulk-phase CdS. They argued that the heat-treated CdS resulted in sulfur vacancies which contributed to the formation of Cd(0) on the surface.

Since the formation of Cd(0) on the surface appears to precede the production of H<sub>2</sub>, can use a simple steady-state analysis<sup>125</sup> to predict the kinetics of the photoreduction. The production of Cd(0) after excitation to produce electrons,  $e_{\text{cb}}^-$ , and holes,  $h_{\text{vb}}^+$ , and on

the surface of CdS can be written as follows:

$$\frac{d[\text{Cd}(0)]_{\text{surf}}}{dt} = k_{\text{red}}[\text{Cd}(\text{II})]_{\text{surf}}[\text{e}_{\text{cb}}^-]^2 \quad (5.43)$$

$$\begin{aligned} \frac{d[\text{e}_{\text{cb}}^-]}{dt} = & \alpha I_0 - k_{\text{rc}}[\text{e}_{\text{cb}}^-][\text{h}_{\text{vb}}^+] - k_{\text{red}}[\text{e}_{\text{cb}}^-][\text{Cd}(\text{II})]_{\text{surf}} - k_{\text{tr}}[\text{e}_{\text{cb}}^-][\cdot\text{CH}_2\text{CH}_2\text{OH}] \\ & - k_1[\text{e}_{\text{cb}}^-][\text{H}^+]_{\text{surf}} - k_2[\text{e}_{\text{cb}}^-][\text{H}\cdot]_{\text{surf}} \end{aligned} \quad (5.44)$$

$$\frac{d[\text{h}_{\text{vb}}^+]}{dt} = \alpha I_0 - k_{\text{rc}}[\text{e}_{\text{cb}}^-][\text{h}_{\text{vb}}^+] - k_3[\text{CH}_3\text{CH}_2\text{OH}]_{\text{surf}} \quad (5.45)$$

If we assume steady-state conditions for eqs. 5.43–5.45, we obtain

$$[\text{e}_{\text{cb}}^-]_{\text{ss}} = \frac{\alpha I_0}{(k_{\text{red}}[\text{Cd}(\text{II})]_{\text{surf}} + k_{\text{tr}}[\cdot\text{CH}_2\text{CH}_2\text{OH}]_{\text{surf}})} \quad (5.46)$$

$$[\text{h}_{\text{vb}}^+]_{\text{ss}} = \frac{\alpha I_0}{(k_3[\text{CH}_3\text{CH}_2\text{OH}]_{\text{surf}})} \quad (5.47)$$

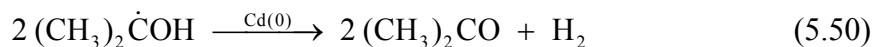
$$[\cdot\text{CH}_2\text{CH}_2\text{OH}]_{\text{ss}} = \frac{(k_3[\text{CH}_3\text{CH}_2\text{OH}]_{\text{surf}} - k_{\text{red}}[\text{Cd}(\text{II})]_{\text{surf}})}{(k_{\text{rc}})} = \beta \quad (5.48)$$

With eqs. 5.46–5.48, we can recast eq. 5.43 as follows:

$$\frac{d[\text{Cd}(0)]_{\text{surf}}}{dt} = \frac{\alpha I_0^2 k_{\text{red}}[\text{Cd}(\text{II})]_{\text{surf}}}{(k_{\text{red}}[\text{Cd}(\text{II})]_{\text{surf}} + k_{\text{tr}}\beta)^2} = \gamma I_{\text{abs}}^2 \quad (5.49)$$

where  $I_{\text{abs}} = \alpha I_0^2$  and  $\alpha k_{\text{red}}[\text{Cd}(\text{II})]_{\text{surf}} / (k_{\text{red}}[\text{Cd}(\text{II})]_{\text{surf}} + k_{\text{tr}}\beta)^2 = \gamma$ . Equation 49 shows that the rate of production of elemental cadmium on the surface of CdS depends on the absorbed light intensity squared (i.e.,  $I_{\text{abs}} = \alpha I_0$ ).

Colloidal Cd(0) has been shown to mediate H<sub>2</sub> formation in the presence of organic radicals. For example, colloidal Cd(0) particles are able to produce H<sub>2</sub> from 1-hydroxy-1-methylethyl radicals as follows<sup>128</sup>:



Resch et al.<sup>73</sup> observed a strong dependence of the fluorescence behavior of stabilized CdS colloids in which the most intense fluorescence is obtained with solvent with the lowest dielectric constants. These results coupled with our own observations, allows us to conclude that the alcohols have a dual purpose. They serve primarily as sacrificial electron donors but also allow stronger interactions of protons with charged CdS or zeolite surfaces by decreasing the dimensions of the charge field or the electric double layer. In effect, the closer bonding interaction with the surface of CdS and Cd(0) resulted in more favorable conditions for electron transfer to surface-bound protons and subsequently for the production of molecular oxygen.

Since the early work of Herron and co-workers<sup>70-72,76</sup> on CdS-Zeolite composites, there have been a number of investigations of the photocatalytic properties of CdS encapsulated in zeolite cavities. Most often the enhanced reactivity has been attributed to enhanced electron-hole charge separation and the increased stability<sup>70</sup> of the CdS has been explained in terms of stabilization of oxygen atoms in the zeolite cages.

Guan and co-workers<sup>129</sup> reported that CdS formed in zeolite-ETS-4 and titanium silicate loaded ETS-4 were effective catalysts for H<sub>2</sub> production at  $\lambda > 420$  nm in the presence of HS<sup>-</sup> and SO<sub>3</sub><sup>2-</sup> as sacrificial electron donors at pH 14 (i.e., 1.0 M NaOH), and that the CdS embedded in the ETS-4 cavities was resistant to photocorrosion. Furthermore, nanoparticulate CdS in the ETS-4-Zeolite showed enhanced activity relative to naked CdS suspensions. The enhanced activity is often explained in terms of the injection of conduction band electrons into the lower-lying bands of the host material. This is consistent with the observed blue shifts (Figure 5.4) which were noted in the fluorescence spectra that are attributed to ‘quantum confinement’ within zeolite cages.

The order of photocatalytic activity for the potassium niobate composites with respect to H<sub>2</sub> production is Ni(0)/NiO/KNbO<sub>3</sub>/CdS > Ni(0)/KNbO<sub>3</sub>/CdS > KNbO<sub>3</sub>/CdS under identical reaction conditions. The KNbO<sub>3</sub> backbone of the composite has unusual chemical and physical material properties. Potassium niobate crystals are used in optical waveguides, in nonlinear optical devices (e.g., frequency doubling and wavelength mixing), in piezoelectric devices (e.g., tunable frequency ultrasound transducers), in holographic image storage, and as a wide-band gap photocatalyst ( $\Delta E_g = 3.4$  eV).

Hayashi et al.<sup>130</sup> synthesized KNbO<sub>3</sub> hydrothermally and found that the fine crystalline powders were efficient photocatalysts for the production of H<sub>2</sub> under UV light illumination at 254 nm. Under slightly different synthesis conditions, they produced K<sub>4</sub>Nb<sub>6</sub>O<sub>17</sub> which was found to be substantially less active than KNbO<sub>3</sub> for H<sub>2</sub> production. They also provided ESR evidence for photoreduction of ion-exchanged Ni<sup>2+</sup> on KNbO<sub>3</sub> to form Ni(0) in the presence of methanol. In addition, Hayashi et al. found that hydrothermally produced KNbO<sub>3</sub> was more photoreactive than potassium niobate (K<sub>4</sub>Nb<sub>6</sub>O<sub>17</sub>) synthesized by the solid-state reaction at 1130 °C. Moreover, high H<sub>2</sub> production rates and actual photosplitting of water to form O<sub>2</sub> also required Ni(0) formation on the surface.

Other unique properties<sup>131</sup> of KNbO<sub>3</sub> that may explain its cooperative effects in the Ni(0)/NiO/KNbO<sub>3</sub>/CdS. For example, Ewart et al.<sup>131</sup> reported that mobile electrons are generated in electrochemically reduced and Fe-doped KNbO<sub>3</sub> upon excitation at 532 nm. The electrons photoexcited at 532 nm had lifetimes of 4 ns and electron mobility of 0.5 cm<sup>2</sup> V<sup>-1</sup> s<sup>-1</sup>. They conclude that the photoexcited electrons are trapped within 4 ns (i.e.,

loss of detectable mobility), however, the trapped-state electrons are thermally activated on a millisecond timeframe and eventually recombine with the internal donor states.

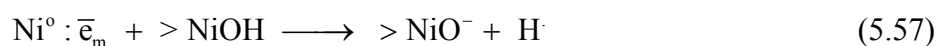
In the case of  $\text{KNbO}_3$  produced by our synthetic procedure, we thermally treated the pure  $\text{KNbO}_3$  powders at  $500\text{ }^\circ\text{C}$  in an  $\text{H}_2$  atmosphere. This treatment step may lead to creation of oxygen vacancies or formation of Nb(IV) and Nb(III) states. After reduction with  $\text{H}_2$  the white  $\text{KNbO}_3$  samples are converted into a gray material which seems to indicate Nb(V) reduction has taken place. Kesselman et al.<sup>132</sup> had observed a similar reduction in  $\text{Nb}_2\text{O}_5/\text{TiO}_2$  composites that were reduced over hydrogen at high temperatures.

A portion of the enhanced reactivity in the  $\text{KNbO}_3$  composites may be due to involvement of the reduced states of niobium and/or oxygen vacancies that allow for the photoexcitation of mobile electrons with visible light. The longer lifetimes ( $\tau_{\text{tr}} > \text{ms}$ ) of the trapped electrons may contribute to the higher reduction rates for bound protons or hydroxides. Reduction of  $\text{Nb}_2\text{O}_5$  is known to form a variety of phases such as  $\text{Nb}_{12}\text{O}_{29}$ ,  $\text{Nb}_{22}\text{O}_{54}$ ,  $\text{Nb}_{25}\text{O}_{62}$ , and  $\text{Nb}_{47}\text{O}_{116}$  that involve partial oxygen loss coupled with the formation of Nb(IV). Similar mixed valence state phases should coexist within the framework of reduced  $\text{KNbO}_3$  and contribute to the photoexcitation of electrons and to the overall photoreactivity with visible light.

Another relevant feature of the metal niobates<sup>133</sup>(e.g.,  $\text{LiNbO}_3$  and  $\text{KNbO}_3$ ) for electro-optic and photorefractive applications is the activation of surface protons (i.e., protons bound in hydroxyl ions,  $\text{OH}^-$ ). The hydroxyl bound protons have activation energies in the range of 1 eV for mobility in  $\text{KNbO}_3$  crystals.

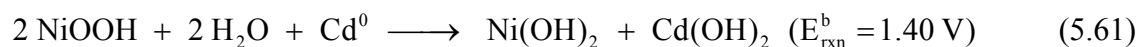
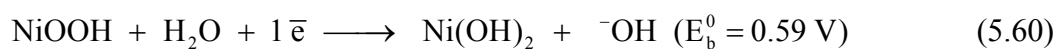
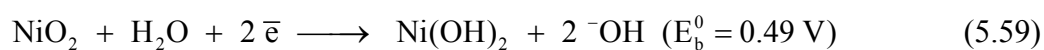
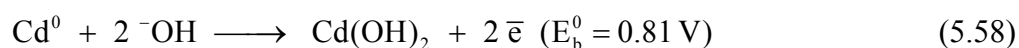
In order to understand the complex interactions taking place on

Ni(0)/NiO/KNbO<sub>3</sub>/CdS we need to account for the impact of the NiO coated Ni deposits on the surface of KNbO<sub>3</sub>. It is generally understood that Ni serves of collect conduction band electrons similar to Pt deposits on semiconducting surfaces. The NiO surface mostly likely reacts in similar fashion as in the case of the >NbOH surface groups. The pH<sub>zpc</sub> of NiO ranges from 7.5 to 7.9. Thus, the catalytic effect of combined Ni/NiO deposits may be due to the following sequence involving surface hydroxyl groups on the hydrated NiO surface:

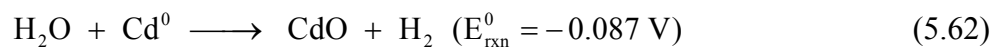


In this pathway, the mobile electrons from both photoactivated CdS and KNbO<sub>3</sub> are captured by the NiO and transferred to the >NiOH surface groups for formed hydrogen atoms and eventually molecular hydrogen.

In conclusion, we note that the Ni/NiO/KNbO<sub>3</sub>/CdS composite after photoreduction has some of the components that comprise a Ni-Cd battery. At pH 14, the redox chemistry of a Ni-Cd battery is as follows:



During recharging of a Ni-Cd battery with a sufficient over-potential, H<sub>2</sub> is evolved. The bandgap energy of NiO is 3.5 eV<sup>134</sup>, and thus, it should not be photoactive in our experiments. However, given the redox potential of eq. 5.62, it may be possible to run the reaction with light < 900 nm. At 500 nm (i.e., 2.48 eV), a sufficient over-potential could be achieved to generate H<sub>2</sub>.



## Acknowledgements

We are grateful to the Hydrogen Energy R&D Center of the 21<sup>st</sup> Century Frontier Research and Development Program of the Ministry of Science and Technology of Korea for financial support. Additional support was provided graciously by the Fellowship Program of the Korean Science & Engineering Foundation (KOSEF) and the Davidow Research Fund of the California Institute of Technology.

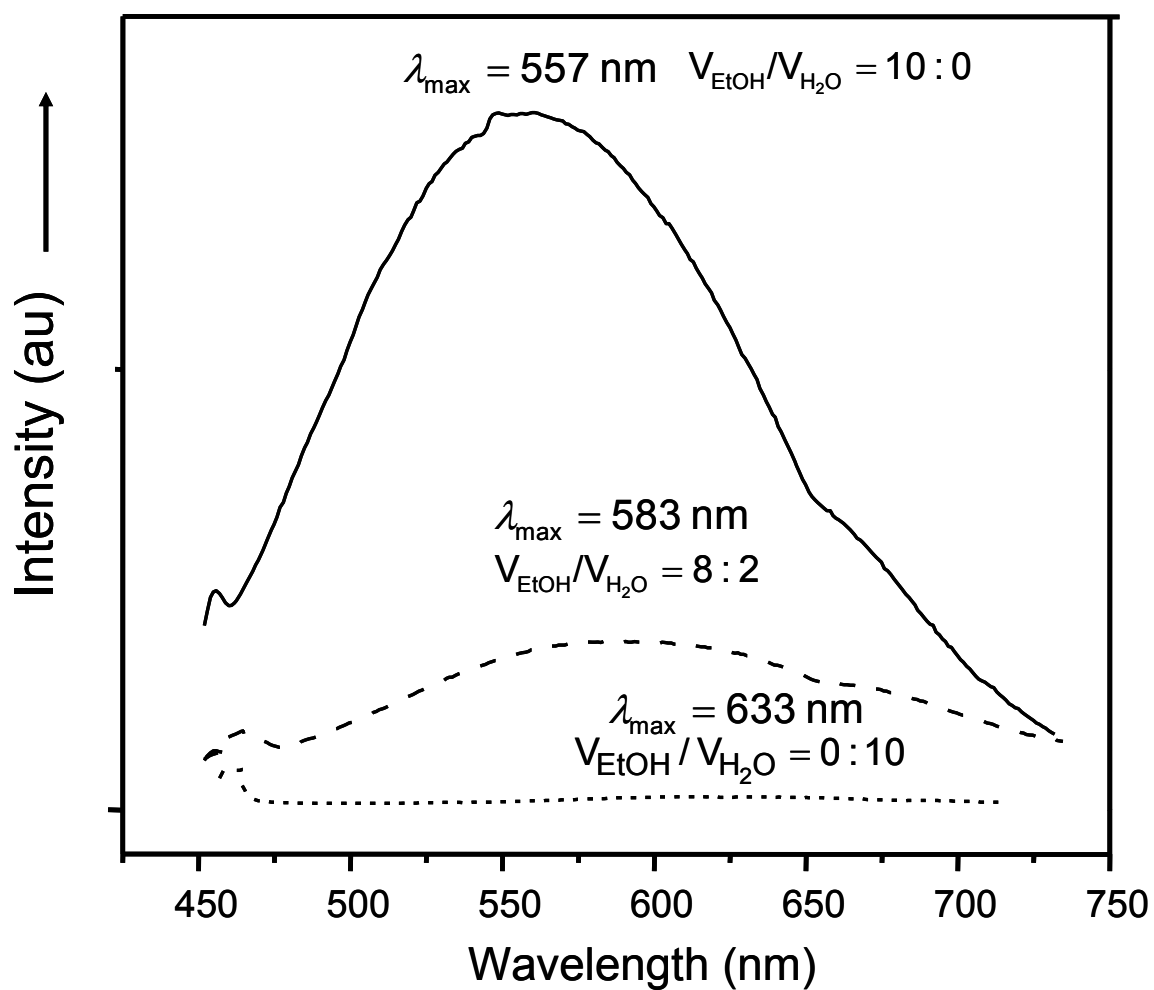


**Figure 5.1.** Fluorescence emission spectra of CdS colloids ( $5.0 \times 10^{-4} \text{ M}$ ) a function of the ethanol-water volume ratio,  $V_{\text{EtOH}}/V_{\text{H}_2\text{O}}$ . The highest intensity is obtained in neat ethanol with a small amount ( $\approx 1.0 \text{ mM}$ )  $\text{H}_2\text{O}$  present as a trace contaminant.  $V_{\text{EtOH}}/V_{\text{H}_2\text{O}} = 0:10$  represents pure water and  $V_{\text{EtOH}}/V_{\text{H}_2\text{O}} = 10:0$  is 99.99% ethanol.

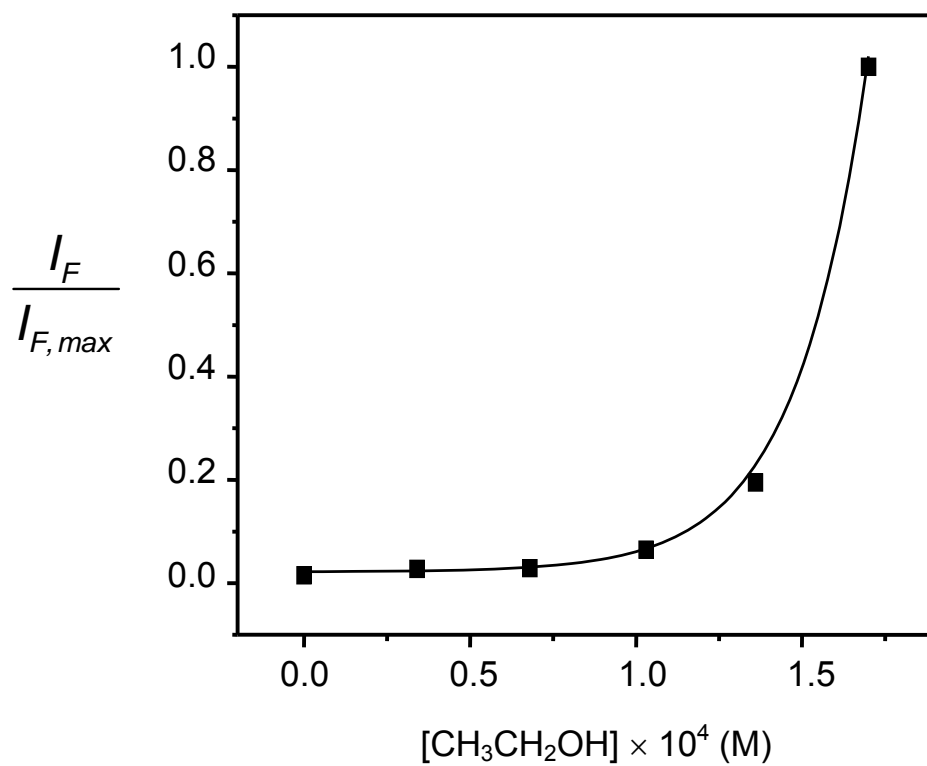


**Figure 5.2.** Fluorescence emission intensity of CdS colloids as a function of  $[\text{CH}_3\text{CH}_2\text{OH}]$  in  $\text{H}_2\text{O}$  at  $25^\circ\text{C}$

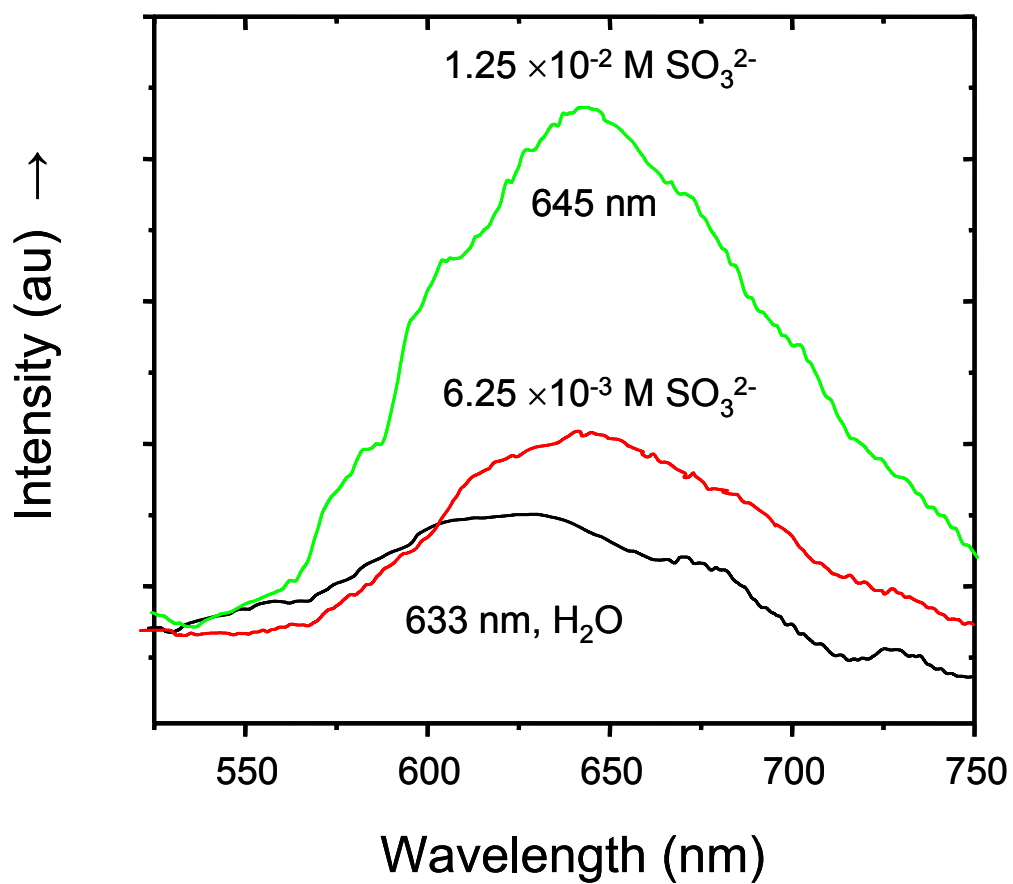


**Figure 5.3.** Fluorescence emission spectra of CdS colloids ( $5.0 \times 10^{-4} \text{ M}$ ) vs.  $[\text{SO}_3^{2-}]$  at pH 8. (a)  $\text{H}_2\text{O}$ , (b)  $6.25 \times 10^{-3} \text{ M K}_2\text{SO}_3$ , and (c)  $1.25 \times 10^{-2} \text{ M K}_2\text{SO}_3$

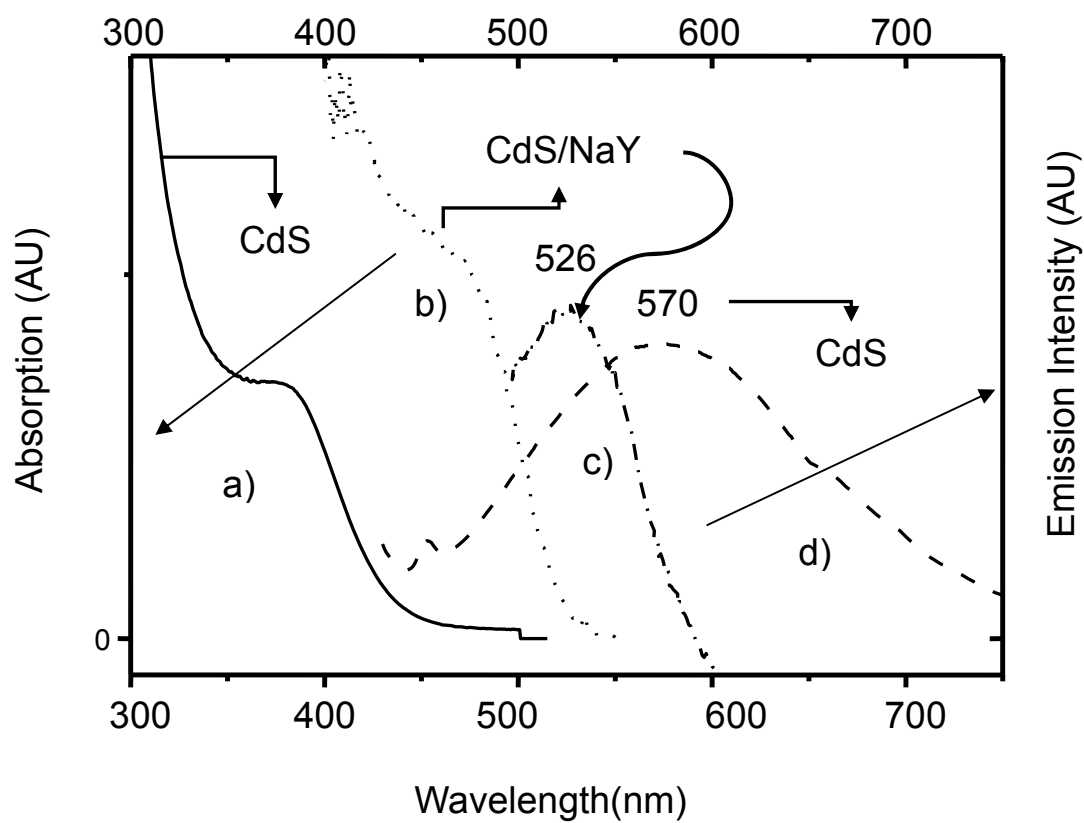


**Figure 5.4.** Diffuse reflectance and fluorescence emission spectra of CdS embedded in NaY zeolite as compared to naked Q-size CdS colloids in EtOH. a) absorption of the CdS colloids in EtOH, b) absorption of CdS/NaY zeolite, c) emission of CdS/NaY zeolite, and d) emission of the CdS colloids in EtOH

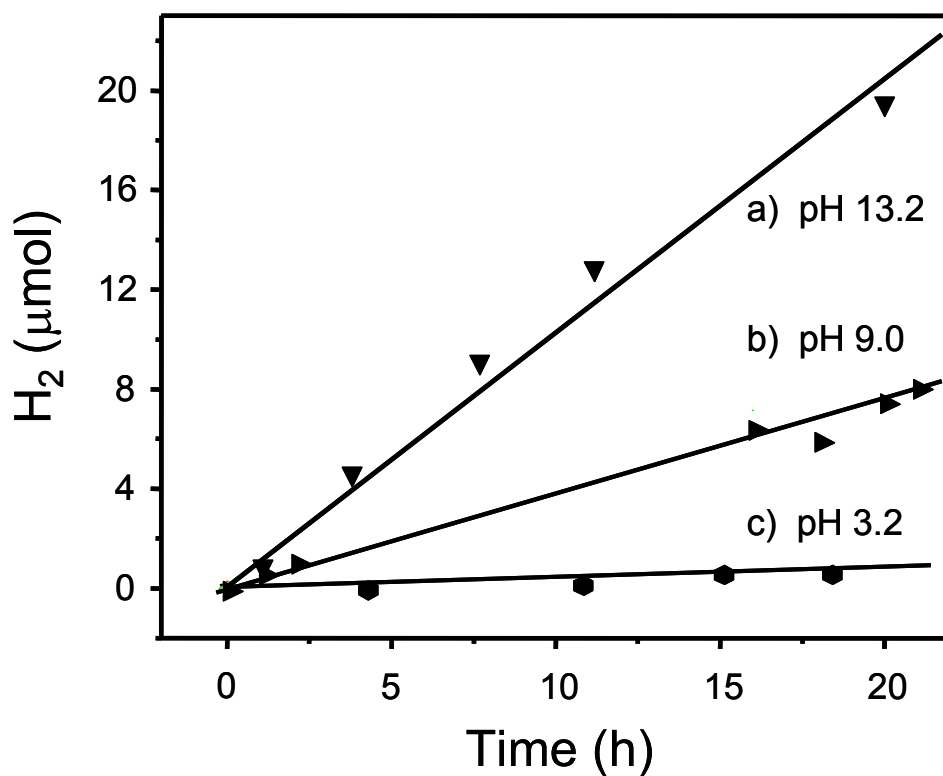


**Figure 5.5.** H<sub>2</sub> production rates on nanoparticulate CdS colloids at  $[\text{CdS}] = 5.0 \times 10^{-4} \text{ M}$  in EtOH:H<sub>2</sub>O = 1:1 mixtures.  $V_{\text{T}} = 40 \text{ mL}$ ). a)  $[\text{NaOH}] = 0.1 \text{ M}$ , pH 13.2; b)  $[\text{K}_2\text{SO}_3] = 5.0 \times 10^{-3} \text{ M}$  and  $[\text{Cd}(\text{OOCCH}_3)_2] = 5.0 \times 10^{-4} \text{ M}$  pH 9; c)  $[\text{K}_2\text{SO}_3] = 5.0 \times 10^{-4} \text{ M}$  and  $[\text{CH}_3\text{CO}_2\text{H}] = 0.1 \text{ M}$ , pH 3.2.

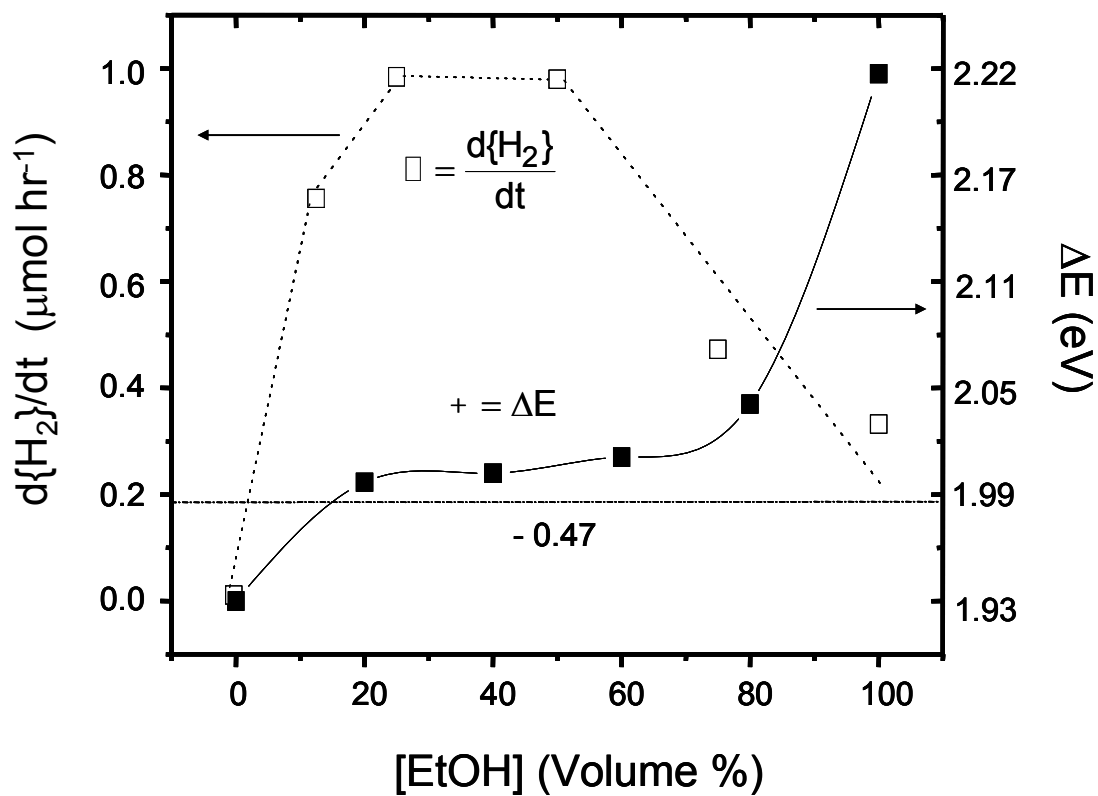


**Figure 5.6.** A plot of the energy gap,  $\Delta E$  (eV), between the emissive state and the ground state calculated from the fluorescence emission spectra as a function of ethanol volume ratio in water. The squares show the rate of  $H_2$  evolution as a function of  $V_{\text{EtOH}}/V_{\text{H}_2\text{O}}$  calculated from the slopes of linear reaction progress plots for the photolysis condition given in Figure 5. The dashed line (-----) denotes the relative energy position for  $2 H^+ + 2 e^- \rightarrow H_2$  at pH 8.

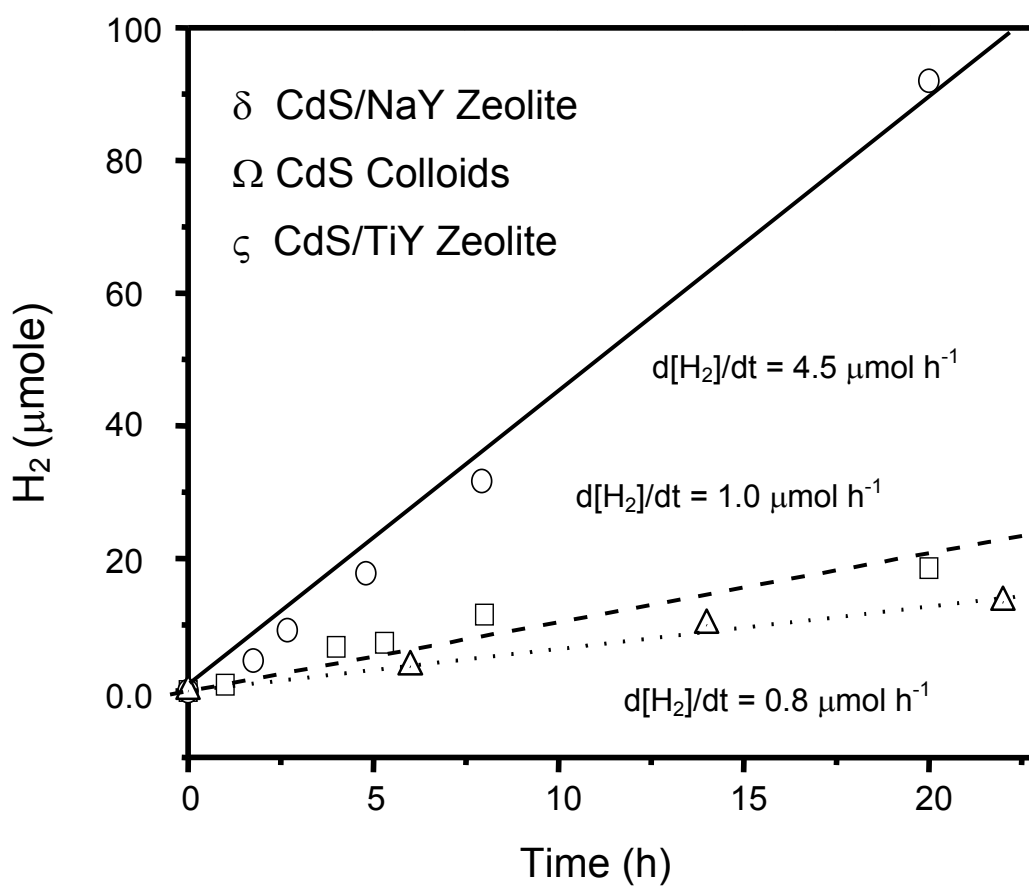


**Figure 5.7.** Rates of H<sub>2</sub> evolution in a mixed ethanol water solvent (EtOH:H<sub>2</sub>O = 1:3 V/V) for V<sub>T</sub> = 40 mL with visible light irradiation ( $\lambda > 400$  nm) versus time. Data presented for CdS colloids, □, ([CdS] =  $2.5 \times 10^{-4}$  M), for CdS/NaY zeolite, ○, ([CdS/NaY] = 0.2 g in 40 mL at 2.9 wt% CdS), and for CdS/TiY zeolite, △, ([CdS/TiY] = 0.2 g in 40 mL at 2.9 wt% CdS)

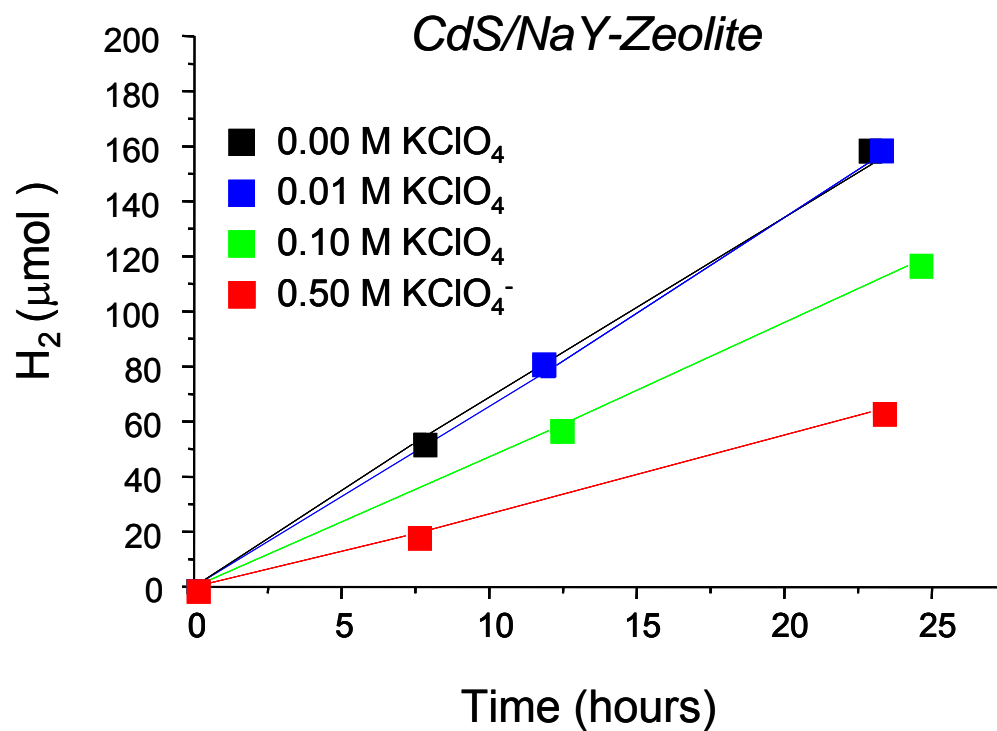


**Figure 5.8.** Rates of H<sub>2</sub> evolution in a mixed ethanol water solvent (EtOH:H<sub>2</sub>O = 1:3 V/V) for V<sub>T</sub> = 40 mL as a function of ionic strength with visible light irradiation ( $\lambda > 400$  nm) using the NaY-Zeolite/CdS composite

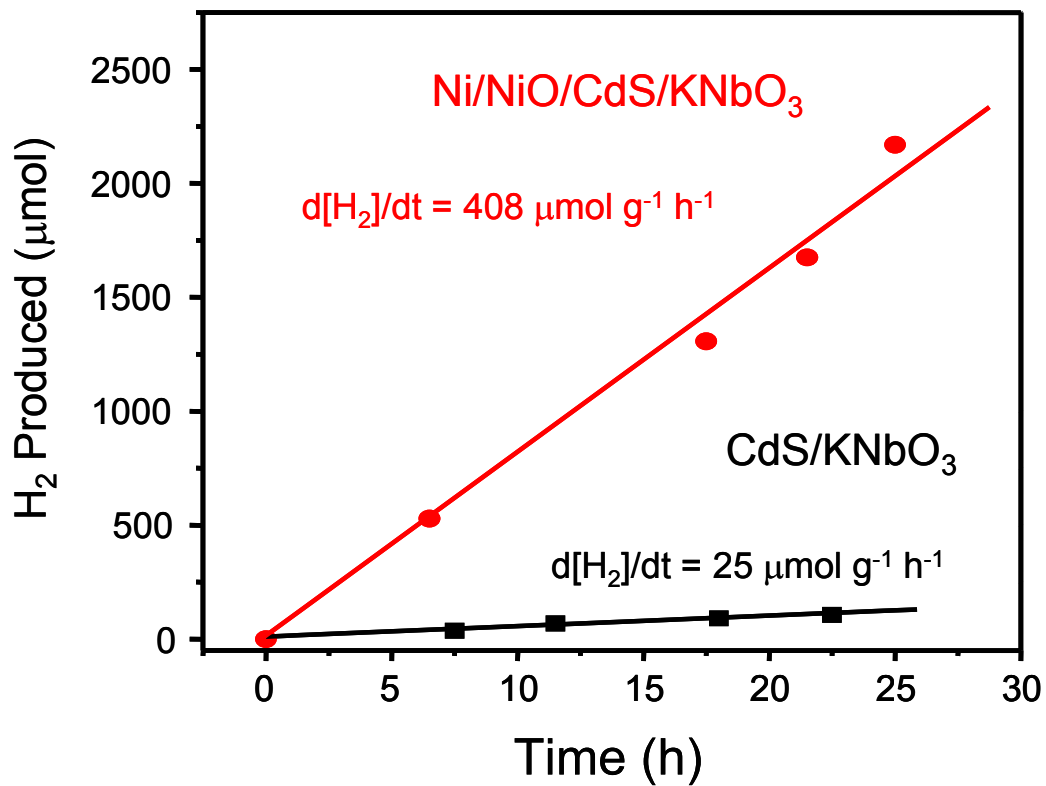


**Figure 5.9.** Rate of H<sub>2</sub> evolution under visible light irradiation ( $\lambda > 400$  nm) in a mixed ethanol water solvent (EtOH:H<sub>2</sub>O = 1:3 V/V, V<sub>T</sub> = 40 mL) for the Ni/NiO/KNbO<sub>3</sub>/CdS nanocomposite

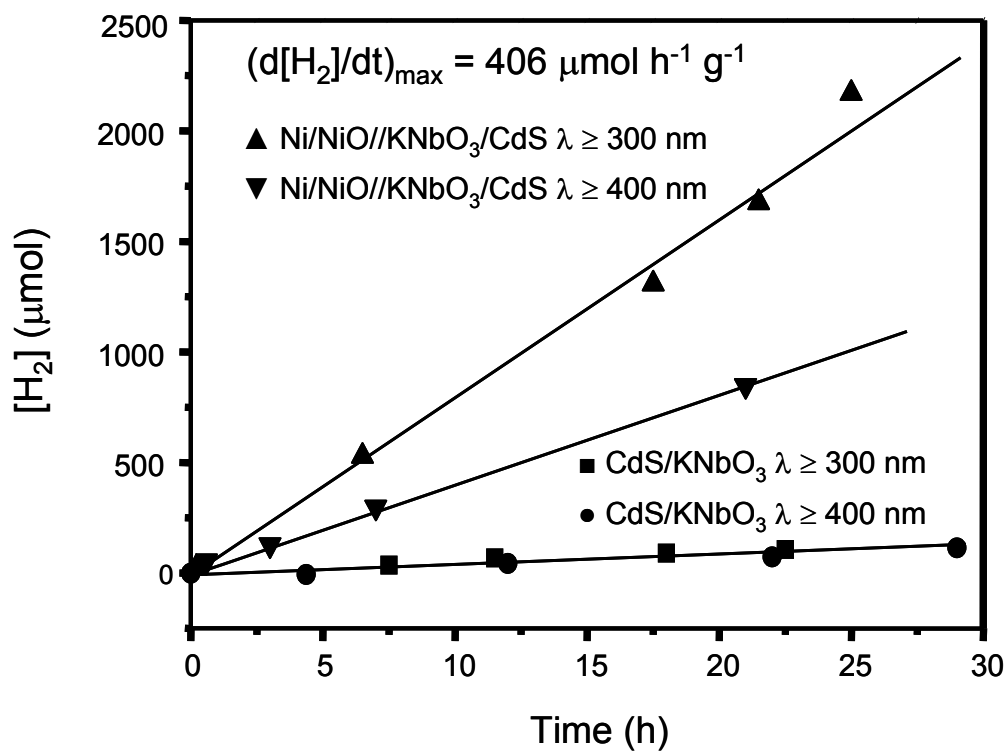


**Figure 5.10.** Comparison of the rate of  $H_2$  evolution under visible light irradiation ( $\lambda > 400 \text{ nm}$ ) compared to UV-vis light ( $\lambda > 300 \text{ nm}$ ) in a mixed ethanol water solvent (EtOH:H<sub>2</sub>O = 1:3 V/V,  $V_T = 40 \text{ mL}$ ) for the Ni/NiO/KNbO<sub>3</sub>/CdS nanocomposite

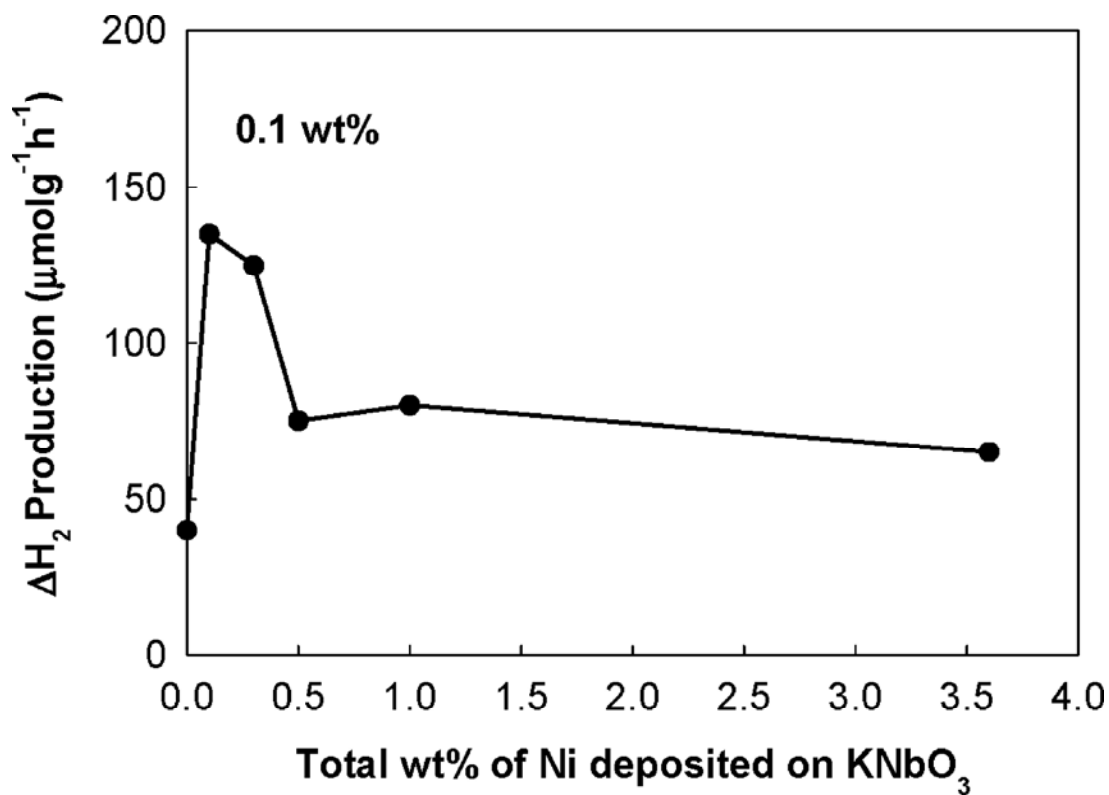


**Figure 5.11.** Differential rate ( $\mu\text{mol h}^{-1}$ ) of  $\text{H}_2$  production on  $\text{Ni}(0)/\text{NiO}/\text{KNbO}_3/\text{CdS}$  as a function of the weight percent Ni deposition. The optimal is approximately 0.1 wt%. [nanocomposite] =  $0.2 \text{ g L}^{-1}$ ,  $V_T = 50 \text{ mL}^{-1}$ . Saturated with Ar at  $t = 0$ . Samples irradiated with a 500 W Xenon lamp at  $\lambda \geq 400 \text{ nm}$

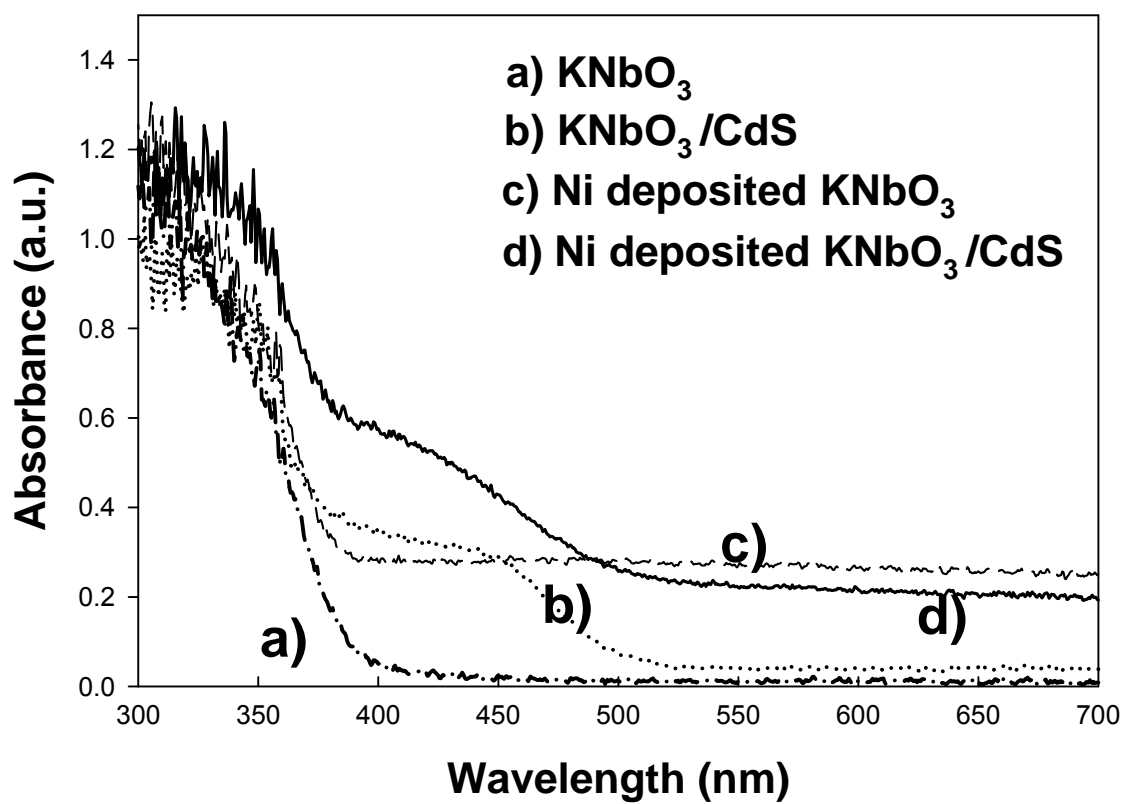


**Figure 5.12.** UV-vis spectra for a) KNbO<sub>3</sub>, b) KNbO<sub>3</sub>/CdS, c) 0.1 wt% Ni(0)/NiO/KNbO<sub>3</sub>, and d) 0.1 wt% Ni(0)/NiO/KNbO<sub>3</sub>/CdS

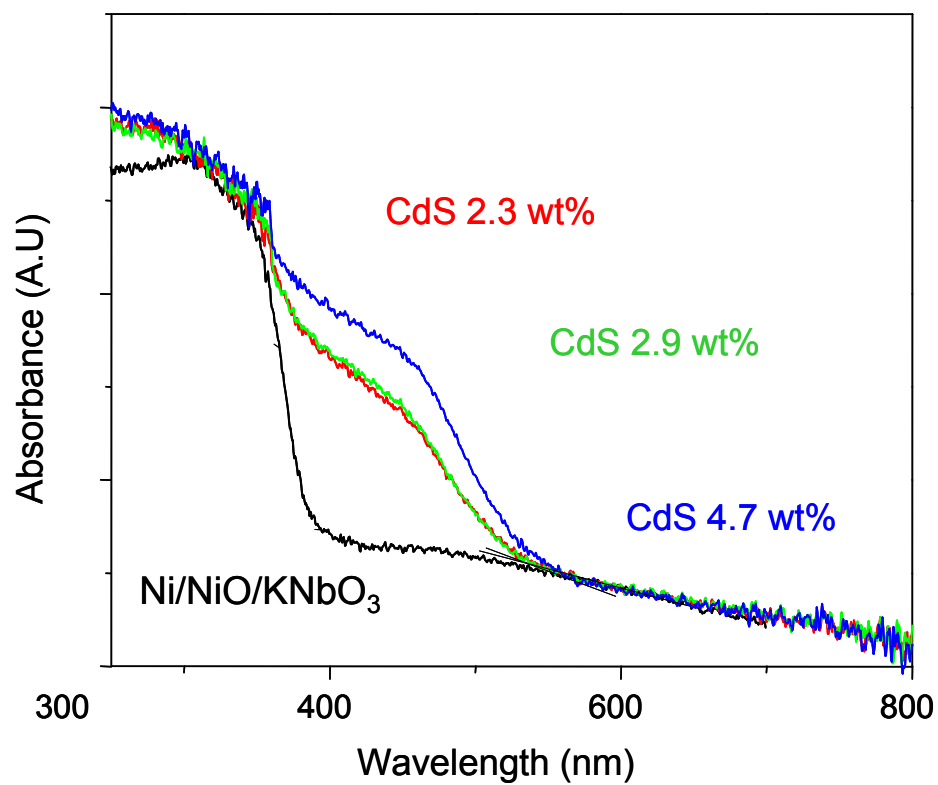


**Figure 5.13.** UV-vis spectra for Ni/NiO/KNbO<sub>3</sub>/CdS as a function of the wt% loading of Q-CdS

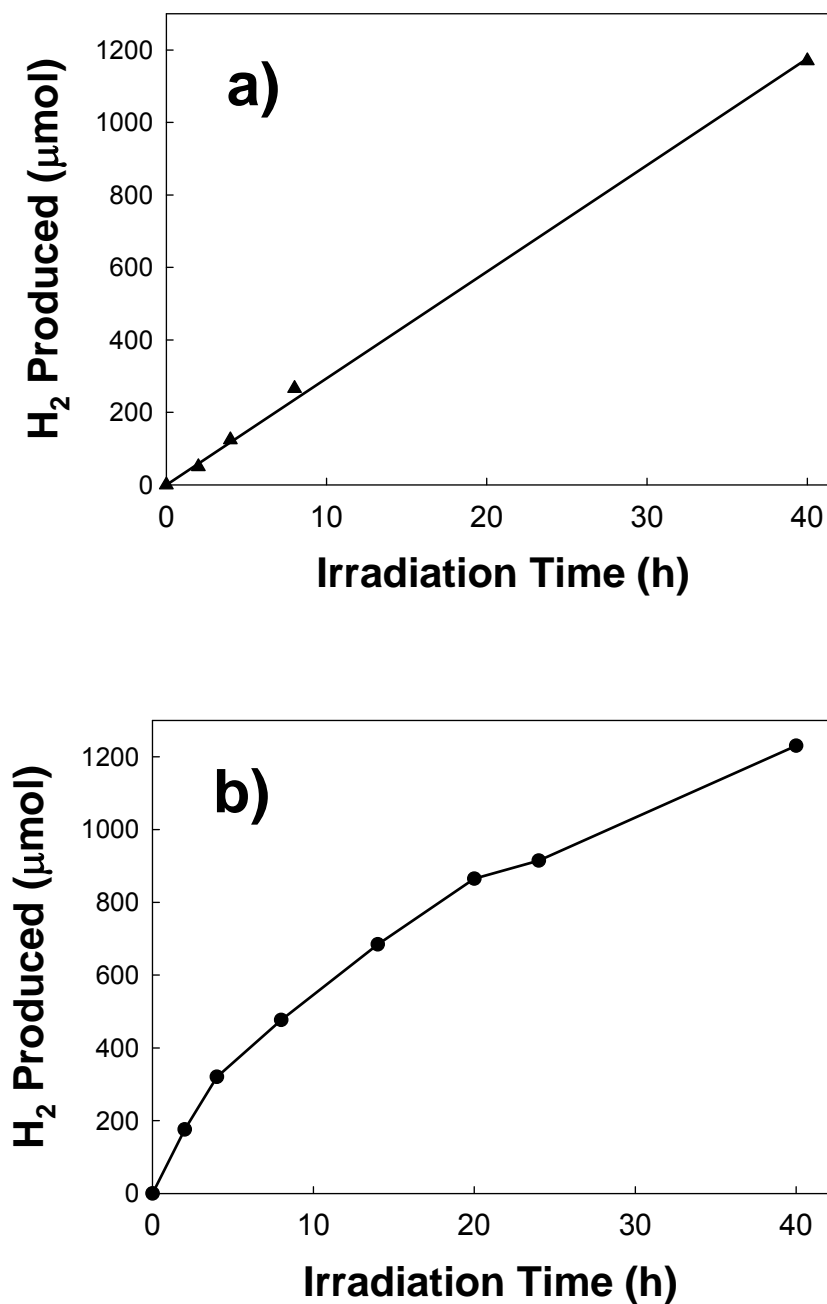


**Figure 5.14.** Hydrogen production on nanocomposite KNbO<sub>3</sub>/CdS in an isopropanol/water solvent mixture (1:3). a) Ni(0) and NiO deposits on the surface of KNbO<sub>3</sub>/CdS. b) Ni(0) deposits only on the surface of KNbO<sub>3</sub>/CdS. 0.1 wt% Ni as Ni(0) or Ni(0)/NiO on CdS/KNbO<sub>3</sub> samples. [nanocomposite] = 0.2 g, V<sub>T</sub> = 50 mL.

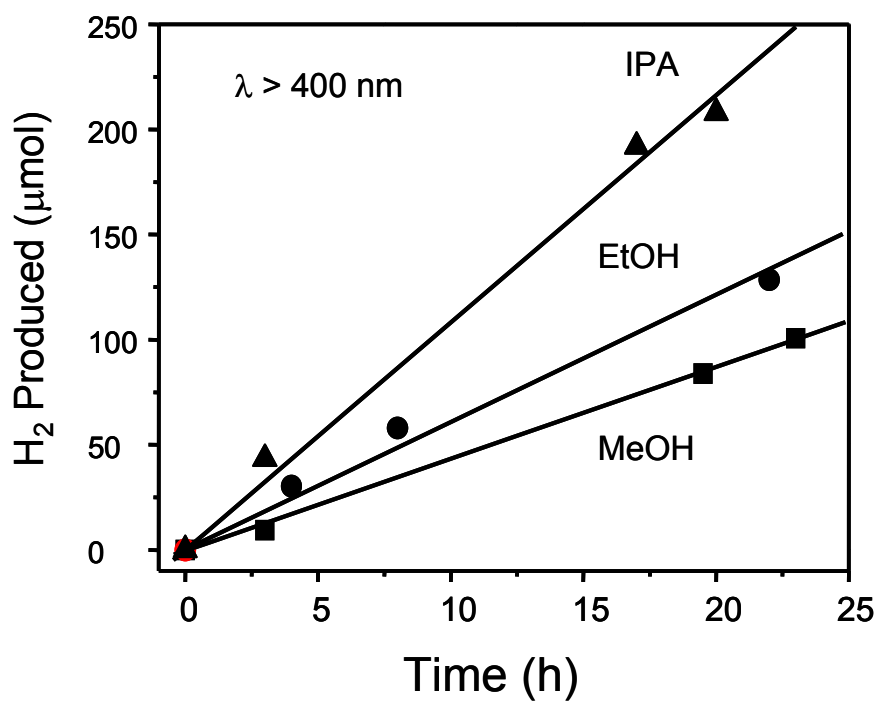


**Figure 5.15.** Relative rates of H<sub>2</sub> production as a function of the electron donor (ROH) on KNbO<sub>3</sub>/CdS

**TABLE 5.1.** H<sub>2</sub> evolution rates of Q-CdS /KNbO<sub>3</sub> nanocomposites

<b>Sample</b>	<b>Band-gap/eV</b>	<b>Incident light/nm</b>	<b>H<sub>2</sub> evolution rate(μmole/g-h)</b>	<b>Q.Y</b>
KNbO <sub>3</sub>	3.26	>300 nm	No	
NiKNbO <sub>3</sub>	3.15	>300 nm	< 1	
CdS/KNbO <sub>3</sub>	2.65	>300 nm	25	
CdS/KNbO <sub>3</sub>	2.65	>400 nm	20	
CdS/Ni(0.1%)KNbO <sub>3</sub>	2.38	>300 nm	408	
CdS/Ni(0.1%)KNbO <sub>3</sub>	2.38	>400 nm	203.5	8.8 %
CdS/Pt(0.1%)KNbO <sub>3</sub>	2.46	>400 nm	147	

\* The amount of CdS is  $5 \times 10^{-4}$  mole/g, solvent: IPA:H<sub>2</sub>O (1:3 (v/v))

## References

- (1) Bard, A. J. *Journal of Photochemistry* **1979**, *10*, 59.
- (2) Sakata, T.; Kawai, T. *Chemical Physics Letters* **1981**, *80*, 341.
- (3) Karakitsou, K. E.; Verykios, X. E. *Journal of Catalysis* **1992**, *134*, 629.
- (4) Domen, K.; Naito, S.; Onishi, T.; Tamaru, K. *Chemical Physics Letters* **1982**, *92*, 433.
- (5) Inoue, Y.; Asai, Y.; Sato, K. *Journal of the Chemical Society-Faraday Transactions* **1994**, *90*, 797.
- (6) Yoshimura, J.; Ebina, Y.; Kondo, J.; Domen, K.; Tanaka, A. *Journal of Physical Chemistry* **1993**, *97*, 1970.
- (7) Inoue, Y.; Kubokawa, T.; Sato, K. *Journal of Physical Chemistry* **1991**, *95*, 4059.
- (8) Bolton, J. R. *Solar Energy* **1996**, *57*, 37.
- (9) Ashokkumar, M. *International Journal of Hydrogen Energy* **1998**, *23*, 427.
- (10) Ashokkumar, M.; Maruthamuthu, P. *International Journal of Hydrogen Energy* **1991**, *16*, 591.
- (11) Amouyal, E. *Solar Energy Materials and Solar Cells* **1995**, *38*, 249.
- (12) Fujishima, A.; Honda, K. *Nature (London, United Kingdom)* **1972**, *238*, 37.
- (13) Kudo, A.; Kato, H.; Tsuji, I. *Chemistry Letters* **2004**, *33*, 1534.
- (14) Buxton, G. V.; Greenstock, C. L.; Helman, W. P.; Ross, A. B. *Journal of Physical and Chemical Reference Data* **1988**, *17*, 513.
- (15) Shangguan, W. F.; Yoshida, A. *Journal of Physical Chemistry B* **2002**, *106*, 12227.
- (16) Koca, A.; Sahin, M. *International Journal of Hydrogen Energy* **2002**, *27*, 363.

- (17) Milczarek, G.; Kasuya, A.; Mamykin, S.; Arai, T.; Shinoda, K.; Tohji, K. *International Journal of Hydrogen Energy* **2003**, *28*, 919.
- (18) Roy, A. M.; De, G. C. *Journal of Photochemistry and Photobiology a-Chemistry* **2003**, *157*, 87.
- (19) Dewitt, R.; Kirschdemesmaeker, A. *Applied Physics Letters* **1984**, *45*, 146.
- (20) Zhang, W. U.; Zhong, Y.; Fan, J.; Sun, S. Q.; Tang, N.; Tan, M. Y.; Wu, L. M. *Science in China Series B-Chemistry* **2003**, *46*, 196.
- (21) Linkous, C. A.; Muradov, N. Z.; Ramser, S. N. *International Journal of Hydrogen Energy* **1995**, *20*, 701.
- (22) Naman, S. A.; Almishhadani, N. H.; Alshamma, L. M. *International Journal of Hydrogen Energy* **1995**, *20*, 303.
- (23) Chen, F.; Zhu, Y. P.; Ma, H. L.; Bo, Z. L.; Zhang, J. L. *Acta Physico-Chimica Sinica* **2004**, *20*, 1292.
- (24) Zhang, J. L.; Xiao, M.; Liu, Z. M.; Han, B. X.; Jiang, T.; He, J.; Yang, G. Y. *Journal of Colloid and Interface Science* **2004**, *273*, 160.
- (25) Innocenti, M.; Cattarin, S.; Loglio, F.; Cecconi, T.; Seravalli, G.; Foresti, M. L. *Electrochimica Acta* **2004**, *49*, 1327.
- (26) Yoshimura, J.; Tanaka, A.; Kondo, J. N.; Domen, K. *Bulletin of the Chemical Society of Japan* **1995**, *68*, 2439.
- (27) Shangguan, W. F.; Yoshida, A. *Solar Energy Materials and Solar Cells* **2001**, *69*, 189.
- (28) Shangguan, W.; Yoshida, A. *Journal of Physical Chemistry B* **2002**, *106*, 12227.
- (29) Darwent, J. R.; Porter, G. *Journal of the Chemical Society, Chemical*

*Communications* **1981**, 145.

(30) Borgarello, E.; Kalyanasundaram, K.; Graetzel, M.; Pelizzetti, E. *Helvetica Chimica Acta* **1982**, 65, 243.

(31) Meissner, D.; Memming, R.; Kastening, B. *Solar Energy R&D in the European Community, Series D: Photochemical, Photoelectrochemical and Photobiological Processes* **1983**, 2, 110.

(32) Meissner, D.; Memming, R.; Kastening, B. *Chemical Physics Letters* **1983**, 96, 34.

(33) Buehler, N.; Meier, K.; Reber, J. F. *Journal of Physical Chemistry* **1984**, 88, 3261.

(34) Serpone, N.; Borgarello, E.; Graetzel, M. *Journal of the Chemical Society, Chemical Communications* **1984**, 6, 342.

(35) Kakuta, N.; Park, K. H.; Finlayson, M. F.; Ueno, A.; Bard, A. J.; Campion, A.; Fox, M. A.; Webber, S. E.; White, J. M. *Journal of Physical Chemistry* **1985**, 89, 732.

(36) Ueno, A.; Kakuta, N.; Park, K. H.; Finlayson, M. F.; Bard, A. J.; Campion, A.; Fox, M. A.; Webber, S. E.; White, J. M. *Journal of Physical Chemistry* **1985**, 89, 3828.

(37) Furlong, D. N.; Grieser, F.; Hayes, D.; Hayes, R.; Sasse, W.; Wells, D. *Journal of Physical Chemistry* **1986**, 90, 2388.

(38) Kolts, J. H. Photochemical production of hydrogen from hydrogen sulfide; (Phillips Petroleum Co., USA). 1986, pp. 7.

(39) Matsumura, M.; Saho, Y.; Tsubomura, H. *NATO ASI Series, Series C: Mathematical and Physical Sciences* **1986**, 174, 581.

(40) Reber, J. F.; Rusek, M. *Journal of Physical Chemistry* **1986**, 90, 824.

(41) Kobayashi, J.; Kitaguchi, K.; Tanaka, H.; Tsuiki, H.; Ueno, A. *Journal of the Chemical Society-Faraday Transactions I* **1987**, 83, 1395.

- (42) Matsumura, M.; Tsubomura, H. *Journal of the Electrochemical Society* **1987**, *134*, C462.
- (43) Mayo, P. d.; Wenska, G. *Tet. Lett.* **1987**, *43*, 1661.
- (44) Muradov, N. Z.; Rustamov, M. I.; Guseinova, A. D.; Bazhutin, Y. V. *Reaction Kinetics and Catalysis Letters* **1987**, *33*, 279.
- (45) Muradov, N. Z.; Rustamov, M. I.; Guseinova, A. D.; Bazhutin, Y. V. *Reaction Kinetics and Catalysis Letters* **1987**, *33*, 279.
- (46) Vucemilovic, M. I.; Vukelic, N.; Rajh, T. *Journal of Photochemistry and Photobiology, A: Chemistry* **1988**, *42*, 157.
- (47) Bahnemann, D. W.; Kormann, C.; Hoffmann, M. R. *J. Phys. Chem.* **1987**, *91*, 3789.
- (48) Hoffman, A. J.; Carraway, E. R.; Hoffmann, M. R. *Environ. Sci. Technol.* **1994**, *28*, 776.
- (49) Hoffman, A. J.; Mills, G.; Yee, H.; Hoffmann, M. R. *Journal of Physical Chemistry* **1992**, *96*, 5546.
- (50) Hoffman, A. J.; Yee, H.; Mills, G.; Hoffmann, M. R. *Journal of Physical Chemistry* **1992**, *96*, 5540.
- (51) Aparisi, A.; Fornes, V.; Marquez, F.; Moreno, R.; Lopez, C.; Meseguer, F. *Solid-State Electronics* **1996**, *40*, 641.
- (52) Liu, X. S.; Iu, K. K.; Thomas, J. K. *Chemical Physics Letters* **1992**, *195*, 163.
- (53) Liu, X. S.; Lu, K. K.; Thomas, J. K. *Journal of the Chemical Society-Faraday Transactions* **1993**, *89*, 1861.
- (54) Fluckiger, U.; Arend, H.; Oswald, H. R. **1977**, *56*, 575.

- (55) Domen, K.; Kudo, A.; Shibata, M.; Tanaka, A.; Maruya, K.; Onishi, T. **1986**, 1706.
- (56) Fischer, C. H.; Weller, H.; Katsikas, L.; Henglein, A. *Langmuir* **1989**, 5, 429.
- (57) Fischer, C. H.; Lilie, J.; Weller, H.; Katsikas, L.; Henglein, A. *Ber. Bunsen-Ges. Phys. Chem. Chem. Phys.* **1989**, 93, 61.
- (58) Henglein, A.; Gutiérrez, M. *Ber. Bunsenges. Phys. Chem.* **1983**, 87, 852.
- (59) Henglein, A. *Chemical Reviews* **1989**, 89, 1861.
- (60) Duran, J. D. G.; Guindo, M. C.; Delgado, A. V.; GonzalezCaballero, F. *Journal of Colloid and Interface Science* **1997**, 193, 223.
- (61) Guindo, M. C.; Zurita, L.; Duran, J. D. G.; Delgado, A. V. *Materials Chemistry and Physics* **1996**, 44, 51.
- (62) Liu, J. C.; Huang, C. P. *Langmuir* **1992**, 8, 1851.
- (63) Nicolau, Y. F.; Menard, J. C. *Journal of Colloid and Interface Science* **1992**, 148, 551.
- (64) Hoffman, A. J.; Mills, G.; Yee, H.; Hoffmann, M. R. *J. Phys. Chem.* **1992**, 96, 5546.
- (65) He, Y. J.; Hu, Y. Positron-Annihilation in Cd<sup>2+</sup> Ion-Exchanged and Cds Loaded Zeolite-Y. In *Zeolites and Related Microporous Materials: State of the Art 1994*, 84, 2295.
- (66) Li, B. H.; Wang, L. J.; Jin, Q. G.; Guo, Z. Y.; Tang, S. X.; Ding, D. T. *Journal of Porous Materials* **2002**, 9, 287.
- (67) Peng, H.; Liu, S. M.; Ma, L.; Lin, Z. J.; Wang, S. J. *Journal of Crystal Growth* **2001**, 224, 274.

- (68) Chen, W.; Wang, Z. G.; Lin, L. Y. *Journal of Luminescence* **1997**, *71*, 151.
- (69) Jentys, A.; Grimes, R. W.; Gale, J. D.; Catlow, C. R. A. *Journal of Physical Chemistry* **1993**, *97*, 13535.
- (70) Herron, N.; Wang, Y.; Eddy, M. M.; Stucky, G. D.; Cox, D. E.; Moller, K.; Bein, T. *Journal of the American Chemical Society* **1989**, *111*, 530.
- (71) Wang, Y.; Herron, N. *Journal of Physical Chemistry* **1988**, *92*, 4988.
- (72) Wang, Y.; Herron, N. *Journal of Physical Chemistry* **1987**, *91*, 257.
- (73) Resch, U.; Eychmuller, A.; Haase, M.; Weller, H. *Langmuir* **1992**, *8*, 2215.
- (74) Lakowicz, J. R. *Principles of Fluorescence Spectroscopy*; Kluwer Academic/Plenum: New York, 1999.
- (75) Wang, Y.; Herron, N. *Journal of Physical Chemistry* **1991**, *95*, 525.
- (76) Herron, N.; Wang, Y.; Eckert, H. *Journal of the American Chemical Society* **1990**, *112*, 1322.
- (77) Yeshchenko, O. A.; Dmitruk, I. M.; Koryakov, S. V.; Pundyk, I. P.; Barnakov, Y. A. *Solid State Communications* **2005**, *133*, 109.
- (78) Yu, Z. H.; Li, J. B.; O'Connor, D. B.; Wang, L. W.; Barbara, P. F. *Journal of Physical Chemistry B* **2003**, *107*, 5670.
- (79) Liu, S. M.; Xu, Z.; Wageh, H.; Xu, X. R. *Spectroscopy and Spectral Analysis* **2002**, *22*, 908.
- (80) Li, J. B.; Xia, J. B. *Physical Review B* **2000**, *62*, 12613.
- (81) Woggon, U.; Saleh, M.; Uhrig, A.; Portune, M.; Klingshirn, C. *Journal of Crystal Growth* **1994**, *138*, 988.
- (82) Korgel, B. A.; Monbouquette, H. G. *Journal of Physical Chemistry B* **1997**, *101*,

5010.

- (83) Davis, A. P.; Huang, C. P. *Water Research* **1991**, *25*, 1273.
- (84) Tang, W. Z.; Huang, C. P. *Chemosphere* **1995**, *30*, 1385.
- (85) Davis, A. P.; Hsieh, Y. H.; Huang, C. P. *Chemosphere* **1994**, *28*, 663.
- (86) Hsieh, Y. H.; Huang, C. P.; Davis, A. P. *Chemosphere* **1993**, *27*, 721.
- (87) Hsieh, Y. H.; Huang, C. P.; Davis, A. P. *Chemosphere* **1992**, *24*, 281.
- (88) Hsieh, Y. H.; Huang, C. P. *Colloids and Surfaces* **1991**, *53*, 275.
- (89) Henglein, A. *Berichte der Bunsen-Gesellschaft* **1982**, *86*, 301.
- (90) Hatchard, C. G.; Parker, C. A. *Proc. Roy. Soc. (London)* **1956**, *A235*, 518.
- (91) Calvert, J. G.; Pitts, J. N. *Photochemistry*, 1966.
- (92) Cornu, C. J. G.; Colussi, A. J.; Hoffmann, M. R. *Journal of Physical Chemistry B* **2001**, *105*, 1351.
- (93) Cornu, C. J. G.; Colussi, A. J.; Hoffmann, M. R. *Journal of Physical Chemistry B* **2003**, *107*, 3156.
- (94) Park, S. W.; Huang, C. P. *Journal of Colloid and Interface Science* **1987**, *117*, 431.
- (95) De, G. C.; Roy, A. M. *Journal of Surface Science and Technology* **1999**, *15*, 147.
- (96) Daskalakis, K. D.; Helz, G. R. *Environmental Science & Technology* **1992**, *26*, 2462.
- (97) Licht, S.; Longo, K.; Peramunage, D.; Forouzan, F. *Journal of Electroanalytical Chemistry* **1991**, *318*, 111.
- (98) Licht, S.; Manassen, J. *Journal of the Electrochemical Society* **1987**, *134*, 918.
- (99) Licht, S.; Forouzan, F.; Longo, K. *Analytical Chemistry* **1990**, *62*, 1356.

- (100) Schoonen, M. A. A.; Barnes, H. L. *Geochimica Et Cosmochimica Acta* **1988**, *52*, 649.
- (101) Myers, R. J. *Journal of Chemical Education* **1986**, *63*, 687.
- (102) Migdisov, A. A.; Williams-Jones, A. E.; Lakshtanov, L. Z.; Alekhin, Y. V. *Geochimica Et Cosmochimica Acta* **2002**, *66*, 1713.
- (103) Meyer, B.; Ward, K.; Koshlap, K.; Peter, L. *Inorganic Chemistry* **1983**, *22*, 2345.
- (104) Park, S. W.; Huang, C. P. *Journal of Colloid and Interface Science* **1987**, *117*, 431.
- (105) Parks, G. A. *Chemical Reviews* **1965**, *65*, 177.
- (106) Matijevic, E.; Wilhelmy, D. M. *Journal of Colloid and Interface Science* **1982**, *86*, 476.
- (107) Faust, B. C.; Hoffmann, M. R.; Bahnemann, D. W. *Journal of Physical Chemistry* **1989**, *93*, 6371.
- (108) Albers, C. *Zeitschrift fuer Physikalische Chemie (Leipzig)* **1968**, *237*, 278.
- (109) Bontinck, W.; Dekeyser, W. *Naturwissenschaften* **1956**, *43*, 323.
- (110) Davidson, R. S.; Willsher, C. J. *Journal of the Chemical Society, Dalton Transactions: Inorganic Chemistry (1972-1999)* **1981**, 833.
- (111) Davidson, R. S.; Willsher, C. J. *Faraday Discussions of the Chemical Society* **1981**, *70*, 177.
- (112) Gisolf, J. H. *Physica (The Hague)* **1939**, *6*, 84.
- (113) Guntz, A. A. *Annali di Chimica Applicata* **1926**, *5*, 363.
- (114) Lenard, P. *Annalen der Physik (Berlin, Germany)* **1922**, *68*, 553.
- (115) Merz, W. J. *Helvetica Physica Acta* **1957**, *30*, 244.

- (116) Niekisch, E. A.; Pflaum, U.; Rompe, R. *Zeitschrift fuer Physikalische Chemie (Leipzig)* **1956**, 205, 146.
- (117) Schleede, A.; Herter, M. *Zeitschrift fuer Elektrochemie und Angewandte Physikalische Chemie* **1923**, 29, 411.
- (118) Schleede, A.; Herter, M.; Kordatzki, W. *Z. physik. Chem.* **1923**, 106, 386.
- (119) Shionoya, S.; Watanabe, K. *Bull. Chem. Soc. Japan* **1957**, 30, 118.
- (120) Sviszt, P. *Acta Physica Polonica* **1964**, 26, 823.
- (121) Stroyuk, A. L.; Shvalagin, V. V.; Raevskaya, A. E.; Korzhak, A. V.; Kuchmii, S. Y. *Theoretical and Experimental Chemistry (Translation of Teoreticheskaya i Eksperimental'naya Khimiya)* **2003**, 39, 341.
- (122) Job, A.; Ernschwiler, G. *Compt. rend.* **1923**, 177, 313.
- (123) Markham, M. C.; Barry, J.; Iava, M.; Haddad, J. *Journal of Physical Chemistry* **1957**, 61, 1665.
- (124) Gutierrez, M.; Henglein, A. *Berichte der Bunsen-Gesellschaft* **1983**, 87, 474.
- (125) Shiragami, T.; Ankyu, H.; Fukami, S.; Pac, C.; Yanagida, S.; Mori, H.; Fujita, H. *Journal of the Chemical Society-Faraday Transactions* **1992**, 88, 1055.
- (126) Reber, J. F.; Meier, K. *Journal of Physical Chemistry* **1984**, 88, 5903.
- (127) Ohtani, B.; Kusakabe, S.; Okada, K.; Tsuru, S.; Nishimoto, S.; Amino, Y.; Izawa, K.; Nakato, Y.; Matsumura, M.; Nakaoka, Y.; Nosaka, Y. **2001**, 201.
- (128) Henglein, A.; Lindig, B.; Westerhausen, J. *Journal of Physical Chemistry* **1981**, 85, 1627.
- (129) Guan, G.; Kida, T.; Kusakabe, K.; Kimura, K.; Fang, X.; Ma, T.; Abe, E.; Yoshida, A. *Chemical Physics Letters* **2004**, 385, 319.

- (130) Hayashi, H.; Hakuta, Y.; Kurata, Y. **2004**, *14*, 2046.
- (131) Ewart, M.; Biaggio, I.; Zgonik, M.; Gunter, P. **1994**, *49*, 5263.
- (132) Kesselman, J. M.; Weres, O.; Lewis, N. S.; Hoffmann, M. R. *Journal of Physical Chemistry B* **1997**, *101*, 2637.
- (133) Yariv, A.; Orlov, S. S.; Rakuljic, G. A. **1996**, *13*, 2513.
- (134) Nel, J. M.; Auret, F. D.; Wu, L.; Legodi, M. J.; Meyer, W. E.; Hayes, M. **2004**, *100*, 270.

## Chapter 6

# Photocatalytic Hydrogen Production with Visible Light over Pt-Interlinked Hybrid Composites of Cubic-Phase and Hexagonal- Phase CdS

Sections reprinted with permission from Silva, L.A.; Ryu, S.Y.; Choi, J.; Choi, W.; Hoffmann, M. R. *Journal of Physical Chemistry C* **2008**, *112*, 12069.  
© 2008 American Chemical Society

### Abstract

A hybrid photocatalytic system, which is based on a mixed-phase cadmium sulfide matrix composed of nano-particulate cubic-phase CdS (c-CdS) with average particle diameters of 13 nm and a bandgap energy of 2.6 eV, is coupled with bulk-phase hexagonal CdS (hex-CdS) that has a bandgap energy of 2.3 eV and is interlinked with elemental platinum deposits. The resulting hybrid nano-composite catalysts are photocatalytically efficient with respect to hydrogen gas production from water with visible light irradiation at  $\lambda > 420$  nm. Rates of H<sub>2</sub> production approaching 1.0 mmol-H<sub>2</sub> g<sup>-1</sup> h<sup>-1</sup> are obtained with a c-CdS/Pt/hex-CdS composite photocatalyst, in the presence of a mixed sodium sulfide and sodium sulfite background electrolyte system at pH 14. In contrast, the same composite produces H<sub>2</sub> at a rate of 0.15 mmol g<sup>-1</sup> h<sup>-1</sup> at pH 7 in a water-isopropanol solvent system. The relative order of reactivity for the synthesized hybrid catalysts was found to be: c-CdS/Pt/hex-CdS > Pt/c-CdS/hex-CdS > c-CdS/hex-CdS > Pt/hex-CdS > hex-CdS > quantum-sized c-CdS. A mechanism involving enhanced lifetimes of electron-hole trapping states that are dependent on the surface chemistry of hydrated CdS involving surface hydroxyl (>CdOH) and sulfhydryl groups (>CdSH) are invoked.

## Introduction

Photocatalytic splitting of water using metal oxide or metal sulfide semiconductors and sunlight may provide an alternative approach to convert water into hydrogen and oxygen. For example, bulk-phase cadmium sulfide in the cubic form, c-CdS, which has a nominal band gap energy of 2.4 eV and appropriate band positions, has the thermodynamic potential to drive water-splitting with visible light illumination<sup>1-7</sup>.



Cubic-phase CdS (c-CdS) is readily obtained by sol-gel procedures using mixed aqueous solutions of an appropriate cadmium salt mixed with sodium sulfide at low temperatures. In contrast, the synthesis at high temperature results in the formation of hexagonal-phase CdS (hex-CdS) in a ‘wurtzite’ crystal structure. Matsumura et al.<sup>2</sup> reported that higher H<sub>2</sub> production rates and higher photo-efficiencies are obtained with bulk-phase hex-CdS when compared to bulk-phase c-CdS suspensions.

In the case of quantum-sized (Q-sized) c-CdS produced by sol-gel methods, the band edges are shift to yield larger overall redox potentials<sup>8-10</sup>. For example, Hoffman et al. prepared c-CdS in glycerol with average particle diameters of 4 nm and band gap energies shifted to 3.1 eV<sup>11</sup>. The increased thermodynamic driving force of the 3.1 eV particles should increase the net rate of interfacial charge transfer in the normal Marcus regime<sup>12-14</sup>, and thus result in higher rates and efficiencies of photocatalysis<sup>15</sup>. In this regard, Hoffman et al.<sup>16</sup> reported a tenfold increase in the photo-efficiency for production of H<sub>2</sub>O<sub>2</sub> on quantum-sized ZnO as the particle diameters were decreased from 4.0 to 2.3 nm, while similar effects were observed during the photo-polymerization of methylmethacrylate (MMA), as initiated by CdS, ZnO, and TiO<sub>2</sub>. In each case, the

photo-initiated polymerization of MMA on quantum-sized particles of CdS, ZnO, and TiO<sub>2</sub> resulted in much higher quantum yields and mass production rates, when compared to their bulk-phase counterparts at the same total surface area<sup>11,17</sup>.

In an effort to increase the photo-activity of CdS with respect to hydrogen production from water in the presence of sacrificial electron donors, we have synthesized a series of hybrid catalytic systems that couple the higher efficiency hexagonal phase CdS (hex-CdS) in the bulk-phase size domain with quantum-sized cubic-phase CdS interlinked with elemental Pt deposits. The overall goal is to increase higher photoefficiencies for water splitting with hybrid catalytic systems.

## Experimental

Bulk-phase, hex-CdS (orange crystallites) was synthesized by the thermal treatment (i.e., calcination) of commercial-grade c-CdS (Aldrich, yellow powders) at 800 °C under a flowing-nitrogen atmosphere for one hour. The nano-composite photocatalysts were prepared using several different procedures. In the first procedure, quantum-sized c-CdS was prepared *in situ* as a colloidal suspension in ethanol as described previously<sup>11</sup> and subsequently deposited directly on to the much larger hex-CdS crystallite surfaces. In a second synthetic step, metallic platinum was deposited on the hybrid c-CdS/hex-CdS aggregates by the photodecomposition of PtCl<sub>6</sub><sup>2-</sup> to form Pt/c-CdS/hex-CdS nanocomposite. In a separate procedure, elemental platinum was photodeposited on the hex-CdS surfaces before c-CdS deposition to form c-CdS/Pt/hex-CdS composite. c-CdS deposition on to 1.0 g of the base substrate [hex-CdS or Pt/hex-CdS] surface was accomplished by mixing 20 mL of a 0.01 M Cd<sup>2+</sup> solution into ethanol with stirring for

one day at room temperature. After 24 hours, a stoichiometric amount of Na<sub>2</sub>S was added to the Cd<sup>2+</sup>/hex-CdS or Cd<sup>2+</sup>/Pt/hex-CdS suspensions. The reaction products were filtered, washed with ethanol, and air dried.

The Pt-loaded hybrid particles were prepared by irradiation of hex-CdS or c-CdS/hex-CdS suspensions (1.0 g in 50 mL of a mixed solvent H<sub>2</sub>O/isopropanol (70:30 v/v)) for 30 min using a 500-W xenon-arc lamp in the presence of H<sub>2</sub>PtCl<sub>6</sub>·6H<sub>2</sub>O (0.3 wt% of Pt). The final pH of the solution after photodeposition was 4. After irradiation, the filtered Pt-loaded samples were washed with distilled water and ethanol. The resulting nanocomposite catalysts were characterized by XRD, diffuse reflectance spectroscopy, TEM, and XPS analysis.

UV-vis diffuse reflectance spectra were recorded on a Shimadzu UV-2101PC with an integrating sphere attachment (Shimadzu ISR-260), using Ba<sub>2</sub>SO<sub>4</sub> powder as an internal reference. SEM images were taken on a LEO 1550VP FESEM while XRD spectra were recorded on a Phillips X-Pert PRO X-ray diffraction system. XPS measurements were made with an M-probe surface spectrometer (VG Instruments) using monochromatic Al K<sub>α</sub> X-rays (1486.6 eV).

A high-pressure Hg-Xe arc lamp was used as the light source for the photolyses. The collimated light beam was passed through an IR filter, a focusing lens and a 400 nm cut-off filter before reaching the cylindrical photolysis cell, which was air-cooled to maintain a constant temperature. Since it is well known that colloidal CdS suspensions undergo photocorrosion and photocatalytic dissolution under oxic conditions, H<sub>2</sub> production experiments were carried out under a nitrogen atmosphere. Before each

experiment, the quartz photolysis cell was purged with N<sub>2</sub> for 30 min in order to eliminate O<sub>2</sub>.

Hydrogen gas evolution was measured using gas chromatography (HP 5890 Series II) with thermal conductivity detection (TCD). Due to similar conductivity values for He and H<sub>2</sub>, nitrogen was used as a carrier gas. The separations were achieved with a molecular sieve column (30 m × 0.32 mm × 12.00 μm). The GC oven temperature was set at 30 °C in order to achieve the best spatial resolution between N<sub>2</sub> (i.e., the reactor purge gas) and H<sub>2</sub>. Calibration curves were found to be linear over a broad range of H<sub>2</sub> concentrations.

In a typical photolysis experiment, 50 mg of a target hybrid photocatalyst preparation was dispersed 1) in an aqueous solution (total volume = 50 mL) containing 30% isopropanol or 2) in an aqueous solution (total volume = 50 mL) containing 0.1 M Na<sub>2</sub>S, 0.02 M Na<sub>2</sub>SO<sub>3</sub>, and 1.0 M NaOH. The isopropanol and mixed sulfide (HS<sup>-</sup>/S<sup>2-</sup>; pK<sub>a2,H<sub>2</sub>S</sub> = 17.3) sulfite (HSO<sub>3</sub><sup>-</sup>/SO<sub>3</sub><sup>2-</sup> pK<sub>a2</sub> = 7.2) were used as electron donors to prevent photo-corrosion of CdS. Sample aliquots of the headspace gas of the photolysis cell, where the total headspace volume was 100 mL, were taken with a gas-tight syringe in increments of 50 μL through a rubber septum. Multiple sample aliquots were taken at each time point to ensure precision.

## Results and Discussion

The X-ray diffraction patterns of bulk-phase c-CdS and hex-CdS, which are shown in Figure 6.1, confirms that calcination of bulk-phase c-CdS at 800 °C results in the formation of hex-CdS in a highly-crystalline wurtzite structure. This result is consistent

with earlier reports<sup>2,7</sup>. On the other hand, the bulk-phase precursor, c-CdS, has an X-ray diffraction pattern that is typical of semi-amorphous materials.

The apparent bandgap energies for c-CdS and hex-CdS were determined from diffuse reflectance spectra as shown in Figure 6.2a. The corresponding bandgap energies,  $\Delta E_g$ , were obtained: 1) 2.33 eV for bulk-phase c-CdS, 2) 2.31 eV for hex-CdS, and 3) 2.62 eV for nano-particulate c-CdS. The UV-vis spectrum of hex-CdS exhibits a sharp edge at 570 nm. In contrast, the corresponding spectrum of nano-particulate c-CdS is blue shifted by 0.3 eV compared to the corresponding bulk phase c-CdS or hex-CdS. The observed blue shift for Q-CdS is consistent with the much smaller sizes of the colloidal nano-particles compared to the micrometer-sized, bulk-phase c-CdS or hex-CdS powders<sup>11</sup>.

For comparison, the diffuse reflectance spectra of the composite catalysts are shown in Figure 6.2b. The spectrum of the c-CdS/hex-CdS composite appears to be a linear combination of the individual spectra of the two CdS crystalline phases. The particle sizes of the base hex-CdS material range from 6–9  $\mu\text{m}$  based on the TEM analysis. TEM micrographs of nano-particulate c-CdS clearly show Q-sized islands deposited on the surface of the Pt/hex-CdS core (i.e., c-CdS/Pt/hex-CdS) while, in contrast, the Pt/c-CdS/hex-CdS composite appears to be devoid of Q-sized islands. It appears that the specific sequence of photodeposition of Pt may control whether or not c-CdS remains attached to the core hex-CdS surface. Surface attached c-CdS islands are apparent only when the c-CdS is deposited during the last step in the composite catalyst preparation. The average particle diameter of c-CdS islands that were deposited on the hex-CdS surfaces is 13 nm.

Hydrogen generation rates were measured for the series of composite catalysts using either an aqueous solution of isopropanol at circum-neutral pH or an aqueous solution of a mixed sulfide ( $\text{HS}^-/\text{S}^{2-}$ ) and sulfite ( $\text{SO}_3^{2-}$ ) solution at high pH (pH 14), which was determined by the concentration of NaOH (1.0 M). The gaseous hydrogen production was measured during the first eight hours of irradiation at sampling intervals of two hours with the final sample aliquot taken after 22 hours of irradiation. In contrast, the dark control showed no  $\text{H}_2$  production in the absence of light. In addition, suspensions of plain hex-CdS and Pt/hex-CdS were found to be photocatalytic with respect to  $\text{H}_2$  production with time.

From the kinetic data shown in Table 6.1, it appears that the Pt/c-CdS/hex-CdS composite has very low catalytic activity with isopropanol as an electron donor, but it shows much higher activity at pH 14 with the mixed sulfide/sulfite electron donor system. In contrast, the c-CdS/Pt/hex-CdS hybrid composite yields much higher rates of  $\text{H}_2$  production under the same irradiation conditions for both electron donor systems. When normalized to the weight of the catalyst sample, hydrogen production rates were found to be  $d[\text{H}_2]/dt = 153$  and  $668 \mu\text{mol g}^{-1} \text{h}^{-1}$  for isopropanol (pH 7) as an electron donor and sulfide/sulfite as electron donors (pH 14), respectively. Nanoparticulate c-CdS islands on the Pt/hex-CdS surface have an average radius of 6.5 nm, while in contrast, on Pt/c-CdS/hex-CdS no c-CdS deposits were observed by TEM. In addition, XPS analysis shows that there is only one species of Cd (i.e., Cd(II)) present in c-CdS/Pt/hex-CdS composite, while the Pt/c-CdS/hex-CdS composite spectrum shows two different forms of cadmium. These results suggest that the c-CdS, which was deposited on the orange hex-CdS crystals, underwent photocorrosion during irradiation of  $\text{PtCl}_6^{2-}$  to generate the

Pt(0) islands. Quantum-sized c-CdS is much less stable than bulk phase hex-CdS, due to its less crystalline structure and smaller particle size with a corresponding higher specific surface area-to-volume ratio.

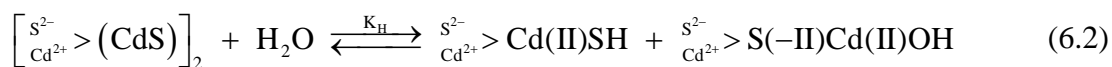
In addition to the apparent loss of c-CdS due to photocorrosion, the lower activity of Pt/c-CdS/hex-CdS may be due to the presence of several higher oxidation state species of platinum on the surface. When a  $4f_{7/2}$  peak is used as a reference, the binding energy of Pt(0) is determined to be 71.0 eV<sup>4</sup>. However, the XPS spectrum for Pt/c-CdS/hex-CdS has a  $4f_{7/2}$  peak at 72.4 eV (not shown); the slight shift to higher energies indicates the presence of higher oxidation states of platinum. This observation is consistent with the results of Jin et al.<sup>1</sup> who reported that platinum sulfide, Pt(II)S, was formed instead of Pt(0) as the photo-reduction product of  $\text{PtCl}_6^{2-}$  on bulk-phase c-CdS under acidic conditions in water. On the other hand, the XPS spectrum of c-CdS/Pt/hex-CdS sample has a binding energy of 71.6 eV close to Pt(0) reference peak of 71.0 eV.

The kinetic results tabulated in Table 6.1 indicate that Pt/c-CdS/hex-CdS has the highest hydrogen production rate in the sulfide/sulfite electron donor system that is substantially higher on a relative basis compared to isopropanol as the sole electron donor. In the case of the sulfide-sulfite electron-donor system, there appears to be no significant difference between rates of H<sub>2</sub> production from both Pt/c-CdS/hex-CdS and c-CdS/Pt/hex-CdS composites during the early stages of illumination. However, after 22 hours of continuous irradiation, the activity of the Pt/c-CdS/hex-CdS composite was clearly lower. The average rates of hydrogen production for Pt/c-CdS/hex-CdS and c-CdS/Pt/hex-CdS composites were 537  $\mu\text{mol g}^{-1}\text{h}^{-1}$  and 668  $\mu\text{mol g}^{-1}\text{h}^{-1}$ , respectively. In

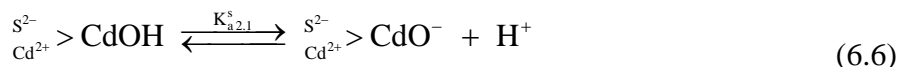
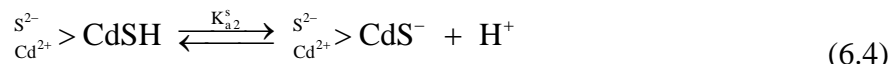
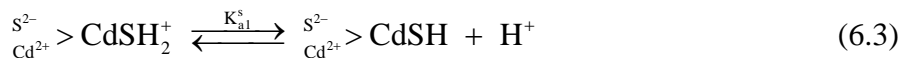
the case of Pt/c-CdS/hex-CdS in the sulfide/sulfite electron system,  $\text{SO}_3^{2-}$  may substitute for  $\text{S}^{2-}$  which may have been lost from the surface lost during the photodeposition of platinum. In addition, during the course of irradiation, Pt(II) can be reduced back to Pt(0) at high pH; this may account for the increase in activity of Pt/c-CdS/hex-CdS at high pH compared to pH 7. The gradual change in the oxidation state of Pt during the course of photocatalytic reaction has been demonstrated previously in the case of Pt/TiO<sub>2</sub> catalysts<sup>18</sup>. Platinum oxides on TiO<sub>2</sub> are reduced to zero-valent platinum during irradiation.

The effect of quantum-sized c-CdS on hydrogen production rates can be seen in the data of Table 6.1. With isopropanol as the electron donor, the hydrogen production rate is increased 3.4-fold compared to samples without Q-sized c-CdS (c-CdS/Pt/hex-CdS vs. Pt/hex-CdS). A smaller enhancement of 1.6-fold was observed for the same samples with the  $\text{S}^{2-}/\text{SO}_3^{2-}/\text{H}_2\text{O}$  electron donor system.

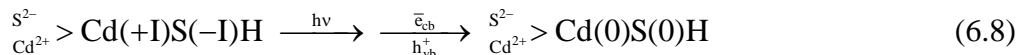
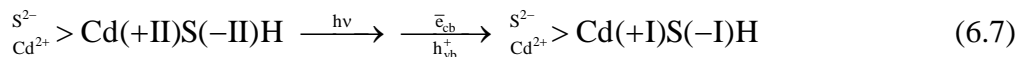
As previously noted by Jin et al.<sup>4</sup>, the photocatalytic dehydrogenation of aliphatic alcohols can be initiated by reaction with surface bound hydroxyl radicals, which are generated at the surface of CdS. However, based on our previous work<sup>19,20</sup>, another possible mechanism for the photocatalytic production of H<sub>2</sub> with visible light is feasible. Hex-CdS, bulk-phase c-CdS, and quantum-sized c-CdS react readily with water as follows:



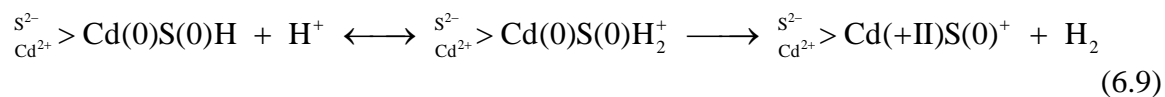
The hydrolyzed surface sites,  $>\text{Cd(II)SH}$  and  $>\text{CdOH}$ , undergo the following proton transfer reactions:



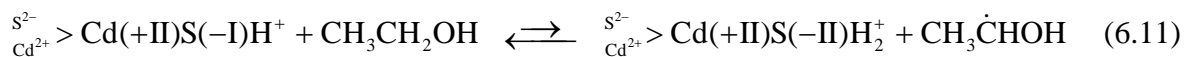
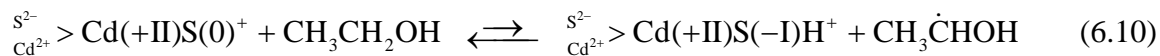
Upon equilibration in water, the CdS composites can be photo-excited to produce trapped electrons and holes at the various surface sites. In the case of cadmium sulfide, this leads to photo-reduction of a certain fraction of the available surface sites.

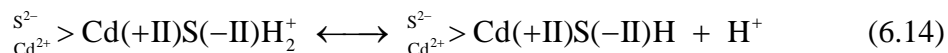


Electron transfer to form molecular hydrogen may take place at the reduced surface states as follows:



On the other hand, isopropanol, sulfide, and sulfite oxidation are initiated at surface-trapped holes (e.g.,  $>\text{Cd(+II)S(0)}^+$ ) as follows:

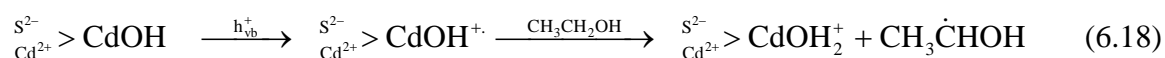
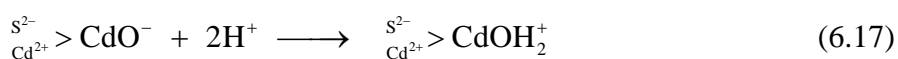




In addition, bandgap excitation and subsequent surface trapping of electrons and holes may take place on cadmium hydroxyl surface sites:

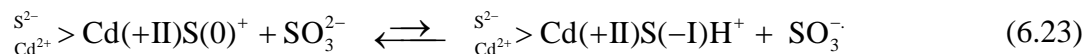
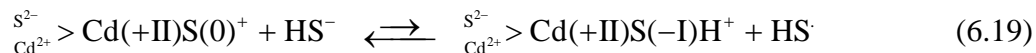


At higher pH, the  $>\text{CdOH}$  surface site may play an important role in the initial steps of proton reduction (a proton bound to  $\text{O}^{2-}$ ) on the surface of CdS.



Elemental platinum, Pt(0), islands serve as transient reservoirs for trapped electrons effectively increasing the lifetime of the trapped states on both hex-CdS and Q-sized c-CdS.

Similar surface reactions take place in the presence of the mixed  $\text{HS}^-/\text{SO}_3^{2-}$ -sulfide electron donor systems<sup>21,22</sup>. Sulfite ( $\text{SO}_3^{2-}$ ) and bisulfide ( $\text{HS}^-$ ) are readily oxidized to  $\text{SO}_4^{2-}$  and polysulfide ions,  $\text{S}_n^{2-}$ , such as  $\text{S}_4^{2-}$  and  $\text{S}_5^{2-}$ , which impart a yellow color to the aqueous suspension at high pH. However, the polysulfide ions may also act as optical filters and effectively compete for the photoreduction of protons<sup>22</sup>. The formation of the yellow polysulfide ions can be suppressed by reaction with sulfite ions to give  $\text{HS}^-$  and thiosulfate,  $\text{S}_2\text{O}_3^{2-}$ . In addition, excess sulfide in solution stabilizes the CdS surface by eliminating surface defects due to photo-corrosion. A plausible mechanism for this sequence is as follows:



In a recent study<sup>23</sup>, we examined a variety of combinations of c-CdS, TiO<sub>2</sub>, and Pt to determine optimal synthesis conditions for hybrid nano-composite catalysts suitable for visible light activation ( $\lambda > 420$  nm). We found that the specific preparation procedure and order of reagent addition significantly influenced the observed photocatalytic activity of the ternary hybrid catalysts. In these cases, formation of a potential gradient at the interface between cubic CdS and TiO<sub>2</sub> is necessary in achieving the efficient charge separation and transfer. In addition, the mode of Pt deposition on the c-CdS/TiO<sub>2</sub> hybrid catalysts determined the overall hydrogen production efficiency. For example, photoplatinization of the CdS/TiO<sub>2</sub> hybrid [Pt-(CdS/TiO<sub>2</sub>)] proved to be much less efficient than an initial Pt photodeposition on naked TiO<sub>2</sub>, which was then followed by the deposition of CdS [CdS/(Pt-TiO<sub>2</sub>)]. This result is quite similar that observed in the present study using c-CdS and hex-CdS composites. For example, the CdS/(Pt-TiO<sub>2</sub>) had a hydrogen production rate ranging from 6 to  $9 \times 10^{-3}$  mol h<sup>-1</sup> g<sup>-1</sup>, which was higher by a factor of 3 to 30 than that of Pt-(CdS/TiO<sub>2</sub>). The photocatalytic activity of the ternary

catalysts is sensitive to the location of platinum island deposition and synthesis conditions. In both systems, the sensitivity of the preparation method on the hydrogen production activity needs to be considered during the design and synthesis of hybrid photocatalysts.

In conclusion, we have developed a new hybrid photocatalytic system that is based on a mixed-phase cadmium sulfide matrix composed of quantum-sized, cubic CdS and bulk-phase hexagonal CdS interlinked with elemental platinum. This unusual hybrid composite catalyst is efficient for the photochemical production of molecular hydrogen from water with visible light irradiation, while at the same time it appears to be resistant to photocorrosion.

## **Acknowledgements**

Dr. Luciana A. Silva received fellowship support from CAPES (Coordenação de Aperfeiçoamento de Pessoal de Nível Superior), which is Brazil's Ministry of Education Agency responsible for post-graduate training. The research at Caltech was funded by the Hydrogen Energy R&D Center of the 21<sup>st</sup> Century Frontier Research and Development Program of the Ministry of Science and Technology of Korea.

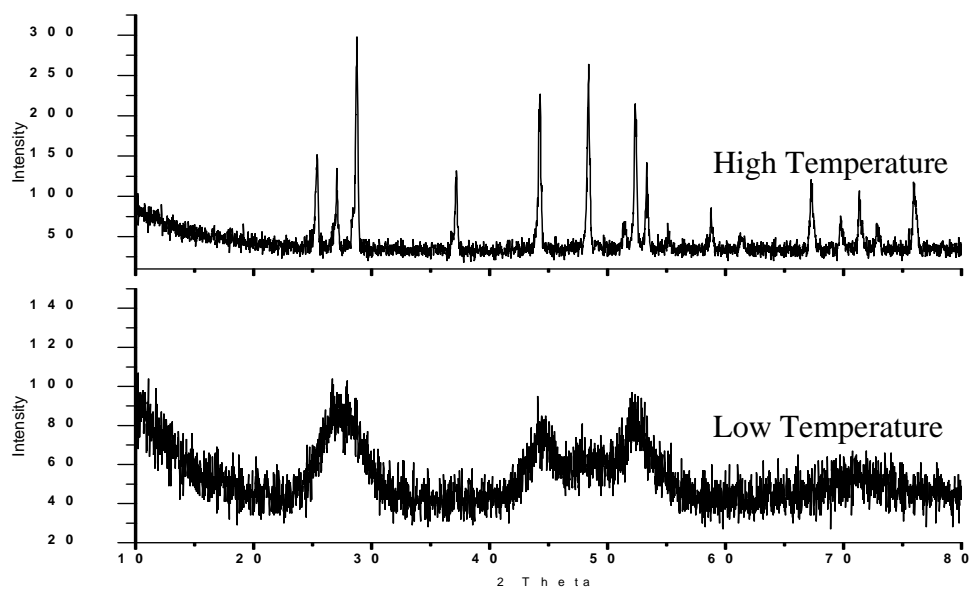


**Figure 6.1.** X-ray diffraction patterns of comparing the high-temperature, hexagonal phase CdS (hex-CdS) to the thermodynamically favored cubic crystalline bulk-phase CdS (c-CdS)

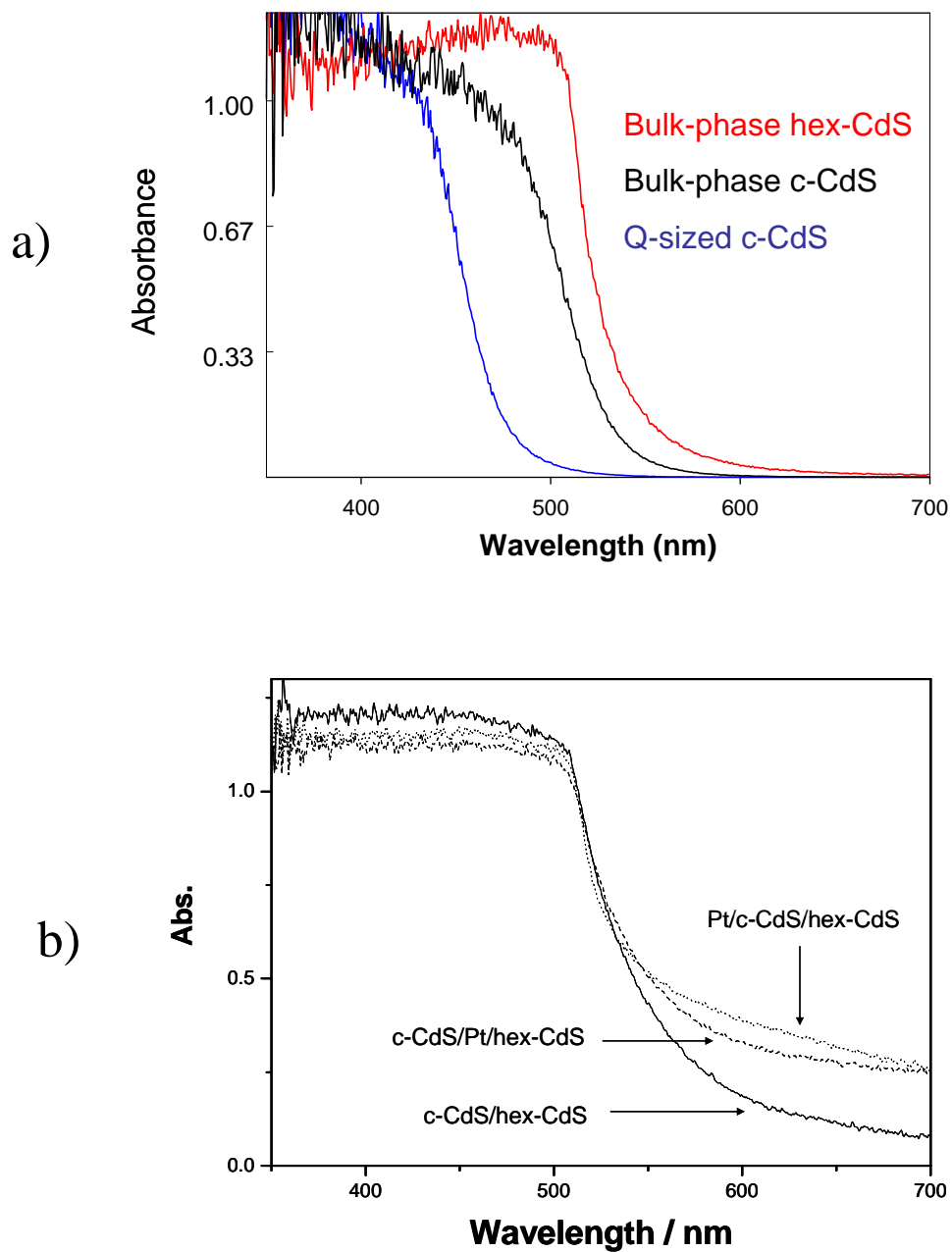


**Figure 6.2.** Diffuse reflectance spectra of a) the three base CdS materials: quantum-sized c-CdS, yellow crystalline bulk-phase cubic c-CdS, and orange hexagonal hex-CdS; b) the corresponding spectra of the three hybrid nanocomposite catalysts

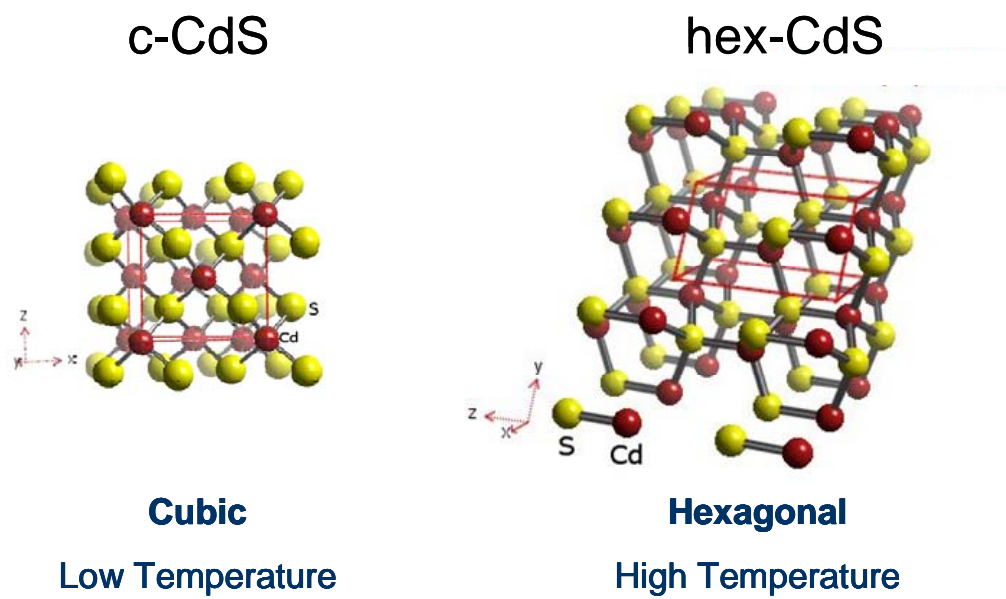


**Figure 6.3.** The structures of CdS

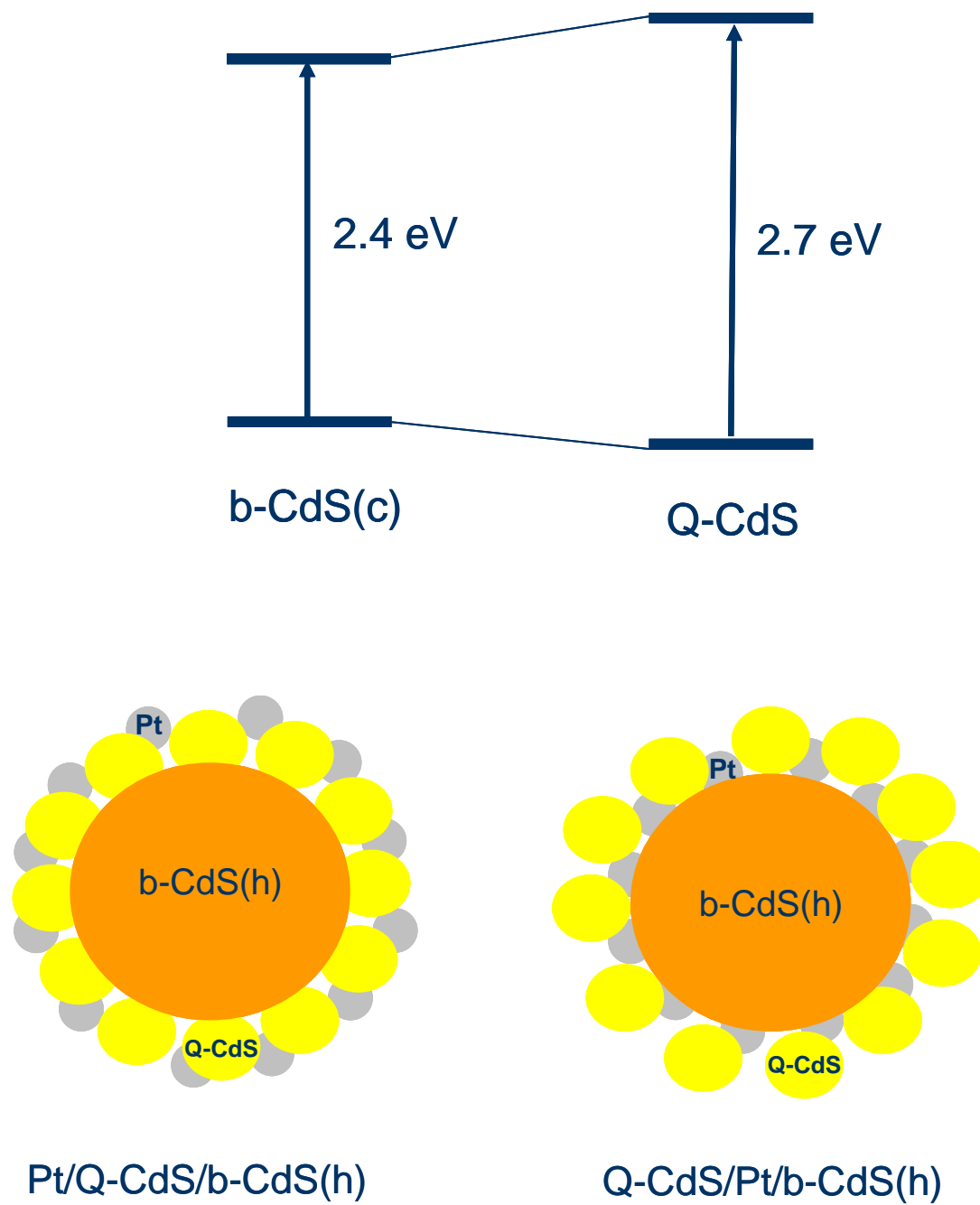


**Figure 6.4.** The schemes of synthesized nanocomposites

**TABLE 6.1.** Comparison of the observed rates of hydrogen production over CdS composites from two different aqueous solutions sacrificial electron donors: a) 30% Isopropanol (IPA) in water and b) sulfide/sulfite/hydroxide, 0.1 M Na<sub>2</sub>S, 0.02 M Na<sub>2</sub>SO<sub>3</sub>, and 1.0 M NaOH, with illumination at  $\lambda > 400$  nm

Photocatalyst	$d[\text{H}_2]/dt$ ( $\mu\text{mol g}^{-1} \text{h}^{-1}$ )	
	IPA	S <sup>2-</sup> /SO <sub>3</sub> <sup>2-</sup> /NaOH
c-CdS/Pt/hex-CdS	153	668
Pt/c-CdS/hex-CdS	1.8	537
c-CdS/hex-CdS	3.5	201
Pt/hex-CdS	45	412
hex-CdS	27	332

## References

- (1) Matsumura, M.; Ohnishi, H.; Hanafusa, K.; Tsubomura, H. *Bull. Chem. Soc. Jpn.* **1987**, *60*, 2001.
- (2) Matsumura, M.; Furukawa, S.; Saho, Y.; Tsubomura, H. *Journal of Physical Chemistry* **1985**, *89*, 1327.
- (3) Nosaka, Y.; Yamaguchi, K.; Kuwabara, A.; Miyama, H.; Baba, R.; Fujishima, A. *J. Photochem. Photobiol. A-Chem.* **1992**, *64*, 375.
- (4) Jin, Z. S.; Li, Q. L.; Zheng, X. H.; Xi, C. J.; Wang, C. P.; Zhang, H. Q.; Feng, L. B.; Wang, H. Q.; Chen, Z. S.; Jiang, Z. C. *J. Photochem. Photobiol. A-Chem.* **1993**, *71*, 85.
- (5) Mills, A.; Green, A. *J. Photochem. Photobiol. A-Chem.* **1991**, *59*, 199.
- (6) Janet, C. M.; Viswanath, R. P. *Nanotechnology* **2006**, *17*, 5271.
- (7) Jang, J. S.; Li, W.; Oh, S. H.; Lee, J. S. *Chem. Phys. Lett.* **2006**, *425*, 278.
- (8) Kormann, C.; Bahnemann, D. W.; Hoffmann, M. R. *Journal of Physical Chemistry* **1988**, *92*, 5196.
- (9) Bahnemann, D. W.; Kormann, C.; Hoffmann, M. R. *Journal of Physical Chemistry* **1987**, *91*, 3789.
- (10) Hoffmann, M. R.; Martin, S. T.; Choi, W. Y.; Bahnemann, D. W. *Chem. Rev.* **1995**, *95*, 69.
- (11) Hoffman, A. J.; Mills, G.; Yee, H.; Hoffmann, M. R. *Journal of Physical Chemistry* **1992**, *96*, 5546.
- (12) Martin, S. T.; Morrison, C. L.; Hoffmann, M. R. *Journal of Physical Chemistry* **1994**, *98*, 13695.

- (13) Martin, S. T.; Herrmann, H.; Choi, W. Y.; Hoffmann, M. R. *J. Chem. Soc.-Faraday Trans.* **1994**, *90*, 3315.
- (14) Martin, S. T.; Herrmann, H.; Hoffmann, M. R. *J. Chem. Soc.-Faraday Trans.* **1994**, *90*, 3323.
- (15) Choi, W. Y.; Termin, A.; Hoffmann, M. R. *Journal of Physical Chemistry* **1994**, *98*, 13669.
- (16) Hoffman, A. J.; Carraway, E. R.; Hoffmann, M. R. *Environ. Sci. Technol.* **1994**, *28*, 776.
- (17) Hoffman, A. J.; Yee, H.; Mills, G.; Hoffmann, M. R. *Journal of Physical Chemistry* **1992**, *96*, 5540.
- (18) Lee, J. S.; Choi, W. Y. *J. Phys. Chem. B* **2005**, *109*, 7399.
- (19) Ryu, S. Y.; Balcerski, W.; Lee, T. K.; Hoffmann, M. R. *J. Phys. Chem. C* **2007**,
- (20) Ryu, S. Y.; Choi, J.; Balcerski, W.; Lee, T. K.; Hoffmann, M. R. *Ind. Eng. Chem. Res.* **2007**, *46*, 7476.
- (21) Tsuji, I.; Kudo, A. *J. Photochem. Photobiol. A-Chem.* **2003**, *156*, 249.
- (22) Bessekhoud, Y.; Mohammedi, M.; Trari, M. *Sol. Energy Mater. Sol. Cells* **2002**, *73*, 339.

## **Chapter 7**

Sub-Pilot-Scale Hybrid Electrochemical System  
for Water Treatment and Hydrogen Production  
using a solar PV panel

## Abstract

There is a clear need for environmentally-friendly alternative energy sources (without carbon emissions) and photovoltaic/electrolysis for hydrogen production via water splitting using organic contaminants as sacrificial electron donors can be a potential solution. This chapter demonstrates the feasibility of a sub-pilot scaled rooftop hybrid photovoltaic-electrolysis system for wastewater treatment with simultaneous hydrogen production. Application of an anodic bias of  $> 2.0$  V to bismuth-doped  $\text{TiO}_2$  ( $\text{BiO}_x$ - $\text{TiO}_2$ )/Ti metal electrode results in the electrochemical degradation of a variety of organic contaminants (i.e., rhodamine B (Rh.B), methylene blue (MB), salicylic acid, triclosan, and phenol) and real wastewater from chemical industry, while molecular hydrogen is released at the counter stainless steel (SS) electrode. The kinetics of anodic substrates oxidation is investigated as a function of the cell current ( $I_{\text{cell}}$ ), substrate concentration, and background electrolytes such as NaCl and  $\text{Na}_2\text{SO}_4$ , and average current efficiencies are shown in the range of 4–22 %. Cathodic current efficiency and energy efficiency for hydrogen production was achieved at 50–70% and 20–40%, respectively.

## Introduction

In recent years, there has been increasing interest in an developing electrochemical method for wastewater treatment because of its advantages, including versatility, energy efficiency, amenability to automation, and robustness<sup>1-3</sup>. This technology was first tested with various synthetic wastewaters containing specific target compounds such as dyes and phenol<sup>4-7</sup>, and more recently has focused on the treatment of actual wastewaters, including domestic wastewater, industrial wastewater, and landfill leachate<sup>8-10</sup>. However, the main drawback of electrochemical wastewater treatment is its high operating cost due to high electric energy consumption.

Hydrogen is considered as a possible alternative energy resource<sup>11</sup>. However, most hydrogen is produced by the well-established thermal process known as steam methane reforming (SMR), which has both supply issues and significant carbon emissions. Therefore, transition to a hydrogen economy may be considered when alternative renewable technologies to replace fossil-based hydrogen production methods are developed. In this context, electrolytic production of hydrogen (i.e., water electrolysis) is a potential solution to produce large amounts of hydrogen without the carbon emission associated with fossil fuel. However, the primary disadvantage of water electrolysis is also the high electric consumption, especially in large-scale application.

Over the past decades, electrochemical applications for water splitting and for wastewater treatment have been independently studied. A dual-purpose hybrid electrolysis system that couples wastewater treatment with hydrogen generation may make the electrolysis system economically feasible. In a hybrid system, electrochemical oxidation of organic contaminants takes place at an anode while a reduction reaction

simultaneously takes place at the cathode, resulting in hydrogen production. In previous studies, our group successfully demonstrated a hybrid electrochemical cell consisting of  $\text{BiO}_x\text{-TiO}_2/\text{Ti}(0)$  anodes and stainless steel (SS) cathodes for the complete oxidation of phenol with simultaneous hydrogen production<sup>12-14</sup>.

In this study, we scaled up the hybrid electrolysis system to a sub-pilot size (a volume of 20 L) with  $\text{BiO}_x\text{-TiO}_2/\text{Ti}(0)$  anodes and SS cathodes to investigate the feasibility of a practical application. The kinetics of oxidative degradation of a variety of target substrates such as methylene blue (MB), rhodamine B (Rh.B), phenol, salicylic acid, triclosan, and waste organics in real industrial wastewater are investigated with simultaneous hydrogen production. In addition, a solar-driven rooftop hybrid electrolysis system using a commercial photovoltaic (PV) array is also investigated.

## **Experimental**

### **Electrode Preparation**

$\text{BiO}_x\text{-TiO}_2/\text{Ti}(0)$  electrode was used as an anode and stainless steel (SS, Hastelloy C-22) was used as a cathode. The anode consists of a series of metal oxide coatings on a titanium metal plate: (a) a Ti metal substrate, (b) an anti-passivation layer (pre-coat) having the mixture of  $\text{IrO}_2$  and  $\text{Ta}_2\text{O}_5$ , (c) an intermediated layer (seal coat) of  $\text{SnO}_2$  and  $\text{Bi}_2\text{O}_3$ , (d) a slurry coat containing particles of  $\text{TiO}_2$  doped with Bismuth (Bi), and (e) the overcoat with  $\text{TiO}_2$  and  $\text{Bi}_2\text{O}_3$ . Slurry coat and overcoat together form the electrocatalytic outer layer of the electrode and each coating step requires a specific heat treatment at different temperatures and durations. This electrode exhibits excellent stability and long service life<sup>15</sup>. More details on the anode preparation are provided elsewhere<sup>14,15</sup>. Each

electrode plate is about 800 cm<sup>2</sup> and a reactor consists of 5 anodes and 6 cathodes that face each other with an interelectrode gap of 2 mm. (Figure 7.1)

### **Electrolysis Experiments**

Electrolysis experiments were carried out in a sub-pilot scaled reactor with a volume of 20 L. Schematic diagram of the overall hybrid electrolysis is shown in Figure 7.1. The electrode couple (5 BiO<sub>x</sub>-TiO<sub>2</sub>/Ti(0) anodes and 6 SS cathodes) was immersed in 20 L of tap water. NaCl (J.T.Baker) was used as a primary supporting electrolyte in the range of 0–75 mM (typically 50 mM) and Na<sub>2</sub>SO<sub>4</sub> (EMD) was also used to compare electrolyte effect to NaCl. Seawater, which was collected from a beach area near Los Angeles, CA, was used as a source of electrolyte as well. For the electrochemical oxidation, the target substrates such as Methylene Blue (MB, J.T.Baker), Rhodamine B (Rh.B, Aldrich), salicylic acid (SA, Aldrich), phenol (PhOH, Mallinckrodt), and 5-chloro-2-(2,4-dichlorophenoxy)phenol (triclosan, Fluka) were added in a background electrolyte solution and the solution was continuously circulated by the pump connected to the bottom of a reactor. Most experiments were performed at circumneutral pH except the experiment of triclosan at pH 12 adjusted with NaOH (EM Science) because of its very low solubility in neutral pH. Electrochemical degradation of highly contaminated chemical industry wastewater, which was sampled from the wastewater stream of a manufacturing facility located in Minnesota, was also investigated. Original wastewater was diluted with tap water to a proper COD concentration for laboratory experiments (150–300 ppm). A constant current in a range between 7.5 A and 40 A (typically 25 A) or voltage (3–4 V) was applied to the electrode couples by a DC power supply (HP

6260B), and cell voltage ( $E_{\text{cell}}$ ) and cell current ( $I_{\text{cell}}$ ) were measured during electrolysis by multimeters (Fluke).

### **Solar-Driven Electrolysis Experiment**

For solar-driven electrolysis, a commercial polycrystalline silicon solar photovoltaic (PV) panel (Silicon Solar, Inc.) with a peak power output of 180 W ( $E_{\text{peak}} = 25.9$  V and  $I_{\text{peak}} = 6.95$  A, respectively) and with surface area of 1.50 m<sup>2</sup> (dimensions: 0.95 m × 1.57 m) was installed on the roof of the W. M. Keck Laboratories in Pasadena, CA. The solar PV panel was directly connected to a sub-pilot reactor to drive various electrochemical reactions such as the oxidative degradation of various organic contaminants and wastewater with simultaneous hydrogen production. Aqueous solutions of 50 mM NaCl and 2L (10 v/v %) of seawater were used as the primary electrolytes in the rooftop experiments. In addition to measurement of  $E_{\text{cell}}$  and  $I_{\text{cell}}$ , a real-time solar radiation was also monitored by a pyranometer (Apogee) with a datalogger (Campbell Scientific).

### **Analytical Methods**

Sample aliquots were withdrawn from the solution intermittently during the electrolysis and analyzed. The color removal of dyes was monitored by measuring the absorbance at 665 nm and 550 nm for MB and Rh.B, respectively, with a UV/Vis spectrophotometer. The degradation of phenol, salicylic acid, and triclosan were monitored using a HPLC (Agilent 1100 series) equipped with a C18 column and a UV detector. The mobile phase was composed of 45 % acetonitrile and 55 % Milli-Q water containing 0.1 wt % acetic acid. For real wastewater, the chemical oxygen demand

(COD) was measured titrimetrically with COD reagent vials (Hach), which use dichromate as the oxidant in acidic solution at 150 °C for 2 hrs. AgNO<sub>3</sub> (Aldrich) was added into sample solution before measuring COD to eliminate the chloride interference in cases where NaCl was used as an electrolyte. In addition, COD removal of other substrates was also measured to determine the current efficiencies for the anodic oxidations.

Molecular hydrogen (H<sub>2</sub>) produced from water during electrolysis was detected by a quadruple mass spectrometry (MS, Balzers). As shown in Figure 7.1, the reactor was sealed and the headspace gas of the reactor was extracted with a peristaltic pump and pushed into a quadruple MS with 70 eV electron ionization energy via a turbo pump (Pfeiffer; 5.0 × 10<sup>-6</sup> Torr). The production rate of H<sub>2</sub> was calculated from the volume percent of H<sub>2</sub> in the headspace gas, which was measured assuming that it was directly proportional to the percent of ion current of H<sub>2</sub> in total ion currents measured by MS.

### **Current Efficiency and Energy Efficiency**

The instantaneous current efficiencies (ICE) for anodic oxidations were calculated using the following equation introduced by Comninellis and Pulgarin<sup>6,16</sup>:

$$ICE (\%) = \frac{[COD_0 - COD_t]FV}{8It} \times 100$$

where COD<sub>0</sub> and COD<sub>t</sub> are the COD (in g O<sub>2</sub>/L) before and after electrolysis, respectively, F is the Faraday constant (96,487 C/mol), V is volume of the electrolyte (in L), I is the current (in A), and t is a reaction time (in s).

Since the ICE decreases with time during electrolysis to finally reach about zero, the electrochemical oxidation index (EOI), which expresses the average current efficiency, was also calculated from following equation:

$$EOI(\%) = \frac{\int ICE}{\tau}$$

where  $\tau$  is the time of electrolysis at which ICE is almost zero.

For H<sub>2</sub> production, the cathodic current efficiencies (CE) were calculated by the following:

$$CE (\%) \text{ for } H_2 = \frac{2 \times \text{numbers of } H_2 \text{ molecules produced}}{\text{numbers of electron flew}} \times 100$$

Energy efficiencies (EE) for H<sub>2</sub> production use the higher heating value of H<sub>2</sub> (HHV, 39 Wh/g) and the energy consumed by the system:

$$EE (\%) \text{ for } H_2 = \frac{39 \text{ Wh/g} \times H_2 \text{ prod. rate (mol/h)}}{E_{cell} (V) \times I_{cell} (A)} \times 100$$

In solar-powered electrolysis system, the energy efficiencies were calculated by the following equations:

$$\text{solar to } PV_{cell} \text{ EE (\%)} = \frac{E_{cell} (V) \times I_{cell} (A)}{\text{solar flux (W/m}^2) \times PV \text{ area (m}^2)} \times 100$$

$$\text{solar to } H_2 \text{ EE (\%)} = \frac{H_2 \text{ EE (\%)} \times \text{solar to } PV_{cell} \text{ EE (\%)}}{100}$$

## Results and Discussion

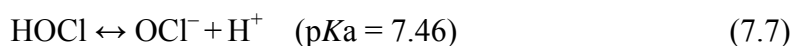
### Electrochemical Water Treatment

Figure 7.2(a) shows a typical  $E_{cell}$ - $I_{cell}$  curve at the BiO<sub>x</sub>-TiO<sub>2</sub>/Ti(0) anode coupled with stainless steel cathode in a sub-pilot reactor in presence of sodium chloride or

sodium sulfate as a supporting electrolyte. The current is generated around 2.0 V of applied voltage linearly increased above 2.5 V of  $E_{\text{cell}}$ . The use of  $\text{Na}_2\text{SO}_4$  as a supporting electrolyte generates higher current density than  $\text{NaCl}$  at the same applied voltage. We also measured  $E_{\text{cell}}-I_{\text{cell}}$  curve in the presence of 10 v/v% seawater, which was sampled from a beach area near Los Angeles, CA, instead of adding  $\text{NaCl}$  (since seawater typically contains 0.5 M  $\text{NaCl}$ ) and observed that current density in the presence of 10 v/v % seawater was slightly higher than that in 50 mM  $\text{NaCl}$ , which may be because of other salts present in seawater; conductivity of solution adding 10 v/v % of seawater was measured at 5.3–5.6 mS/cm. Figure 7.2(b) shows the current density as a function of the concentration of electrolytes at 3 V of applied voltage. The current density increases with the addition of electrolyte, but it does not increase much at high concentration of electrolyte (i.e., more than 50 mM). Therefore, the concentration of electrolytes was fixed at 50 mM (or 10 v/v % seawater) in the following experiments.

Figure 7.3 shows the effect of applied current density on the electrochemical degradation of organic substrates using  $\text{NaCl}$  or  $\text{Na}_2\text{SO}_4$  as supporting electrolytes in a sub-pilot reactor. Figure 7.3(a) shows the electrochemical degradation (i.e., color removal) of MB at different applied cell current in the presence of  $\text{NaCl}$ . As expected, increasing the current density resulted in a faster decolorization of MB due to a greater charge entering the cell and more electro-generating of oxidants such as  $\text{OH}\cdot$  radicals and active chlorine species. The decolorization follows first-order kinetics and the apparent degradation rate constant of MB ( $k_{\text{MB}}$ ) was proportional to the current density (Figure 7.3a, inset). Figure 7.3(b) also shows that the degradation rate constant of triclosan ( $k_{\text{TCS}}$ ) is increased as higher current density is applied in the presence of 50 mM  $\text{Na}_2\text{SO}_4$ .

The effect of type and concentration of electrolytes on MB degradation is investigated in Figure 7.4. Figure 7.4(a) shows that MB degradation in the presence of NaCl was much faster than Na<sub>2</sub>SO<sub>4</sub> although current density in the presence of NaCl was relatively lower than that in the presence of Na<sub>2</sub>SO<sub>4</sub> (Figure 7.2). The same tendency was observed in the degradation of other organic substrates, such as Rhodamine B (Rh.B) and salicylic acid (S.A.), as shown in Table 7.1. In the presence of 50 mM NaCl, half-life time ( $t_{1/2}$ ) for the degradation of Rh.B and S.A. was estimated less than 2 min each, whereas it was remarkably increased to 27 min and 77 min, respectively, in the presence of Na<sub>2</sub>SO<sub>4</sub>. It has been frequently reported that NaCl enhances the electrochemical degradation efficiency for various organic substrates (e.g., MB, phenol, glucose, and 17  $\beta$ -estradiol) as compared to Na<sub>2</sub>SO<sub>4</sub><sup>4,6,17,18</sup>. The electrochemical degradation of organic substrates can occur via direct oxidation on the anode surface (eq.7.1), indirect oxidation mediated by OH $\cdot$  radicals (eq.7.2), and indirect oxidation mediated by electro-generated oxidant from electrolyte solution such as Cl $\cdot$ , Cl<sub>2</sub> $\cdot^-$ , and OCl $\cdot^-$  in the presence of NaCl (eqs.7.3–7.7):



In the presence of NaCl electrolyte, active chlorine species such as  $\text{Cl}\cdot$ ,  $\text{Cl}_2\cdot^-$ , and  $\text{OCl}\cdot^-$ , which are electrochemically generated at the anode surface, act as powerful oxidants during electrolysis, resulting in fast substrates oxidation when compared to the use of other electrolytes. In our previous study,  $\text{Cl}_2\cdot^-$  was assumed the primary oxidant among various active chlorine species since the observed degradation rates are found to be proportional only to the bimolecular rate constants of  $\text{Cl}_2\cdot^-$  with the substrate<sup>13</sup>. On the other hand, indirect oxidation by  $\text{OH}\cdot$  radicals and  $\text{SO}_4\cdot^-$  radicals (eq.7.8) can take place in  $\text{Na}_2\text{SO}_4$  solution as well. However, substrates oxidation rates with  $\text{Na}_2\text{SO}_4$  are observed very low, implying that a lower concentration of  $\text{OH}\cdot$  radicals are produced in  $\text{Na}_2\text{SO}_4$  solution and(or)  $\text{SO}_4\cdot^-$  radicals are less determining of the reaction rates, in spite of their high redox potential. It is ascribed to the generation of surface-bound  $\text{SO}_4\cdot^-$  radicals at metal oxide electrode surface and reaction with another  $\text{SO}_4\cdot^-$  to produce persulfate (eq.7.9):



A substrate oxidation rate with 10 v/v % of seawater was even higher than that with 50 mM NaCl, suggesting that the seawater could be a good alternative source of NaCl electrolyte, as shown in Figure 7.4(a). Figure 7.4(b) shows the effect of the concentration of NaCl (SW) electrolyte on MB degradation rates. In the absence of NaCl electrolyte, MB was degraded very slowly ( $k_{\text{MB}} \sim 1.8 \times 10^{-2} \text{ min}^{-1}$ ) while MB degradation rates increased by an order of magnitude ( $k_{\text{MB}} = 1.1\text{--}3.9 \times 10^{-1} \text{ min}^{-1}$ ) as NaCl was added. However, degradation rates do not increase at higher concentration, which is similar to the change of current density as a function of the concentration of electrolyte (Figure

7.2b). Inset of Figure 7.4(b) shows a linear relationship of the degradation rates and current densities generated by adding different concentration of electrolytes, suggesting that electrolyte concentration can affect the degradation rates by a change of current density.

Table 7.1 summarizes the degradation rate constants of several organic substrates under various conditions. The initial concentration had no significant effect on MB degradation rate. For example,  $k_{\text{MB}}$  at  $[\text{MB}]_0 = 5 \mu\text{M}$  was faster than those at higher concentration of MB, however,  $k_{\text{MB}}$  does not decrease further over the range of 10–250  $\mu\text{M}$  (see Figure 7.5(a), inset, also). The half-life time ( $t_{1/2}$ ) for MB degradation at  $[\text{MB}]_0 = 10 \mu\text{M}$  and 250  $\mu\text{M}$  was estimated at 5 min and 7 min, respectively. However, the initial concentration of phenol significantly affects the apparent degradation rate of phenol. For example,  $k_{\text{PhOH}}$  decreased remarkably at higher concentration, which is due to production of a large number of reaction intermediates such as chlorinated phenols. Figure 7.5 also compares COD removal with the substrate removal of MB and phenol. For MB degradation, as expected, COD removal rate was slower than color removal rate, suggesting that MB was oxidized first to colorless intermediates and then oxidized further to  $\text{CO}_2$ . However,  $k_{\text{COD}}$  was almost similar to  $k_{\text{obs}}$  at  $[\text{MB}]_0 = 10 \mu\text{M}$  and 2 times higher than  $k_{\text{obs}}$  at  $[\text{MB}]_0 = 100 \mu\text{M}$  (Table 7.1). For phenol degradation, however, substrate degradation was completed within 2 min, but COD reduction was continued for more than 10 min (i.e.,  $k_{\text{COD}} \gg k_{\text{obs}}$  in Figure 7.5b). It implies that the COD reduction and full oxidation step of MB is simpler and(or) intermediates do not significantly interfere with parent MB molecules as compared to the process of COD reduction and mineralization of phenol.

The current efficiencies (i.e., ICE) of anodic substrate oxidations determined from COD measurement are shown in Figure 7.6. The current efficiency was higher at the initial stages (e.g., 85 % for MB oxidation) and decreased with time during electrolysis (Figure 7.6a). Current efficiency also depends on the type of substrates and applied current density. Low initial concentration results in higher current efficiencies. For example, low initial concentration of MB showed higher current efficiency than high initial concentration. In addition, current efficiency increases also with low applied current density whereas the substrate removal efficiency increases with high current density. The current efficiency of phenol at applied  $I_{\text{cell}}$  of 8 A was higher than that with 25 A applied. Figure 7.6(b) compares the average current efficiencies (i.e., EOI) for various substrates oxidation. The average current efficiencies were in the range of 10–20 % with the order of MB > Rh.B > phenol at the same initial concentration.

Figure 7.7 shows the electrochemical oxidation of real wastewater from chemical industry. COD decreased during electrolysis and the removal efficiency increased at high applied voltage. The average current efficiency was determined to be about 4%. It is relatively lower than current efficiencies (10–20 %) for the oxidation of a specific substrate, indicating that the real wastewater likely contain more persistent organic substrates and(or) other unknown species present in wastewater may compete to desirable substrate oxidation, resulting in low current efficiency.

In conclusion, our sub-pilot electrochemical system is proven for complete oxidation and mineralization of a variety of environmental organic pollutants and real wastewater. NaCl is the most effective electrolyte for fast wastewater treatment in our system, which can be replaced by seawater.

### **Simultaneous H<sub>2</sub> Production via Water Electrolysis**

A significant amount of H<sub>2</sub> is simultaneously produced from water electrolysis at the cathode in a sub-pilot hybrid electrochemical reactor under various conditions (Table 7.2). For pure water splitting in the absence of organic substrates, H<sub>2</sub> production rates are in the range of 3–5 L/hr and current efficiencies (CE) and energy efficiencies (EE) are about 50–60% and 20–35%, respectively. As expected, a sub-pilot reactor showed lower efficiency than a small size reactor with 35–60% of EE. The current efficiency and energy efficiency for H<sub>2</sub> production also decreased with increasing applied power, which showed the same tendency as substrates oxidation at the anode. In addition, we compared Na<sub>2</sub>SO<sub>4</sub> with NaCl and observed that Na<sub>2</sub>SO<sub>4</sub> was better than NaCl for the H<sub>2</sub> production efficiency. It may be due to high current densities generated in Na<sub>2</sub>SO<sub>4</sub> solution as compared to the same concentration of NaCl (Figure 7.2) and no electron relay between the anode and the cathode via chlorine species. In NaCl solution, active chlorine species produced at anode can be reduced again at the cathode and fewer electrons are available for H<sub>2</sub> production at cathode. When 10 v/v % of seawater was used as an electrolyte source, H<sub>2</sub> production rate is higher than in 50 mM NaCl.

In the presence of organic substrates such as MB and phenol, H<sub>2</sub> production rates measured at 5–6 L/hr of with simultaneous oxidation of substrates. H<sub>2</sub> production rates remained almost constant before and after adding organic substrates. In addition, a similar H<sub>2</sub> production rate was obtained with industrial wastewater as well, suggesting that the presence of waste organics in solution does not have a negative effect on cathodic H<sub>2</sub> production. In previous studies, we have suggested that some organic substrates can actually increase H<sub>2</sub> production energy efficiencies by 30–50% in a NaCl electrolyte

system by quenching active chlorine species, which compete with H<sub>2</sub> production reactions for cathodic electrons<sup>13,14</sup>. Active chlorine species can act as an electron shuttle by being oxidized at the anode and reduced at the cathode. If organic substrates are added, however, substrates are rapidly oxidized by active chlorine species and this electron relay can be consequently inhibited, resulting in increasing H<sub>2</sub> production rates by making more electrons available at the cathode. However, this synergic effect on H<sub>2</sub> production was not observed with industrial wastewater treatment in a sub-pilot electrolysis system, which may be because a synergic effect is dependent on the type of organic substrates<sup>13</sup>. It may also be due to relatively low production rates of active chlorine species as compared with H<sub>2</sub> production rates in a sub-pilot system. For example, we compared H<sub>2</sub> production rate with hypochlorite (OCl<sup>-</sup>) production rate, which is one of the active chlorine species and easily detected using UV/vis spectrometer. In a small size of electrochemical reactor, H<sub>2</sub> production rate of 100–300 μM/min was comparable to OCl<sup>-</sup> production rate of 100–150 μM/min, which can result in big inhibition effect of active chlorine species on the H<sub>2</sub> production reactor. In a sub-pilot reaction, however, H<sub>2</sub> production rate significantly increased to 3–5 mM/min whereas OCl<sup>-</sup> production rate was still remained similar (200 μM/min).

### **Solar-Driven Hybrid Electrolysis System**

Figure 7.8 shows the results of solar-driven photovoltaic-electrolysis experiments with our sub-pilot hybrid reactor, which was performed on the rooftop of W. M. Keck Laboratories at Caltech in August 2009. We directly connected 180 W<sub>peak</sub>-rated commercial PV panel with surface area of 1.50 m<sup>2</sup> to BiO<sub>x</sub>-TiO<sub>2</sub>/Ti(0) anode and SS

cathode. Figure 7.8(a) shows typical time profiles of solar light radiation energy measured by a pyranometer,  $E_{\text{cell}}$ , and  $I_{\text{cell}}$  on sunny day. The peak of solar radiation energy was measured about  $1000 \text{ W/m}^2$  around 12:30 PM and decreased to  $600 \text{ W/m}^2$  in the late afternoon.  $E_{\text{cell}}$  measured 3.3 V in the presence of 10 v/v % seawater as an electrolyte and slightly decreased to 3.0 V in the afternoon as solar irradiation energy decreased while  $I_{\text{cell}}$  was measured about 7 A both in the morning and in late afternoon. Solar irradiation energy,  $E_{\text{cell}}$  and  $I_{\text{cell}}$  was measured for several days including a partly cloudy day on August, 2009 and remained approximately constant with  $E_{\text{cell}}$  of 2.7–3.3 V and  $I_{\text{cell}}$  of 6–7 A. The actual PV output power was measured 23 W, which is only 13 % of  $PV_{\text{peak}}$  output power reported by supplier, possibly due to losses from wiring, heat, and coupling to the electrolyzer. Solar-to- $PV_{\text{cell}}$  energy efficiency was determined to be 1.6–2.0 %, whereas it was about 2.5 % with a system consisting of a  $6.4 \text{ W}_{\text{peak}}$ -rated small PV panel (the area of  $0.13 \text{ m}^2$ ) and a small electrolyzer (200 mL).

MB and industrial wastewater were effectively treated in spite of low output power, as shown in Figure 7.8(b). For example, the apparent kinetic constant for COD reduction ( $k_{\text{COD}}$ ) of 3M wastewater with solar-driven system by PV array operating at 21 W ( $E_{\text{cell}} \times I_{\text{cell}} = 3.0 \text{ V} \times 7 \text{ A}$ ) was estimated to be  $9.0 \times 10^{-3} \text{ min}^{-1}$ , which is a similar  $k_{\text{COD}}$  to DC-powered oxidation operated at 45 W ( $E_{\text{cell}} \times I_{\text{cell}} = 3.0 \text{ V} \times 15 \text{ A}$ ). The average current efficiency for industrial wastewater oxidation was increased to 15% in solar-driven system, which is almost 4 times higher than that with DC-powered oxidation. This high efficiency may be because the photo-assisted electrochemical (i.e., photoelectrochemical, PEC) reactions took place in solar-powered rooftop experiment. A sub-pilot electrolyzer was installed on the roof as well to connect directly to the PV panel, and therefore some

of the solar-light could pass through the reactor and the PEC processes could be initiated by doped TiO<sub>2</sub> particles coated on an anode surface. Preliminary results of laboratory experiment with a medium size of electrochemical reactor and using the artificial UV lamp shows that the electrochemical oxidation rates of phenol were increased with UV light irradiation, indicating that the PEC processes actually take place on BiO<sub>x</sub>-TiO<sub>2</sub>/Ti(0).

In solar-driven hybrid electrolysis system, it was also observed that sufficient amount of H<sub>2</sub> was continuously produced with simultaneous oxidation of waste organic substrates. H<sub>2</sub> production rate was measured at 2.2 L/hr, which was smaller than that of the DC-powered system (Table 7.2). In spite of relatively low power, however, CE and EE were increased to 74 % and 38 %, respectively. Like anodic oxidation, high CE and EE for H<sub>2</sub> production in solar-driven electrolysis system can be ascribed to photocatalytic activity of TiO<sub>2</sub> on anode surface. In DC-powered electrolysis with a medium size of electrolyzer, we also found that photoelectrochemical (PEC) H<sub>2</sub> production rates under UV light irradiation were almost 2 times higher than electrochemical H<sub>2</sub> production rates in the absence of UV light. Solar-to-H<sub>2</sub> energy efficiency was determined 0.8 %.

### **Practical Application**

The above results show an example of a sub-pilot hybrid photovoltaic-electrolysis system, which has dual purposes for both wastewater treatment and H<sub>2</sub> production. In the solar-driven experiment, solar-to-H<sub>2</sub> energy efficiency was estimated less than 1 %, which was lower than other commercial PV-electrolysis systems in the range of 2–10 %<sup>19-22</sup>. However, it is difficult to compare our hybrid PV-electrolysis system with other

commercial PV-electrolysis systems since ours has several distinguishable advantages for practical application. First, our hybrid PV-electrolysis system can be operated at mild conditions, whereas other types of PV-electrolysis systems can be only operated at much harsher conditions. For example, the alkaline water electrolyzer, the most commercialized electrolyzer, uses an extremely high concentration of alkaline electrolytes (i.e., 6–7 M KOH) resulting in high pH environment which is also operated at about 70–80 °C in general and under pressure is desirable to minimize energy requirement<sup>23</sup>. However, our hybrid PV-electrolysis system can be effectively operated at circum-neutral pH condition and relatively low concentration of electrolyte (e.g., 50 mM NaCl). Second, our PV-electrolysis system has dual purposes for real wastewater treatment and H<sub>2</sub> production, which can make this technology economically feasible. Other PV-electrolysis systems that previously reported generally use alkaline electrolyzer or PEM electrolyzer (a second commercially available electrolyzer), which is impractical for application to water treatment. On the other hand, our sub-pilot PV-electrolysis system is also working for various wastewater treatments, suggesting that electrochemical water treatment can be successfully implanted with water splitting into hydrogen.

The PV-electrolysis system employed in this study can be also distinguished from other electrochemical water treatment system in terms of using new types of anode material and PV array for power supply. For example, boron-doped diamond electrode (BDD) is known as the most promising anode for wastewater treatment because of its high stability, wide potential window of water discharge, and a relatively low background current<sup>24-26</sup>. Jiang et al. also showed that the decomposition of waste organics and

simultaneous hydrogen production are feasible with a boron-doped diamond (BOD) electrode<sup>24</sup>. However, pilot scale application would be limited with BOD electrode due to its high price and size limitation since the production typically involves chemical vapor deposition (CVD) or high pressure-high temperature (HPHT) processes<sup>27</sup>. On the other hand, the Bi-doped TiO<sub>2</sub> anode employed in this study had been easily manufactured in a pilot scale with relatively low cost<sup>15</sup>. In addition, a PV-electrolysis system for environmental applications (i.e., water treatment) was proposed to reduce the operating cost– in a way not demonstrated before to our knowledge<sup>24</sup>. In this study, we demonstrated a sub-pilot PV-electrolysis system for water treatment and also showed a synergic effect on water treatment as compared to DC-powered system, since photoelectrochemical processes can be possible with Bi-doped TiO<sub>2</sub> anodes when a photovoltaic system is combined.

**Figure 7.1.** Schematic diagram of a sub-pilot electrochemical reactor and overall hybrid system

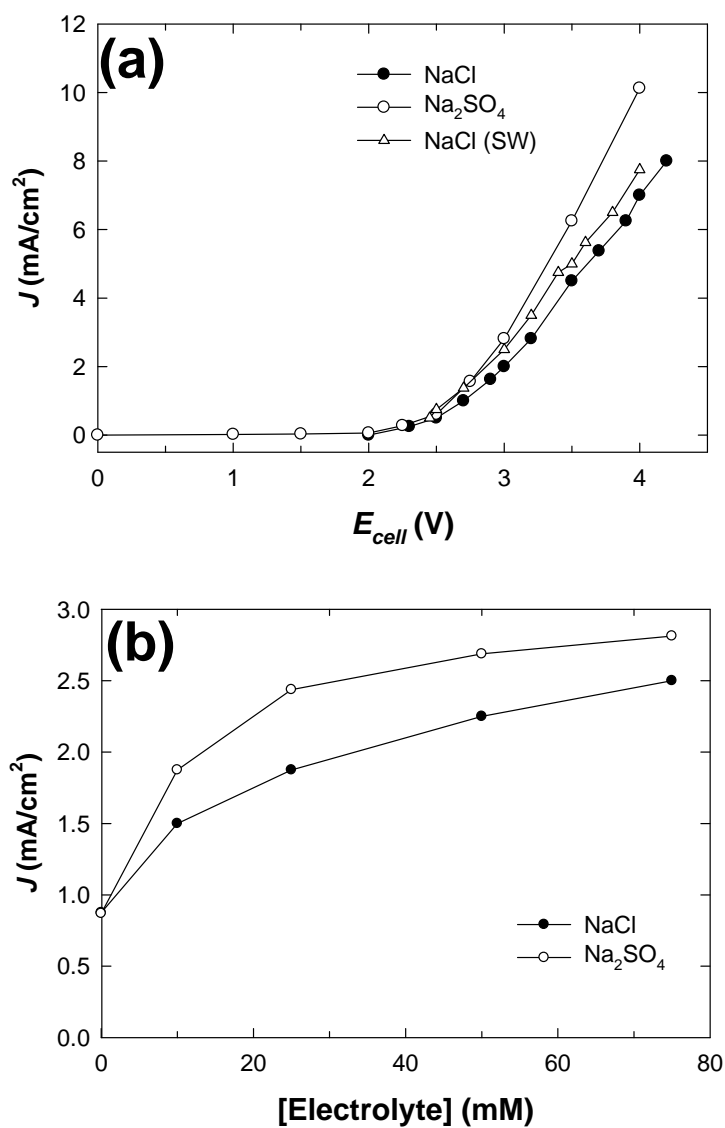


**Figure 7.2.** (a)  $E_{cell}$ - $I_{cell}$  plot in the presence of 50 mM NaCl or Na<sub>2</sub>SO<sub>4</sub> as a supporting electrolyte. NaCl (SW) indicates 10 v/v % of seawater as a source of NaCl electrolyte. (b) The current density ( $J_{cell}$ ) as a function of the concentration of the electrolyte (mM) at applied  $E_{cell} = 3.0$  V

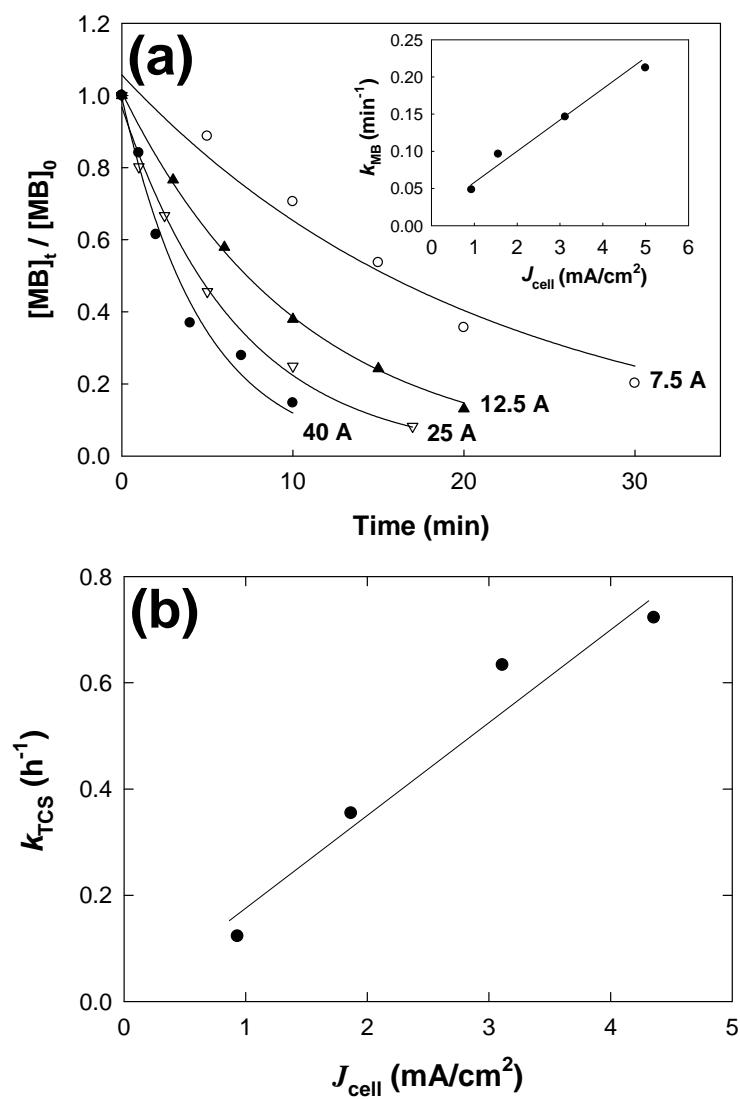


**Figure 7.3.** Electrochemical degradation of organic substrates as a function of applied current density: (a) The degradation of methylene blue ( $[MB]_0 = 10 \mu\text{M}$ ) in 50 mM NaCl, (b) the degradation of triclosan ( $[TCS]_0 = 100 \mu\text{M}$ ) in 50 mM  $\text{Na}_2\text{SO}_4$ .

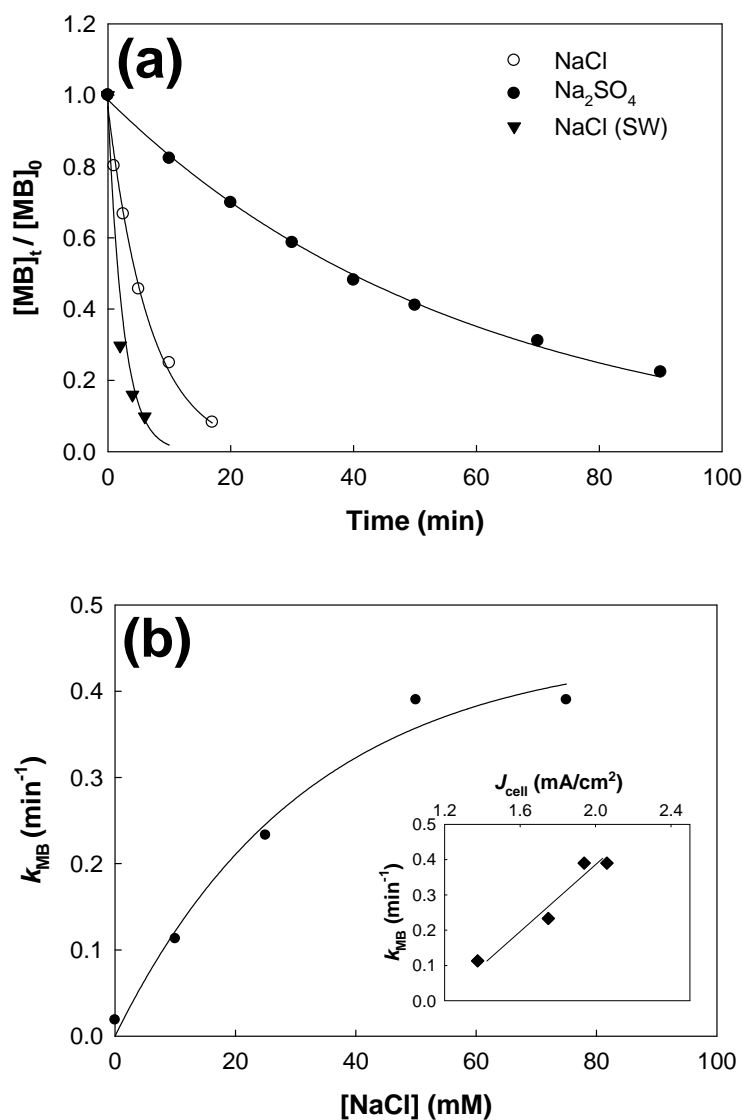


**Figure 7.4.** (a) Electrochemical degradation of methylene blue (MB) in the presence of different types of electrolyte at  $I_{cell}= 25A$ ,  $[MB]_0= 10 \mu M$ . 50 mM NaCl, 50 mM  $Na_2SO_4$ , and 10 v/v % seawater (NaCl, SW) were used as background electrolytes. (b) The color removal rate constant of MB as a function of the concentration of NaCl (SW) electrolyte at  $E_{cell}= 3 V$ ,  $[MB]_0= 10 \mu M$ .

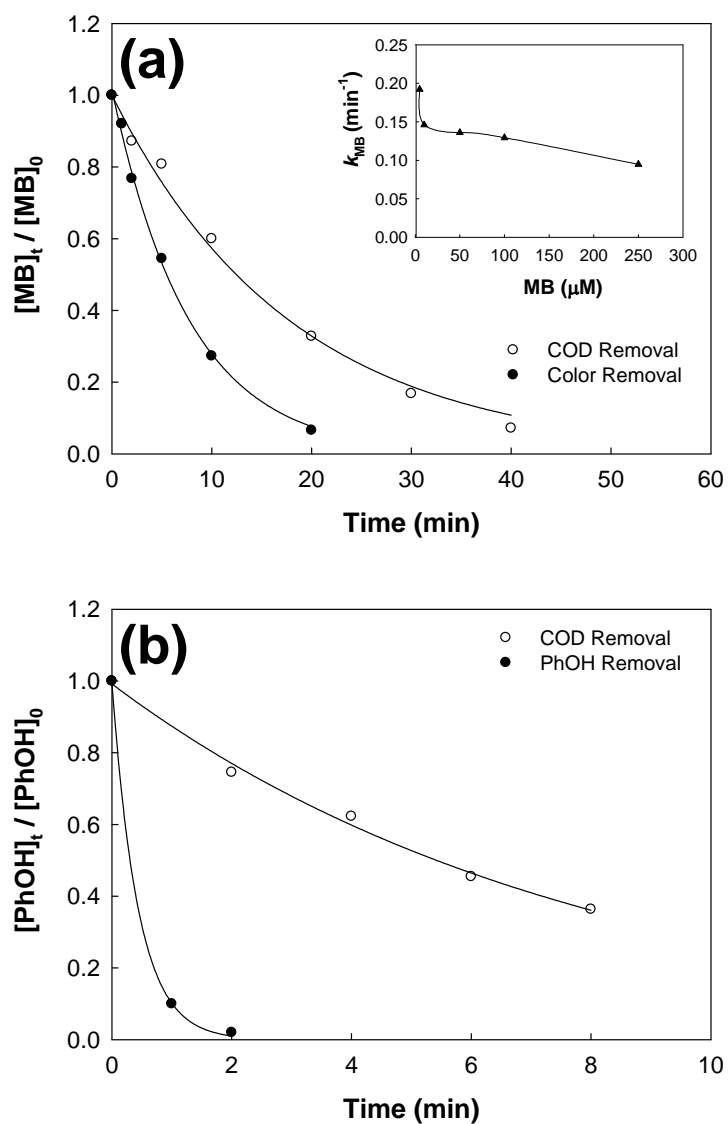


**Figure 7.5.** The electrochemical degradation of organic substrates vs. COD removal for (a) MB and (b) phenol at applied  $I_{cell} = 25A$  in the presence of 50 mM NaCl ( $[MB]_0 = 10$  or 100  $\mu$ M,  $[PhOH]_0 = 100 \mu$ M)

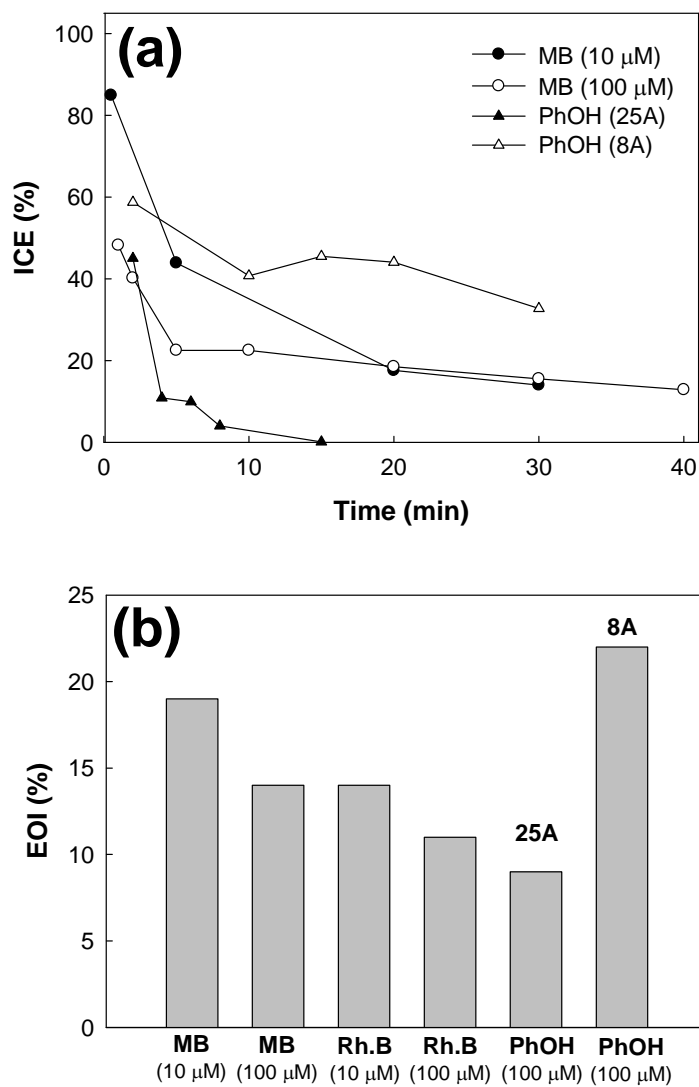


**Figure 7.6.** (a) Time profile of current efficiencies (ICE) and (b) average current efficiencies (EOI) for various substrates oxidations:  $[\text{MB}]_0 = 10$  or  $100 \mu\text{M}$ ,  $[\text{Rh.B}]_0 = 10$  or  $100 \mu\text{M}$ ,  $[\text{PhOH}]_0 = 100 \mu\text{M}$ ,  $[\text{NaCl}(\text{SW})] = 50 \text{ mM}$ ,  $I_{\text{cell}} = 25 \text{ A}$  applied except PhOH(8A).

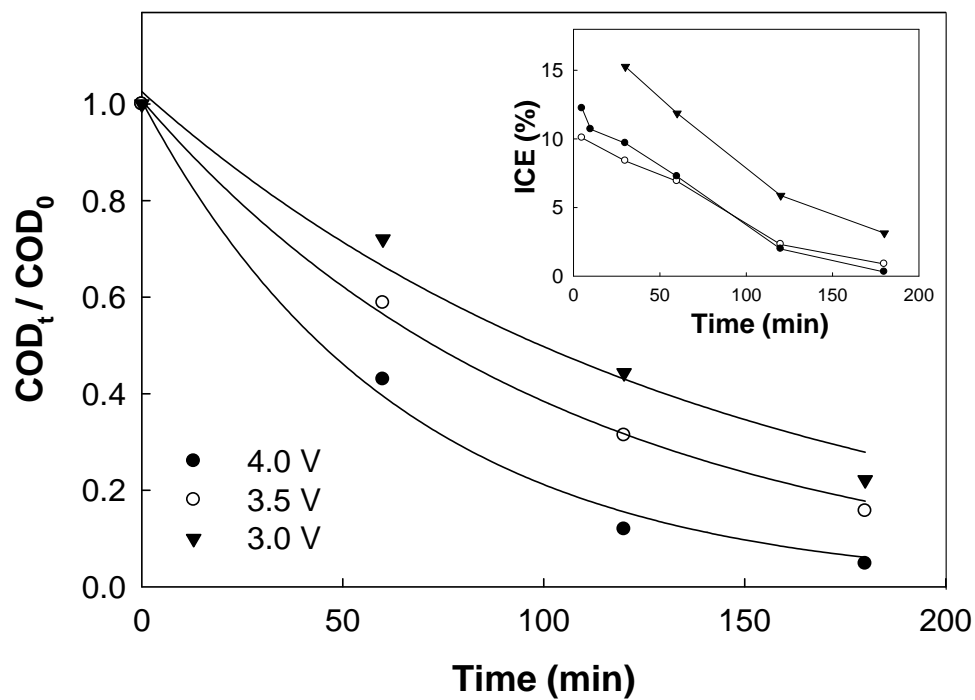


**Figure 7.7.** Electrochemical oxidation of industrial wastewater samples ( $COD_0= 100\text{--}150$  ppm) at different applied voltages. 10 v/v % (2L) seawater was used as a source of NaCl electrolyte. Inset graph shows the current efficiencies and average current efficiency was determined about 4 %.

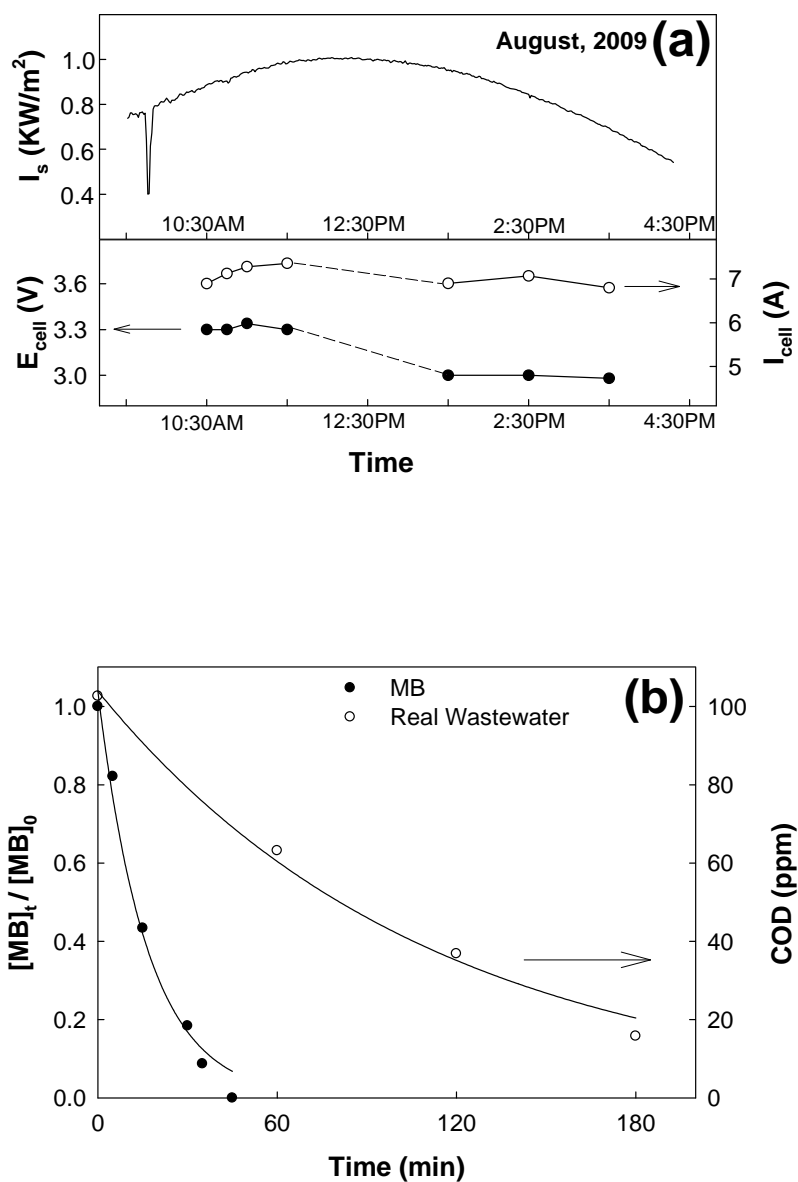


**Figure 7.8.** Solar-powered rooftop experiment: (a) solar intensity, cell current and cell voltage, which are measured during daytime. (b) The degradation of MB ( $[MB]_0 = 100 \mu\text{M}$ ) and COD removal of industrial wastewater ( $\text{COD}_0 = 100 \text{ ppm}$ ). 10 v/v % (2L) seawater was used as an electrolyte in all experiments.

**TABLE 7.1.** The degradation rate constants for anodic oxidation of several organic substrates: 20 L sub-pilot reactor,  $I_{\text{cell}} = 25$  A applied, [electrolyte]= 0.05M.

Substrate	Conc. ( $\mu\text{M}$ )	Electrolyte	$k_{\text{obs}}$ ( $\text{min}^{-1}$ )	$t_{1/2}$ (min)	$k_{\text{COD}}$ ( $\text{min}^{-1}$ )
MB	5	NaCl	0.192	3.6	
	10	NaCl	0.146	4.7	0.130
	50	NaCl	0.136	5.1	
	100	NaCl	0.129	5.4	0.056
	250	NaCl	0.095	7.3	
PhOH	100	NaCl	2.320	0.3	0.124
	250	NaCl	1.190	0.6	
	1000	NaCl	0.360	1.9	
Rh.B	100	NaCl	0.379	1.8	0.259
	100	Na <sub>2</sub> SO <sub>4</sub>	0.026	27	
S.A.	100	NaCl	0.420	1.7	
	100	Na <sub>2</sub> SO <sub>4</sub>	0.009	77	

**TABLE 7.2.** The rate, cathodic current efficiency (CE), and energy efficiency (EE) of hydrogen production: 20 L sub-pilot reactor, constant current applied, 0.05M of electrolyte used. (s.w. means 10 v/v % of seawater)

<b>Substrate</b>	<b>I<sub>cell</sub> (A)</b>	<b>E<sub>cell</sub> (V)</b>	<b>Electrolyte</b>	<b>H<sub>2</sub> prod. rate (L/hr)</b>	<b>CE (%)</b>	<b>EE (%)</b>
water only	12.5	2.85	NaCl	3.2	60	31
	20	3.00	NaCl	4.0	48	23
	25	3.23	NaCl	4.3	42	19
	25	3.23	s.w.	5.0	48	21
	25	3.17	Na <sub>2</sub> SO <sub>4</sub>	5.2	50	23
MB	25	3.25	s.w.	5.3	51	23
PhOH	25	3.25	s.w.	5.7	55	25
wastewater	25	3.23	s.w.	5.0	48	22
wastewater (PV)	7	2.82	s.w.	2.2	74	38

## References

- (1) Juttner, K.; Galla, U.; Schmieder, H. *Electrochim. Acta* **2000**, *45*, 2575.
- (2) Chen, G. H. *Sep. Purif. Technol.* **2004**, *38*, 11.
- (3) Anglada, A.; Urriaga, A.; Ortiz, I. *Journal of Chemical Technology & Biotechnology* **2009**, DOI: 10.1002/jctb.2214
- (4) Panizza, M.; Barbucci, A.; Ricotti, R.; Cerisola, G. *Sep. Purif. Technol.* **2007**, *54*, 382.
- (5) Shen, Z. M.; Yang, J.; Hu, X. F.; Lei, Y. M.; Ji, X. L.; Jia, J. P.; Wang, W. H. *Environ. Sci. Technol.* **2005**, *39*, 1819.
- (6) Comninellis, C.; Nerini, A. *J. Appl. Electrochem.* **1995**, *25*, 23.
- (7) Iniesta, J.; Michaud, P. A.; Panizza, M.; Cerisola, G.; Aldaz, A.; Comninellis, C. *Electrochim. Acta* **2001**, *46*, 3573.
- (8) Vlyssides, A. G.; Karlis, P. K.; Rori, N.; Zorpas, A. A. *J. Hazard. Mater.* **2002**, *95*, 215.
- (9) Vaghela, S. S.; Jethva, A. D.; Mehta, B. B.; Dave, S. P.; Adimurthy, S.; Ramachandraiah, G. *Environ. Sci. Technol.* **2005**, *39*, 2848.
- (10) Urriaga, A.; Rueda, A.; Anglada, A.; Ortiz, I. *J. Hazard. Mater.* **2009**, *166*, 1530.
- (11) *International Energy Outlook 2006; DOE/EIA=0484(2008)*; Energy Information Administration, U.S. Department of Energy: Washington, DC, 2008.
- (12) Park, H.; Vecitis, C. D.; Choi, W.; Weres, O.; Hoffmann, M. R. *J. Phys. Chem. C* **2008**, *112*, 885.
- (13) Park, H.; Vecitis, C. D.; Hoffmann, M. R. *J. Phys. Chem. C* **2009**, *113*, 7935.
- (14) Park, H.; Vecitis, C. D.; Hoffmann, M. R. *J. Phys. Chem. A* **2008**, *112*, 7616.

- (15) Weres, O. Electrode with Surface comprising Oxides of Titanium and Bismuth and Water Purification Process Using This Electrode. In *United States Patent*, January 4, 2007.
- (16) Comninellis, C.; Pulgarin, C. *J. Appl. Electrochem.* **1991**, *21*, 703.
- (17) Murugananthan, M.; Yoshihara, S.; Rakuma, T.; Uehara, N.; Shirakashi, T. *Electrochim. Acta* **2007**, *52*, 3242.
- (18) Bonfatti, F.; Ferro, S.; Lavezzo, F.; Malacarne, M.; Lodi, G.; De Battisti, A. *J. Electrochem. Soc.* **2000**, *147*, 592.
- (19) Ahmad, G. E.; El Shenawy, E. T. *Renewable Energy* **2006**, *31*, 1043.
- (20) Hollmuller, P.; Joubert, J. M.; Lachal, B.; Yvon, K. *Int. J. Hydrogen Energy* **2000**, *25*, 97.
- (21) Lehman, P. A.; Chamberlin, C. E.; Pauletto, G.; Rocheleau, M. A. *Int. J. Hydrogen Energy* **1997**, *22*, 465.
- (22) Gibson, T. L.; Kelly, N. A. *Int. J. Hydrogen Energy* **2008**, *33*, 5931.
- (23) Srinivasan, S. *Fuel cells: from fundamentals to applications*; Springer: New York, 2006.
- (24) Jiang, J. Y.; Chang, M.; Pan, P. *Environ. Sci. Technol.* **2008**, *42*, 3059.
- (25) Cabeza, A.; Urtiaga, A. M.; Ortiz, I. *Ind. Eng. Chem. Res.* **2007**, *46*, 1439.
- (26) Montanaro, D.; Petrucci, E.; Merli, C. "Anodic, cathodic and combined treatments for the electrochemical oxidation of an effluent from the flame retardant industry", 2008.
- (27) Kraft, A. *Int. J. Electrochem. Sci.* **2007**, *2*, 355.